Efficient first principles computational approaches to non-equilibrium electron-ion dynamics in solids

Gutachter/innen der Dissertation:	Prof. Dr. Angel Rubio
	Dr. Aaron Kelly
Zusammensetzung der Prüfungskommission:	Prof. Dr. Angel Rubio
	Prof. Dr. Francesca Calegari
	Dr. Aaron Kelly
	Prof. Dr. Caterina Cocchi
	Prof. Dr. Michael Potthoff
Vorsitzender der Prüfungskommission:	Prof. Dr. Michael Potthoff
Datum der Disputation:	7. Dezember 2023
Vorsitzender Fach-Promotionsausschusses PHYSIK:	Prof. Dr. Günter H.W. Sigl
Leiter des Fachbereichs PHYSIK:	Prof. Dr. Wolfgang J. Parak
Dekan der Fakultät MIN:	Prof. Dr. Heinrich Graener

Eidesstattliche Versicherung

Hiermit versichere ich an Eides statt, die vorliegende Dissertationsschrift selbst verfasst und keine anderen als die angegebenen Hilfsmittel und Quellen benutzt zu haben.
Die eingereichte schriftliche Fassung entspricht der auf dem elektronischen Speichermedium.
Die Dissertation wurde in der vorgelegten oder einer ähnlichen Form nicht schon einmal in einem früheren Promotionsverfahren angenommen oder als ungenügend beurteilt.

Hamburg, den 20.7.2023

Preface

The work leading up to this cumulative dissertation was conducted from October 2018 to April 2023 at the Max Planck Institute for the Structure and Dynamics of Matter and the University of Hamburg under the supervision of Prof. Dr. Angel Rubio and Dr. Aaron Kelly. This thesis is based on the publications and manuscript presented in Sec. 2, done in collaboration with Dr. Shunsuke Sato and Dr. Guillermo Albareda, in which we develop novel computational correlated dynamics approaches and utilize semi-classical simulation techniques to capture electron-nuclear interactions in molecules and solids in both equilibrium and laser driven non-equilibrium regimes.

Acknowledgements

This thesis would not have been possible without the support of many, many people. First of all I would like to thank Angel for his generous support, who gave me wide ranging opportunities and encouraged me to take all of them, Aaron, who supported and guided me throughout the past five years, Shunsuke, whose understated insights often changed the entire trajectory of projects, and Guillermo whose creativity and persistence acted as an inspiration. I would like to thank many people for innumerable illuminating discussions especially Ruggi whose clarity and wit brought seemingly opaque concepts into sharp relief and Andrey with whom wide ranging late night conversations invigorated the imagination. I am grateful to Ofer, Jonathan, Mukhtar, Hannes and Umberto for their clarity in explaining several key concepts in non-equilibrium dynamics, semi-classical dynamics and transient absorption, and to the Octopus crew for helping me navigate the many armed creature, specifically Heiko, Martin, Micael, Nicolas and Sebastian, as well as Meisam for showing us around München and recommending 8 hour long Hungarian films. Neda also has my gratitude for bending the rules to facilitate more opportunities and being a strong advocate and friend to all the IMPRS students.

This thesis would also not have been possible without time to recover my wits after every week, and it's in this regard that I'm extremely fortunate to have made so many good friends and fond memories over the last five years. The free flowing, long ranging and delightfully weird conversations about life, the universe and everything with Miguel, Giacomo and Chris, the evenings of food, dancing and expert cocktails with Meredith, lessons in sustainable agriculture and St. Petersburg post-punk from Dima, vigorous debates on the nature of society and morality with Karen, long walks and mountains of food with Ilke and Francesco, stream of consciousness discussions with Lukas in the style of the neighbor from Home Improvement, Valeriia's impeccable fashion sense, exploring the outer limits of shock comedy with Shahram, hiking in the Schwarzwald with Ed, Joe and Abishek, the ever growing Friday night dinner club, and being soundly beaten by Paolo at darts, Damian at chess, and mixed results with Niloo at Mortal Kombat.

I would not be here if it were not for my parents encouraging and supporting my love for science from an early age, as well as my godfather Jim who is ever engaging to a curious mind. Finally, the person who undergirded me throughout, whose love, understanding, patience and outstanding cookery were an unfailing source of respite, Mona. To all of you and those others too numerous to mention, thank you all!

Contents

1 | Abstract

The development of laser technology allowing precision control over the temporal and spatial profile of ultrafast, highly intense laser pulses, together with the advent of novel means of manipulating static material properties such as layering of 2D materials and tuning cavity confined photon interactions, present substantial opportunities for the engineering of exotic, technologically desirable properties through coherent manipulation of quantum degrees of freedom. However, due to being developed within an equilibrium, perturbative or steady-state context, the theoretical capacity to predict and interpret the rich diversity of ultrafast, far-from equilibrium phenomena observed in experiments in extended systems is oftentimes lacking beyond a coarse phenomenological explanation, or a perturbative approach which oftentimes fails for such strong driving. This is particularly true when assessing one of the most fundamental interactions in matter: the electron-nuclear interaction. While the simulation of strongly driven, non-equilibrium, electron-nuclear dynamics can be done with near exactness for small molecular systems, these quantum chemistry methods face substantial challenges in being applied to extended systems. This thesis collects research done by the author and collaborators to develop and extend simulation methods originating from quantum chemistry which can capture strongly driven electron-nuclear dynamics without dependence on the Born-Oppenheimer framework to extended systems. By transitioning away from the constraints of Born-Oppenheimer, our goal is to develop robust, scalable simulation protocols which can replicate and predict experimental observations in a first-principles, *ab-initio* manner, across a broad range of dynamical regimes and material phases.

After giving an overview of some of the experimental phenomena we are trying to address, we give a brief introduction to some aspects of the existing theoretical framework for addressing electron-nuclear interactions as embodied in the Born-Oppenheimer approximation as well as the perturbative and non-perturbative real time-dynamics approaches used to calculate material properties. In the subsequent sections we contextualize the papers presented with a discussion of the primary questions addressed by each, the progress made by others in the field and the contribution made by the author. We first discuss our development of a unique, real-space, grid based ab-intio wavefunction dynamics approach which is capable of exactly capturing electron-nuclear and electron-electron correlation effects in both equilibrium and laser driven regimes across a variety of physical systems and discuss the developments which would be required in order to make this method scalable and competitive. We next apply a semi-classical dynamics method, Multi-trajectory Ehrenfest (MTEF), based on an ensemble of nuclear trajectories which can exactly recover the initial quantum nuclear state, while capturing the electron-nuclear dynamics at the mean-field level. The equations of motion underlying this method are universally implemented throughout real-time ab-initio dynamics code bases, making this approach instantly accessible to the broader community. We find that in combination with a real-space basis treatment of the electronic degrees of freedom, MTEF is able to recover quantum nuclear effects on the equilibrium absorption spectrum of molecules, and demonstrate the ease with which this method can be incorporated into existing simulation protocols. Being semi-classical in nature, MTEF allows for scaling to very large system sizes, while the real space representation

1 Abstract

of the electronic system allows arbitrarily strong laser driving and the dynamical treatment of the ions allows significant nuclear rearrangement of the nuclear system.

We subsequently apply MTEF for the first time to realistic periodic systems in a manner which is generically applicable to any material in order to simulate the sub-30 fs phonon-mediated relaxation of valley selectively excited charge carriers in hexagonal Boron Nitride (hBN) across temperatures spanning 2000 K. We are able to use MTEF to simulate arbitrarily strong pump-probe measurements of the carrier relaxation and directly replicate a recent 'light-wave engineering' experiment on hBN *in-silico*. We find that MTEF constitutes a natural extension of static methods which are widely used to calculate the phonon renormalized equilibrium properties of materials, and that for the far-from-equilibrium phenomena studied, our method converges with a very small number of trajectories. Thus we ultimately develop and present a method which is simple to use, accurate, rapidly convergent, and which is capable of capturing strongly driven electron-phonon dynamics in periodic systems under arbitrary pump-probe setups. We conclude with a discussion on the research which will follow on the basis of our providing this much needed tool to simulate the strongly driven dynamics of quantum materials.

2

1.1 Zusammenfassung

Die Entwicklung von Lasertechnologie, die eine präzise Steuerung des zeitlichen und räumlichen Profils ultraschneller, hochintensiver Laserpulse ermöglicht, bietet zusammen mit dem Aufkommen neuartiger Mittel zur Manipulation statischer Materialeigenschaften, wie z. B. der Schichtung von 2D-Materialien und der Abstimmung hohlraumbegrenzter Photonenwechselwirkungen, beträchtliche Möglichkeiten für die Entwicklung exotischer, technologisch wünschenswerter Eigenschaften durch kohärente Manipulation von Quantenfreiheitsgraden. Da die zugrundeliegende Theorie jedoch in einem Gleichgewichts-, Störungs- oder Steady-State-Kontext entwickelt wurde, ist die theoretische Kapazität zur Vorhersage und Interpretation der großen Vielfalt ultraschneller, gleichgewichtsferner Phänomene, wie sie in ausgedehnten Systemen beobachtet werden, oft nicht ausreichend, um über eine grobe phänomenologische Erklärung oder einen störungsbasierten Ansatz hinauszugehen. Letzterer versagt jedoch häufig bei stark getriebenen Systemen. Dies gilt insbesondere für eine der grundlegendsten Wechselwirkungen in der Materie: die Elektron-Nukleon-Wechselwirkung. Während die Simulation stark getriebener, nicht im Gleichgewicht befindlicher Elektron-Nukleon-Dynamik für kleine molekulare Systeme mit nahezu exakter Genauigkeit durchgeführt werden kann, stehen diese quantenchemischen Methoden bei der Anwendung auf ausgedehnte Systeme vor erheblichen Herausforderungen. Diese Arbeit fasst die Forschungsergebnisse zusammen, die der Autor mit seinen Kollaborateuren innerhalb seiner Promotion erlangt hat und die darauf abzielen, aus der Quantenchemie stammende Simulationsmethoden so weiterzuentwickeln, dass diese ohne Abhängigkeit vom Born-Oppenheimer-Ansatz auf stark getriebene, ausgedehnte Systeme angewandt werden können. Unser Ziel war es, robuste, skalierbare Simulationsprotokolle zu entwickeln, die experimentelle Beobachtungen in einer First-Principles, *ab-initio* Weise über einen weiten Bereich von dynamischen Regimen und Materialphasen replizieren und vorhersagen können, indem wir uns von den Einschränkungen von Born-Oppenheimer lösen.

Nach einem Überblick über einige der experimentellen Phänomene, mit denen wir uns befassen, geben wir eine kurze Einführung in einige Aspekte des bestehenden theoretischen Rahmens für die Untersuchung von Elektron-Nukleon-Wechselwirkungen, wie sie in der Born-Oppenheimer-Näherung verkörpert sind, sowie in die störungstheoretischen und nicht-störungstheoretischen Ansätze der Echtzeitdynamik, die zur Berechnung von Materialeigenschaften verwendet werden. In den folgenden Abschnitten werden die vorgestellten Arbeiten in einen Kontext gestellt und die darin behandelten Hauptfragen, die Fortschritte anderer Forschungsgruppen auf diesem Gebiet und der Beitrag des Autors diskutiert. Zunächst erörtern wir unsere Entwicklung eines neuen, gitterbasierten ab-intio Wellenfunktionsdynamik-Ansatzes für den Ortsraum, der in der Lage ist, Elektron-Nukleon- und Elektron-Elektron-Korrelationseffekte sowohl im Gleichgewicht als auch in lasergesteuerten Regimen in einer Vielzahl von physikalischen Systemen exakt zu erfassen, und diskutieren die Entwicklungen, die erforderlich wären, um diese Methode skalierbar und wettbewerbsfähig zu machen. Als Nächstes wenden wir eine halbklassische Dynamikmethode an, das *Multi-Trajektorien-Ehrenfest-Theorem* (MTEF), das auf einem Ensemble von Kerntrajektorien basiert, die den anfänglichen Quantenkernzustand genau wiederherstellen und gleichzeitig die Elektron-Nukleon-Dynamik auf der Ebene der Molekularfeldtheorie erfassen kann. Die Bewegungsgleichungen, die dieser Methode zugrunde liegen, sind universell in Echtzeit-Ab-initio-Dynamik-Codebasis implementiert, was diesen Ansatz für eine breitere Gemeinschaft zugänglich macht. Wir stellen fest, dass MTEF in Kombination mit einer Behandlung der elektronischen

1 Abstract

Freiheitsgrade auf Basis des Ortsraums in der Lage ist, quantennukleare Effekte auf das Gleichgewichtsabsorptionsspektrum von Molekülen abzubilden, und zeigen, wie einfach diese Methode in bestehende Simulationsprotokolle integriert werden kann. Da MTEF halbklassisch ist, kann es auf sehr große Systeme skaliert werden, während die Darstellung des elektronischen Systems im Ortsraum eine beliebig starke Laseransteuerung und die dynamische Behandlung der Ionen eine signifikante nukleare Umstrukturierung des Kernsystems ermöglicht.

Anschließend wenden wir MTEF zum ersten Mal auf realistische periodische Systeme an, um die durch Phononen vermittelte Relaxation von selektiv angeregten Ladungsträgern in hexagonalem Bornitrid (hBN) bei Temperaturen von bis zu 2000 K zu simulieren. Die Anwendung von MTEF ist dabei generisch und kann beliebig auf andere Materialien angewandt werden. Wir stellen fest, dass MTEF eine natürliche Erweiterung der statischen Methoden darstellt, die weithin zur Berechnung der nach Phononen normalisierten Gleichgewichtseigenschaften von Materialien verwendet werden. Dabei konvergiert unsere Methode für die untersuchten gleichgewichtsfernen Phänomene mit einer kleinen Anzahl von Trajektorien. So entwickeln und präsentieren wir eine Methode, die einfach zu benutzen ist, genau und schnell konvergiert und die in der Lage ist, die stark getriebene Elektron-Phonon-Dynamik in periodischen Systemen unter beliebigen Pump-Probe-Anordnungen zu erfassen. Wir schließen mit einer Diskussion über die Forschung, die auf der Grundlage unserer Bereitstellung dieses dringend benötigten Werkzeugs zur Simulation der stark getriebenen Dynamik von Quantenmaterialien folgen kann.

2 | List of Publications

   I Guillermo Albareda, **Kevin Lively**, Shunsuke A. Sato, Aaron Kelly, and Angel Rubio; "Conditional Wave Function Theory: A Unified Treatment of Molecular Structure and Nonadiabatic Dynamics"; *Journal of Chemical Theory and Computation* 2021, 17, 7321-7340; https://doi.org/10.1021/acs.jctc.1c00772

   II **Kevin Lively**, Guillermo Albareda, Shunsuke A. Sato, Aaron Kelly, and Angel Rubio; "Simulating Vibronic Spectra without Born-Oppenheimer Surfaces"; *The Journal of Physical Chemistry Letters* 2021, 12, 3074-3081; https://pubs.acs.org/doi/pdf/10.1021/acs.jpclett.1c00073

  III **Kevin Lively**, Shunsuke A. Sato, Guillermo Albareda, Angel Rubio, and Aaron Kelly; "Revealing Ultrafast Phonon Mediated Inter-Valley Scattering through Transient Absorption and High Harmonic Generation Spectroscopies"; Under Review, arXiv:2306.16010; https://arxiv.org/pdf/2306.16010.pdf

2.1 Declaration of contribution

   I K. Lively wrote code for the H_2 model with results shown in Figures 3, 4, 9, 10 and 11, as well as refactored G. Albareda's code for the Shin-Metiu model in order to generate the data shown in Figures 7 and 15. S. A. Sato wrote CIS/Hartree-Fock code for the H_2 model results shown in Figure 2 as well as code for the electronic scattering results shown in Figures 5 and 12. G. Albareda wrote code for the H_2, Shin-Metiu and 2D Shin-Metiu models, shown in Figures 2, 6, 7, 8, 13, 14 and 15. All authors participated in the planning of the project, discussions and analysis of the data and writing of the paper.

   II K. Lively wrote the code for the H_2 model and ran the simulations with the assistance of A. Kelly. All authors participated in the planning of the project, analysis of the data and writing of the paper.

  III K. Lively wrote the tight binding code for hBN/graphene, performed all simulations and created all plots. All authors participated in the planning of the project, analysis of the data, and writing of the paper. The full code is available at https://gitlab.com/kevin.lively_mpsd/graphene-tight-binding

3 | Introduction

Much of the advance of technology in the last century was made possible through the development of theories which could describe the microscopic behavior of atoms, molecules and solids. Semiconducting transistors, magnetic data storage, and photovoltaic cells are integral to modern civilization and they owe their existence to the understanding of the properties of matter in thermodynamic equilibrium. By being able to rationally predict and engineer desired system properties, the size and efficiency of such devices was iteratively optimized until manufacturing them was sufficiently cheap and reliable for them to become ubiquitous. Concurrently, the development of laser technology since the 1960s has allowed condensed matter physicists to selectively probe and coherently excite matter with increasing levels of precision. By now the intensity with which matter can be driven from equilibrium, and the degree of temporal and spatial control over laser pulses is so advanced, as to constitute an entirely new landscape of opportunities to engineer materials [1–6].

Matter has a large number of degrees of freedom consisting of electronic and nuclear spins, charges and their spatial configuration with respect to one another. The interactions between these can manifest as highly complicated phase diagrams, displaying macroscopic behavior emergent from the competing energetic effects of these component subsystems. Equilibrium thermodynamics studies these phase spaces through static magnetic fields (spin), chemical substitutions (charge) and pressure or crystallographic strain (configuration). Expanding on this rich landscape of parameters is the development of novel methods to engineer new states of matter through amplification of vacuum photon coupling via cavity confinement [7] and tuning electron dispersion through moiré layering [8–10]. For a given point in the phase diagram, subsequent analysis can reveal the response of the system to weak external stimuli and thus inspire applications of the material under these conditions. Furthermore, by exciting particular degrees of freedom one can *dynamically* manipulate a particular subsystem. Doing so with sufficient intensity and speed, one enters the nonadiabtic regime: the component subsystems don't have time to find their local equilibrium and thus the system can enter transient phases which display properties that are normally inaccessible [4, 5]. The key advantage of laser technology is the capacity to finely tune this manipulation to specific excitation channels within matter. By resonantly driving or suddenly biasing the system within particular energy windows, the balance between component subsystems can be rearranged in a coherent and deterministic manner which subsequently affects the emergent properties of the material. Thus these 'non-thermal pathways' [5], can serve a vital role in rationally developing quantum materials in which exotic phenomena desirable for technological application such as high temperature superconductivity or topologically protected states for use as thermally robust qubits manifest under conditions normally prohibited by equilibrium thermodynamics [11].

As a concrete example consider the laser driven dynamics of nuclei. By resonantly pumping vibrational modes, the ions can develop large amplitude motion with respect to their crystallographic local equilibrium. Due to anharmonic coupling between vibrational modes, this

can cause a net displacement of the lattice structure which subsequently changes the coupling of electronic orbitals [12]. Driving nuclear dynamics in this manner has been experimentally demonstrated to cause transient phases of matter such as signatures of superconductivity in K_3C_{60} up to room temperature [13–15], crystal structure phase transitions from para- to ferro-electric order in $SrTiO_3$ which remain stable for hours after irradiation [16, 17], and deterministic enhancement or suppression of ferromagnetic phases in $YTiO_3$ far away from the equilibrium critical temperature [18]. Similar experiments have been done by driving the electronic system such as inducing a semi-metal to insulator transition through steady-state Floquet driving in graphene [19], as well as the spin degrees of freedom through direct manipulation of ferromagnetism by light pulses [20] and selective excitation of spin polarized electronic bands [21]. For recent experimental and theoretical reviews see [2, 4–6]. Because of the numerous ways in which intra- and inter-subsystem interactions can locally reduce energy through forming quasi-particles (polarons, polaritons, phonon-polaritons, plasmons, excitons, Cooper-pairs, . . .), simply under-standing how the energy is picked up by the system and how it subsequently moves between the constituent parts can be a formidable challenge. Thus a key analysis is to track the flow of energy within a system in real time by probing how its spectroscopic properties change following an excitation [3]. In chemistry for instance, such ultrafast transient spectroscopies have been used to study the effects of nuclear motion on photo-disassociation, non-radiative relaxation and charge transfer in photoactive molecules for nearly thirty years [1, 22].

Thus given the plethora of opportunities, there is a clear demand for robust and predictive theoretical tools which can interpret, inspire and confirm experiments in far-from-equilibrium condensed matter physics. However there are significant challenges even for one of the most fundamental interactions responsible for the behavior of matter: the electron-nuclear interaction. In periodic systems nuclear motion is treated almost exclusively in terms of small deviations from equilibrium, and their interaction with the electronic system is generally treated in a perturbative or even phenomenological manner [23, 24]. By contrast, due to having a finite and small system size, in quantum chemistry methods have been developed in which the nuclear degrees of freedom can be treated non-perturbatively, under non-adiabatic conditions and in some cases even fully quantum mechanically [22, 25]. For the smallest molecules these methods have been developed to the point being considered exact solutions, and have become a necessary tool for the interpretation of experimental spectra [22]. These successes generally rely on the Born-Oppenheimer framework, its non-adiabatic counterpart the Born-Huang ansatz, and approximations made from these as starting points. However, due to requiring an electronic solution for every nuclear configuration, methods relying on this framework are prohibitively expensive to scale beyond a handful of degrees of freedom. Subsequently over the last 20 years there has been increasing interest in developing methods which can capture quantum effects in electron-nuclear dynamics, can be scaled to extended systems and long-time dynamics, and is capable of simulating the behavior of strongly driven, far-from-equilibrium matter [26–29].

Broadly speaking these efforts take the form of methods with a high degree of correlation between the electronic and nuclear subsystems such as wavefunction ansätze [30–32], density matrix [33, 34], and diagrammatic Non-Equilibrium Green's Function based approaches (when taking high level expansions) [35, 36], or conversely methods with a lower degree of correlation usually entailing some semi-classical approximation such as linearized path integral or ring-polymer molecular dynamics [37], time-dependent Boltzmann and Bloch equations [23, 38] and trajectory based ensemble approaches such as Ab-Initio Multiple Spawning or Ehrenfest dynamics

[25]. While the former category generally leads to more quantitatively accurate results, the computational and theoretical overhead can be extremely demanding, oftentimes limiting the applicability to smaller systems or shorter time scales unless restricted to simple models or significant approximations are made. The latter category is more tractable in these regards while simultaneously being less accurate for strongly correlated systems by virtue of the semi-classical approximation, defects which in some cases can be improved upon at increasing computational cost.

In chapter 4 we discuss some of the recent methodological developments in the former category, focused primarily on wavefunction dynamics to which the author and collaborators contributed with paper **I**. In this paper we developed an ab-initio real-space, real-time, fully quantum mechanical electron-nuclear dynamics simulation method which is capable of accurately capturing the spectrum of equilibrium states as well as perturbatively and strongly driven dynamics, while still being amenable to optimization which can scale the calculation to larger systems. In chapters 5 and 6 we focus on semi-classical dynamics, providing a short overview in chapter 5 of the wide ranging methods existing under this umbrella before focusing on Multi-trajectory Ehrenfest (MTEF), which is amenable to large systems, long time scales and non-adiabatic dynamics. This method has the further benefit of its equations of motion already being widely implemented, and when derived in the context of the Quanutm Classical Liouville Equation, forms the basis for systematic reintroduction of higher electron-nuclear correlation terms. In paper **II** we systematically investigated the application of MTEF with the electronic system represented in a real-space grid basis, finding that we recover quantized nuclear effects on the absorption spectrum of molecules, and are able to straightforwardly apply this technique to ab-intio simulations of real molecules. This work made clear that one can capture such effects at a low computational cost. We follow up these results with paper **III** in which we, for the first time, apply MTEF in an ab-initio manner to periodic systems under strong laser driven dynamics. This work presents a methodology which simultaneously captures the equilibrium phonon properties of real materials at arbitrary temperatures, the effects of phonon renormalization of the electronic system at equilibrium for strong coupling, and the phonon scattering induced charge-carrier equalization of valley selective excitation following intense irradiation in a manner consistent with experiment and complementary theory calculations.

In order to contextualize the import of these findings, we first begin in this chapter by providing a brief overview of the Born-Oppenheimer (BO) approximation and its extension to non-adiabatic dynamics. Next we discuss the real-time dynamics approach for simulating system properties under perturbative excitation, and demonstrate how it is used within the BO framework to calculate the vibronic spectra. This quantity constitutes the primary focus of paper **II**, one of the primary demonstrations of which was that vibronic spectra could be calculated without reference to the standard BO approach. We next provide a brief recap of strongly driven processes and how they can calculated non-perturbatively as done is in papers **I** and **III**, whose primary contributions are to demonstrate techniques capable of calculating strongly driven phenomena and their nuclear dependencies without relying on BO concepts. We finish this chapter with a comment on the features of the BO framework which limit the applicability of methods developed exclusively within it to address the kind of strongly driven, far-from-equilibrium experiments described above, and finally conclude with a more detailed outline of the proceeding chapters.

3.1 The Born-Oppenheimer Approximation and Non-Adiabatic Extensions

The Born-Oppenheimer (BO) Approximation and its extension to non-adiabatic dynamics through the Born-Huang (BH) ansatz constitute the backbone of quantum chemistry, being foundational to the way that chemists and physicists think about the structure and dynamics of molecules, and indeed formally serves as a framework for understanding the properties of phonons in periodic systems. Given the ubiquity of the BO/BH framework, it's necessary to understand its limitations and the subsequent growing body of literature working outside of it, to which this thesis contributes.

The BO approximation relies on the disparity of masses between the electronic degrees of freedom m_e and the proton mass M_p. Since $M_p/m_e \sim 1836$, one can separate the electronic motion from the nuclear motion and treat the nuclear motion as a perturbation on top of the electronic degrees of freedom. Although attributed to the 1927 paper by Max Born and Robert J. Oppenheimer [39], the formulation presented there was perturbative in $\epsilon = (m/M)^{1/4}$, with small nuclear deviation from the equilibrium nuclear configuration $\underline{\mathbf{R}}_0$ giving the lowest energy electronic configuration $\propto \mathcal{O}(\epsilon^0)$ followed by vibrational $\propto \mathcal{O}(\epsilon^2)$, and rotational energies $\propto \mathcal{O}(\epsilon^4)$ [40]. In fact the generic validity of this expansion for any nuclear configuration, and indeed whether one can separate the nuclear motion and still retain discretized electronic potential energy surfaces at all, has been asserted to be inconsistent with a quantized treatment of indistinguishable nuclei [41–43]. However, despite this somewhat niche objection, when taken as an *ad-hoc* assumption arising from initially treating the nuclei as classical, distinguishable particles of infinite mass *and then* quantizing and allowing them to move, the BO framework is an indisputably successful tool. The following can be found in many standard references [44–46], though we adapt their presentation and notation for this introduction.

Starting from the full system Hamiltonian, $\hat{H}$, of a system consisting of N_n nuclei and N_e electrons we can write it in the real space basis of the nuclear positions $\underline{\mathbf{R}} = (\mathbf{R}_1, \ldots, \mathbf{R}_{N_n}) \in \mathbb{R}^{dN_n}$ and electronic positions, $\underline{\mathbf{r}} = (\mathbf{r}_1, \ldots, \mathbf{r}_{N_e}) \in \mathbb{R}^{dN_e}$ where d is the Cartesian dimension of the system:

$$
\begin{aligned}
H(\underline{\mathbf{r}}, \underline{\mathbf{R}}) &= -\sum_{\nu}^{N_n} \frac{1}{2M_\nu} \boldsymbol{\nabla}_{\mathbf{R}_\nu}^2 - \sum_i^{N_e} \frac{1}{2} \boldsymbol{\nabla}_{\mathbf{r}_i}^2 + \sum_{i \neq j} \frac{1}{|\mathbf{r}_i - \mathbf{r}_j|} - \sum_{i\nu} \frac{Z_\nu}{|\mathbf{r}_i - \mathbf{R}_\nu|} + \sum_{\nu \neq \mu} \frac{Z_\nu Z_\mu}{|\mathbf{R}_\nu - \mathbf{R}_\mu|} \\
&= -\frac{1}{2} \underline{\underline{M}}^{-1} \boldsymbol{\nabla}_{\underline{\mathbf{R}}}^2 + H_e(\underline{\mathbf{r}}, \underline{\mathbf{R}}),
\end{aligned}
\tag{3.1}
$$

where we have rewritten the nuclear kinetic energy term as $\boldsymbol{\nabla}_{\underline{\mathbf{R}}}^2 = (\boldsymbol{\nabla}_{\mathbf{R}_1}^2, \ldots, \boldsymbol{\nabla}_{\mathbf{R}_{N_n}}^2)^T$ with diagonal inverse mass matrix $\underline{\underline{M}}^{-1}$, and implicitly defined the electronic Hamiltonian H_e which gathers the electronic kinetic energy and all Coulomb potential terms. The charge and mass of the nucleus ν are referred to by Z_ν and M_ν respectively, and we have used atomic units $\hbar = e = m_e = \frac{1}{4\pi\epsilon_0} = 1$ as will generally be done throughout the rest of the text. The spectral resolution of this Hamiltonian describes the states of the full system within the Hilbert space $\mathcal{H}$ composed of the direct product of the electronic and nuclear Hilbert spaces $\mathcal{H} = \mathcal{H}^e \otimes \mathcal{H}^N$. As briefly mentioned earlier, we now assume that we can treat the nuclei as *distinguishable* particles and take the approximation that $M_\nu \to \infty$. Doing so allows us to treat the electronic Hamiltonian as a well defined operator acting on $\mathcal{H}^e$, parameterized at each fixed nuclear configuration $\underline{\mathbf{R}}$,

whose spectral decomposition defines the adiabatic electronic wavefunction solutions $\Phi_n(\underline{\mathbf{r}}; \underline{\underline{\mathbf{R}}})$:

$$H_e(\underline{\mathbf{r}}; \underline{\underline{\mathbf{R}}})\Phi_n(\underline{\mathbf{r}}; \underline{\underline{\mathbf{R}}}) = U_n(\underline{\underline{\mathbf{R}}})\Phi_n(\underline{\mathbf{r}}; \underline{\underline{\mathbf{R}}})$$
$$\Phi_n(\underline{\mathbf{r}}; \underline{\underline{\mathbf{R}}}) := \langle \underline{\mathbf{r}} | \Phi_n(\underline{\underline{\mathbf{R}}}) \rangle . \tag{3.2}$$

For simplicity we will disregard the ionized-continuum states which coexist alongside the bound state solutions. Each adiabatic electronic state $|\Phi_n(\underline{\underline{\mathbf{R}}})\rangle$ defines a static potential $U_n(\underline{\underline{\mathbf{R}}})$ for each nuclear configuration, referred to as a Born-Oppenheimer Potential Energy Surface (BOPES). In practice BOPESs are not written in terms of the (lab-frame) Cartesian coordinates for the nuclear degrees of freedom, but constructed in terms of non-translational, non-rotational internal degrees of freedom. While the procedure used to define this coordinate system, and the implications on the effective electron masses can also be a contentious point [43], oftentimes simply the normal modes of vibration and the rest mass of the electron are utilized for molecules. For simplicity we keep the $\underline{\underline{\mathbf{R}}}$ notation, with the understanding that it has been transformed to refer to the internal degrees of nuclear freedom, which will sometimes explicitly be referred to as $\underline{\underline{\mathbf{Q}}}$. Furthermore since the electronic system doesn't have to be solved in terms of the real space basis we can introduce the general Hilbert space notation $\hat{H}_e(\underline{\underline{\mathbf{R}}}) |\Phi_n(\underline{\underline{\mathbf{R}}})\rangle = U_n(\underline{\underline{\mathbf{R}}}) |\Phi_n\rangle$. Throughout this thesis adiabatic Born-Oppenheimer states will be referred to as $|\Phi_n\rangle$, and to decrease notational clutter, we will occasionally suppress their implicit dependence on the nuclear configuration.

By construction the adiabatic states are orthogonal at each nuclear configuration $\underline{\underline{\mathbf{R}}}$:

$$\langle \Phi_n(\underline{\underline{\mathbf{R}}}) | \Phi_m(\underline{\underline{\mathbf{R}}}) \rangle = \int d\underline{\mathbf{r}} \Phi_n^*(\underline{\mathbf{r}}; \underline{\underline{\mathbf{R}}}) \Phi_m(\underline{\mathbf{r}}; \underline{\underline{\mathbf{R}}})$$
$$= \delta_{nm} . \tag{3.3}$$

With these states forming a basis within the electronic Hilbert space $\mathcal{H}^e$ for each $\underline{\underline{\mathbf{R}}}$, we can now construct a wavefunction in the full system Hilbert space $\mathcal{H} = \mathcal{H}^e \otimes \mathcal{H}^N$ through the Born-Huang ansatz:

$$|\Psi(\underline{\underline{\mathbf{R}}}, t)\rangle = \sum_n \chi_n(\underline{\underline{\mathbf{R}}}, t) |\Phi_n(\underline{\underline{\mathbf{R}}})\rangle . \tag{3.4}$$

This ansatz is composed of nuclear wavepackets, $\chi_n(\underline{\underline{\mathbf{R}}}, t)$, each associated with a particular electronic adiabatic BO state. We can see how the nuclear wavepackets depend on the electronic system by applying the system Hamiltonian Eq. (3.1) to the above ansatz. The equation of motion of the nuclear wavepackets then becomes:

$$i\partial_t \chi_n(\underline{\underline{\mathbf{R}}}, t) = \langle \Phi_n | \hat{H} | \Psi \rangle$$
$$= \langle \Phi_n(\underline{\underline{\mathbf{R}}}) | \left(-\frac{1}{2}\underline{\underline{M}}^{-1}\boldsymbol{\nabla}_{\underline{\underline{\mathbf{R}}}}^2 + \hat{H}_e(\underline{\underline{\mathbf{R}}}) \right) \chi_m(\underline{\underline{\mathbf{R}}}) | \Phi_m(\underline{\underline{\mathbf{R}}}) \rangle$$
$$= \left(-\frac{1}{2}\underline{\underline{M}}^{-1}\boldsymbol{\nabla}_{\underline{\underline{\mathbf{R}}}}^2 + U_n(\underline{\underline{\mathbf{R}}}) \right) \chi_n(\underline{\underline{\mathbf{R}}}) - \frac{1}{2}\underline{\underline{M}}^{-1} \sum_m (2\boldsymbol{\tau}_{nm} \cdot \boldsymbol{\nabla}_{\underline{\underline{\mathbf{R}}}} + \tau_{nm}^{(2)})\chi_m(\underline{\underline{\mathbf{R}}}), \tag{3.5}$$

where $\boldsymbol{\tau}_{nm}$ is the first order non-adiabatic coupling vector (NACV) between adiabatic states n

and m:

$$\boldsymbol{\tau}_{mn} = \langle \Phi_m(\underline{\mathbf{R}}) | \boldsymbol{\nabla}_{\underline{\mathbf{R}}} | \Phi_n(\underline{\mathbf{R}}) \rangle$$
$$= \frac{\langle \Phi_m | \boldsymbol{\nabla}_{\underline{\mathbf{R}}} \hat{H}_e(\underline{\mathbf{R}}) | \Phi_n \rangle}{U_n(\underline{\mathbf{R}}) - U_m(\underline{\mathbf{R}})} \quad \text{for } n \neq m. \tag{3.6}$$

The second line follows from the Hellman-Feynman Theorem or equivalently from the solution to the Sternheimer Equation when treating the nuclear configuration as a perturbative parameter [47]. The second order non-adiabatic coupling matrix (NACM) $\tau_{mn}^{(2)}$ is defined as:

$$\tau_{mn}^{(2)} = \langle \Phi_m(\underline{\mathbf{R}}) | \boldsymbol{\nabla}_{\underline{\underline{\mathbf{R}}}}^2 | \Phi_n(\underline{\mathbf{R}}) \rangle . \tag{3.7}$$

Collectively the NACVs and NACMs are referred to as non-adiabatic coupling terms (NACTs); the effect of NACMs is typically small and therefore they are often disregarded. As can be seen from the form of the NACV in Eq. (3.6) in the case of well separated BOPESs or a vanishing numerator, the NACTs can be entirely disregarded, giving rise to the Born-Oppenheimer approximation. Under this approximation we can fully characterize the nuclear subsystem via it's behavior on the various BOPESs. In conjunction with the kinetic energy operator, this gives rise to vibrational states ν belonging to each BOPES n:

$$H_n(\underline{\mathbf{R}}) \chi_{n\nu}(\underline{\mathbf{R}}) = \left(-\frac{1}{2} \underline{\underline{M}}^{-1} \boldsymbol{\nabla}_{\underline{\underline{\mathbf{R}}}}^2 + U_n(\underline{\mathbf{R}}) \right) \chi_{n\nu}(\underline{\mathbf{R}})$$
$$= E_{n\nu} \chi_{n\nu}(\underline{\mathbf{R}}). \tag{3.8}$$

These vibrational states often serve as a handle for interpreting spectra, as in the Franck-Condon effect, and can serve as a basis in which to represent the nuclear wavefunctions $\chi_n(\underline{\mathbf{R}})$, although strictly speaking they are only well defined when the NACTs are disregarded.

Conversely as the gap between surfaces decreases these states become coupled and at nuclear configurations where the BOPES are degenerate, the NACT can diverge. The regions in nuclear configuration space where this occurs are known as a Conical Intersections (CIs). When occurring between the electronic ground state and higher states, the static consequences of CIs manifest as the Jahn-Teller effect: instead of being in the high-symmetry CI configuration at which the electronic states are degenerate, the nuclear geometry spontaneously distorts, lifting the electronic state degeneracy. Dynamically, CIs play an integral role in the physics of molecules. Nuclear wavepackets passing through the area around CIs interact strongly with other BOPESs and can 'transfer' through them thus creating a channel for electronic state relaxation (or excitation) due to nuclear motion. This constitutes a non-radiative means of energy relaxation and plays a critical role in numerous photo-excitation pathways. These include the detection of light in the human eye [48], the robustness of DNA against photo-damage [49] and the recombination of photo-excited charge carriers [50]. Developing the means to efficiently simulate such phenomena constitutes a central focus of the non-adiabatic quantum chemistry community.

The dynamics captured by the Born-Huang ansatz in Eq. (3.5) constitute an exact representation of the excited behavior in an isolated molecular system, accomplished by shifting the dynamics entirely onto the nuclear degrees of freedom. This in fact is the central utility of this picture since while the full system wavefunction is out of reach for any realistically sized problem, electronic structure methods allow calculation of all of the ingredients in Eq. (3.5),

namely the BOPESs $U_n(\underline{\mathbf{R}})$ and NACTs, $\boldsymbol{\tau}_{mn}$, $\tau_{mn}^{(2)}$ [51]. Of course this just shifts the problem, as calculating or even storing the BOPES and NACTs becomes extremely expensive when one wants to treat systems with relatively modest numbers of nuclear degrees of freedom. In practice one isolates their attention to a few degrees of freedom of interest (or a combination of degrees of freedom in a reaction coordinate) and takes a collection of configurations $\{\underline{\mathbf{R}}_i; \; i = 1, \ldots, N_c\}$ at which the BOPES and NACTs are calculated. These points are then used to calculate a 'global' fit.

Regardless of the electronic structure technique used, this procedure is generally expensive for each configuration, and can be quite sensitive to the details of the problem at hand. Consistent results for excited state energies typically require a high level method such as Coupled Cluster – which scales as $\mathcal{O}\left(N_e^7\right)$ – or Complete Active Subspace Self-Consistent Field (CASSCF), which can scale exponentially [45]. Oftentimes comparatively cheaper electronic structure methods such as Linear Response Time Dependent Density Functional Theory (LR-TDDFT) are chosen, although the accuracy compared to more sophisticated methods can be quite poor [52]. Due to the presence of CIs it can be preferable to perform a change of basis in order to remove the singularities and minimize the effects of the NACTs [44]. Such a 'diabatization' procedure results in smooth diabatic potential energy surfaces (PESs). There is no unique definition of a diabatic PES, thus this requires further choices about what is appropriate for a given situation [53]. Particularly important types of diabatic models are linear or quadratic vibronic coupling models (LVC and QVC respectively), which derive from first or second order Taylor expansions of the electronic Hamiltonian: $\hat{H}_{\mathrm{e}}(\underline{\mathbf{R}}) \approx \hat{H}_{\mathrm{e}}(\underline{\mathbf{R}}_0) + \boldsymbol{\nabla}_{\underline{\mathbf{R}}} \hat{H}_{\mathrm{e}}(\underline{\mathbf{R}})|_{\mathbf{R}_0} \cdot (\underline{\mathbf{R}} - \underline{\mathbf{R}}_0) + \mathcal{O}((\underline{\mathbf{R}} - \underline{\mathbf{R}}_0)^2)$ [54]. These are projected onto the diabatic states $|\Phi_n(\underline{\mathbf{R}}_0)\rangle$, which are eigenstates of the electronic Hamiltonian only at reference configuration $\underline{\mathbf{R}}_0$. The resulting Hamiltonian governing the nuclear dynamics is composed of smooth 'diabatic surfaces' which depend on coupling terms proportional to $(\underline{\mathbf{R}} - \underline{\mathbf{R}}_0)$ and $(\underline{\mathbf{R}} - \underline{\mathbf{R}}_0)^2$, restricted to symmetrically allowed couplings. The construction of LVC and QVC models is a non-trivial process and constitutes an active field of research [55].

3.2 Real Time Dynamics

As a concrete example of how the BO/BH picture is used to calculate system properties, here we describe how real time dynamics simulations can be used to study the response of finite and extended systems to coherent light sources. We first discuss the linear absorption coefficient analysed in the context of perturbation theory under the dipole approximation. This quantity describes the absorption of light in a system due to weak incident radiation, acting as a probe of the optically active excited states intrinsic to a system, and is the focus of paper II, in which we use both the perturbative correlation function approach described here, as well as direct non-perturbative propagation, discussed here in section 3.2.2 and in more detail in chapter 5. We also discuss one of the simplest possible coupled electron-nuclear excitations, the *vibronic* transition. Such information is of course necessary to understand the manifold of excited states which can be accessed upon stronger driving. However, providing a detailed accounting of the origin of spectral lines by calculating this fundamental system property for mixed vibrational/electronic excitations is an ongoing research challenge. We also briefly discuss how non-linear optical response properties can be calculated both perturbatively and non-perturbatively.

3.2.1   Linear Absorption

Samples of matter, say a uniform gas consisting of a single species of molecule or a block of a crystalline solid, will develop an induced polarization $\delta\mathbf{P}$ upon irradiation with coherent light of a given frequency ω. This can be described in a power series of the incident $\mathbf{E}$ field [56]:

$$
\begin{aligned}
\delta\mathbf{P}(t) &= \int dt' \chi^1(t-t')\mathbf{E}(t') + \int dt' \int dt'' \chi^2(t-t', t-t'')\mathbf{E}(t')\mathbf{E}(t'') + \mathcal{O}(\mathbf{E}^3) \\
&= \delta\mathbf{P}^1 + \delta\mathbf{P}^2 + \mathcal{O}(\delta\mathbf{P}^3),
\end{aligned}
\tag{3.9}
$$

where χ^n is the n^{th} order response function (which is a tensor of order $n+1$). If we assume the incident field is weak, the second and higher order terms can be dropped, and we can turn to the first-order polarization [57]:

$$
\delta\mathbf{P}^1(t) = \int dt' \underline{\underline{\chi}}^1(t-t')\mathbf{E}(t').
\tag{3.10}
$$

In the case of a molecular system, the first order change of the polarization is often written in terms of the dipole operator $\hat{\boldsymbol{\mu}} = \hat{\boldsymbol{\mu}}^e + \hat{\boldsymbol{\mu}}^N = -\sum_i \hat{\mathbf{r}}_i + \sum_\nu Z_\nu \hat{\mathbf{R}}_\nu$, comprised of the electronic ($\hat{\mathbf{r}}_i$) and nuclear ($\hat{\mathbf{R}}_\nu$) position operators and nuclear charge Z_ν:

$$
\delta\mathbf{P}^1(t) = \overline{\langle \delta\hat{\boldsymbol{\mu}}^1(t)\rangle}.
\tag{3.11}
$$

The expectation value of this operator is $\langle\delta\hat{\boldsymbol{\mu}}^1\rangle$, and the bar overhead in Eq. (3.11) indicates the spatial average. For solids, interaction with light is written in terms of Maxwell's equations in matter, where the most important constiutents for our purposes are the electric current $\mathbf{J}$ and displacement $\mathbf{D}$, whose proportionality to the external field $\mathbf{E}$ define the dielectric function ϵ and conductivity σ [58]:

$$
\begin{aligned}
\mathbf{D} &= \epsilon\mathbf{E} \\
\mathbf{J} &= \sigma\mathbf{E}.
\end{aligned}
\tag{3.12}
$$

Due to the absorption of photons, the intensity of light propagating within the medium will decay with penetration depth $|\mathbf{r}|$ according to the macroscopic Beer-Lambert law:

$$
I(|\mathbf{r}|) = I(0)e^{-\alpha|\mathbf{r}|}.
\tag{3.13}
$$

The rate of intensity decay is determined by the absorption coefficient α. Through Maxwell's equations in matter, the frequency dependence of this absorption can be expressed can be expressed as the following spatial average [57, 59]:

$$
\alpha(\omega) = \frac{4\pi\omega}{3c}\text{Im}\sum_{j=1}^{3} \chi_{jj}(\omega),
\tag{3.14}
$$

where c is the speed of light in the vacuum and $\chi_{ij}(\omega) \in \mathbb{C}$ is the susceptibility of the material in cartesian direction i to an input field in direction j. For periodic systems, this quantity is

written in terms of the dielectric function and conductivity as [58]:

$$\alpha(\omega) = \frac{2\omega}{3c} \text{Im} \sum_{j=1}^{3} N_{ii}(\omega)$$
$$N(\omega) = \sqrt{\epsilon(\omega)\mu} \tag{3.15}$$
$$\epsilon(\omega) = \epsilon_1 + \frac{4\pi i}{\omega} \sigma(\omega).$$

The magnetic permeability μ and real dielectric function ϵ_1 are usually set to 1 in calculations. Naturally, the microscopic details of the system can be tied to the susceptibility, allowing us to assign the origin of particular spectral features. We start by taking the dipole approximation in which the wavelength of the exciting field is much larger than the molecule itself allowing us to ignore it's spatial dependence. Taking the Fourier transform of the response function Eq. (3.10) gives the frequency dependent linear susceptibility $\chi(\omega)$. The matrix elements of the susceptibility and conductivity are dependent on dipole, current and field directions i, j as:

$$\chi_{ij}(\omega) = \frac{\langle \delta\hat{\mu}_i(\omega) \rangle}{E_j(\omega)}$$
$$\sigma_{ij}(\omega) = \frac{\langle J_i(\omega) \rangle}{E_j(\omega)}. \tag{3.16}$$

In order to obtain an expression for the observables $\langle \delta\hat{\boldsymbol{\mu}}(\omega) \rangle$ and $\langle \mathbf{J}(\omega) \rangle$, we first find an expression for their time dependence by explicitly treating the coupling of the field with the molecular Hamiltonian $\hat{H}_0$ in a semi-classical manner:

$$\hat{H}(t) = \hat{H}_0 + \hat{\boldsymbol{\mu}} \cdot \mathbf{E}(t). \tag{3.17}$$

For the periodic case we use the velocity gauge:

$$\hat{H}(t) = -\frac{1}{2\underline{\underline{M}}}(\hat{\underline{\mathbf{p}}} - \frac{1}{c}\mathbf{A}(t))^2 + \hat{U}, \tag{3.18}$$

where $\underline{\underline{M}}$ and $\underline{\mathbf{p}}$ collects the particle masses and momenta, $\hat{U}$ collects the remaining potential terms and vector potential $\mathbf{A}$ is defined by $\mathbf{E} = -\frac{1}{c}\partial_t\mathbf{A}$. This approach is semi-classical in the sense that the laser field is treated as a classical parameter, rather than being expanded in terms of a quantized phonon field. We take a first order expansion to the time evolution operator $\hat{U}(t, t_0)$ written in the interaction picture, where operators evolve according to $\hat{O}(t) = e^{i\hat{H}_0 t}\hat{O}e^{-i\hat{H}_0 t}$. In this picture we have [60]:

$$\hat{U}(t, t_0) \approx e^{-i\hat{H}_0(t-t_0)} \left[1 - i \int_{t_0}^{t} dt' \mathbf{E}(t') \cdot \hat{\boldsymbol{\mu}}(t' - t_0) \right]$$
$$= e^{-i\hat{H}_0(t-t_0)} \left[1 - i\underline{\underline{M}}^{-1} \int_{t_0}^{t} \frac{dt'}{2c} \mathbf{A}(t') \cdot \hat{\underline{\mathbf{p}}}(t' - t_0) \right] \tag{3.19}$$

For simplicity we make the zero temperature assumption that the system is in it's global ground state E_0: $\hat{H}_0 |\Psi_0\rangle = E_0 |\Psi_0\rangle$, although the derivation presented here can be straightforwardly generalized to temperature dependent situations by replacing the wavefunction with a density matrix $\hat{\rho}(t)$, and propagating it via the Liouville-von Neumann equation [57]. By initalizing $|\Psi(t = 0)\rangle = |\Psi_0\rangle$ and propagating via Eq. (3.19) we can evaluate $\langle \boldsymbol{\mu}(t) \rangle = \langle \Psi(t)|\hat{\boldsymbol{\mu}}|\Psi(t)\rangle$ or

$\langle \mathbf{J}(t) \rangle = \langle \Psi(t) | \hat{\mathbf{J}} | \Psi(t) \rangle$, where the current oprerator $\mathbf{J}$ is proportional to the system momentum. Given that Eq. (3.19) only depends on the incident field to the first order, by subtracting the static 0^{th} order $e^{-i\hat{H}_0(t-t_0)}$ term, $\langle \hat{\boldsymbol{\mu}}^0 \rangle = \langle \Psi_0 | \hat{\boldsymbol{\mu}} | \Psi_0 \rangle$ (without a static DC bias, there is no steady state current $\langle \mathbf{J}_0 \rangle$), we obtain the first order response:

$$
\begin{aligned}
\langle \delta\hat{\mu}_i{}^1(t) \rangle &= -i \int_{t_0}^{t} dt' \, \langle \Psi_0 | \left[\hat{\mu}_i(t - t'), \hat{\mu}_j \right] | \Psi_0 \rangle \, E_j(t') \\
\langle \hat{J}_i^1(t) \rangle &= -i \int_{t_0}^{t} \frac{dt'}{c} \, \langle \Psi_0 | \left[\hat{J}_i(t - t'), \hat{J}_j \right] | \Psi_0 \rangle \, A_j(t').
\end{aligned}
\tag{3.20}
$$

We further simplify the expressions by defining the correlation function $C_{ij}(t) = \langle \Psi_0 | \left[\hat{O}_i(t), \hat{O}_j \right] | \Psi_0 \rangle$, where the current or dipole operator stands in for $\hat{O}$. One can observe that the Fourier transform of the time dependent correlation function can be written via the convolution property as $\langle \delta\hat{\mu}_i^1(\omega) \rangle = -iC_{ij}(\omega)E_j(\omega)$, and similarly for the current. Therefore:

$$
\begin{aligned}
C_{ij}(\omega) &= i \frac{\langle \delta\hat{\mu}_i^1(\omega) \rangle}{E_j(\omega)} = i\chi_{ij}^1(\omega) \\
&= i \frac{\langle \delta\hat{J}_i^1(\omega) \rangle}{E_j(\omega)} = i\sigma_{ij}^1(\omega),
\end{aligned}
\tag{3.21}
$$

where $\mathbf{A}/c$ has gone to $\mathbf{E}$ via the convolution. Notice that the expression for the linear susceptibility depends only on the dipole-dipole or current-current correlation of the propagated system, and not on the electric field. This is because it's defined entirely by the intrinsic properties of the system, and isn't dependent on the structure of the incident field. In contrast, the response of systems to stronger pumping fields explored in papers **I** and **III** depends on the temporal profile of the pump, as this strongly influences the population of excited states induced by the laser. However, in those cases we will still restrict ourselves to the semi-classical dipole approximation, meaning that the system response is dependent only on the temporal profile of the field.

Since by construction the population of excited states induced by the perturbative laser field is vanishingly small, we can also analyze the response via Fermi's Golden Rule. Following some manipulation of the Fourier transform of Eq. (3.10), one can write the absorption coefficient as [60, 61]:

$$
\begin{aligned}
\alpha(\omega) &= \frac{4\pi^2\omega}{3c} \sum_{i=1}^{3} \sum_{n} |\langle \Psi_n | \mu_i | \Psi_0 \rangle|^2 \delta(\hbar\omega - E_n) - |\langle \Psi_n | \mu_i | \Psi_0 \rangle|^2 \delta(\hbar\omega + E_n) \\
\alpha(\omega) &= \frac{16\pi^2}{3\omega c} \sum_{i=1}^{3} \sum_{n} |\langle \Psi_n | v_i | \Psi_0 \rangle|^2 \delta(\hbar\omega - E_n) - |\langle \Psi_n | v_i | \Psi_0 \rangle|^2 \delta(\hbar\omega + E_n)
\end{aligned}
\tag{3.22}
$$

where v_i refers to the total velocity of the system's charge carriers in the i direction, $|\Psi_n\rangle$ refers to excited states in the system, and the second term in both lines corresponds to stimulated emission, which is of course forbidden in the case of the initial state being the global molecular ground state. This perturbative analysis directly shows how the energetic profile of the absorption depends on the transition dipole $(|\langle \Psi_n | \mu_i | \Psi_0 \rangle|^2)$ or velocity $(|\langle \Psi_n | v_i | \Psi_0 \rangle|^2)$ moments.

Vibronic Contributions to Linear Absorption

One of the simplest scenarios of coupled electron-nuclear excitation is the *vibronic* transition. In this situation, the BO framework is invoked from the outset by assuming electronic degrees of freedom are instantly excited with respect to to the nuclear degrees of freedom. Here we focus on the molecular case, and return to the role of phonons on the absorption spectrum in the periodic case in chapter 6. Starting from Eq. (3.22) we invoke a static Born-Huang wavefunction ansatz, Eq. (3.4), for the molecular states, and isolate our attention to the transition between the molecular ground state consisting of the electronic state $|\Phi_0\rangle$ and a given higher lying electronic state $|\Phi_n\rangle$. Disregarding the NACTs, and writing the vibrational states in ket notation as $\chi_{n\nu}(\underline{\mathbf{R}}) \coloneqq \langle\underline{\mathbf{R}}|\chi_{n\nu}\rangle$, we have the following peaks contained within this transition:

$$\alpha(\omega) = \frac{4\pi^2\omega}{3c} \sum_{i=1}^{3} \sum_{\nu} |\langle\Phi_n\chi_{n\nu}|\hat{\mu}_i^e|\Phi_0\chi_{00}\rangle|^2 \delta(\omega - E_{n\nu}), \tag{3.23}$$

Note that we have dropped the nuclear term from the dipole operator since by construction it only connects intra-BOPES vibrational states. Traditionally, at this point one invokes the Condon approximation which assumes that the dependence of the electronic dipole on the nuclear configuration through the BO states is smooth and slowly varying such that it can be evaluated at some characteristic configuration $\underline{\mathbf{R}}_0$, allowing the absorption to be rewritten in terms of electronic transition dipole moments $\langle\Phi_n(\underline{\mathbf{R}}_0)|\hat{\mu}_i^e|\Phi_0(\underline{\mathbf{R}}_0)\rangle$ and the much used Franck-Condon factors $|\langle\chi_{n\nu}|\chi_{00}\rangle|^2$. Finding approximations to these two components and the energies of the states constitutes the framework in which much of the work on vibronic spectral analysis throughout the 20$^\text{th}$ century was conducted. However, in the latter part of the century the increasing availability of computational resources began to allow for explicit *real-time* propagation to go from niche applications [62, 63] to commonplace (for example, one can already see a review article written on time dependent methods from 1988 [64]), meaning that response functions such as Eq. (3.20) could be directly calculated.

This time dependent calculation can proceed in one of two ways. Either one restricts oneself to the perturbative limit, under which one is explicitly interested in the correlation function on the right hand side of Eq. (3.20). Alternatively, by recalling the starting point of Eq. (3.9), one can simply directly take some weak external field, $|\mathbf{E}| << 1$, such that only the lowest order provides any significant signal to the system polarization $\delta\mathbf{P}$ [65, 66]. We remain in the dipole approximation by keeping the field spatially uniform across the system. This latter method is referred to as non-perturbative, even when used to calculate the linear response, because it is in principle not restricted to the dynamics of a particular order in the observable expansion with respect to external field strength. We utilize this approach to calculate the vibronic absorption in papers **I** and **II**. In paper **II** we also use the perturbative approach within the BO picture, which appears again in the case of periodic systems in chapter 6. Therefore, we briefly sketch here the structure of the perturbative real-time calculation in the BO picture.

Disregarding the NACTs the molecular Hamiltonian and dipole operator between the ground and excited state $n = 1$ is written as:

$$\begin{aligned}
H_0(\underline{\mathbf{R}}) &= \frac{1}{2}\underline{\underline{M}}^{-1}\boldsymbol{\nabla}_{\underline{\mathbf{R}}}^2 + U_0(\underline{\mathbf{R}})|\Phi_0(\underline{\mathbf{R}})\rangle\langle\Phi_0(\underline{\mathbf{R}})| + U_1(\underline{\mathbf{R}})|\Phi_1(\underline{\mathbf{R}})\rangle\langle\Phi_1(\underline{\mathbf{R}})| \\
\hat{\boldsymbol{\mu}} &= \hat{\boldsymbol{\mu}}^N \otimes \mathbb{1}_e + |\Phi_0\rangle\bar{\boldsymbol{\mu}}^{01}\langle\Phi_1| + c.c.,
\end{aligned} \tag{3.24}$$

where we have incorporated the Condon approximation directly into the dipole operator. Treating the initial state as $|\Psi_0\rangle = |\chi_{00}\Phi_0\rangle$, one can directly evaluate the dipole-dipole correlation function:

$$
\begin{aligned}
C_{ii}(t) &= \langle \chi_{00}\Phi_0| \ e^{i\hat{H}_0 t}\hat{\mu}_i e^{-i\hat{H}_0 t}\hat{\mu}_i \ |\chi_{00}\Phi_0\rangle \\
&= e^{iE_0 t}\bar{\mu}_i^{01}\bar{\mu}_i^{10} \ \langle \chi_{00}| \langle \Phi_1| e^{-i\hat{H}_0 t}|\Phi_1\rangle |\chi_{00}\rangle \\
&= e^{iE_0 t}|\bar{\mu}_i^{01}|^2 \ \langle \chi_{00}| \, e^{-i(\hat{T}_N + \hat{U}_1)t}|\chi_{00}\rangle,
\end{aligned}
\tag{3.25}
$$

where $\hat{U}_1$ is the operator form of the BOPES, $\langle \underline{\mathbf{R}}|\hat{U}_1|\underline{\mathbf{R}}'\rangle = U_1(\underline{\mathbf{R}})\delta_{\underline{\mathbf{R}},\underline{\mathbf{R}}'}$, and we've dropped the counter-rotating ('anti-resonant') contribution [57]. One can read this expression as a series of instructions: (1) obtain a representation of the lowest lying vibronic state $|\chi_{00}\rangle$, and target surface $\hat{U}_n$; (2) 'instantly excite the electronic state' i.e. place χ_{00} on the upper surface, and then propagate the nuclear wave packet $|\chi_{00}\rangle$ exposed to the excited electronic configuration, as encoded in the BOPES Hamiltonian:

$$
i\partial_t \chi_{00}(\underline{\mathbf{R}}) = \left(-\frac{1}{2M_{(R)}}\boldsymbol{\nabla}_{\underline{\underline{\mathbf{R}}}}^2 + U_1(\underline{\mathbf{R}}) \right) \chi_{00}(\underline{\mathbf{R}});
\tag{3.26}
$$

(3) compute the overlap of the out of equilibrium propagated nuclear wavepacket with it's equilibrium propagated self. By decomposing $|\chi_{00}\rangle$ onto the excited surface vibrational steady states $|\chi_{00}\rangle = \sum_\nu \langle \chi_{n\nu}|\chi_{00}\rangle |\chi_{n\nu}\rangle$ at time 0, propagating and Fourier transforming one can easily recover the energy and state resolved linear absorption Eq. (3.23). In chapter 6, we show how phonon assisted optical absorption in solids can be calculated by averaging over static classically treated nuclear configurations by starting from an expression effectively identical to Eq. 3.25.

3.2.2 Beyond Linear Response

Linear absorption provides a tool to probe the excited states of a system. However, the availability of highly intense table-top laser sources alongside technologies to compress pulses to femto- and atto-second timescales provide opportunities to directly study the role these states play in the absorption and flow of energy following excitation [22]. The basic idea is quite simple, by pumping the system and then probing the system with a secondary pulse at some delay, one obtains a picture of the instantaneous state of the system at that delay time. Following the initial excitation, the distribution of energy in the system evolves due to interaction between the subsystems, and correspondingly the response to the secondary pulse will change over time. In terms of the perturbative treatment of the system response in Eq. (3.9) it's clear that because of the dependence of the response on the relative time of the first and second laser, such processes must be dictated by the second or higher order response functions χ^n.

Examples of such phenomena include harmonic generation, where the outgoing radiation from the system has signals at frequencies $n\omega$ for the input frequency ω, governed by the n^{th} order response functions [56], and Two-Dimensional Electron Spectroscopy (2DES). 2DES relies on a sequence of three pulses, and thus is a measure of the third order response χ^3. Techniques for calculating such higher order response functions in the perturbation approach were pioneered by the group of Shaul Mukamel [67], and require evaluating nested commutators of the dipole response at different times analgously to the right hand side of the first order case

in Eq. (3.20). Performing this calculation requires propagating and evaluating the overlap of multiple wavepackets evolving on different surfaces simultaneously which naturally leads to a large increase in the computational cost of the simulation [32, 68, 69].

However, rather than using this perturbative approach, calculating the response of the system for each order of the expansion in the field strength separately, one can simply take the system and directly propagate under the influence of an external field via Eq. (3.17). Doing so directly calculates the system response $\delta \mathbf{P}(t)$ at all orders. By crafting an external field $\mathbf{E}(t)$ composed of a sequence of lasers $\mathbf{E}_i(t; \phi_i)$ dependent on parameters $\phi_i = (\omega_i, \tau_i, T_i, \mathbf{r}_i)$, like frequency ω, pulse center τ, pulse duration T, propagation direction $\mathbf{r}$, etc., one can simply track the induced dipole (or in the case of periodic systems, the current):

$$\delta \boldsymbol{\mu}(t; \phi_1, \phi_2, \ldots) = \langle \Psi(t) | \hat{\boldsymbol{\mu}} | \Psi(t) \rangle$$
$$i \partial_t | \Psi(t) \rangle = \left(\hat{H}_0 + \hat{\boldsymbol{\mu}} \cdot [\mathbf{E}_1(t; \phi_1) + \mathbf{E}_2(t; \phi_2) + \ldots] \right) | \Psi(t) \rangle . \tag{3.27}$$

By scanning over different pulse-probe parameters this *non-perturbative* approach in principle allows one break apart the contributions to $\delta \boldsymbol{\mu}(t)$ into specific orders of the system response [70, 71]. Due to the generality of this approach it can be used to recreate nearly any experimental setup or time dependent observable and is a standard approach when calculating transient absorption spectroscopy (TAS) [72–74], high harmonic generation [75–77], time and angle resolved photoelectron spectroscopy [78, 79] and laser induced magnetization and phonon dynamics [80, 81], to name just a few phenomena. These calculations often require a number of dynamical runs, for example in TAS one must simulate the weak field response, pump response and pump + probe response at the desired delays. However the benefit is that when done, the recovered signal automatically contains all contributions at that laser intensity to the signal capable of being resolved by the simulation method. In contrast for a perturbative calculation, the contributions of each n^{th} order channel have to be calculated separately. Thus, for disentangling the excitation and relaxation channels contributing to the experimental signals under far-from-equilibrium driving, non-perturbative real-time dynamics simulations offer the most flexibility, ease and breadth of application, with the caveat that the system's relevant degrees of freedom must be accurately and efficiently represented [82]. In this regard, since we are interested in the role of phonon dynamics on such processes, we again run in to the limitations of the BO/BH picture.

Limitations: Breaking out of BO/BH

The BO/BH framework contains a host a conceptual and practical problems. The issues of calculation and storage have already been mentioned, and even with state of the art 'Direct Dynamics' or 'on-the-fly' approaches, which give semi-local information for wavepackets [83, 84] or semi-classical trajectories [25, 85], the number of nuclear degrees of freedom whose dynamics can be resolved for realistic ab-initio systems, remains in the realm of small to medium sized molecules [25, 86]. Furthermore, as mentioned in the outset, some of the most exciting phenomena of modern condensed matter and ultrafast science involve strongly modifying the electronic states via coupling to intense light fields. This is done statically through cavity enhanced vacuum fluctuation [87–91], in a steady-state manner via Floquet engineering [2, 5, 19, 92] or in an transient manner via strongly driving the nuclear degrees of freedom [13, 18, 80]. All of these

provide significant challenges to the already limited utility of the BO framework. For example, although inclusion of strongly coupled cavity modes into the BOPES can be done formally [88], being able to practically calculate even just electronic properties in ab-initio cavity-molecule systems is still in its infancy [93, 94], while attempts to treat non-adiabatic dynamics on Floquet PESs have been limited to model systems [95, 96]. For nonlinear electronic spectroscopies, there is also the conceptual problem of having to a-priori calculate the BO states within the energy range of the experimental observation, and when using the perturbative method, one must explicitly analyze how the nuclear wavepackets transfer between all active surfaces in the manner of Mukamel, thus limiting the predictive power of the ab-initio simulation and increasing the complexity of the calculation.

The limitations are even more striking when driving the nuclear degrees of freedom. Crucially, many of the experiments cited above are done in solid state systems. For such extended systems the BO framework is invoked almost exclusively to find the ground state BOPES. This defines the equilibrium lattice geometry, and small deviations from it define the phonons. Virtually the entire condensed matter formalism for treating electron-phonon interactions consists of studying electronic states – defined with respect to the equilibrium geometry – being dressed by the underlying bosonic phonon field [24, 97, 98]. Generally this centers on interactions mediated by the first-order or second order anharmonic electron-phonon interaction operators. However these non-equilibrium phase transitions are rooted in strong driving which induces highly anharmonic motion and dramatic realignment of the electronic structure [14, 18, 19, 80]. All of these effects can be very challenging for perturbative methods starting from the equilibrium system to capture. Therefore, it's necessary to find robust theoretical methods which do not rely from the outset on an adiabatic framework, and instead are capable of systematically capturing both strongly renormalized equilibrium system properties and transiently driven far-from equilibrium behavior.

3.3   Outline

This thesis collects contributions the author and collaborators have made over the last five years towards this goal. Working with Prof. Dr. Angel Rubio, Dr. Aaron Kelly, Dr. Shunsuke Sato and Dr. Guillermo Albareda, its core contribution consists of two papers and a manuscript currently under review, in which we develop novel wavefunction dynamics approaches and utilize semi-classical dynamics to treat electron-nuclear interaction in both molecules and solids under equilibrium and non-equilibrium laser driven regimes. The specific contributions of the author to each paper are detailed in section 2.1. In chapters 4, 5, and 6 we briefly introduce and contextualize papers **I**, **II**, and **III** respectively, in terms of what principle questions they address, an overview of the relevant research in that field and the contributions those papers made. The publication of paper **II** precedes that of paper **I** and methods developed in that paper are explored in paper **I** and summarized in chapter 4. Here we briefly summarize what is discussed in the chapters preceding the papers.

Chapter 4 focuses on the question of how to efficiently simulate the fully entangled electron-nuclear dynamics of a system under arbitrarily strong laser driving. Although we mention in passing other fully correlated approaches such as Non-Equilibrium Green's Functions (correlated up to the choice of interactions included in the self energy) and the density matrix

based Hierarchichal Equations of Motion, the focus is on methods which can efficiently represent high dimensional wavefunctions through tensor decompositions, in order to give context for our novel mixed species wavefunction ansatz, the Interacting Conditional Wavefuntion (ICWF) method. Less correlated semi-classical approaches are covered in chapter 5. In chapter 4 we give a brief overview of the method of tensor network decompositions and how they reconstruct high dimensional objects from lower dimensional data, and discuss the 'golden standard' of non-adiabatic nuclear wavefunction dynamics simulation methods: Multi-Configurational Time-Dependent Hartree, which is entirely dependent on diabatic approximations to the BOPESs. I also review some of the recent literature which expanded tensor network methods for coupled electron-nuclear dynamics methods outside of the BO basis, a category in which ICWF belongs. I detail the framework and development of ICWF up to the publication of paper **I** within this context, and give an overview of the contributions of paper **I**. In brief, this work developed several algorithmic advancements which allow the ground and equilibrium excited states of mixed electron-nuclear systems to be calculated, following which they can be propagated under arbitrarily strong laser dynamics while being entirely represented on a real-space grid for all the degrees of freedom. Thus ICWF is presented as a self-contained algorithm for the ab-initio calculation of non-equilibrium mixed-species phenomena, and it's performance is demonstrated for a variety of model physical situations, demonstrating high accuracy for every case. We end by pointing out some of the flaws in the method, and steps which would be required to make it competitive.

In chapter 5 we turn the discussion to semi-classical dynamics methods, where the nuclear degrees of freedom are represented by classical-like point particles. Our goal is to address the question of what coupled electron-nuclear dynamics effects can be recovered when treating the electronic system in a real-space grid basis, rather than in the BO basis. In this chapter to provide a brief, high level overview of the common features of semi-classical dynamics approaches, which allow for systems of much larger sizes to be simulated, and is oftentimes utilized in the BO picture alongside direct dynamics to treat the ab-initio dynamics of larger molecular systems. Using these approaches while representing the electornic system on a real-space grid allows us to capture the properties of all the electronic excited states which can be resolved at a given grid spacing, while in principle allowing for a wide range of nuclear motion. We focus on a particular branch of this literature stemming from the Quantum Classical Liouville Equation, wherein the starting point is an exact transformation of the quantum nuclear degrees of freedom into a phase space picture. This allows for a series of controlled approximations which effectively tune the level of electron-nuclear correlation, before focusing on the mean-field limit: Multi-Trajectory Ehrenfest (MTEF). We discuss how the MTEF algorithm is implemented and how we use it to calculate the linear absorption of molecules. In paper **II** we found that MTEF is able to recover quantized nuclear effects in the vibronic absorption spectrum of molecules and that this is easily applied to ab-initio molecular simulations, prompting questions about what aspects of the far-from-equilibrium phenomena of larger systems can be captured.

In paper **III** we directly address this question by extending MTEF to periodic systems in a generic ab-initio manner, and explore the what effects on the electronic carrier dynamics can be captured when treating the phonon subsystem with MTEF. In chapter 6 we discuss the limitations of the perturbative framework in which condensed matter theory typically treats electron-phonon coupling. Next we cover the semi-classical 'frozen-phonon' approach to capturing phonon renormalized electronic properties, drawing parallels to the molecular vibronic

spectra discussed above. MTEF corresponds to a natural extension of this widely used successful method to include dynamics, and we motivate its application by summarizing some of the examples in literature where single trajectory Ehrenfest dynamics has been applied. As discussed in paper **II** these fail to capture the quantized nuclear effects that MTEF can resolve. In summary we find that MTEF captures equilibrium electron-phonon renormalization, as well as sub-30fs phonon scattering of selectively excited charge carriers in hexagonal Boron Nitride (hBN) due to strong driving, with agreement across different theoretical methods and experimental observations in analagous sytems. We also simulate two experimental pump-probe set ups under ultrafast and ultrastrong laser regimes, one of our own design and one replicating the results of a recent paper, finding a direct connection to the population dynamics in the former and broad agreement with the results of the latter.

We conclude in chapter 7 with a summary of the preceding chapters and a discussion covering their implication for future studies of non-equilibrium phenomena, in particular the potential of MTEF and 'frozen-phonon' static disorder methods to significantly impact the immediate future of non-equilibrium ab-initio simulation in periodic systems.

4 | Conditional Wave Function Theory: A Unified Treatment of Molecular Structure and Nonadiabatic Dynamics

Given a particle in a particular state, the accumulated effects of interactions due to fundamental forces biases the probability of finding nearby particles to be in particular states. On top of these intuitive, classical-like correlations, the indistinguishablity of quantum particles and their capacity to be in a superposition of states leads to far less intuitive effects. Properties such as non-trivial exchange statistics and entangled states can lead to highly non-local correlations. Consequently, trying to simulate these effects within and between subsystems, and especially the role they play in the strongly driven, far-from-equilibrium behavior of matter, is a formidable challenge. Breaking the quantum nature of a given subsystem through a semi-classical approach can reduce the complexity, and we discuss such techniques in chapters 5 and 6. Here instead we focus on methods which attempt to address the full correlation between the electron and phonon subsystem. There are of course many techniques, which start from different assumptions and try to move towards exactness. For example, diagrammatic approaches such as NEGF start from the assumption of a non-interacting system, and systematically build the interactions back in [36, 99–101]. In contrast Hierarchical Equations of Motion start from the fully correlated, but reduced ensemble of the electronic system and systematically build in the non-Markovian time dependent effects of the phonon bath when driving the system non-perturbatively [33, 34]. While both of these methods can approach exactness through the inclusion of ever higher orders of interaction diagrams or hierarchical equations, this can rapidly become expensive in cases of slow convergence or strong coupling.

Wavefunction based approaches intrinsically include all levels of interaction between the component systems, up to the restrictions of the ansatz used to represent the problem and the errors accumulated during propagation. However they are notoriously difficult to scale to large system sizes, and generally based around the BO framework. Thus it is an open research question how much one can build in the fully quantum mechanical non-linear dynamics of coupled electron-nuclear systems, the degree to which this can be done independently of the limitations of the BO framework, and whether the resulting method can be scaled to large system sizes. In paper I we demonstrated that by breaking the wavefunction into component degrees of freedom and representing each on a real-space grid, we can reconstruct strongly driven, highly correlated, electron-nuclear and electron-electron phenomena in a very accurate manner. In this chapter we introduce the class of wavefunction ansätze to which this approach belongs, give an overview of the developments which lead to paper I and discuss the challenges of scaling up this method.

4.1 Straining Against the Curse of Dimensionality

Being able to resolve and propagate the full system wavefunction $\Psi(\underline{\mathbf{r}}, \underline{\mathbf{R}})$ for any given problem has been the unobtainable goal of quantum mechanics for over 100 years. If one tries to naively represent the wavefunction of a fully entangled multi-particle system in a computer, the number of bits of memory required will rapidly exceed the number of atoms within the observable universe ($\approx 10^{78}$). For the simplest possible case, a series of two level qubit systems, this unimaginable information explosion already happens for around 260 qubits! This property of entanglement is referred to as the 'curse of dimensionality' and is one of the arguments underlying the push for simulating quantum systems with quantum computers. Nonetheless, in 2019 when researchers at Google took a task which was asserted to take 10,000 years on classical hardware and performed it in 3 minutes on a 53 qubit device [102], this result was later recreated by an unoptimized Graphics Processing Unit (GPU) program in 15 hours [103].

The reason this is possible is because of the advances which have been made in the last 30 years in simulating extremely high dimensional data. Much of this work was done independently by computer scientists working on signal processing [104, 105], physicists looking for the ground state of fermions interacting on a 1D chain [106] and chemists simulating the dynamics of nuclear wavepackets in the BO picture [107]. It was only later that the connections between these apparently disparate fields became clear and the unifying factor between all of them was *tensor decompositions*. Here we briefly review tensor decompositions, and some of the most successful wavefunction dynamics methods which rely on them to combat the 'curse of dimensionality'.

Tensor Decompositions

Matrices (or tensors of order 2), can be written in terms of sums over 'outer products' of vectors. A particularly important example for any matrix $A \in \mathbb{D}^{m \times n}$ with $\mathbb{D} = \mathbb{R}$ or $\mathbb{C}$, is the Singular Value Decomposition (SVD):

$$A = \sum_{i=1}^{R} \sigma_i \mathbf{u}_i \otimes \mathbf{v}_i, \tag{4.1}$$

where the basis vectors $\{\mathbf{u}_i\} \in \mathbb{D}^m$, and $\{\mathbf{v}_i\} \in \mathbb{D}^n$, form orthornomal sets within their respective subspaces. The singular values σ_i are scalars in $\mathbb{R}$, with $\sigma_i \geq 0$, and the matrix rank, $R \leq \min\{n, m\}$, is the number of non-zero singular values. A given entry of the matrix can be found as

$$A_{kl} = \sum_i \sigma_i u_{i,k} v_{i,l}, \tag{4.2}$$

where $u_{i,k}$ is the k^{th} entry of the vector $\mathbf{u}_i$. The magnitude of a singular value σ_i is in effect a measure of how important the vectors $\mathbf{u}_i$ and $\mathbf{v}_i$ are in representing the matrix A in the full space. Numerically this can help define a compression of the matrix by throwing away small values of σ_i below some cut off σ_c, and reconstructing a *low-rank* approximation. It is also useful for defining a *pseudo-inverse* of a stiff matrix by inverting the low rank approximation [108]. In physics contexts the SVD also appears as the Schmidt decomposition between two coupled Hilbert spaces $\mathcal{H}_1 \otimes \mathcal{H}_2$, and plays a role in the Löwdin symmetric orthogonalization of hybridized atomic orbitals [109].

Such decompositions can be generalized to higher dimensional objects. For example, given a multi-dimensional function such as a PES $U(\underline{\underline{\mathbf{Q}}})$, depending on f degrees of freedom, $\underline{\underline{\mathbf{Q}}} = \left(\mathbf{Q}^{(1)}, \ldots, \mathbf{Q}^{(f)}\right)$, we can represent each degree of freedom $\mathbf{Q}^{(i)}$ on a grid $Q_{i_k}^{(i)}$, $i_k \in [1, \ldots, n_i]$, consisting of n_i points such that $U(\underline{\underline{\mathbf{Q}}}) \in \mathbb{D}^{n_1 \times \ldots \times n_f}$. This constitutes a multi-dimensional matrix or tensor of order f. The higher order SVD (HOSVD) of U can be constructed as:

$$U(\mathbf{Q}^{(1)}, \ldots, \mathbf{Q}^{(f)}) = \sum_{j_1}^{R_1} \cdots \sum_{j_f}^{R_f} s_{j_1, \ldots, j_f} \mathbf{u}_{j_1}^{(1)} \otimes \ldots \otimes \mathbf{u}_{j_f}^{(f)}, \tag{4.3}$$

and a given element of U can be found as

$$U(Q_{i_1}^{(1)}, \ldots, Q_{i_f}^{(f)}) = \sum_{j_1}^{R_1} \cdots \sum_{j_f}^{R_f} s_{j_1, \ldots, j_f} u_{j_1, i_i}^{(1)} \ldots u_{j_f, i_f}^{(f)}. \tag{4.4}$$

This particular format of a tensor decomposition is called a Tucker form, consisting of the core tensor $s \in \mathbb{C}^{R_1 \times \ldots \times R_f}$, and the orthogonal rank 1 tensor bases $B = \{\mathbf{u}_{j_1}^{(1)} \otimes \ldots \otimes \mathbf{u}_{j_f}^{(f)}\} \in \mathbb{D}^{n_1 \times \ldots \times n_f}$ constructed by outer products of the single particle functions (SPFs) $\{\mathbf{u}_{j_l}^{(l)}\} \in \mathbb{D}^{n_l}$. The HOSVD was independently derived in the 1960s for analyzing three dimensional psychometric data [104] and generalized for multi-dimensional signal processing in 2000 [105]. Independently it was also derived by quantum chemists in 1996 appealing to the Schmidt decomposition to represent PESs [107]. It has since found applications in machine learning, signal processing, genetics and virtually every field which requires analysis of the correlations within high dimensional data [110, 111]. Due to the properties of the SVD, low-rank approximations are guaranteed to be optimal in the sense of minimizing the L^2 norm with respect to the full rank tensor, and thus the HOSVD (or POTFIT algorithm) is often referred to as a variational procedure [112]. This derivation alongside the application of the Tucker decomposition to nuclear wavepackets were the principle innovations leading to the most refined non-adiabtic dynamics method for small molecules: Multi-Configurational Time-Dependent Hartree (MCTDH).

'Exact Solutions'

MCTDH was already well established by 2000 [113], and is generally regarded as a theoretically exact benchmark for small molecules [25]. The central premise of MCTDH is to perform a Tucker decomposition of the nuclear wavepackets as well as the PESs in the Heidelberg package of Hans-Dieter Meyer [114]. The SPFs and the core tensor are then treated as variational parameters in the Time Dependent Variational Procedure (TDVP) [115, 116]. The low-rank decomposition of both the nuclear wavepackets and the PESs allows storing both objects in memory and the subsequent sum-over-products format for both makes propagation of Eq. (3.26) possible for larger numbers of degrees of freedom. Finally the TDVP guarantees convergence towards the exact solution of the POTFIT surface dynamics. The MCTDH ansatz can be used for any entangled bosonic system (with extensions to fermionic systems in Multi-Configurational Time Dependent Hartree-Fock), and has been applied to treat coupled nuclear and cavity degrees of freedom in the BO picture [117]. The specific technical details such as the choice of static basis underlying the time dependent SPFs, equation of motion projectors to force SPFs to remain orthogonal throughout the time evolution, regularization strategies, and choice of tensor format for the wavefunction expansion coefficients and potential energies are far beyond the scope of

this introduction and interested readers can consult the relevant literature [114, 118, 119].

While the results obtained with MCTDH can be quite accurate compared to experiment, there are significant obstacles to using this approach. Beyond constructing BOPESs and reducing their complexity to vibronic coupling models, even with the compression of information at a certain point representing the core tensor becomes prohibitive, requiring the decomposition *of the core tensor itself* in what is known as the Hierarchical Tucker format in Multi-Layer (ML-) MCTDH [120]. When applied to LVC models ML-MCTDH can be used for many thousands of degrees of freedom [121, 122], though it's only due to the implicit simplicity of these models that the wavefunction ansatz is able to effectively simulate them [120]. This approach is very complex and in general, beyond a few experimental algorithms, there is no way to know a-priori which degrees of freedom to group together and how to decompose them [123, 124]. However, the (Hierarchical) Tucker format used in (ML-)MCTDH is just one of a huge variety of possible decompositions which have been applied to solve high dimensional entangled problems [125, 126]. In 2019 the time-dependent Denisty Matrix Renormalization Group (td-DMRG) [127–129], originally developed for 1D fermionic models, was applied to LVC [130] and QVC [131] models, and has since inspired reformulations of MCTDH [132]. These methods can help improve problem scaling in some cases, though they still suffer from having to calculate BOPES and the subsequent vibronic reductions.

Wavefunction Dynamics Beyond Born Oppenheimer

Methods such as multi-component DFT [133] the Nuclear Electronic Orbital (NEO) approach [134] and the Exact Factorizaion approach [26] have been developed which treat a selection of the nuclear degrees of freedom quantum mechanically from the outset. This is in sharp contrast to the BO framework where all the nuclei are treated classically to define the BOPES and NACTs, following which they are quantized. However since 2020, there has been an increasing interest in incorporating modern tensor decomposition techniques into fully entangled electron-nuclear dynamics. In that year three papers came out essentially simultaneously which presented a Second Quantized Representation (SQR) of the full electron-nuclear Hamiltonian [30, 31, 135] thus allowing a complete resolution of the combined Hilbert space. Casting the Hamiltonian in this form requires only definitions of the electronic and nuclear orbitals, with no explicit dependence on the BO basis. By encoding the bosonic and fermionic statistics directly into the Hamiltonian, this formulation allows the application of various wavefunction ansätze. Both the Tucker form as well as the DMRG ansatz have subsequently been used to treat the non-adiabatic dynamics of electrons and nuclei in a fully quantum mechanical fashion [30, 31, 136]. While the NEO method provides an elegant choice of orbitals, there is no optimal choice of basis in which to resolve the operators of in the SQR Hamiltonian [135]. From variational arguments it's reasonable to expect that for strongly driven systems, one needs bases with many nodes in order to capture the excited state properties [137]. Conversely one can simply have a basis which evolves in time thus 'tracking' with the excited state properties. This behavior has been argued as a key reason behind the success of MCTDH [118].

4.2 The Interacting Conditional Wavefunction Method

In the calculations of paper I we utilized both static and dynamic basis approaches while defining a generic algorithm for generating electronic and nuclear bases in the real space basis. This algorithm stems from work with *conditional wave functions* (CWFs) of the electronic and nuclear degrees of freedom [138]. For the sake of brevity the composite coordinate for the full system are written as $\underline{\mathbf{x}} = \left(\underline{\mathbf{r}}, \underline{\mathbf{R}}\right)$. A particular coordinate which can be either an electronic or nuclear coordinate is referred to as $\mathbf{x}_i$, and $\underline{\overline{\mathbf{x}_i}}$ refers to every other system coordinate besides that particular one (the complementary degrees of freedom). Each CWF is defined as the instantaneous 'slice' of the full system wavefunction at time t:

$$
\psi_\alpha^{(i)}(\mathbf{x}_i, t; \underline{\overline{\mathbf{x}_i}}^\alpha(t)) \coloneqq \int d\underline{\overline{\mathbf{x}_i}} \delta(\underline{\overline{\mathbf{x}_i}} - \underline{\overline{\mathbf{x}_i}}^\alpha(t)) \Psi(\underline{\mathbf{x}}, t)
$$
$$
\underline{\overline{\mathbf{x}_i}}^\alpha(t) = (\mathbf{r}_1^\alpha(t), \ldots, \mathbf{r}_{N_e}^\alpha(t), \mathbf{R}_1^\alpha(t), \ldots, \mathbf{R}_{N_n}^\alpha(t)) \setminus \mathbf{x}_i^\alpha(t)
$$

(4.5)

with the complementary degrees of freedom evaluated at the configuration $\underline{\overline{\mathbf{x}_i}}^\alpha(t)$. The initial positions of the ensemble of trajectories $\underline{\mathbf{x}}^\alpha(0) = \{\underline{\mathbf{r}}^\alpha(t), \underline{\mathbf{R}}^\alpha(t)\}$ are obtained by sampling some approximation to $|\Psi(\underline{\mathbf{x}}, 0)|^2$. Separately, each CWF constitutes an open quantum system, with the other degrees of freedom being the 'bath'. This is conceptually quite similar to the Exact Factorization approach which factorizes the full system wavefunction between subsystems, these parallels are explored in detail here: [139].

In [138], it's proven that the full system wavefunction can be exactly decomposed into ensemble of CWFs for a particular subsystem if (1) the corresponding ensemble of trajectories $\underline{\mathbf{x}}^\alpha(t)$ explores the support of the probability distribution $|\Psi(\underline{\mathbf{x}}, t)|^2$ at any time and (2) if the CWFs obey non-hermitian equations of motion derived from application of the chain rule:

$$
d_t \psi_\alpha(\mathbf{x}) = \partial_t \psi_\alpha(\mathbf{x}) + \boldsymbol{\nabla}_{\underline{\mathbf{x}}} \Psi|_{\underline{\mathbf{x}}^\alpha} \cdot \underline{\mathbf{v}}^\alpha
$$
$$
i\partial_t \psi_\alpha^{(i)}(\mathbf{x}_i) = \left(-\frac{1}{2m_i} \boldsymbol{\nabla}_{\mathbf{x}_i}^2 + V(\mathbf{x}_i, \underline{\overline{\mathbf{x}_i}}^\alpha(t)) + \eta[\Psi(\underline{\mathbf{x}}, t)](\mathbf{x}_i, \underline{\overline{\mathbf{x}_i}}^\alpha(t)) \right) \psi_\alpha^{(i)}(\mathbf{x}_i),
$$

(4.6)

where $V(\mathbf{x}_i, \underline{\overline{\mathbf{x}_i}}^\alpha(t))$ is the electron-electron, electron-nuclei, and nuclei-nuclei potential operator evaluated along the trajectory defined by velocity $\underline{\overline{\mathbf{v}_i}}^\alpha(t)$, and η is a complex functional dependent on the full system wavefunction. Thus by propagating a large enough ensemble of CWFs the dynamics of the full system can be recovered. The only constraint on the trajectories is that they sample the support of $|\Psi(\underline{\mathbf{x}}, t)|^2$, a property which is satisfied by the Bohmian velocity field [140]:

$$
\underline{\mathbf{v}}(\underline{\mathbf{x}}) = \operatorname{Im}\left(\frac{\boldsymbol{\nabla}_{\underline{\mathbf{x}}} \Psi(\underline{\mathbf{x}})}{\Psi(\underline{\mathbf{x}})} \right).
$$

(4.7)

The ensemble approach is reminiscent of the Coupled-Trajectory Mixed Quantum/Classical Method (CT-MQC) for integrating the Exact Factorizaiton equations of motion by utilizing a swarm of trajectories to reconstruct the wavefunction [96, 141]. Thus in contrast to the evolution equations in MCTDH and DMRG, the CWF approach is not variational in nature, instead it stems purely from physical arguments concerning open quantum systems coupled by 'Bohmian particles' which sample the support of the full system wavefunction.

The advantage sought by utilizing CWFs is to be able to reconstruct the full dynamics of the wavefunction $\Psi(\underline{\mathbf{x}}, t)$, an object whose storage for a grid of n points along each degree of freedom

scales as $\mathcal{O}(n^{(N_e+N_n)})$, by propagating a collection of N_c CWFs scaling as $\mathcal{O}(N_c(N_e + N_n)n)$. However there's a self-consistency problem in Eq. (4.6) due to the dependence of $\underline{\mathbf{v}}^\alpha(t)$ on Ψ which itself is being recovered by the CWFs. Although some applications were able to be made by disregarding $\eta(\underline{\mathbf{x}})$ and utilizing only the independent velocity fields of the CWFs [138, 142], a more exact construction of the wavefunction was established by explicitly using the CWFs as SPFs in a wavefunction ansatz [27]:

$$
\begin{aligned}
\Psi(\underline{\mathbf{x}}, t) &= \sum_{\alpha=1}^{N_c} C_\alpha(t) \psi_\alpha^{(1)}(\mathbf{x}_1, t; \underline{\overline{\mathbf{x}_1}}^\alpha(t)) \otimes \ldots \otimes \psi_\alpha^{(N_e+N_n)}(\mathbf{x}_{N_e+N_n}, t; \underline{\overline{\mathbf{x}}}_{N_e+N_n}^\alpha(t)) \\
&= \sum_{\alpha=1}^{N_c} C_\alpha(t) \boldsymbol{\psi}_\alpha(\underline{\mathbf{x}}, t; \underline{\mathbf{x}}^\alpha(t))
\end{aligned}
\tag{4.8}
$$

From here equations of motion for the expansion coefficients $C_\alpha(t) \in \mathbb{C}$ are made by inserting Eq. (4.8) into Schrödinger's equation and projecting onto the CWF basis. By subsequently using Eq. (4.8) to calculate the fully correlated velocity field in Eq. (4.7) as an input to the CWF equations of motion in Eq. (4.6), the self-consistency problem can be closed. This ansatz is not specific to electron-nuclear dynamics and was also applied to a electron-cavity photon model [27]. While the context of the CWF basis is purely physically inspired, this particular wavefunction ansatz is widely used, and referred to as the 'canonical' tensor decomposition (or CANDECOMP/PARAFAC or the Canonical Polyadic Decomposition [143, 144]). Compared to the Tucker decomposition, the structure is extremely simple, eliminating the storage issue associated with high dimensional core tensors, and in some cases can result in accurate low-rank representations [143, 145]. This however comes at the cost of having non-orthogonal bases, which manifests in ICWF as very stiff overlap matrices $S_{\alpha\beta} = \int d\underline{\mathbf{x}} \psi_\alpha^*(\underline{\mathbf{x}}) \psi_\beta(\underline{\mathbf{x}})$, which need to be treated with the SVD based pseudo-inverse in order to integrate the equations of motion.

The final development which led to the work in paper **I** was actually conducted in the background of paper **II**. In that work we extended ICWF to be able to calculate the full system ground state via freezing the CWFs and trajectories, and performing imaginary time evolution on the expansion coefficients. In that paper we also modified the initial definition of the CWFs so that instead of being slices of some initially known wavefunction as in Eq. (4.5), we initialized them as eigenstates of the Hermitian CWF propagators in Eq. (4.6). That is, instead of slices of the wavefunction, the CWFs were defined as eigenstates of slices of the Hamiltonian. Inclusion of the excited state CWFs increases the flexibility of the basis to capture higher energy without strongly increasing the stiffness of the overlap matrix. These two innovations allowed ICWF to constitute a closed loop algorithm:

1. Sample initial particles from some approximation to the initial wavefunction, $\underline{\mathbf{x}}^\alpha \sim |\tilde{\Psi}(\underline{\mathbf{x}})|^2$

2. Construct and diagonalize $-m_i^{-1} \boldsymbol{\nabla}_{\mathbf{x}_i}^2 + V(\mathbf{x}_i, \underline{\overline{\mathbf{x}_i}}^\alpha)$ to give excited state CWFs $\psi_\alpha^{(i),m}$.

3. Build $\Psi(\underline{\mathbf{x}})$ with the CWFs via Eq. (4.8), and propagate $C_\alpha(\tau)$ in imaginary time τ, minimizing the energy. If desired take $\Psi(\underline{\mathbf{x}}, \tau) \to \tilde{\Psi}(\underline{\mathbf{x}})$ and restart from 1.

4.3 Scientific Contribution and Outlook

Thus in paper **I** we explore the versatility of this closed-loop, fully quantum mechanical, mixed electron-nuclear, real-space, real-time method in capturing the equilibrium properties, perturbative, and non-perturbative dynamics of various model systems. We demonstrate that ICWF, without any reference to the BOPES and their vibrational solutions, captures the vibronic absorption of an H_2 model when calculating the response of a non-perturbative real-time weak external field, as we did in paper **II**. We furthermore show that sta-ICWF is able to exactly capture the non-perturbative dynamics following a resonant driving of the electronic system at the $S_2 \leftarrow S_0$ transition energy while semil-classical MTEF qualitatively fails after the laser is switched off. We also find that dyn-ICWF can accurately capture electron-electron elastic and ineslatic scattering in a 1D model, as well as the laser driven excitation and subsequent vibrationally induced relaxation in a proton transfer model.

Finally we studied the self-interference dynamics of a nuclear wavepacket in a problem whose BOPESs contain a CI. Doing so we find that, without restricting the nuclear wavepacket to a given BO surface during its dynamics, it still avoids the CI region and displays self interference which is typically explained as manifesting from the Berry phase induced by restriction of the wavepacket onto the BOPES [46]. All together, by showing that ICWF can accurately calculate BOPESs, vibronic absorption peaks, inter-state relaxation, and nuclear self-interference we conclusively demonstrate that this real-space wavefunction dynamics method contains the BO framework, while the electron-electron scattering and non-perturbative driving (which could be done at any strength to any number of excited electronic states) demonstrate it is not limited to it.

While the simulation results are impressive as proofs of concept, there are significant difficulties in applying this method to realistic systems. To begin with, we utilized the first quantized representation without explicitly accounting for spin, thus implicitly treating our two electron systems as singlet states. To improve on this one would either have to build the wavefunction as Slater determinants or incorporate the fermionic statistics directly into an SQR representation of the Hamiltonian. On that front, the definition of CWFs we've used here provide a unique starting point for developing bases which could be of some use in other applications, seeing as they diagonlize restricted subspaces of the Hamiltonian. However, the non-orthogonality of the CWFs is a major drawback, and can lead to significant problems in the propagation of ICWF, primarily through inclusion of redundant degrees of freedom leading to a stiff overlap matrix. Although some CWFs may be redundant at a given time in the simulation, they could become important later, leading to a hoarders dilemma.

The consequence is that for the four-dimensional nuclear self-interference example, even with significant numerical optimizations and exploiting parallel GPU resources, propagating the 4096 CWFs necessary to converge the results took four times longer than the numerically exact solution on the same hardware. This problem is common in TDVP ansätze, and there exist strategies to alleviate it such as choosing relevant bases from a pool in a way which minimizes redundancy [146] or by projecting the propagator onto a linearly independent subset of the bases [147]. Thus further expansion of the ideas presented would require significant investment in optimization of the algorithm through exploration of alternative tensor formats, optimizations of the on the fly evaluation of the two-body potentials, and an optimal choice of basis set. While

the physical arguments underlying the CWFs and their equations of motion are compelling, it's unclear the advantage they would have in contrast to a fully variational approach, which is mathematically guaranteed to converge with increasing non-redundant degrees of freedom. Instead for the rest of the research presented in this thesis we turned to expanding the realm of applicability of a tool already common to the real-time ab-initio dynamics community, though often not used to its full potential: semi-classical dynamics.

Conditional Wave Function Theory: A Unified Treatment of Molecular Structure and Nonadiabatic Dynamics

Guillermo Albareda,* Kevin Lively,* Shunsuke A. Sato,* Aaron Kelly,* and Angel Rubio*

Read Online

ACCESS | Metrics & More | Article Recommendations

ABSTRACT: We demonstrate that a conditional wave function theory enables a unified and efficient treatment of the equilibrium structure and nonadiabatic dynamics of correlated electron−ion systems. The conditional decomposition of the many-body wave function formally recasts the full interacting wave function of a closed system as a set of lower-dimensional (conditional) coupled "slices". We formulate a variational wave function ansatz based on a set of conditional wave function slices and demonstrate its accuracy by determining the structural and time-dependent response properties of the hydrogen molecule. We then extend this approach to include time-dependent conditional wave functions and address paradigmatic nonequilibrium processes including strong-field molecular ionization, laser-driven proton transfer, and nuclear quantum effects induced by a conical intersection. This work paves the road for the application of conditional wave function theory in equilibrium and out-of-equilibrium ab initio molecular simulations of finite and extended systems.
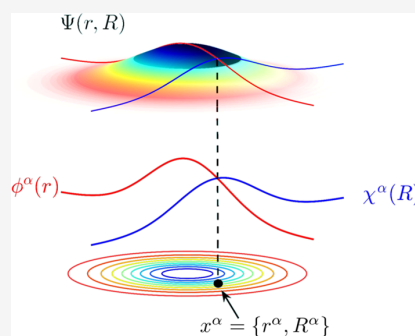
1. INTRODUCTION

Emerging experimental capabilities in the precise manipulation of light and matter are opening up new possibilities to understand and exploit correlations and quantum effects that can be decisive in the functional properties of molecules and materials. Light-driven states can not only be designed to monitor and/or control the structure of molecules[1−7] and solids[8−12] but also form light−matter hybrid states with new physical properties.[13−21] In view of these exciting developments, accurate first-principles theoretical techniques are also needed to help interpret observations, to enable the predictions of simplified models to be scrutinized, and, ultimately, to help gain predictive control. Our ability to treat the full correlated quantum structure and dynamics of general electron−ion systems unfortunately remains limited by the unfavorable scaling of the many-body problem.

A standard approach to address this problem in molecular and solid-state systems has been to "divide-and-conquer" in the sense that the electronic structure and the electron−nuclear interactions are treated separately. Introduced almost a century ago by Born and Oppenheimer,[22] the adiabatic approximation, i.e., the assumption that electrons adjust instantaneously to the motion of nuclei, is the cornerstone of this so-called standard approach. The Born−Oppenheimer (BO) approximation has been crucial to the development of a vast majority of approaches in quantum chemistry and condensed-matter theory,[23,24] and the concept of ground-state Born−Oppenheimer potential-energy surface (BOPES) is the foundation for understanding the properties of systems at thermal equilibrium such as chemical

reactivity[25−27] and nuclear quantum effects,[28−31] as well as of systems driven out of equilibrium.[32−35]

Accurately describing systems driven away from equilibrium and including nonadiabatic electron−nuclear effects places even more stringent demands on the development of practical first-principles tools. In the standard approach, one directly builds upon the BO approximation by expanding the full molecular wave function in the Born−Huang basis.[36] Within this framework, nonadiabatic processes can be viewed as nuclear wavepacket dynamics with contributions on several BOPESs, connected through nonadiabatic coupling terms that induce electronic transitions.[37] In this picture, trajectory-based quantum dynamics methods offer a trade-off between physical accuracy and computational cost.[38−40] Of these approaches, perhaps the most popular are the Ehrenfest mean-field theory[41] and Tully's surface hopping dynamics.[42] Both of these approaches consist of an ensemble of uncorrelated trajectories. Reintroducing correlation, for example, using a variety of wave function ansatz,[43−48] semiclassical techniques,[49,50] the quantum-classical Liouville equation,[51−53] path-integral meth-

ods,[54,55] or methods based on the exact factorization,[56−58] allows for further accuracy with increased computational effort.

While advances in the ab initio electronic structure theory in quantum chemistry and condensed matter have made computing the ground-state energies both routinely efficient and rather accurate in many cases, obtaining accurate excited-state information remains a challenging problem in its own right. Even in cases where the excited-state electronic structure is available, performing fully quantum nuclear dynamics calculations using the standard approach quickly becomes infeasible[35,43] as the memory required to store the information contained in the BOPESs grows rapidly with the number of correlated degrees of freedom. In this respect, gaining the ability to rigorously treat selected nuclear degrees of freedom quantum mechanically without incurring an overwhelming computational cost is the goal.

An alternative approach for describing quantum effects in coupled electron−ion systems is using a real-space representation of all degrees of freedom. This route might sound less intuitive as it avoids routine concepts such as BOPESs and nonadiabatic couplings that are fundamental in the present description and understanding of quantum molecular dynamics. However, this feature might be turned into an attractive playground from the computational point of view, as these quantities are usually demanding to obtain and fit from ab initio electronic structure calculations. In this framework, one of the leading approximate methods to describe the coupled electron−nuclear dynamics for large systems is time-dependent density functional theory coupled to classical nuclear trajectories through the Ehrenfest method.[59] Due to its favorable system-size scaling, the real-space picture Ehrenfest method has been successful for a great many applications, from capturing phenomena associated with vibronic coupling in complex molecular systems[60] and photodissociation dynamics in small molecules[61] to radiation damage in metals;[62] its efficiency allows calculations on large systems for even hundreds of femtoseconds.[63] It has also been recently combined with the nuclear-electronic orbital method as a way to include quantum effects for selected nuclear degrees of freedom to study proton transfer processes in molecular excited states.[64]

It is well known, however, that the Ehrenfest approach can be inaccurate due to its mean-field nature. One classic example of this breakdown occurs in photochemical reaction dynamics, where mean-field theory can often fail to correctly describe the product branching ratios.[39,65] Generally speaking, the mean-field description of any transport property can potentially suffer some deficiency; this is sometimes referred to as a violation of detailed balance,[66] but it ultimately stems from the lack of time-translational invariance that is inherent to any approximate method that does not rigorously preserve the quantum Boltzmann distribution.[67]

The conditional wave function (CWF) framework introduced in ref 68 offers a route to go beyond the limits of mean-field theory while retaining a real-space picture; it is an exact decomposition and recasting of the total wave function of a closed quantum system.[69] When applied to the time-dependent Schrödinger equation, the conditional decomposition yields a set of coupled, non-Hermitian, equations of motion.[68] One can draw connections between CWF theory and other formally exact frameworks proposed in the literature to develop novel approximate schemes that provide a completely new perspective to deal with the long-standing problems of nonadiabatic dynamics of complex interacting systems.[70,71] An example is

the time-dependent interacting conditional wave function approach (ICWF),[72,73] a recently introduced method for performing quantum dynamics simulations that is multi-configurational by construction. Using a stochastic wave function ansatz that is based on a set of interacting single-particle CWFs, the ICWF method is a parallelizable technique, which achieves quantitative accuracy for situations in which mean-field theory drastically fails to capture qualitative aspects of the dynamics, such as quantum decoherence, using orders of magnitude fewer trajectories than the converged mean-field results.[72]

In this work, we introduce an exact time-independent version of the CWF mathematical framework. The time-independent CWF framework is formulated in real space, and it is an exact decomposition of the time-independent wave function of a closed quantum system that yields a set of coupled nonlinear eigenvalue problems and associated conditional eigenstates. Based on this framework, we put forth a static-basis version of the ICWF method, which allows us to establish an efficient and accurate algorithm for calculating the ground- and excited-state structures of correlated electron−nuclear systems and eventually extended systems. Importantly, the combination of the static version of the ICWF method using a time-dependent conditional eigenstate basis sets the stage for the implementation of a general-purpose ab initio molecular simulator that is formulated in the real-space picture and that self-consistently treats stationary states, as well as driven dynamics.

This manuscript has the following structure: in Section 2, we define the mathematical structure of the time-independent version of the CWF framework. Based on these results, we put forth an imaginary-time version of the ICWF technique in Section 3 for solving the time-independent Schrödinger equation and the performance of the resulting algorithm is assessed through the calculation of the ground-state and the low-lying excited-state BOPESs of the hydrogen molecule in one dimension (1D). In Section 4, a real-time extension of this multiconfigurational ansatz is presented, along with an algorithm for solving the time-dependent Schrödinger equation using a stochastic static-basis ansatz. The ability of the resulting algorithm in capturing static and dynamic properties is then assessed by evaluating the absorption spectrum and a laser-induced dynamics of the aforementioned H_2 model system. In Section 5, we revisit the exact time-dependent CWF framework, and in Section 6, we present the dynamical ICWF (dyn-ICWF) approach to the time-dependent Schrödinger equation. The performance of the time-dependent ICWF method in combination with its imaginary-time variation for preparing the initial state is demonstrated for three model systems, viz., a laser-driven proton-coupled electron transfer model, an electron-atom scattering process, and an example of nuclear quantum effects in the dynamics through a conical intersection (CI). A summary of the main results of this work and an outlook on future directions are offered in Section 7.

2. CONDITIONAL EIGENSTATES

We begin by considering a closed system with n electrons and N nuclei, collectively denoted by $x = (r, R)$. We use the position representation for both subsets; lowercase symbols will be used for the electronic subsystem, e.g., $r = \{r_1 s_1, ..., r_n s_n\}$, and uppercase symbols $R = \{R_1 \sigma_1, ..., R_N \sigma_N\}$ for the nuclear subsystem. Hereafter, electronic and nuclear spin indices, respectively, s_j and σ_j, will be made implicit for notational
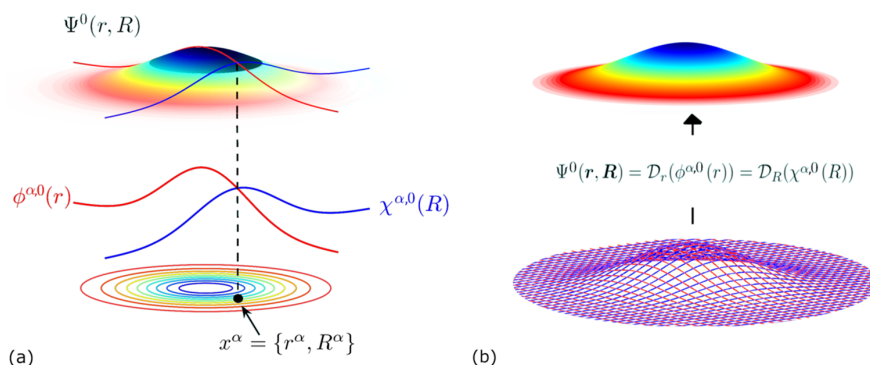
Figure 1. Schematic representation of the CWF approach to the time-independent Schrödinger equation for one electron and one nucleus in one dimension, i.e., $\boldsymbol{x} = (r, R)$. (a) The full ground-state $\Psi^0(r, R)$ is plotted together with a pair of conditional ground states $\phi^{\alpha,0}(r)$ for the electronic degree of freedom (in red) and $\chi^{\alpha,0}(R)$ for the nuclear degree of freedom (in blue) for a given position of the full configuration space $\{r^\alpha, R^\alpha\}$. Contour plots of the molecular wave function are also shown for clarity. (b) The exact solution of the time-independent Schrödinger equation in eq 1 can be reconstructed provided a sufficiently large ensemble of sampling points $x^\alpha = \{r^\alpha, R^\alpha\}$. This can be done by applying the reassembling transformation $\mathcal{D}_r$ or $\mathcal{D}_R$ (whose definition can be found in Appendix A) to the ensemble of electronic $\phi^{\alpha,0}(r)$ or nuclear $\chi^{\alpha,0}(R)$ conditional eigenstates, respectively.

simplicity, and, unless otherwise stated, all expressions will be given in atomic units.

The time-independent CWF can be constructed starting from the nonrelativistic time-independent Schrödinger equation in the position representation

$$\hat{H}\Psi^\gamma(\boldsymbol{x}) = E^\gamma \Psi^\gamma(\boldsymbol{x}) \tag{1}$$

where $\Psi^\gamma(\boldsymbol{x})$ is an eigenstate of the molecular Hamiltonian $\hat{H}$ with label γ and the corresponding energy eigenvalue E^γ. The molecular Hamiltonian operator $\hat{H}$ in eq 1 can be written as

$$\hat{H} = \sum_{j=1}^{N \times n} \hat{T}_j(\boldsymbol{x}_j) + W(\boldsymbol{x}) \tag{2}$$

where the kinetic energy operators are $\hat{T}_j = \frac{1}{2m_j}(-i\hbar\nabla_j - z_j\mathbf{A}(\boldsymbol{x}_j))^2$, m_j and z_j being the characteristic mass and charge of particle j, respectively. The full electron–nuclear potential energy of the system is $W(\boldsymbol{x})$ (written in the position basis rather than, say, the BO or Born–Huang basis), and $\mathbf{A}$ is the vector potential due to an arbitrary static external electromagnetic field.

Note that the total Hamiltonian in eq 1 is invariant under translations and rotations of all particles. This means that the eigenstates of the system will be invariant under transformations by the translation and rotation groups. Together with the inversion symmetry, this implies that all one-body quantities such as the electron density or any nuclear-reduced density are constant and that two-particle position correlation functions only depend on the distance between their arguments. This is obviously not a convenient starting point to describe the structure of a quantum system. The solution to this problem relies on transforming the Hamiltonian to a fixed coordinate system that reflects the internal properties of the system.[a] This is, in general, not a trivial task, and hereafter, we will assume that eq 1 already reflects such internal properties, either by exploiting a particular symmetry of the system or by simply introducing a parametric dependence on, e.g., a fixed (heavy) nuclear position.

At this point, we can decompose the eigenstates $\Psi^\gamma(\boldsymbol{x})$ in terms of single-particle conditional eigenstates of either of the two subsystems, which are defined as follows

$$\psi_i^{\alpha,\gamma}(\boldsymbol{x}_i) := \int d\bar{\boldsymbol{x}}_i \, \delta(\bar{\boldsymbol{x}}_i^\alpha - \bar{\boldsymbol{x}}_i)\Psi^\gamma \tag{3}$$

Here, the index α denotes the particular conditional slice and $\bar{\boldsymbol{x}}_i = (\boldsymbol{x}_1, ..., \boldsymbol{x}_{i-1}, \boldsymbol{x}_{i+1}, ..., \boldsymbol{x}_{n\times N})$ are the coordinates of all degrees of freedom in the system except $\boldsymbol{x}_i$. Similarly, $\bar{\boldsymbol{x}}_i^\alpha = (\boldsymbol{x}_1^\alpha, ..., \boldsymbol{x}_{i-1}^\alpha, \boldsymbol{x}_{i+1}^\alpha, ..., \boldsymbol{x}_{n\times N}^\alpha)$ are some particular positions of all system degrees of freedom except $\boldsymbol{x}_i$. As shown schematically in Figure 1, the conditional eigenstates in eq 3 represent one-body slices of the full many-body eigenstates $\Psi^\gamma(\boldsymbol{x})$ taken along the coordinate of the ith degree of freedom. The particle placement $\boldsymbol{x}^\alpha$ defining the CWFs has not yet been specified, and although, in principle, it can be chosen arbitrarily, it will be proven convenient in practice to exploit important sampling techniques.

Evaluating eq 1 at $\bar{\boldsymbol{x}}_i^\alpha$ by applying the integral operator in eq 3 yields conditional eigenstates that are the solutions of the following eigenvalue problem

$$(\hat{T}_i + W_i^\alpha + \eta_i^{\alpha,\gamma})\psi_i^{\alpha,\gamma} = E^\gamma\psi_i^{\alpha,\gamma} \tag{4}$$

where we introduced $W_i^\alpha(\boldsymbol{x}_i) = W(\boldsymbol{x}_i\bar{\boldsymbol{x}}_i^\alpha)$, with $W(\boldsymbol{x})$ being the full electron–nuclear interaction potential appearing in the Hamiltonian of eq 2. In addition, $\eta_i^{\alpha,\gamma}(\boldsymbol{x}_i)$ are the kinetic correlation potentials given by

$$\eta_i^{\alpha,\gamma}(\boldsymbol{x}_i) = \sum_{j\neq i}^{n\times N} \frac{\hat{T}_j\Psi^\gamma}{\Psi^\gamma}\bigg|_{\bar{\boldsymbol{x}}_i^\alpha} \tag{5}$$

Provided a large enough collection of CWFs satisfying eq 4, an exact solution of eq 1 can be reconstructed by undoing the conditional decomposition of eq 3 (see Figure 1b).[68] That is, given a set of conditional slices that sufficiently span the support of Ψ^γ, then the corresponding conditional eigenstates can be used to reassemble the full electron–nuclear wave function

$$\Psi^\gamma(\boldsymbol{x}) = \mathcal{D}_{\boldsymbol{x}_i}(\psi_i^{\alpha,\gamma}) \tag{6}$$

using the transformations $\mathcal{D}_{\boldsymbol{x}_i}$, which are discussed in more detail in Appendix A. This expression, eq 6, can be used to evaluate the kinetic correlation potentials in eq 5. In this way, the generalized one-body eigenvalue problem in eq 4 can be understood as an exact decomposition and recasting of the eigensolution of the full electron–nuclear system, which yields a set of coupled, non-Hermitian, eigenvalue problems.

2.1. Time-Independent Hermitian Approximation. An approximate solution to eq 4 can be formulated by expanding the kinetic correlation potentials around the sampling coordinates $\boldsymbol{x}^\alpha$ using Taylor series and then truncating at zeroth order, i.e.

$$\eta_i^{\alpha,\gamma}(\boldsymbol{x}_i) \approx f(\overline{\boldsymbol{x}}_i^\alpha) \tag{7}$$

At this level, the kinetic correlation potentials engender only a global phase that can be simply omitted as expectation values are invariant under such global phase transformations. Note that these approximated kinetic correlation potentials can be alternatively obtained by introducing a mean-field ansatz $\Psi^\gamma(\boldsymbol{x}) = \prod_{i=1}^{n \times N} \psi(\boldsymbol{x}_i)$ into eq 5. By making this approximation, the eigenvalue problems in eq 4 are restored to a Hermitian form

$$(\hat{T}_i + W_i^\alpha)\psi_i^{\alpha,\gamma} \approx E^\gamma \psi_i^{\alpha,\gamma} \tag{8}$$

The Hermitian limit allows the full many-body problem to be approximated as a set of independent single-particle problems. That is, the superscript γ refers exclusively to the conditional eigenstate excitation number.

3. STATIC PROPERTIES WITH CONDITIONAL EIGENSTATES

In general, the higher-order terms in the Taylor expansion of the kinetic correlation potentials are non-negligible. However, one can still take advantage of the simple Hermitian form of the conditional eigenvectors (hereafter referred to as conditional wave functions (CWFs)) in eq 8 to design an efficient many-body eigensolver by utilizing them as bases for electronic and nuclear degrees of freedom in a variational wave function ansatz.

While there is a diverse literature spanning decades on different forms for variational electron–nuclear wave function ansatz, for illustrative (and practical) purposes, we employ a sum-of-product form, which in the language of tensor decompositions is referred to as the canonical format.[76] For each degree of freedom $\boldsymbol{x}_i$, we utilize a given electronic or nuclear CWF, respectively, coming from solutions to eq 8, to approximate the γth full system exact excited state as follows

$$\Psi^\gamma(\boldsymbol{x}) = \sum_{(\lambda,\nu)=(1,1)}^{(N_c,M)} C_{\lambda,\nu}^\gamma \prod_{i=1}^{n \times N} \psi_i^{\lambda,\nu}(\boldsymbol{x}_i)$$
$$= \sum_{\alpha=1}^{N_cM} C_\alpha^\gamma \prod_{i=1}^{n \times N} \psi_i^\alpha(\boldsymbol{x}_i) \tag{9}$$

where in the second line, we have rearranged the sum over particle position $\lambda \in \{1, ..., N_c\}$ and excited CWF $\nu \in \{1, ..., M\}$ into a single index $\alpha = \lambda + N_c(\nu - 1)$, such that $\alpha \in \{1, ..., N_cM\}$. The particle placement $\boldsymbol{x}^\alpha$ defining the conditional potentials W_i^α has not yet been specified, and, in principle, it can be chosen arbitrarily; however, in practice, we choose to sample from initial guesses for the reduced densities of the electronic and nuclear subsystems.

We refer to this ansatz (eq 9) as being in canonical format because we do not mix all possible CWFs $\psi_i^{\lambda,\nu}$ for all possible degrees of freedom $\boldsymbol{x}_i$, as one does with a single-particle function bases across the different system degrees of freedom in the Tucker format employed in the multiconfigurational time-dependent Hartree (Fock)—MCTDH(F)[43] and multiconfigurational electron–nuclear dynamics ansatz.[77] In principle, this choice can be relaxed, and one can utilize various choices of tensor network representation for the expansion coefficients $\mathbf{C}$,

such as matrix product states or hierarchical Tucker formats, which when employed in the multilayer extension[78,79] of MCTDH allow for an increase in efficiency for certain problems. However, since the time dependence of the ansatz in eq 9 is entirely within the expansion coefficients, one only needs to calculate the matrix elements at time zero, creating a quite efficient time propagation framework. Note that although we use a simple Hartree product over electronic degrees of freedom, the above ansatz can be straightforwardly extended to have fermionic antisymmetry via treating the CWFs as the spatial component of spin orbitals in Slater determinants.

Hereafter, and for reasons that will be apparent later, we will call eq 9 the static-basis ICWF (or sta-ICWF) ansatz. With this ansatz in hand, we then consider a solution of eq 1 based on the imaginary-time propagation technique,[80] i.e.

$$\frac{\mathrm{d}}{\mathrm{d}\tau}\Psi^\gamma(\boldsymbol{x}, \tau) = -\hat{H}^\gamma \Psi^\gamma(\boldsymbol{x}, \tau) \tag{10}$$

where

$$\hat{H}^\gamma(\boldsymbol{x}) = \left(\mathbb{I} - \sum_{\zeta=1}^{\gamma-1} \hat{P}^\zeta\right)\hat{H}(\boldsymbol{x})\left(\mathbb{I} - \sum_{\zeta=1}^{\gamma-1} \hat{P}^\zeta\right) \tag{11}$$

and $\hat{P}^\zeta = \Psi^\zeta \Psi^{\zeta\dagger}$ are projectors used to remove the wave functions Ψ^ζ from the Hilbert space spanned by $\hat{H}$. The first excited state, for instance, is thus obtained by removing the ground state from the Hilbert space, which makes the first excited state the ground state of the new Hamiltonian.

By introducing the ICWF ansatz of eq 9 into eq 10, we find an equation of motion for the coefficients $\mathbf{C}^\gamma = \{C_1^\gamma, ..., C_{N_cM}^\gamma\}$

$$\frac{\mathrm{d}\mathbf{C}^\gamma}{\mathrm{d}\tau} = -\mathbb{S}^{-1}\mathbb{H}\mathbf{C}^\gamma(\tau) + \mathbb{S}^{-1}\sum_{\xi=1}^{\gamma-1}(\mathbb{H}\mathbb{C}^\xi\mathbb{S} + \mathbb{S}\mathbb{C}^\xi\mathbb{H})\mathbf{C}^\gamma(\tau)$$
$$- \mathbb{S}^{-1}\sum_{\xi=1}^{\gamma-1}\sum_{\nu=1}^{\gamma-1}\mathbb{S}\mathbb{C}^\xi\mathbb{H}\mathbb{C}^\nu\mathbb{S}\mathbf{C}^\gamma(\tau) \tag{12}$$

where $\mathbb{C}^\xi = \mathbf{C}^\xi\mathbf{C}^{\xi,\dagger}$, and the matrix elements of $\mathbb{H}$ and $\mathbb{S}$ are

$$\mathbb{S}_{\alpha\beta} = \prod_{i=1}^{n \times N} \int \mathrm{d}\boldsymbol{x}_i \, \psi_i^{\alpha*}\psi_i^\beta \tag{13}$$

$$\mathbb{H}_{\alpha\beta} = \prod_{i=1}^{n \times N} \int \mathrm{d}\boldsymbol{x}_i \, \psi_i^{\alpha*}\hat{H}\psi_i^\beta \tag{14}$$

where again, the α, β indices refer to the index over particle placement and excited CWFs. Obtaining these matrix elements involves a sum over all two-body interactions across each degree of freedom and a sum across one-body operators. In practice, $\mathbb{S}$ may be nearly singular, but its inverse can be approximated by the Moore–Penrose pseudo-inverse.

Based on solving the system of equations in eq 12 for $\mathbf{C}^\gamma$, one already has the ingredients to put forth a time-independent ICWF eigensolver algorithm that will ultimately be used to evaluate the expectation value of generic observables $\hat{O}(\boldsymbol{x})$. Given an approximate solution to the eigenfunction $\Psi^\gamma(\boldsymbol{x})$, the expectation value of $\mathbb{O}$ reads

$$\langle \hat{O} \rangle_\gamma = \mathbf{C}^{\gamma\dagger}\mathbb{O}\mathbf{C}^\gamma \tag{15}$$

with the matrix elements of $\mathbb{O}$ being given by an analogous expression to eq 14.

3.1. Example I: Ground and Excited BOPESs of H_2. As an illustrative example, we now calculate the BOPESs of a model for the H_2 molecule. We adopt a model where the motion of all particles is restricted to one spatial dimension, and the center-of-mass motion of the molecule can be separated off.[81,82] In this model, the relevant coordinates are the internuclear separation, R, and the electronic coordinates, r_1 and r_2. The Hamiltonian, written in terms of these coordinates, is

$$H(r_1, r_2, R) = -\frac{1}{2\mu_n}\frac{\partial^2}{\partial R^2} + \frac{1}{R} + W_{ee}(r_1, r_2)$$
$$+ \sum_{i=1}^{2}\left(-\frac{1}{2\mu_e}\frac{\partial^2}{\partial r_i^2} + W_{en}(r_i, R)\right) \quad (16)$$

where for M being the proton mass, $\mu_e = M/(2M + 1)$ is the reduced electronic mass and $\mu_n = M/2$ is the reduced nuclear mass. In eq 16, the electron−electron repulsion and the electron−nuclear interaction are represented by soft-Coulomb potentials

$$W_{ee}(r_1, r_2) = \frac{1}{\sqrt{(r_1 - r_2)^2 + \epsilon_{ee}}} \quad (17)$$

$$W_{en}(r, R) = -\frac{1}{\sqrt{(r - R/2)^2 + \epsilon_{en}}} - \frac{1}{\sqrt{(r + R/2)^2 + \epsilon_{en}}} \quad (18)$$

i.e., the Coulomb singularities are removed by introducing smoothing parameters $\epsilon_{ee} = 2$ and $\epsilon_{en} = 1$. The above model system qualitatively reproduces all important strong-field effects such as multiphoton ionization, above-threshold ionization, or high-harmonic generation.[83−85] Moreover, it has provided valuable information in the investigation of electron correlation effects.[86−88]

For this model, the BOPESs are defined by the following electronic eigenvalue problem

$$\mathcal{H}_{el}(r_1, r_2; R)\Phi^\gamma(r_1, r_2; R) = \epsilon^\gamma(R)\Phi^\gamma(r_1, r_2; R) \quad (19)$$

where $\mathcal{H}_{el} = \hat{H} - \hat{T}_{nuc}$, and $\{\Phi^\gamma(r_1, r_2; R)\}$ are the (complete, orthonormal) set of BO electronic states. A parametric dependence on the nuclear coordinates is denoted by the semicolon in the argument. The BOPESs, $\epsilon^\gamma(R)$, can be calculated using the imaginary-time sta-ICWF method described in eqs 10−14 along with a simplified version of the ansatz in eq 9 that is specialized to this particular case of parametric nuclear dependence. A thorough description of the numerical procedure, as well as the convergence behavior of the sta-ICWF method for this model can be found in Appendix B.1.

In Figure 2, we show the first five BOPESs calculated via the sta-ICWF approach using $(N_c, M) = (32, 5)$. In the top panel, the exact BOPESs are plotted against the sta-ICWF data, overlaid as solid gold lines. The results demonstrate that the sta-ICWF ansatz used in a variational context captures the entire group of the excited BOPES landscape over this energy range. As a point of comparison, in the bottom panel of Figure 2, we also show the result of mean-field-type calculations of the BOPESs for this system. Specifically, we show Hartree−Fock and configuration interaction singles (CIS) data for the ground-state and excited-state BOPESs, respectively, which suffer from well-known
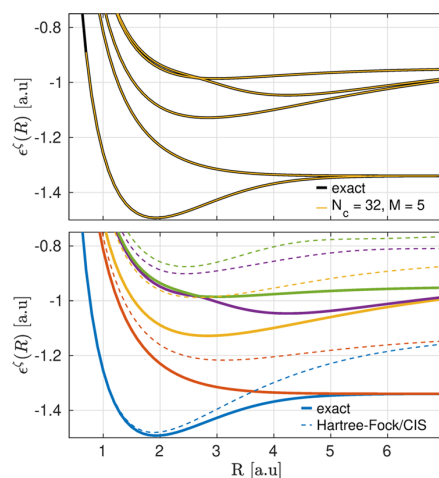
Figure 2. Exact first five BOPESs of the one-dimensional H_2 model system (solid black lines). sta-ICWF results for $(N_c, M) = (32, 5)$ are shown in the top panel (solid gold lines). Hartree−Fock and CIS results for the ground-state and excited-state BOPESs, respectively, are shown in the bottom panel (dashed lines) alongside exact results (solid lines) and color-coordinated via calculated excited states.

inaccuracies in capturing the binding energy and excited-state properties of the system.

4. TIME-DEPENDENT PROPERTIES WITH CONDITIONAL EIGENSTATES

The sta-ICWF eigensolver described above can be easily extended to describe dynamical properties. For that, we consider the time-dependent Schrödinger equation

$$i\frac{d}{dt}\Psi(x, t) = \hat{H}(t)\Psi(x, t) \quad (20)$$

where $\Psi(x, t)$ is the electron−nuclear time-dependent wave function, and the Hamiltonian of the system $\hat{H}(t)$ may contain a time-dependent external electromagnetic field.

In practice, we are interested in situations where the initial wave function is the correlated electron−nuclear ground state, i.e., $\Psi(x, 0) = \Psi^{\gamma=0}(x)$, and some nonequilibrium dynamics is triggered by the action of an external driving field (hereafter, we omit the superscript γ for clarity). We can then decompose the time-dependent many-body wave function as in eq 9 by restricting it to the case of $\gamma = 0$. We choose to restrict, for the moment, the time dependence of our ansatz to the expansion coefficients C_α. Although in this formulation the basis remains static, by choosing sufficient excited CWF states, $\gamma > 0$ in eq 8, for x_α covering some anticipated range of motion for the dynamics, we can expect to capture the support of $\Psi(t)$. The equations of motion for C_α can be obtained either by inserting eq 9 directly into eq 20 or by utilizing the Dirac−Frenkel variational procedure[b]

$$\frac{d}{dt}\mathbf{C}(t) = -i\mathbb{S}^{-1}\mathbb{H}(t)\mathbf{C}(t) \quad (21)$$

In eq 21, the matrix elements of $\mathbb{S}$ and $\mathbb{H}$ are identical to those defined in eqs 13 and 14, with the Hamiltonian's time dependence coming from any external fields and the wave function decomposed into single-particle CWFs for the nuclear and both electronic degrees of freedom. The values of the coefficients at time $t = 0$, i.e., $\mathbf{C}(0)$, may be obtained from the

imaginary-time sta-ICWF method of eq 12. In this way, the combination of the imaginary-time and real-time sta-ICWF methods yields a "closed-loop" algorithm for the structure and dynamics of molecular systems that does not require explicit BO state information as an input to the method. For the interested reader, a detailed flowchart of the resulting sta-ICWF method can be found in Appendix D.
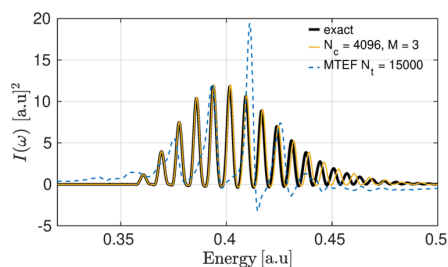
4.1. Example II: Optical Absorption Spectrum of H_2. Here, we demonstrate an application of the real-time sta-ICWF approach to simulate the optical absorption spectrum for the molecular hydrogen model introduced in Section 3.1. We utilize the "δ-kick" method of Yabana and Bertsch,[89] where an instantaneous electric field $E(t) = \kappa\delta(t)$ with perturbative strength $\kappa \ll 1$ au^{-1} couples to the dipole moment operator $\mu = r_1 + r_2$ and thereby produces an instantaneous excitation of the electronic system to all transition dipole allowed states. The resulting (linear) absorption spectra can then be calculated via the dipole response, $\Delta\mu(t) = \mu(t) - \mu(0^-)$

$$I(\omega) = \frac{4\pi\omega}{c\kappa}\Im\left[\int_0^\infty e^{i\omega t}\langle\Delta\mu(t)\rangle\,dt\right] \tag{22}$$

In practice, due to the finite time propagation, the integrand is also multiplied by a mask function $\mathcal{M}(t)$ that smoothly vanishes at the final simulation time T_f.

The system is first prepared in the ground state using the imaginary-time sta-ICWF. See Appendix B.2 for a thorough description of the imaginary-time sta-ICWF method and its use for preparing the ground state of the H_2 model system. The field-driven dynamics is then generated by applying the kick operator to the relevant degree of freedom. A thorough description of the numerical procedure, as well as the convergence behavior of the sta-ICWF method for this model, can be found in Appendix B.3. The reader can also find a detailed flowchart of the (real and imaginary) sta-ICWF method in Appendix D.

For the H_2 model, the occupation of excited electronic states and subsequent coupled electron–nuclear dynamics produce a characteristic vibronic peak structure usually explained via the Franck–Condon vertical transition theory. In the top panel of Figure 3, we show vibronic spectra calculated both with sta-ICWF for the absorption from S_0 to S_2 in comparison with the numerically exact results also calculated via the δ-kick approach. For sta-ICWF, we found that $N_c = 4096$ and $M = 3$ was sufficient to obtain accurate results. The results demonstrate that the sta-ICWF ansatz used in a variational context achieves an accurate vibronic spacing, and furthermore, it not only captures the

electron–nuclear correlation inherent to vibronic spectra but also solves the electron–electron subsystem accurately. The deviation from the exact results does grow with increasing energy, although this is ameliorated with increasing N_c and M, and can, in principle, be eliminated at large enough values of these parameters (see Appendix B.3).

For comparison, we also show mean-field, semiclassical results for the vibronic spectra. Specifically, we calculated the absorption spectrum with the multitrajectory Ehrenfest δ-kick (MTEF-kick) method,[60] overlaid as dashed blue lines. The electronic subsystem was solved exactly as a two-particle wave function over the real-space grid for each independent nuclear trajectory. We see that the vibronic spacing calculated with the MTEF-kick approach fails in capturing the correct peak spacing in addition to showing unphysical spectral negativity.

4.2. Example III: Laser-Driven Dynamics of H_2. The present formalism is not restricted to just perturbative fields and can deal with any arbitrary external field. Going beyond the linear response regime, we investigate the effect of strong driving by a few-cycle, ultrafast laser pulse for this same H_2 model system. The system is first prepared in the ground state using the imaginary-time sta-ICWF, and then the field-driven dynamics is generated by applying an electric field of the form $E(t) = E_0\Omega(t)\sin(\omega t)$, with $E_0 = 0.005$ au and an envelope $\Omega(t)$ with a duration of 20 optical cycles. The carrier wave frequency $\omega = 0.403$ is tuned to the vertical excitation energy between the ground and second excited BOPESs at the mean nuclear position of the ground-state wave function. A thorough description of the numerical procedure, as well as the convergence behavior of the sta-ICWF method for this model, can be found in Appendix B.4, as well as in Appendix D.

The intense laser pulse creates a coherent superposition of the ground and second excited BO states whereby the bond length of the molecule increases, as shown in the bottom panel of Figure 4. The nuclear wavepacket then eventually returns to the Franck–Condon region, creating the resurgence of the electronic dipole oscillation seen in the top panel of Figure 4. In the MTEF mean-field description of this process, the short-
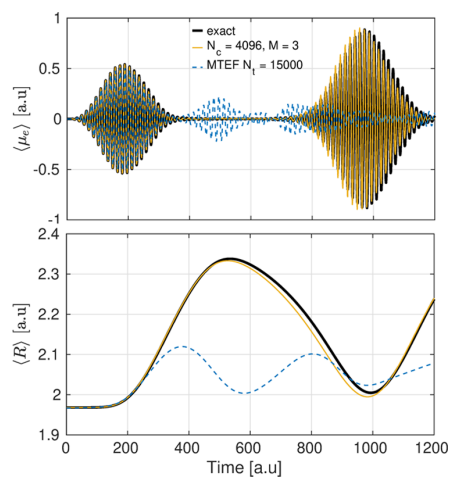
Figure 4. Top panel: evolution of the expectation value of the dipole operator $\langle\mu_e\rangle$ for the 1D H_2 model system for $N_c = 4096$ (from bottom-up) and $M = 3$. Bottom panel: evolution of the expectation value of the nuclear interseparation $\langle R\rangle$ for the 1D H_2 model system for $N_c = 4096$ and $M = 3$.

Figure 3. $S_2 \leftarrow S_0$ spectra of ICWF-kick (gold) and multitrajectory Ehrenfest δ-kick (MTEF-kick) (blue) compared to the exact peak placement overlaid as a black line, showing that while mean-field theory is unable to capture qualitatively the correct vibronic line shape spacing and intensity, the sta-ICWF approach accurately captures the exact spectrum.

time limit is rather accurately captured, while the subsequent effects of the laser pulse on the nuclear dynamics and the resurgence in the dipole response are not. These results show that the sta-ICWF method is able to capture the electronic correlations inherent to the electronic dipole moment during the initial laser-driven dynamics, as well as the electron–nuclear correlations that arise during the subsequent nonequilibrium dynamics. For this particular problem, we found that $(N_c, M) = (4096, 3)$ was sufficient to obtain highly accurate results for both the expectation value of the electronic dipole moment (top panel of Figure 4) and the expectation value of the internuclear separation (bottom panel of Figure 4). Further details can be found in Appendix B.4.

5. TIME-DEPENDENT CONDITIONAL WAVE FUNCTIONS

While the sta-ICWF method shows promising performance in the examples studied thus far, it faces the same limitations as any method that relies on a static basis. Perhaps, the most significant aspect can be framed in terms of capturing the full support of the time-dependent wave function, which is exacerbated in cases where the time-dependent state strays far from the span of the static basis. One strategy to address these scenarios would be to incorporate time-dependent conditional wave functions in the ICWF ansatz. Hence, we take advantage of the time-dependent version of the CWF framework introduced in ref 68, which relies on decomposing the exact many-body wave function, $\Psi(x, t)$, in terms of time-dependent single-particle CWFs of either the electronic or nuclear subsystems as

$$\psi_i^\alpha(x_i, t) := \int d\overline{x}_i \, \delta(\overline{x}_i^\alpha(t) - \overline{x}_i)\Psi(x, t) \tag{23}$$

Evaluating the time-dependent Schrödinger equation in eq 20 at $x_i^\alpha(t)$, one can show that the CWFs in eq 23 obey the following equations of motion

$$i\frac{d}{dt}\psi_i^\alpha(t) = [\hat{T}_i + W_i^\alpha(t) + \eta_i^\alpha(t)]\psi_i^\alpha(t) \tag{24}$$

where $W_i^\alpha(x_i, t) = W(x, \overline{x}_i^\alpha(t), t)$, and we remind that $W(x)$ is the full electron–nuclear interaction potentials that appear in the Hamiltonian of eq 2. In eq 24, $\eta_i^\alpha(x_i, t)$ are time-dependent complex potentials containing kinetic correlations and advective terms, i.e.

$$\eta_i^\alpha(x_i, t) = \sum_{j \neq i}^{n \times N} \left(\frac{\hat{T}_j\Psi(t)}{\Psi(t)}\bigg|_{\overline{x}_i^\alpha} + \dot{x}_j^\alpha(t)\cdot\frac{\nabla_j\Psi(t)}{\Psi(t)}\bigg|_{\overline{x}_i^\alpha} \right) \tag{25}$$

As in the time-independent CWF framework, the conditional wave functions in eq 23 represent slices of the full wave function taken along single-particle degrees of freedom of the two disjoint subsets. Each individual CWF constitutes an open quantum system, whose time evolution is nonunitary, due to the complex potentials $\eta_i^\alpha(x_i, t)$, which now include advective terms due to the inherent motion of the trajectories $x^\alpha(t)$, which evolve according to Bohmian (conditional) velocity fields[68]

$$\dot{x}_i^\alpha(t) = \frac{1}{m_i} \text{Im}\left[\frac{\nabla_i\psi_i^\alpha(x_i, t)}{\psi_i^\alpha(x_i, t)} \right]_{x_i^\alpha(t)} \tag{26}$$

An exact solution to eq 20 can be then constructed provided we use a sufficiently large number of slices $\{x^\alpha(t)\}$ that explore the full support of $|\Psi^\gamma(x, t)|^2$ (in analogy with Figure 1b), i.e.

$$\Psi(x, t) = \mathcal{D}_{x_i}(\psi_i^\alpha(x_i, t)) \tag{27}$$

where the transformations can be found in Appendix A. The one-body equations of motion in eq 24 can be then understood each as a coupled set of nonunitary and nonlinear time-dependent problems.

The derivation of the exact time-dependent CWF mathematical framework corresponds to the transformation of the many-body time-dependent Schrödinger equation to the partially comoving frame in which all coordinates except the ith move attached to the electronic and nuclear flows and only the ith coordinate is kept in the original inertial frame. Within the new coordinates, the convective motion of all degrees of freedom except for the ith coordinate is described by a set of trajectories of infinitesimal fluid elements (Lagrangian trajectories), while the motion of the ith degree of freedom is determined by the evolution of the CWFs in a Eulerian frame.[71] The purpose of this partial time-dependent coordinate transformation is to propagate all trajectories along with the corresponding probability density flow such that they remain localized where the full molecular wave function has a significant amplitude.

5.1. Time-Dependent Hermitian Approximation. In general, the effective potentials in eq 25 exhibit discontinuous steps, which could introduce instabilities in a trajectory-based solution of the many-body dynamics based on eq 24. Therefore, in a similar manner to the time-independent case, an approximate solution can be formulated by expanding the kinetic and advective correlation potentials around the conditional coordinates $x^\alpha(t)$, such that

$$\eta_i^\alpha(x_i, t) = f(\overline{x}_i^\alpha(t)) \tag{28}$$

In this limit, the kinetic and advective correlation potentials only engender a global phase that can be omitted, as expectation values are invariant under such global phase transformations. The resulting propagation scheme is restored to a Hermitian form. That is, eq 24 is approximated as

$$i\frac{d}{dt}\psi_i^\alpha(t) = (\hat{T}_i + W_i^\alpha(t))\psi_i^\alpha(t) \tag{29}$$

while the trajectories $x^\alpha(t)$ are constructed according to eq 26.

This approximation to the time-dependent CWF formalism is clearly a major simplification of the full problem, as it recasts the many-body time-dependent Schrödinger equation as a set of independent single-particle equations of motion. Despite the crudeness of the approximation in eq 28, the set of equations of motion in eq 29 has found numerous applications, e.g., in the description of adiabatic and nonadiabatic quantum molecular dynamics[68,70] and quantum electron transport.[90−94] In ref 68, for example, results using eq 29 for an exactly solvable model system showed a great degree of accuracy of the time-dependent Hermitian approximation in capturing nonadiabatic dynamics. Alternatively, in ref 70, the set of equations in eq 29 was used to describe the adiabatic double proton transfer for an exactly solvable model porphine, showing great promise in capturing quantum nuclear effects. Regarding the comparison of the time-dependent Hermitian approach in eq 29 with conventional mean-field methods, in ref 91, it was shown that quantum electron transport simulations using eq 29 represent an improvement with respect to time-dependent (Hartree-type) mean-field simulations. Similar conclusions were reported in ref 95, where a simplified semiclassical method based on eq 29 was compared with classical mean-field results.

Methods based on eq 29, however, are known to fail to describe important nonadiabatic processes such as the splitting of the time-dependent reduced nuclear density with influences from different BOPESs.[68] This type of dynamics has been commonly associated with decoherence effects that neither the Hermitian approximation in eq 28 nor other mean-field methods such as Ehrenfest or Tully's surface hopping dynamics are able to capture.

6. SIMULATING FAR-FROM-EQUILIBRIUM DYNAMICS WITH CONDITIONAL WAVE FUNCTIONS

In general circumstances where the kinetic and advective correlation potentials are important, we can make use of the simple Hermitian form of the conditional equations of motion in eq 29 to design an efficient many-body wave function propagator. For that, we expand the full electron–nuclear wave function using the ansatz

$$\Psi(\boldsymbol{x}, t) = \sum_{\alpha=1}^{N,M} C_\alpha(t) \prod_{i=1}^{n \times N} \psi_i^\alpha(\boldsymbol{x}_i, t) \tag{30}$$

where the coefficients $C_\alpha(t)$ and the CWFs $\psi_i^\alpha(\boldsymbol{x}_i, t)$ are initialized using the sta-ICWF method and propagated afterward using the approximated equations of motion in eq 29 along with trajectories obeying eq 26.

The time evolution of the coefficients $\mathbf{C}(t)$ can be then obtained by inserting the ansatz of eq 30 into eq 20

$$\frac{d\mathbf{C}(t)}{dt} = -i\mathbb{S}^{-1}(t)\left(\mathbb{H}(t) - \sum_{i=1}^{n \times N} \mathbb{H}_i(t)\right)\mathbf{C}(t) \tag{31}$$

where the matrix elements of $\mathbb{S}$, $\mathbb{H}$ are defined as in eqs 13 and 14, with the time dependence coming from external fields in the Hamiltonian and the time-dependent CWFs, while $\mathbb{H}_i$ are

$$H_{i,\alpha\beta}(t) = \sum_{i=1}^{n \times N} \int d\boldsymbol{x}_i\, \psi_i^{\beta*} h_i^\alpha \psi_i^\alpha \prod_{j \neq i}^{n \times N} \int d\boldsymbol{x}_j\, \psi_j^{\beta*} \psi_j^\alpha \tag{32}$$

where $h_i^\alpha(t)$ are the Hermitian Hamiltonians in eq 29 and $\hat{H}(t)$ is the full time-dependent Hamiltonian in eq 20.

Obtaining these matrix elements is straightforward, involving a sum across single-body operators in eqs 13 and 32 and all sums of two-body interactions across each degree of freedom in eq 14. Note that any operator involving only a single species, e.g., the kinetic energy, is canceled out, and thus the evolution of $\mathbf{C}$ is governed exclusively by matrix elements of operators, which either fully (through $\mathbb{H}$) or conditionally (through $\mathbb{H}_i$) correlate the degrees of freedom.

Equations 26, 29, and 31 define a set of coupled differential equations that hereafter will be referred to as the dynamical ICWF (dyn-ICWF) method. One can then evaluate the expectation value of a generic observable $\langle \hat{O}(\boldsymbol{x}) \rangle$ as given in eqs 15 with dyn-ICWF by simply taking into account that $\psi_i^\alpha(t)$ are now time-dependent CWFs.

The above dyn-ICWF method was first put forth in ref 72. At the time of publishing the work in ref 72, however, there was no theory sustaining the construction of the initial conditional wave function basis $\psi_i^\alpha(\boldsymbol{x}_i,t)$ without relying on an exact solution of the time-independent Schrödinger equation. That has been the main limitation of the method thus far. Here, instead, we have shown that the imaginary-time sta-ICWF method (derived in Section 3) not only allows us to solve accurately the time-independent Schrödinger equation but also serves as a method

to define an optimal set of conditional wave function basis $\psi_i^\alpha(\boldsymbol{x}_i, 0)$. Therefore, the dyn-ICWF in combination with imaginary-time sta-ICWF provides a self-consistent approach to describe observables that are relevant to equilibrium, as well as far-from-equilibrium processes. An example combining these two methods will be shown in the example of Section 6.2, where an initial ground state is prepared using imaginary-time sta-ICWF and a later dynamics, triggered by a laser pulse, is described using dyn-ICWF. The interested reader can find a complete flowchart of the combined method in Appendix D.

6.1. Example IV: Impact Electron Ionization. The theoretical description of electron scattering remains challenging, as it is a highly correlated problem that generally requires treatment beyond perturbation theory.[96,97] We here study a model system of electron–hydrogen scattering that can be exactly solved numerically.[98] In atomic units, the Hamiltonian of this one-dimensional two-electron model system reads

$$\hat{H}(r_1, r_2) = \sum_{i=1}^{2}\left(-\frac{1}{2}\frac{\partial^2}{\partial r_i^2} + v_{\text{ext}}(r_i)\right) + W(r_1 - r_2) \tag{33}$$

where

$$W(r_1 - r_2) = \frac{1}{\sqrt{(r_1 - r_2)^2 + 1}} \tag{34}$$

$$v_{\text{ext}}(r) = \frac{1}{\sqrt{(r - 10)^2 + 1}} \tag{35}$$

are, respectively, the soft-Coulomb interaction and the external potential that models the H atom located at $r = 10$ au. The initial interacting wave function is taken to be a spin singlet, with a spatial part

$$\Psi_0(r_1, r_2) = \frac{1}{\sqrt{2}}(\phi_\text{H}(r_1)\phi_\text{WP}(r_2) + \phi_\text{WP}(r_1)\phi_\text{H}(r_2)) \tag{36}$$

where $\phi_\text{H}(r)$ is the ground-state hydrogen wave function and $\phi_\text{WP}(r)$ is an incident Gaussian wavepacket

$$\phi_\text{WP}(r) = \left(\frac{2\alpha}{\pi}\right)^{1/4} e^{[-\alpha(r-r_0)^2 + ip(r-r_0)]} \tag{37}$$

with $\alpha = 0.1$ representing an electron at $r = -10$ au, approaching the target atom with a momentum p.

The time-resolved picture presents scattering as a fully nonequilibrium problem, where the system starts already in a nonsteady state, and so, the imaginary-time sta-ICWF cannot be applied here to prepare the initial wave function. Instead, we stochastically sample the initial probability density $|\Psi_0(r_1, r_2)|^2$ with N_c trajectories $\{r_1^\alpha(0), r_2^\alpha(0)\}$ that are used to construct CWFs $\phi_1^\alpha(r_1, 0)$ and $\phi_2^\alpha(r_2, 0)$, as defined in eq 23. A thorough description of the numerical procedure, as well as the convergence behavior of the dyn-ICWF method for this model can be found in Appendix C.1. See also Appendix D for a description of the corresponding workflow.

We study the dynamics of the electron–hydrogen scattering by evaluating the time-dependent one-body density, $\rho_e(r_1, t) = 2\int|\Psi(r_1, r_2, t)|^2\, dr_2$, for two different initial momenta, viz., $p = 0.3$ and 1.5 au. For $p = 0.3$ au, the energy is lower than the lowest excitation of the target (which is about $\omega = 0.4$ au) and hence the scattering process is elastic. In this regime, mean-field results (here represented by extended time-dependent Hartree–Fock calculations) and dyn-ICWF results with $N_c = 128$ results both capture the correct dynamics accurately (see Figure 5). In
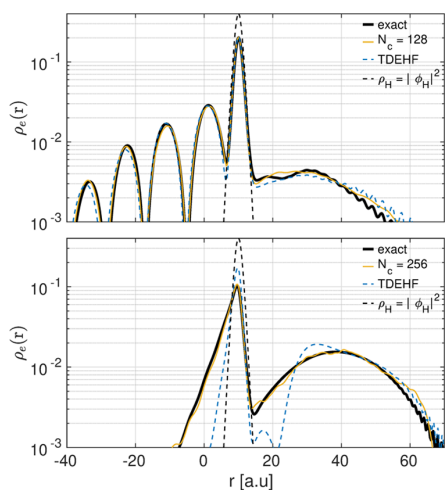
Figure 5. Top panel: reduced electron density at $t = 1.8$ fs for $p = 0.3$ au and $N_c = 128$. Bottom panel: reduced electron density at $t = 0.85$ fs for $p = 1.5$ au and $N_c = 256$ and $N_{in} = 10$.

approaching the target atom with the larger momentum $p = 1.5$ au, the incident wavepacket collides inelastically with the target electron at around 0.24 fs, after which, a part of the wavepacket is transmitted while some is reflected back leaving the target partially ionized. In this regime, the mean-field method fails to describe the transmission process quantitatively and the reflection process even qualitatively due to its inability to capture electron–electron correlation effects. This is in contrast with dyn-ICWF results, which quantitatively capture the correlated dynamics for $N_c = 256$, although a lower number of CWFs already reproduces qualitatively the dynamics (see Appendix C.1 and Figure 5).

6.2. Example V: Laser-Driven Proton-Coupled Electron Transfer. We now show dyn-ICWF results for a prototypical photoinduced proton-coupled electron transfer reaction, using the Shin–Metiu model.[99] The system comprises donor and acceptor ions, which are fixed at a distance $L = 19.0a_0$, and a proton and an electron that are free to move in one dimension along the line connecting the donor–acceptor complex. Based on the parameter regime chosen, this model can give rise to a number of challenging situations where electron–nuclear correlations play a crucial role in the dynamics.

The total Hamiltonian for the system is

$$\hat{H}(r, R) = -\frac{1}{2m}\frac{\partial^2}{\partial r^2} - \frac{1}{2M}\frac{\partial^2}{\partial R^2} + \hat{W}(r, R) \tag{38}$$

where m is the electron mass, and M is the proton mass. The coordinates of the electron and the mobile ion are measured from the center of the two fixed ions and are labeled r and R, respectively. The full electron–nuclear potential reads

$$\hat{W}(r, R) = \frac{1}{\left|\frac{L}{2} - R\right|} + \frac{1}{\left|\frac{L}{2} + R\right|} - \frac{\text{erf}\left(\frac{|R-r|}{R_f}\right)}{|R-r|}$$
$$- \frac{\text{erf}\left(\frac{\left|r - \frac{L}{2}\right|}{R_r}\right)}{\left|r - \frac{L}{2}\right|} - \frac{\text{erf}\left(\frac{\left|r + \frac{L}{2}\right|}{R_l}\right)}{\left|r + \frac{L}{2}\right|} - (r-R)E(t) \tag{39}$$

where erf() is the error function. The parameter regime studied for this model ($R_f = 5a_0$, $R_l = 4a_0$, and $R_r = 3.1a_0$) is chosen such that the ground-state BOPES, ϵ_{BO}^1, is strongly coupled to the first excited adiabatic state, ϵ_{BO}^2, around the mean nuclear equilibrium position $R_{eq} = -2a_0$. The coupling to the rest of the BOPESs is negligible.

We set the system to be initially in the full electron–nuclear ground state obtained from the imaginary-time propagation method described above, i.e., $\Psi(r, R, 0) = \Psi^0(r, R)$ (the interested reader can find a general workflow of the simulation in Appendix D). We then apply an external strong electric field, $E(t) = E_0\Omega(t)\sin(\omega t)$, with $E_0 = 0.006$ au, $\Omega(t) = \sin(\pi t/20)^2$, and $\omega = \epsilon_{BO}^1(R_{eq}) - \epsilon_{BO}^0(R_{eq})$. The external field induces a dynamics that involves a passage through an avoided crossing between the first two BOPESs, with further crossings occurring at later times as the system evolves. When the system passes through the nonadiabatic coupling region, the electron transfers probability between the ground state and the first excited state. This is shown in the top panel of Figure 6, where we monitor the
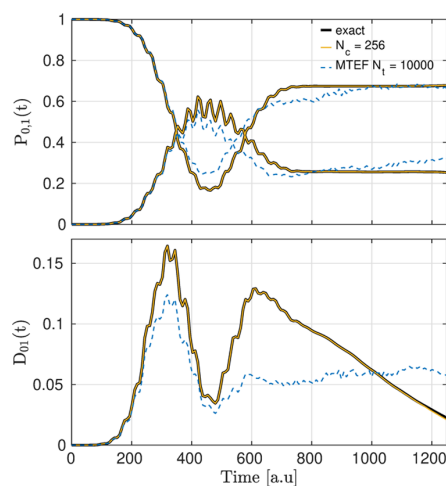
Figure 6. Top panel: population dynamics of the first two adiabatic electronic states $P_{0,1}(t)$. Solid black lines correspond to exact numerical results. Solid blue and red lines correspond to dyn-ICWF results with $(N_c, M) = (256, 1)$ for the ground and first excited adiabatic populations, respectively. Dashed blue and red lines correspond to mean-field MTEF results. Bottom panel: decoherence dynamics between the ground state and first excited adiabatic electronic states, i.e., D_{01}. Solid black lines correspond to exact results. The solid blue line corresponds to dyn-ICWF results with $(N_c, M) = (256, 1)$. The dashed blue line corresponds to mean-field MTEF results.

BO electronic state populations $P_n(t)$ (whose definition can be found in Appendix C.2). As a result of the electronic transition, the reduced nuclear density changes shape by splitting into two parts representing influences from both ground- and excited-state BOPESs. This can be seen in the bottom panel of Figure 6, where, as a measure of decoherence, we use the indicator $D_{nm}(t)$ (whose definition can be found in Appendix C.2). As nonadiabatic transitions occur, the system builds up a degree of coherence that subsequently decays as the system evolves away from the coupling region.

As shown in Figure 6, the dyn-ICWF method reaches quantitative accuracy for $(N_c, M) = (256, 1)$ and vastly outperforms the multitrajectory Ehrenfest mean-field method in describing both the adiabatic populations and the

decoherence measure. More specifically, while both the dyn-ICWF method and MTEF dynamics correctly capture the exact adiabatic population dynamics at short times, the latter breaks down at long times as it fails to capture the qualitative structure of the time-evolving indicator of decoherence. Noticeably, all of these aspects of this problem are qualitatively well described by the dyn-ICWF method using only $(N_c, M) = (16, 1)$ (these results can be found in Appendix C.2).

6.3. Example VI: Interference Effects Near a Molecular Conical Intersection. We next study dynamics around conical intersections (CIs) using a minimal generalization of the above Shin−Metiu model first proposed by Gross and co-workers[100] and extended further by Schaupp and Engel.[101] The model consists of a quantized electron and proton that can move in two Cartesian directions, along with two fixed "classical" protons, R_1, R_2. A CI occurs in this model when (treating the quantized proton as a BO parameter) the protons are in a D_{3h} geometry. The potential energy is

$$W(r, R) = -\frac{1}{\sqrt{a + |r-R|^2}} - \frac{1}{\sqrt{a + |r-R_1|^2}}$$
$$- \frac{1}{\sqrt{a + |r-R_2|^2}} + \frac{1}{\sqrt{b + |R_1-R_2|^2}}$$
$$+ \frac{1}{\sqrt{b + |R-R_1|^2}} + \frac{1}{\sqrt{b + |R-R_2|^2}}$$
$$+ \left(\frac{|R|}{R_0}\right)^4 \tag{40}$$

and we use the parameter values $a = 0.5$, $b = 10$, $R_0 = 1.5$, $R_1 = (-0.4\sqrt{3}, 1.2)$, and $R_2 = (0.4\sqrt{3}, 1.2)$.

We initialize the total system wave function as a direct product of the first excited electronic BO state and a nuclear Gaussian state centered at $R_c = (0, 0.4)$ with standard deviation $\sigma^2 = 5$. For this placement of R_1, R_2, the CI occurs at the origin and, in the BO picture, the initial nuclear wavepacket "falls toward" the CI (see Figure 14 in Appendix C.3). In this picture, the nuclear motion occurs on a single BOPES and the two portions of the nuclear wavepacket around the CI (i.e., the clockwise and anticlockwise components) cause an interference pattern to develop when they do recollide (see Figure 7).

While the interference pattern described in Figure 7 can be understood as the adiabatic circular motion around the position of a conical intersection, it is important to emphasize that the concept of CI makes sense only when the adiabatic picture, i.e.,
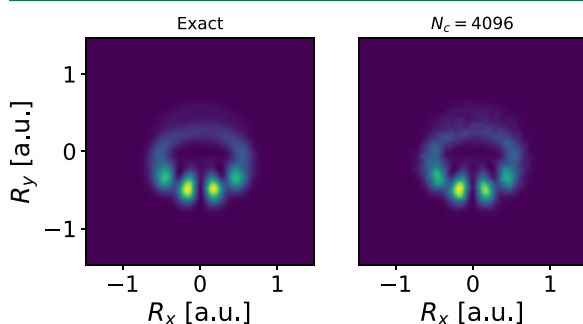
the Born−Huang basis expansion, is used to represent the molecular wave function. However, any observable effect that can be explained on the adiabatic basis must arise also in any other picture such as the diabatic picture or the full real-space grid picture used by the dyn-ICWF method. Therefore, while not depending on the BO picture (beyond defining the initial state), the dyn-ICWF method is able to capture the correct CI curvature effects, as well as any interference pattern that forms in the fully reduced nuclear density

$$\rho(R_x, R_y) = \iint dr_x \, dr_y |\Psi(r_x, r_y, R_x, R_y)|^2 \tag{41}$$

See Appendices C.3 and D for further details on the dyn-ICWF calculation.

7. CONCLUSIONS

In this work, we have introduced an exact mathematical framework that avoids the standard separation between electrons and nuclei and hence enables a unified treatment of molecular structure and nonadiabatic dynamics without relying on the construction and fit of Born−Oppenheimer potential-energy surfaces and the explicit computation of nonadiabatic couplings.

We have introduced a time-independent conditional wave function theory, which is an exact decomposition and recasting of the static many-body problem that yields a set of single-particle conditional eigenstates. Based on the imaginary-time propagation of a stochastic ansatz made of approximated conditional eigenstates, the resulting method, called sta-ICWF, is able to accurately capture electron−electron correlations intrinsic to molecular structure. A real-time counterpart of the above method has been also derived following the Dirac−Frenkel variational procedure, and its combination with the imaginary-time version yields an accurate method for solving out-of-equilibrium properties of molecular systems where nonadiabatic electron−nuclear correlations are important. This has been shown by reproducing the exact structural, linear response, and nonperturbatively driven response properties of an exactly solvable one-dimensional H_2 model system that standard mean-field theories fail to describe.

We have also considered a broader class of conditional wave functions that was formally introduced through time-dependent conditional wave function theory, yielding a set of coupled single-particle equations of motion. An approximated set of these time-dependent conditional wave functions are utilized as time-dependent basis of a stochastic wave function ansatz that is meant to describe observables that are relevant to far-from-equilibrium processes. The resulting propagation technique (called dyn-ICWF) in combination with sta-ICWF provides a fully self-consistent approach and, moreover, the method achieves quantitative accuracy for situations in which mean-field theory drastically fails to capture qualitative aspects of the combined electron−nuclear dynamics.

The sta- and dyn-ICWF methods are wave function-based approaches. Therefore, while the simple sum-of-product forms that we have employed for our ansatz in eqs 9 and 30 can be made more efficient, by introducing a tensor network representation for the expansion coefficients such as matrix product states or hierarchical Tucker formats, for example, an exponential scaling with respect to the number of correlated degrees of freedom is expected unless approximations are introduced. That being said, we want to emphasize that the ICWF method is fundamentally different from wave function

Figure 7. Exact and dyn-ICWF reduced nuclear density showing the interference pattern after having traversed the conical intersection at the origin.

methods that rely on the Born−Huang expansion of the molecular wave function. Alternatively, the ICWF method describes electronic and nuclear degrees of freedom on the same mathematical footing, viz., the real-space grid picture. It is this particular trait that makes the ICWF an original starting point for developing novel, unexplored, approximations that could eventually yield a significant computational advantage compared to methods that rely on the Born−Huang expansion.

Importantly, the conditional decomposition holds for an arbitrary number of subsets (up to the total number of degrees of freedom in the system) and applies to both fermionic and bosonic many-body interacting systems. Our developments thus provide a general framework to approach the many-body problem in and out of equilibrium for a large variety of contexts. For example, using conditional wave functions in a form compatible with time-dependent density functional theory in connection with alternative tensor network decompositions or in combination with classical/semiclassical limits for specified degrees of freedom are particularly appealing routes to follow, and work in this direction is already in progress.[102] Furthermore, the extension to periodic systems is currently under investigation and should allow the ab initio description of driven electron−lattice dynamics such as, for example, laser-driven heating and thermalization,[103−108] correlated lattice dynamics,[109−111] and phase transitions.[112−114]

A. Definition of the "Reassembling" Transformation $\mathcal{D}_{x_i}$ of Equation 6

Here, we consider a reconstruction of the full wave function $\Psi^\gamma(\boldsymbol{x})$ from conditional wave functions defined as in eq 3 of the main text, i.e.

$$\psi_i^{\alpha,\gamma}(\boldsymbol{x}_i) := \int \mathrm{d}\overline{\boldsymbol{x}}_i \, \delta(\overline{\boldsymbol{x}}_i^\alpha - \overline{\boldsymbol{x}}_i)\Psi^\gamma(\boldsymbol{x}) \tag{42}$$

Here, the index $\alpha \in \{1, 2, ..., N_c\}$ denotes the particular conditional slice, and $\overline{\boldsymbol{x}}_i = (\boldsymbol{x}_1, ..., \boldsymbol{x}_{i-1}, \boldsymbol{x}_{i+1}, ..., \boldsymbol{x}_{n\times N})$ are the coordinates of all degrees of the system except $\boldsymbol{x}_i$. Similarly, $\overline{\boldsymbol{x}}_i^\alpha = (\boldsymbol{x}_1^\alpha, ..., \boldsymbol{x}_{i-1}^\alpha, \boldsymbol{x}_{i+1}^\alpha, ..., \boldsymbol{x}_{n\times N}^\alpha)$ are the position of all system's degrees of freedom except $\boldsymbol{x}_i$.

Assuming that the conditional sampling points, $\overline{\boldsymbol{x}}_i^\alpha$, are distributed according to a normalized distribution $\mathcal{N}(\overline{\boldsymbol{x}}_i^\alpha)$, one can approximately reconstruct the full wave function based on the interpolation with a Gaussian function $G^\sigma(\overline{\boldsymbol{x}}_i)$ with a given width σ as

$$\Psi_{N_c,\sigma}^{\mathrm{Rec},\gamma}(\boldsymbol{x}) := \frac{\sum_{\alpha=1}^{N_c} \frac{1}{\mathcal{N}(\overline{\boldsymbol{x}}_i^\alpha)} G^\sigma(\overline{\boldsymbol{x}}_i - \overline{\boldsymbol{x}}_i^\alpha)\psi_i^{\alpha,\gamma}(\boldsymbol{x}_i)}{\sum_{\alpha=1}^{N_c} \frac{1}{\mathcal{N}(\overline{\boldsymbol{x}}_i^\alpha)} G^\sigma(\overline{\boldsymbol{x}}_i - \overline{\boldsymbol{x}}_i^\alpha)} \tag{43}$$

In this way, the full wave function is reconstructed as a Gaussian weighted average: in the numerator of eq 43, the contribution from each conditional slice α is weighted with a Gaussian distribution, and it becomes larger if the evaluated point, $\overline{\boldsymbol{x}}$, is closer to the sampling point $\overline{\boldsymbol{x}}^\alpha$. To compensate the nonuniform sampling distribution contribution, the interpolation weight is divided by the distribution function $\mathcal{N}(\overline{\boldsymbol{x}}_i^\alpha)$. In addition, the denominator of eq 43 ensures normalization of the interpolation weight.

By considering a dense sampling ($N_c \to \infty$), the reconstructed wave function of eq 43 can be rewritten as

$$\lim_{N_c \to \infty} \Psi_{N_c,\sigma}^{\mathrm{Rec},\gamma}(\boldsymbol{x}) = \int \mathrm{d}\overline{\boldsymbol{x}}_i^\alpha \, G^\sigma(\overline{\boldsymbol{x}} - \overline{\boldsymbol{x}}_i^\alpha)\psi_i^{\alpha,\gamma}(\boldsymbol{x}_i) \tag{44}$$

and substituting eq 42 into eq 44, one obtains

$$\lim_{N_c \to \infty} \Psi_{N_c,\sigma}^{\mathrm{Rec},\gamma}(\boldsymbol{x}) = \int \mathrm{d}\overline{\boldsymbol{x}}_i' \, G^\sigma(\overline{\boldsymbol{x}}_i - \overline{\boldsymbol{x}}'_i)\Psi(\overline{\boldsymbol{x}}') \tag{45}$$

where $\overline{\boldsymbol{x}}' = (\boldsymbol{x}'_1, ..., \boldsymbol{x}'_{i-1}, \boldsymbol{x}_i, \boldsymbol{x}'_{i+1}, ..., \boldsymbol{x}'_{n\times N})$. Therefore, for a dense sampling, $\Psi_{N_c,\sigma}^{\mathrm{Rec},\gamma}(\boldsymbol{x})$ can be understood as the convolution of the full wave function $\Psi(\boldsymbol{x})$ and the Gaussian weight $G^\sigma(\overline{\boldsymbol{x}}_i)$. Furthermore, in the narrow Gaussian width limit, ($\sigma \to 0$), $G^\sigma(\overline{\boldsymbol{x}}_i)$ can be treated as a Dirac δ function and hence eq 45 can be written as

$$\lim_{\substack{\sigma \to 0 \\ N_c \to \infty}} \Psi_{N_c,\sigma}^{\mathrm{Rec},\gamma}(\boldsymbol{x}) = \Psi(\boldsymbol{x}) \tag{46}$$

In conclusion, one can exactly reconstruct the full electron−nuclear wave function in terms of conditional wave functions using the reassembling operator $\mathcal{D}_{x_i}$ defined as

$$\mathcal{D}_{x_i}(\psi_i^{\alpha,\gamma}) \equiv \lim_{\substack{\sigma \to 0 \\ N_c \to \infty}} \frac{\sum_{\alpha=1}^{N_c} \frac{1}{\mathcal{N}(\overline{\boldsymbol{x}}_i^\alpha)} G^\sigma(\overline{\boldsymbol{x}}_i - \overline{\boldsymbol{x}}_i^\alpha)\psi_i^{\alpha,\gamma}(\boldsymbol{x}_i)}{\sum_{\alpha=1}^{N_c} \frac{1}{\mathcal{N}(\overline{\boldsymbol{x}}_i^\alpha)} G^\sigma(\overline{\boldsymbol{x}}_i - \overline{\boldsymbol{x}}_i^\alpha)} \tag{47}$$

B. Convergence of the Real- and Imaginary-Time Versions of the sta-ICWF Method

In this section, we discuss the convergence of the imaginary- and real-time sta-ICWF methods for the examples in Sections 3.1, 4.1, and 4.2. For that, we first notice that, due to the stochastic nature of the sta-ICWF method, given a set of sampling points N_c and their conditional eigenstates M, we may also consider a number N_{in} of different sets of N_c sampled points and their associated M conditional eigenstates. This can be accounted for by rewriting the expectation value of eq 15 as

$$\langle \overline{O}(t) \rangle = \frac{1}{N_{\mathrm{in}}} \sum_{p=1}^{N_{\mathrm{in}}} \langle \hat{O}(t) \rangle_p \tag{48}$$

The dispersion of $\langle \overline{O}(t) \rangle$ with respect to N_{in} is then quantified through its standard deviation, i.e.

$$\Delta \overline{O}(t) = \sqrt{\langle \overline{O}^2(t) \rangle - \langle \overline{O}(t) \rangle^2} \tag{49}$$

B.1. Ground and Excited BOPESs of H_2. We discuss here the convergence of the imaginary-time version of the sta-ICWF method in capturing the ground-state and excited-state BOPESs for the H_2 model system introduced in Section 3.1. Finding the BOPESs for this particular model is equivalent to solving eq 19 using the imaginary-time evolution technique

$$\frac{\mathrm{d}}{\mathrm{d}\tau}\Phi^\zeta(r_1, r_2; R, \tau) = -\hat{\mathcal{H}}_{\mathrm{el}}^\zeta \Phi^\zeta(r_1, r_2; R, \tau) \tag{50}$$

where $\{\Phi^\gamma(r_1, r_2; R)\}$ are the (complete, orthonormal) set of BO electronic states, and we have defined $\hat{H}_{\mathrm{el}}^\zeta$ as

$$\hat{H}_{\mathrm{el}}^\zeta(r_1, r_2; R) = \left(\mathbb{1} - \sum_{\xi=1}^{\zeta-1} \hat{P}^\xi\right)\hat{\mathcal{H}}_{\mathrm{el}}\left(\mathbb{1} - \sum_{\xi=1}^{\zeta-1} \hat{P}^\xi\right) \tag{51}$$

where $\hat{P}^\xi = \Phi^\xi\Phi^{\xi\dagger}$ and $\hat{\mathcal{H}}_{\mathrm{el}} = \hat{H} - \hat{T}_{\mathrm{nuc}}$.

The BO electronic states, $\Phi^\gamma(r_1, r_2; R)$, are then expanded in terms of CWFs with the following simplified version of the ansatz in eq 9 that is specialized to the particular case of parametric nuclear dependence

$$\Phi^\gamma(r_1, r_2; R) = \sum_{\alpha=1}^{N_cM} C_\alpha^\gamma \phi_1^\alpha(r_1; R)\phi_2^\alpha(r_2; R) \tag{52}$$

Slicing points (r_1^α, r_2^α) are generated by sampling from reduced one-body electronic densities, which in this case are simply chosen to be Gaussian functions $\rho_e(r_i) = A\, e^{-r_i^2/10}$. The conditional eigenstates $\phi_i^{\alpha,\nu}(r_i; R)$, for $\nu \in \{1, ..., M\}$ are then evaluated on each slice using the Hermitian approximation, i.e.

$$\left(-\frac{\hbar^2}{2m}\nabla_i^2 + W_i^\alpha(r_i, R)\right)\phi_i^{\alpha,\nu}(r_i; R) = E^\nu(R)\phi_i^{\alpha,\nu}(r_i; R)$$

(53)

where $W_i^\alpha(r_i, R) = W_{ee}(r_i, \overline{r}_i^\alpha) + W_{en}(r_i, R)$. The coefficient vector $\mathbf{C}^\gamma$ is randomly initialized and then propagated in imaginary time until the target state is reached according to eq 12 of the main text, with $\hat{H}$ being substituted with $\hat{\mathcal{H}}_{el}$.

To achieve converged results, a grid $(0, 9]$ au for the internuclear separation with 181 grid points is chosen for the nuclear degrees of freedom. For the electron coordinates, the grid covers the interval $[-35, +35]$ au with 200 grid points. The fourth-order Runge−Kutta integration method was used to propagate the imaginary-time sta-ICWF equation of motion (i.e., eq 12) with a time-step $d\tau = 0.01$ au, and the Moore−Penrose pseudo-inversion method with a tolerance of 10^{-8} was used to approximate the numerical inversion of the overlap matrix in eq 13. Importantly, the matrices $\mathbb{S}$ and $\mathbb{H}$ of eqs 12 and 14 need only be constructed at the initial time, requiring only the repeated multiplication of an $N_c \times M$ vector by an $N_c^2 \times M^2$ matrix for the imaginary-time propagation.

In Figure 8, we show sta-ICWF results for the first five BOPESs for two different sets of parameters: $(N_c, M) = (32, 1)$
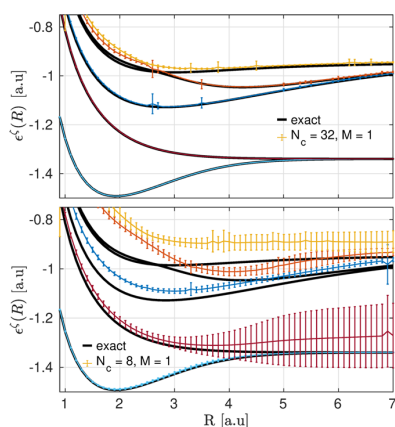
Figure 8. First five BOPESs reproduced with the sta-ICWF method for $(N_c, M) = (8, 1)$ (bottom panel) and $(N_c, M) = (32, 1)$ (top panel). These data are presented alongside (standard deviation) error bars.

(top panel) and $(N_c, M) = (8, 1)$ (bottom panel). The sta-ICWF data are presented alongside (standard deviation) error bars defined in eq 49. Noticeably, even for $M = 1$ (i.e., when only ground-state conditional eigenstates are used in the expansion of eq 52), the results in Figure 8 demonstrate the convergence of the imaginary-time sta-ICWF method to the exact BOPESs. For a large enough number of sampling points and excited CWFs, viz., $(N_c, M) \gtrsim (32, 5)$, the sta-ICWF results are fully converged to the exact BOPESs and the associated error bars become negligible due to the completeness of the CWF basis.

B.2. Ground State of H_2. We investigate here the ground-state energy for the model H_2 introduced in Section 3.1, as well as the

convergence behavior of the imaginary-time version of the sta-ICWF method in capturing it. We aim to solve eq 10, which for this particular model system reduces to

$$\frac{d\Psi^{(0)}(r_1, r_2, R, \tau)}{d\tau} = -\hat{H}\Psi^{(0)}(r_1, r_2, R, \tau)$$

(54)

where $\hat{H}$ is the Hamiltonian in eq 16. For that, we choose the conditional eigenstate basis by sampling N_c points $(r_1^\alpha, r_2^\alpha, R^\alpha)$ from guesses to the reduced electronic and nuclear densities $\rho_e(r_i) = A_e\, e^{-r_i^2/10}$ and $\rho_n(R) = A_n\, e^{-(R-2)^2}$, respectively. Starting from the full H_2 Hamiltonian of eq 16, these positions are then used to construct and diagonalize the Hermitian Hamiltonians in eq 8. In this way, we obtain $3 \times N_c \times M$ conditional eigenstates $\{\phi_1^{\alpha,\zeta}(r_1), \phi_2^{\alpha,\zeta}(r_2), \chi^{\alpha,\zeta}(R)\}$. This allows us to expand the full ground-state wave function as

$$\Psi^{(0)}(r_1, r_2, R) = \sum_{\alpha=1}^{N,M} C_\alpha^0 \phi_1^\alpha(r_1)\phi_2^\alpha(r_2)\chi^\alpha(R)$$

(55)

Given a random initialization of the coefficient vector $\mathbf{C}$, we then evolve it in imaginary time according to eq 12 and the matrix elements of eqs 13 and 14. To achieve converged results, a grid $(0, 9]$ au for the internuclear separation with 181 grid points is chosen for the nuclear degrees of freedom. For the electron coordinates, the grid covers the interval $[-35, +35]$ au with 200 grid points. The fourth-order Runge−Kutta algorithm with a tolerance of 10^{-8} was used to propagate the imaginary-time sta-ICWF equations of motion with a time-step $d\tau = 0.01$ au, and the Moore−Penrose pseudo-inversion method was used to approximate the numerical inversion of the overlap matrix in eq 13. Importantly, the matrices $\mathbb{S}$ and $\mathbb{H}$ of eq 12 need only be constructed at the initial time.

From the exact symmetric ground-state wave function, we found an equilibrium separation of $\langle R \rangle = 2.2$ au and the ground-state energy is $E_0 = -1.4843$ au We then define the relative error of the sta-ICWF calculation with respect to the exact calculation as $E_r = |\langle \overline{H} \rangle_0 - E_0|/|E_0|$, where

$$\langle \overline{H} \rangle_0 = \frac{1}{N_{in}} \sum_{n=1}^{N_{in}} \langle \Psi^{(0)}|\hat{H}|\Psi^{(0)} \rangle_n$$

(56)

and Ψ^0 has been defined in terms of CWFs in eq 55.

The error E_r is presented in Figure 9 as a function of the number of sampling points and for a different number of excited conditional eigenstates, i.e., (N_c, M). Error bars represent the standard deviation $\Delta\overline{H}_0$ defined in eq 49 for a number of different initial sampling points. Due to the variational nature of the method, the relative error decreases with an increasing
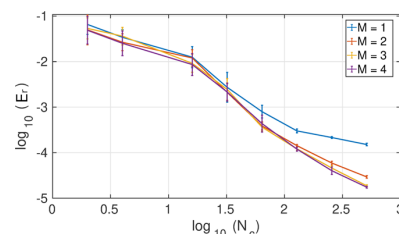
Figure 9. (Left) Logarithm of the mean relative energy error E_{er} as a function of the logarithm of the number of sampling points N_c and for different number of excited CWFs $M = \{1, 2, 3, 4\}$. Error bars represent the standard deviation of the relative error.

number of sampling points N_c. Noticeably, even for $M = 1$ (i.e., when only ground-state conditional eigenstates are used in the expansion of eq 9), the results in Figure 9 demonstrate the convergence of the imaginary-time sta-ICWF method to the exact ground state. The convergence process is accelerated though as we allow a number of excited conditional eigenstates (i.e., $M > 1$) to participate in the ansatz. For a large enough number of basis elements $N_c \times M$, the CWF bases become a complete basis of the problem. This is independent of the initial distribution of sampling points and hence the associated error bars vanish for large enough values of $N_c \times M$.

B.3. Optical Absorption Spectrum of H₂. We discuss here the convergence of the real-time version of the sta-ICWF method in capturing the optical absorption spectrum of the H_2 model system introduced in Section 3.1. The simulation starts with the preparation of the ground-state coefficients $\mathbf{C}(0)$ using the imaginary-time version of the sta-ICWF method described in Appendix B.2. The relevant degree of freedom of the kick operator is then applied to each CWF, the Hamiltonian and inverse overlap matrices of eqs 13 and 14 are reconstructed, and $\mathbf{C}$ is propagated to the desired time according to eq 21. A kick strength of $\kappa = 10^{-4}$ au^{-1} was sufficient to generate the kick spectra within the linear response regime, and a total propagation time of $T_f = 1500$ au was used to generate the spectra, alongside the mask function $\mathcal{M}(x = t/T_f) = 1 - 3x^2 + 2x^3$.

A grid $[-35, +35]$ au with 200 grid points was chosen for the electronic coordinates. The fourth-order Runge−Kutta algorithm was used to propagate the imaginary-time sta-ICWF equations of motion with a time-step $dt = 0.01$ au, and the Moore−Penrose pseudo-inversion method with a tolerance of 10^{-8} was used to approximate the numerical inversion of the overlap matrix in eq 13. Again, the matrices $\mathbb{S}$ and $\mathbb{H}$ of eq 12 need only be constructed at the initial time.

In Figure 10, we show convergence results for sta-ICWF calculations of the optical linear absorption spectra (eq 22) for four different sets of parameters: $(N_c, M) = (512, 3)$, $(N_c, M) = (2048, 3)$ (top panel), and $(N_c, M) = (4096, 1)$ and $(N_c, M) = (4096, 3)$ (bottom panel). In all of these cases, we considered a number of different initial sampling points, which have been
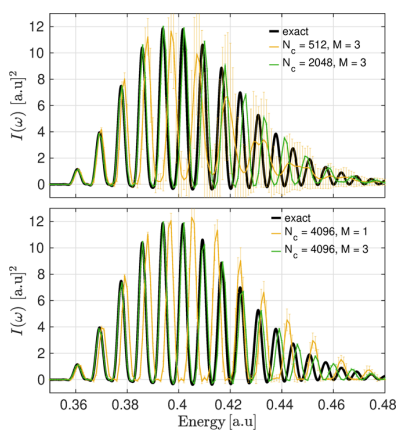
used to calculate the associated (standard deviation) error bars as in eq 49. As the number of conditional eigenstate basis elements in the ansatz expansion of eq 55 increases, the variational nature of the method ensures convergence to the exact linear absorption line shape. Similarly, the error bars shrink as the number of conditional eigenstates in the basis $N_c \times M$ allows us to span the relevant part of the Hilbert space.

B.4. Laser-Driven Dynamics of H₂. We discuss here the convergence of the real-time version of the sta-ICWF method in capturing the laser-driven dynamics of the H_2 model system introduced in Section 3.1. As explained in Section 4.2 of the main text, the system is first prepared in the ground state using the imaginary-time sta-ICWF as explained in Appendix B.2, and then the field-driven dynamics is generated by applying an electric field of the form $E(t) = E_0 \Omega(t) \sin(\omega t)$, with $E_0 = 0.005$ au and an envelope $\Omega(t)$ with a duration of 20 optical cycles. The carrier wave frequency $\omega = 0.403$ is tuned to the vertical excitation between the ground BO state and second excited electronic surface.

For the dynamics we used, a grid $(0, 9]$ au for the internuclear separation with 181 grid points is chosen for the nuclear degrees of freedom. For the electron coordinates, the grid covers the interval $[-35, +35]$ au with 200 grid points. The fourth-order Runge−Kutta algorithm was used to propagate the sta-ICWF equation of motion in eq 21 with a time-step $dt = 0.01$ au, and the Moore−Penrose pseudo-inversion method with a tolerance of 10^{-8} was used to approximate the numerical inversion of the overlap matrix in eq 13.

In Figure 11, we show convergence results for the real-time sta-ICWF calculation of the electronic dipole moment $\langle \hat{\mu}_e \rangle$. We

Figure 11. Evolution of the expectation value of the dipole operator $\langle \mu_e \rangle$ for the 1D H_2 model system for a number of conditional basis configurations. Top panel: $(N_c, M) = (512, 3)$, $(N_c, M) = (4096, 3)$. Bottom panel: $(N_c, M) = (4096, 1)$ and $(N_c, M) = (4096, 3)$. These data are presented along with (standard deviation) error bars.
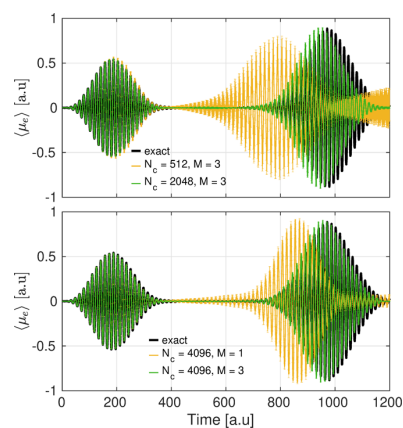

Figure 10. H_2 spectrum for ICWF-Kick with different number of sampling points and excited CWFs. Top panel: $(N_c, M) = (512, 3)$ and $(N_c, M) = (2048, 3)$. Bottom panel: $(N_c, M) = (4096, 1)$ and $(N_c, M) = (4096, 3)$. The results are presented alongside (standard deviation) error bars.

considered four different sta-ICWF configurations, viz., $(N_c, M) = (512, 3)$, $(N_c, M) = (4096, 3)$ (in the top panel), and $(N_c, M) = (4096, 1)$ and $(N_c, M) = (4096, 3)$ (in the bottom panel). As the number of CWFs in the ansatz expansion of eq 55 increases, the variational nature of the method ensures convergence to the exact dynamics. The deviation from the exact results does grow with increasing time lapse, although this is ameliorated with increasing either N_c and/or M and can, in principle, be eliminated at large enough values of these parameters. Similarly, the error bars become negligible when the CWF bases expand

the full support of the Hilbert space explored during the dynamics. This happens for $(N_\sigma, M) \gtrsim (4096, 3)$.

C. Convergence of the dyn-ICWF Method
In this section, we discuss the convergence behavior of the dyn-ICWF method for the examples of Sections 6.1–6.3. As it happened for the sta-ICWF method, the stochastic nature of the dyn-ICWF method allows us to consider a number N_{in} of different initial sampling points for a given set of parameters (N_σ, M). This is taken into account by writing expectation values as in eq 48 and its standard deviation as in eq 49.

C.1. Impact Electron Ionization. We discuss here the convergence behavior of the dyn-ICWF method in capturing the laser-driven proton-coupled electron transfer described in Section 6.1.

The time-resolved picture presents scattering as a fully nonequilibrium problem, where the system starts already in a nonsteady state, and so, the imaginary-time sta-ICWF cannot be applied here to prepare the initial wave function. Instead, we stochastically sample the initial probability density $|\Psi_0(r_1, r_2)|^2$ with N_c trajectories $\{r_1^\alpha(0), r_2^\alpha(0)\}$ that are used to construct CWFs $\phi_1^\alpha(r_1, 0)$ and $\phi_2^\alpha(r_2, 0)$, as defined in eq 23. These CWFs are then used to construct the ansatz in eq 30, i.e.

$$\Psi(r_1, r_2, t) = \sum_{\alpha=1}^{N_\sigma M} C_\alpha(t)\phi_1^\alpha(r_1, t)\phi_2^\alpha(r_2, t) \tag{57}$$

with an initial **C** vector that is obtained using

$$\mathbf{C}(0) = \mathbb{S}^{-1}\mathbf{G} \tag{58}$$

where **G** is the vector containing the overlap between the initial wave function and the CWFs, i.e.

$$G_\alpha = \iint dr_1 \, dr_2 \phi_1^{\alpha*}(r_1, 0)\phi_2^{\alpha*}(r_2, 0)\Psi_0(r_1, r_2) \tag{59}$$

Given $\mathbf{C}(0)$, and $\phi_1^\alpha(r_1, 0)$ and $\phi_2^\alpha(r_2, 0)$ for an ensemble of sampling points $\{r_1^\alpha(0), r_2^\alpha(0)\}$, these objects are then propagated according to the dyn-ICWF equations of motion in eqs 29 and 31.

To achieve converged results, we choose the size of the simulation box to be 150×150 au^2 with a homogeneous grid consisting of 500 grid points in each direction. The fourth-order Runge–Kutta algorithm was used to propagate the dyn-ICWF equations of motion with a time-step dt = 0.01 au, and the Moore–Penrose pseudo-inversion method with a tolerance of 10^{-8} was used to approximate the numerical inversion of the overlap matrix in eq 31.

In Figure 12, we show the one-body electronic density $\rho_e(r_1, t)$, for two different initial momenta and final times, viz., $p = 0.3$ and 1.5 au and $t = 1.8$ and 0.85 fs. For $p = 0.3$ au, a very small number of CWFs $((N_\sigma, M) = (16, 1))$ is already able to capture the correct dynamics quantitatively. In approaching the target atom with the larger momentum $p = 1.5$ au, the conventional mean-field method fails to describe the ionization process due to the lack of electron–electron correlation effects. This is in contrast with dyn-ICWF results, which qualitatively captures the correlated dynamics for a small number of CWFs $(N_\sigma, M) = (64, 1)$.

C.2. Laser-Driven Proton-Coupled Electron Transfer. We discuss here the convergence behavior of the dyn-ICWF method in capturing the laser-driven proton-coupled electron transfer described in Section 6.2. We suppose the system to be initially seating in the full electron–nuclear ground state, i.e., $\Psi(r, R, 0) = \Psi^0(r, R)$. This state is prepared using the imaginary-time
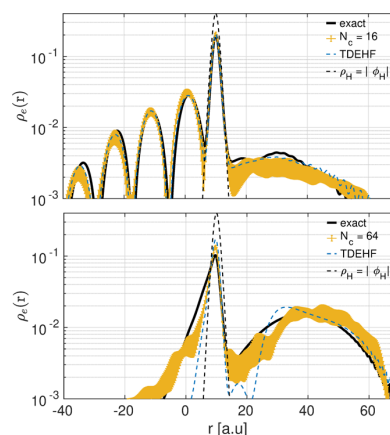
Figure 12. Top panel: reduced electron density at $t = 1.8$ fs for $p = 0.3$ au and $(N_\sigma, M) = (16, 1)$. Bottom panel: reduced electron density at $t = 0.85$ fs for $p = 1.5$ au and $(N_\sigma, M) = (64, 1)$.

version of the sta-ICWF method with ground-state CWFs only (i.e., $M = 1$)

$$\Psi^{(0)}(r, R) = \sum_{\alpha=1}^{N_c} C_\alpha(0)\phi^\alpha(r, 0)\chi^\alpha(R, 0) \tag{60}$$

The sta-ICWF provides as output the initial expansion coefficients $\mathbf{C}(0)$ and the ground-state electronic and nuclear CWFs, $\phi^\alpha(r, 0)$ and $\chi^\alpha(R, 0)$, respectively. We then apply an external strong electric field, defined in Section 6.2 of the main text, and the coefficients and the CWFs are propagated using the dyn-ICWF equations of motion in eqs 29 and 31.

To achieve converged results, a grid $[-9, 9]$ au with 301 grid points is chosen for the nuclear degrees of freedom. For the electron coordinates, the grid covers the interval $[-75, +75]$ au with 250 grid points. The fourth-order Runge–Kutta algorithm was used to propagate the dyn-ICWF equations of motion with a time-step dt = 0.1 au, and the Moore–Penrose pseudo-inversion method with a tolerance of 10^{-8} was used to approximate the numerical inversion of the overlap matrix in eq 31.

By introducing the Born–Huang expansion of the molecular wave function, $\Psi(\mathbf{r}, \mathbf{R}, t) = \sum_n \Phi_{\mathbf{R}}^{(n)}(\mathbf{r}, t)\chi^{(n)}(\mathbf{R}, t)$, we then monitor the dynamics through the BO electronic state populations, $P_m(t) = \int d\mathbf{R} |\chi^{(m)}(\mathbf{R}, t)|^2$, and the overlap integral of projected nuclear densities evolving on different BOPESs, $D_{nm}(t) = \int d\mathbf{R} |\chi^{(n)}(\mathbf{R}, t)|^2 |\chi^{(m)}(\mathbf{R}, t)|^2$. These quantities can be written in terms of the dyn-ICWF basis by re-expressing the adiabatic nuclear components as

$$|\chi^{(m)}(\mathbf{R}, t)|^2 = \left| \sum_{\alpha=1}^{N_\sigma M} C_\alpha(t)\chi^\alpha(R, t) \int dr \, \Phi_{\mathbf{R}}^{(m)}(r)\phi^\alpha(r, t) \right|^2 \tag{61}$$

In Figure 13, we show dyn-ICWF results for $(N_\sigma, M) = (16, 1)$. This very small number of CWFs, even if associated with large deviations across different stochastic particle placements, is able to capture nearly quantitatively both the adiabatic populations and the decoherence indicator. This result demonstrates that the dyn-ICWF technique achieves quantitative accuracy for situations in which the mean-field theory drastically fails to capture qualitative aspects of the dynamics using 3 orders of magnitude fewer trajectories than a mean-field simulation.
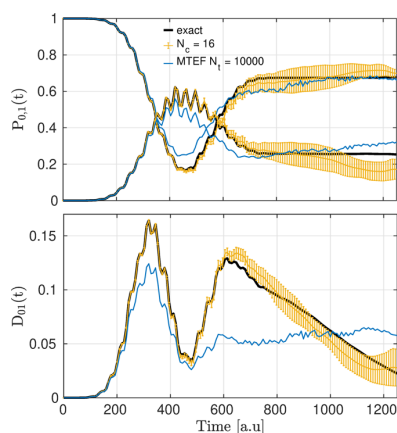
Figure 13. Top panel: population dynamics of the first two adiabatic electronic states $P_{0,1}(t)$. Solid black lines correspond to the exact numerical results. Solid blue and red lines correspond to dyn-ICWF results with $(N_\sigma, M) = (16, 1)$ for the ground and first excited adiabatic populations, respectively. Bottom panel: decoherence dynamics between the ground state and first excited adiabatic electronic states, i.e., D_{01}. Solid black lines correspond to exact results. The solid blue line corresponds to dyn-ICWF results with $(N_\sigma, M) = (16, 1)$.

C.3. Interference Effects Near a Molecular Conical Intersection. We discuss here some of the technical details of the interference effect calculation demonstrated in Section 6.3. As in ref 101, we took an electronic spatial grid $[-12, 12]$ au with 81 grid points and a nuclear grid $[-1.5, 1.5]$ au with 51 grid points alongside a time step of $dt = 0.02$ au. The initial wave function was constructed on this grid, and the exact dynamics were propagated directly using a fourth-order Runge−Kutta integrator.

The time-resolved picture presents this problem as a fully nonequilibrium problem, where the system starts already in a nonsteady state, and so, the imaginary-time sta-ICWF cannot be applied here to prepare the initial wave function. Instead, we stochastically sample the initial probability density $|\Psi_0(r, R)|^2$ with N_c trajectories $\{r^\alpha(0), R^\alpha(0)\}$ that are used to construct CWFs $\phi_r^\alpha(r, 0)$ and $\phi_R^\alpha(R, 0)$, as defined in eq 23. In this process, we respected the symmetry of the underlying initial state by symmetrizing the initial particle placement (and thereby complementarily symmetric slice CWFs) around the R_y, r_y axes, meaning for each particle $R^\alpha = (R_x^\alpha, R_y^\alpha)$, we set $R^{\alpha+1} = (-R_x^\alpha, R_y^\alpha)$.

These CWFs $\phi_r^\alpha(r, 0)$ and $\phi_R^\alpha(R, 0)$ are then used to construct the ansatz in eq 30, i.e.

$$\Psi(r, R, t) = \sum_{\alpha=1}^{N_c} C_\alpha(t)\phi_r^\alpha(r, t)\phi_R^\alpha(R, t) \tag{62}$$

with an initial **C** vector that is obtained using

$$\mathbf{C}(0) = \mathbb{S}^{-1}\mathbf{G} \tag{63}$$

where **G** is the vector containing the overlap between the initial wave function and the CWFs, i.e.

$$G_\alpha = \iint dr\ dR\ \phi_r^{\alpha*}(r, 0)\phi_R^{\alpha*}(R, 0)\Psi_0(r_1, r_2) \tag{64}$$

Given $\mathbf{C}(0)$, and $\phi_1^\alpha(r_1, 0)$ and $\phi_2^\alpha(r_2, 0)$ for an ensemble of sampling points $\{r_1^\alpha(0), r_2^\alpha(0)\}$, these objects are then

propagated according to the dyn-ICWF equations of motion in eqs 29 and 31.

In the dyn-ICWF, the pseudo-inverse tolerance for $\mathbb{S}$ was set to 10^{-8} and the evaluation matrix elements of the electron−nuclear interaction potential term of eq 40

$$\mathbb{W}_{\alpha\beta} = \iint dR\ dr\phi^{\alpha*}(r)\chi^{\alpha*}(R)W_{en}\phi^\beta(r)\chi^\beta(r) \tag{65}$$

was accelerated using a singular value decomposition (SVD) to break up the four index potentials $W_{en}(r_x, r_y, R_x, R_y)$ into a sum over electronic and nuclear two index vectors

$$W_{en}(r_x, r_y, R_x, R_y) = \sum_{l=1}^{N_\sigma} \sigma_l u_l(r_x, r_y)v_l(R_x, R_y) \tag{66}$$

By tossing out $\sigma_l < 10^{-4}$, we found that we were able to retain the accuracy of this potential to within a numerically tolerable limit with a speedup in computation time at a factor between 3.6 and 4.3 depending on hardware. A cubic interpolation to a grid twice as fine was used to smooth the images of the nuclear density

In Figure 14, we show the first and second excited BOPESs associated with the extended Shin−Metiu model introduced in
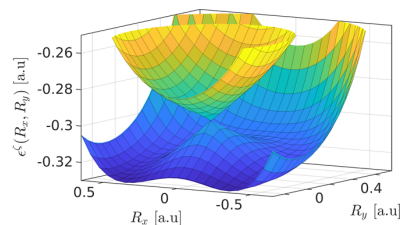

Figure 14. BOPESs for the first two excited states with electronic quantum numbers $\zeta = 1$ (lower surface) and $\zeta = 2$. As mentioned in the main text, the initial nuclear state is initialized as a Gaussian centered at $R = (0, 0.4)$ on the lower surface.

Section 6.3. dyn-ICWF results for $N_c = \{1024, 1600, 2400\}$ are shown in Figure 15. Due to the finesse of the interference pattern and its fragility with respect to the symmetry of the problem, the number of CWFs required to reproduce quantitatively the exact dynamics is relatively high compared to previous examples in Appendices C.1 and C.2. And yet, note that while the $N_c = 1024$
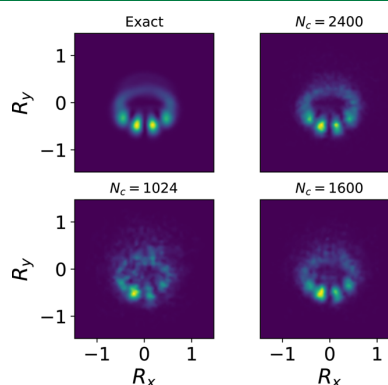
Figure 15. Convergence of the interference pattern arising from the CI with respect to the number of basis elements, N_c. The computational time for each fourth-order Runge−Kutta time step scales as $t = O((N_c)^a)$ for $a = 1.59 \pm 0.06$.
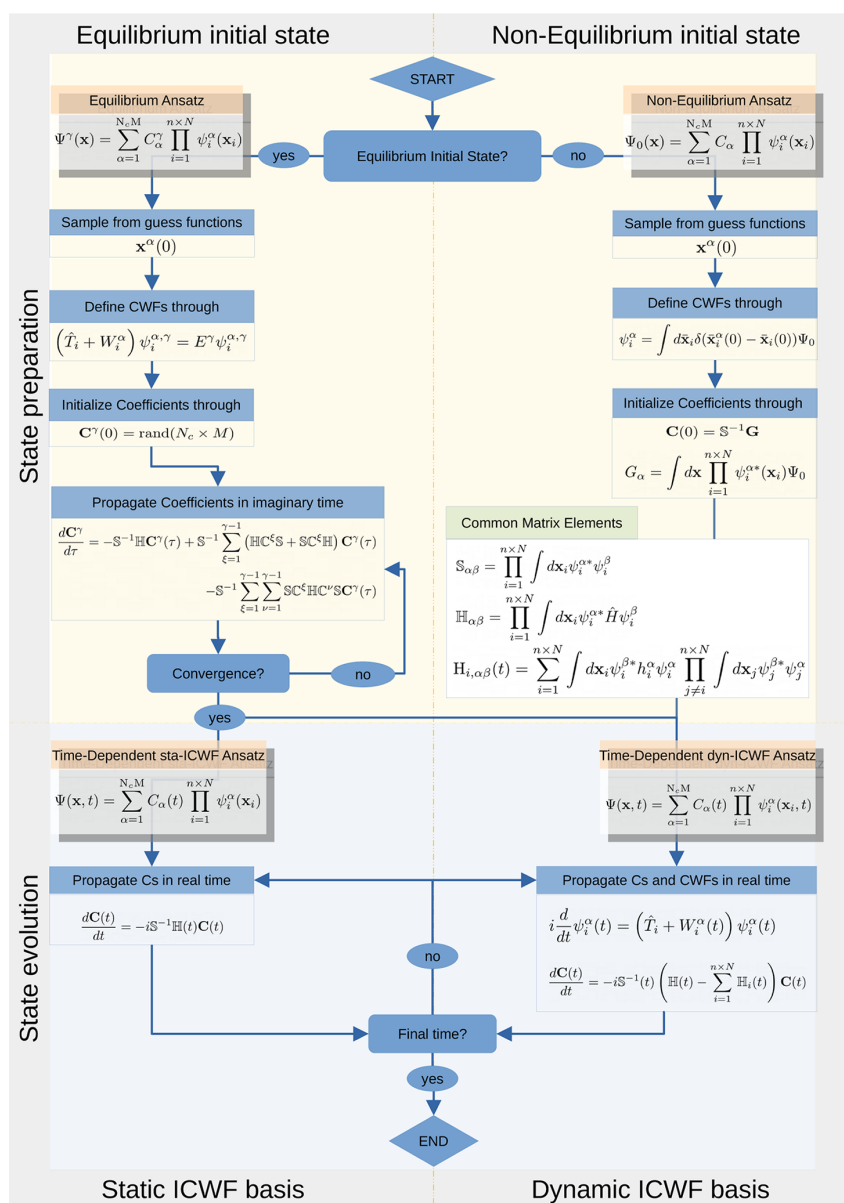
Figure 16. Flowchart of the ICWF method. The flowchart illustrates all possible situations of interest, viz., state preparation using either imaginary-time sta-ICWF for equilibrium states (top-left) or direct matrix inversion for nonequilibrium states (top right), and state propagation using real-time sta-ICWF (bottom left) or dyn-ICWF (bottom right).

result do not reproduce the interference pattern accurately, they do qualitatively capture the nuclear dynamics by avoiding the forbidden region surrounding the conical intersection. This is in contrast to the mean-field result (Figure 7 of ref 101), which fails to capture this qualitative feature of the nuclear dynamics.

D. Implementing the ICWF Method

We discuss here the general workflow associated with the different versions of the ICWF method, as well as some general remarks concerning their scalability with respect to the number of degrees of freedom.

Figure 16 illustrates all possible situations of interest. State preparation using imaginary-time sta-ICWF for equilibrium states is described in the top-left panel. A number N_c of particle

positions $x^\alpha(0)$ are sampled from educated guesses of the single-particle reduced probability densities. These positions are used to construct the Hermitian Hamiltonians of eq 8 and a number M of eigenstates. The randomly initialized vector of coefficients $C^\gamma(0)$ of the Ansatz in eq 9 is then propagated in imaginary time until convergence according to eqs 12−14. At this point, any (equilibrium) property of interest can be evaluated using eq 15 and 48 and 49.

The simulation may continue if the perturbation of an external agent is included. Thereafter, state propagation can be carried out using real-time sta-ICWF (bottom left) or dyn-ICWF (bottom right). As explained in the main text, if one chooses to propagate according to the sta-ICWF equation of motion (eq

21) together with eqs 13 and 14, a sufficient number of excited CWF states, $\gamma > 0$ in eq 9, for $x^\alpha(0)$ covering some anticipated range of motion for the dynamics must be considered. Alternatively, in cases where the time-dependent wave function is expected to stray far apart from the initial sta-ICWF basis, one may choose to address the dynamics using a time-dependent CWF basis as in eq 30 and the corresponding equations of motion in eq 29, together with eqs 31 and 32 and 13 and 14. At this point, any (nonequilibrium) property of interest can be again evaluated using eq 15 together with eqs 48 and 49.

Finally, note that in cases where one aims to study a certain dynamics that is triggered by some predefined out-of-equilibrium initial state, obtaining the initial coefficients $\mathbf{C}(0)$ is done through direct matrix inversion (top right). Afterward, the dynamics must be simulated using the dyn-ICWF algorithm described above.

Importantly, at this level of approximation, the ICWF method is a wave function approach. That is to say that, while the simple sum-of-product form that we employed for our ansatz in Figure 16 can be made more efficient by introducing a tensor network representation for the expansion coefficients (such as matrix product states or hierarchical Tucker formats), an exponential scaling is not expected to be circumvented without introducing any further approximation.

AUTHOR INFORMATION

Corresponding Authors

Guillermo Albareda − *Nano-Bio Spectroscopy Group and European Theoretical Spectroscopy Facility (ETSF), Universidad del País Vasco (UPV/EHU), 20018 San Sebastian, Spain; Institute of Theoretical and Computational Chemistry, University of Barcelona, 08028 Barcelona, Spain; Max Planck Institute for the Structure and Dynamics of Matter and Center for Free-Electron Laser Science, 22761 Hamburg, Germany;* ⓞ orcid.org/0000-0002-2181-7023; Email: guillealpi@gmail.com

Kevin Lively − *Max Planck Institute for the Structure and Dynamics of Matter and Center for Free-Electron Laser Science, 22761 Hamburg, Germany; The Hamburg Centre for Ultrafast Imaging, University of Hamburg, 22761 Hamburg, Germany;* ⓞ orcid.org/0000-0003-2098-1494; Email: kevin.lively@mpsd.mpg.de

Shunsuke A. Sato − *Max Planck Institute for the Structure and Dynamics of Matter and Center for Free-Electron Laser Science, 22761 Hamburg, Germany; Center for Computational Sciences, University of Tsukuba, Tsukuba, Ibaraki 305-8577, Japan;* Email: ssato@ccs.tsukuba.ac.jp

Aaron Kelly − *Max Planck Institute for the Structure and Dynamics of Matter and Center for Free-Electron Laser Science, 22761 Hamburg, Germany; The Hamburg Centre for Ultrafast Imaging, University of Hamburg, 22761 Hamburg, Germany; Department of Chemistry, Dalhousie University, Halifax, Nova Scotia B3H 4R2, Canada;* Email: aaron.kelly@mpsd.mpg.de

Angel Rubio − *Nano-Bio Spectroscopy Group and European Theoretical Spectroscopy Facility (ETSF), Universidad del País Vasco (UPV/EHU), 20018 San Sebastian, Spain; Max Planck Institute for the Structure and Dynamics of Matter and Center for Free-Electron Laser Science, 22761 Hamburg, Germany; The Hamburg Centre for Ultrafast Imaging, University of Hamburg, 22761 Hamburg, Germany; Center for Computational Quantum Physics (CCQ), Flatiron Institute, New York, New York 10010, United States;*

ⓞ orcid.org/0000-0003-2060-3151; Email: angel.rubio@mpsd.mpg.de

Complete contact information is available at:
https://pubs.acs.org/10.1021/acs.jctc.1c00772

Notes

The authors declare no competing financial interest.

ADDITIONAL NOTES

^{a}This has been discussed at length in the literature. A general and very elegant discussion on the various ways the body-fixed frame can be chosen is given in refs 74 and 75.
^{b}Both procedures lead to identical equations of motion due to the only time-dependent variational parameter being the expansion coefficients.

REFERENCES

(1) Mukamel, S. Femtosecond optical spectroscopy: a direct look at elementary chemical events. *Annu. Rev. Phys. Chem.* **1990**, *41*, 647−681.

(2) Zewail, A. H. Femtochemistry: atomic-scale dynamics of the chemical bond using ultrafast lasers (Nobel Lecture). *Angew. Chem., Int. Ed.* **2000**, *39*, 2586−2631.

(3) Corkum, P. B.; Krausz, F. Attosecond science. *Nat. Phys.* **2007**, *3*, 381−387.

(4) Sciaini, G.; Miller, R. D. Femtosecond electron diffraction: heralding the era of atomically resolved dynamics. *Rep. Prog. Phys.* **2011**, *74*, No. 096101.

(5) Blaga, C. I.; Xu, J.; DiChiara, A. D.; Sistrunk, E.; Zhang, K.; Agostini, P.; Miller, T. A.; DiMauro, L. F.; Lin, C. Imaging ultrafast molecular dynamics with laser-induced electron diffraction. *Nature* **2012**, *483*, 194−197.

(6) Lépine, F.; Ivanov, M. Y.; Vrakking, M. J. Attosecond molecular dynamics: fact or fiction? *Nat. Photonics* **2014**, *8*, 195−204.

(7) Nisoli, M.; Decleva, P.; Calegari, F.; Palacios, A.; Martín, F. Attosecond electron dynamics in molecules. *Chem. Rev.* **2017**, *117*, 10760−10825.

(8) Devereaux, T. P.; Hackl, R. Inelastic light scattering from correlated electrons. *Rev. Mod. Phys.* **2007**, *79*, 175.

(9) Fink, J.; Schierle, E.; Weschke, E.; Geck, J. Resonant elastic soft x-ray scattering. *Rep. Prog. Phys.* **2013**, *76*, No. 056502.

(10) Basov, D.; Averitt, R.; Hsieh, D. Towards properties on demand in quantum materials. *Nat. Mater.* **2017**, *16*, 1077−1088.

(11) Buzzi, M.; Först, M.; Mankowsky, R.; Cavalleri, A. Probing dynamics in quantum materials with femtosecond X-rays. *Nat. Rev. Mater.* **2018**, *3*, 299−311.

(12) Ruggenthaler, M.; Tancogne-Dejean, N.; Flick, J.; Appel, H.; Rubio, A. From a quantum-electrodynamical light−matter description to novel spectroscopies. *Nat. Rev. Chem.* **2018**, *2*, No. 0118.

(13) Carusotto, I.; Ciuti, C. Quantum fluids of light. *Rev. Mod. Phys.* **2013**, *85*, 299.

(14) Ebbesen, T. W. Hybrid light-matter states in a molecular and material science perspective. *Acc. Chem. Res.* **2016**, *49*, 2403−2412.

(15) Ribeiro, R. F.; Martínez-Martínez, L. A.; Du, M.; Campos-Gonzalez-Angulo, J.; Yuen-Zhou, J. Polariton chemistry: controlling molecular dynamics with optical cavities. *Chem. Sci.* **2018**, *9*, 6325−6339.

(16) Hertzog, M.; Wang, M.; Mony, J.; Börjesson, K. Strong light−matter interactions: a new direction within chemistry. *Chem. Soc. Rev.* **2019**, *48*, 937−961.

(17) Oka, T.; Kitamura, S. Floquet engineering of quantum materials. *Annu. Rev. Condens. Matter Phys.* **2019**, *10*, 387−408.

(18) Ozawa, T.; Price, H. M. Topological quantum matter in synthetic dimensions. *Nat. Rev. Phys.* **2019**, *1*, 349−357.

(19) Rudner, M. S.; Lindner, N. H. Band structure engineering and non-equilibrium dynamics in Floquet topological insulators. *Nat. Rev. Phys.* **2020**, *2*, 229−244.

(20) Hübener, H.; De Giovannini, U.; Schäfer, C.; Andberger, J.; Ruggenthaler, M.; Faist, J.; Rubio, A. Engineering quantum materials with chiral optical cavities. *Nat. Mater.* **2021**, *20*, 438−442.

(21) Genet, C.; Faist, J.; Ebbesen, T. W. Inducing new material properties with hybrid light-matter states. *Phys. Today* **2021**, *74*, 42−48.

(22) Born, M.; Oppenheimer, R. Zur quantentheorie der molekeln. *Ann. Phys.* **1927**, *389*, 457−484.

(23) Marx, D.; Hutter, J. *Ab Initio Molecular Dynamics: Basic Theory and Advanced Methods*; Cambridge University Press, 2009.

(24) Ashcroft, N. W.; Mermin, N. D. *Solid State Physics*; Holt-Saunders, 1976.

(25) Eyring, H.; Polanyi, M. Uber einfache gasreaktionen. *Z. Phys. Chem. B* **1931**, *12*, 279−311.

(26) Miller, W. H.; Handy, N. C.; Adams, J. E. Reaction path Hamiltonian for polyatomic molecules. *J. Chem. Phys.* **1980**, *72*, 99−112.

(27) Heidrich, D. *The Reaction Path in Chemistry: Current Approaches and Perspectives*; Springer Science & Business Media, 2013; Vol. 16.

(28) Cha, Y.; Murray, C. J.; Klinman, J. P. Hydrogen tunneling in enzyme reactions. *Science* **1989**, *243*, 1325−1330.

(29) Borgis, D.; Hynes, J. T. Dynamical theory of proton tunneling transfer rates in solution: general formulation. *Chem. Phys.* **1993**, *170*, 315−346.

(30) Tuckerman, M. E.; Marx, D.; Klein, M. L.; Parrinello, M. On the quantum nature of the shared proton in hydrogen bonds. *Science* **1997**, *275*, 817−820.

(31) Raugei, S.; Klein, M. L. Nuclear quantum effects and hydrogen bonding in liquids. *J. Am. Chem. Soc.* **2003**, *125*, 8992−8993.

(32) Car, R.; Parrinello, M. Unified approach for molecular dynamics and density-functional theory. *Phys. Rev. Lett.* **1985**, *55*, 2471.

(33) Payne, M. C.; Teter, M. P.; Allan, D. C.; Arias, T.; Joannopoulos, J. D. Iterative minimization techniques for ab initio total-energy calculations: molecular dynamics and conjugate gradients. *Rev. Mod. Phys.* **1992**, *64*, 1045.

(34) Barnett, R. N.; Landman, U. Born-Oppenheimer molecular-dynamics simulations of finite systems: Structure and dynamics of (H 2 O) 2. *Phys. Rev. B* **1993**, *48*, 2081.

(35) Zhang, J. Z. H. *Theory and Application of Quantum Molecular Dynamics*; World Scientific, 1998.

(36) Born, M.; Huang, K. *Dynamical Theory of Crystal Lattices*; Clarendon, Oxford, 1954.

(37) Domcke, W.; Stock, G. Theory of Ultrafast Nonadiabatic Excited-State Processes and Their Spectroscopic Detection in Real Time. *Advances in Chemical Physics*; John Wiley & Sons, Inc., 1997; Vol. 100, pp 1−169.

(38) Miller, W. H. Perspective: Quantum or classical coherence? *J. Chem. Phys.* **2012**, *136*, No. 210901.

(39) Tully, J. C. Perspective: Nonadiabatic dynamics theory. *J. Chem. Phys.* **2012**, *137*, No. 22A301.

(40) Kapral, R. Quantum dynamics in open quantum-classical systems. *J. Phys.: Condens. Matter* **2015**, *27*, No. 073201.

(41) McLachlan, A. A variational solution of the time-dependent Schrodinger equation. *Mol. Phys.* **1964**, *8*, 39−44.

(42) Tully, J. C. Molecular dynamics with electronic transitions. *J. Chem. Phys.* **1990**, *93*, 1061−1071.

(43) Beck, M. H.; Jäckle, A.; Worth, G. A.; Meyer, H.-D. The multiconfiguration time-dependent Hartree (MCTDH) method: a highly efficient algorithm for propagating wavepackets. *Phys. Rep.* **2000**, *324*, 1−105.

(44) Martinez, T. J.; Ben-Nun, M.; Levine, R. Multi-electronic-state molecular dynamics: A wave function approach with applications. *J. Phys. Chem. A* **1996**, *100*, 7884−7895.

(45) Worth, G. A.; Burghardt, I. Full quantum mechanical molecular dynamics using Gaussian wavepackets. *Chem. Phys. Lett.* **2003**, *368*, 502−508.

(46) Worth, G.; Robb, M.; Burghardt, I. A novel algorithm for non-adiabatic direct dynamics using variational Gaussian wavepackets. *Faraday Discuss.* **2004**, *127*, 307−323.

(47) Shalashilin, D. V. Nonadiabatic dynamics with the help of multiconfigurational Ehrenfest method: Improved theory and fully quantum 24D simulation of pyrazine. *J. Chem. Phys.* **2010**, *132*, No. 244111.

(48) Makhov, D. V.; Glover, W. J.; Martinez, T. J.; Shalashilin, D. V. Ab initio multiple cloning algorithm for quantum nonadiabatic molecular dynamics. *J. Chem. Phys.* **2014**, *141*, No. 054110.

(49) Sun, X.; Miller, W. H. Semiclassical initial value representation for electronically nonadiabatic molecular dynamics. *J. Chem. Phys.* **1997**, *106*, 6346−6353.

(50) Miller, W. H. Electronically nonadiabatic dynamics via semiclassical initial value methods. *J. Phys. Chem. A* **2009**, *113*, 1405−1415.

(51) Kapral, R.; Ciccotti, G. Mixed quantum-classical dynamics. *J. Chem. Phys.* **1999**, *110*, 8919−8929.

(52) Kelly, A.; van Zon, R.; Schofield, J.; Kapral, R. Mapping quantum-classical Liouville equation: Projectors and trajectories. *J. Chem. Phys.* **2012**, *136*, No. 084101.

(53) Hsieh, C.-Y.; Kapral, R. Nonadiabatic dynamics in open quantum-classical systems: Forward-backward trajectory solution. *J. Chem. Phys.* **2012**, *137*, No. 22A507.

(54) Richardson, J. O.; Thoss, M. Communication: Nonadiabatic ring-polymer molecular dynamics. *J. Chem. Phys.* **2013**, *139*, No. 031102.

(55) Ananth, N. Mapping variable ring polymer molecular dynamics: A path-integral based method for nonadiabatic processes. *J. Chem. Phys.* **2013**, *139*, No. 124102.

(56) Abedi, A.; Maitra, N. T.; Gross, E. K. U. Exact Factorization of the Time-Dependent Electron-Nuclear Wave Function. *Phys. Rev. Lett.* **2010**, *105*, No. 123002.

(57) Min, S. K.; Agostini, F.; Gross, E. K. Coupled-trajectory quantum-classical approach to electronic decoherence in nonadiabatic processes. *Phys. Rev. Lett.* **2015**, *115*, No. 073001.

(58) Agostini, F.; Min, S. K.; Abedi, A.; Gross, E. K. Quantum-classical nonadiabatic dynamics: coupled- vs independent-trajectory methods. *J. Chem. Theory Comput.* **2016**, *12*, 2127−2143.

(59) Alonso, J. L.; Andrade, X.; Echenique, P.; Falceto, F.; Prada-Gracia, D.; Rubio, A. Efficient formalism for large-scale ab initio molecular dynamics based on time-dependent density functional theory. *Phys. Rev. Lett.* **2008**, *101*, No. 096403.

(60) Lively, K.; Albareda, G.; Sato, S. A.; Kelly, A.; Rubio, A. Simulating Vibronic Spectra without Born−Oppenheimer Surfaces. *J. Phys. Chem. Lett.* **2021**, *12*, 3074−3081.

(61) Castro, A.; Marques, M. A.; Alonso, J. A.; Bertsch, G. F.; Rubio, A. Excited states dynamics in time-dependent density functional theory. *Eur. Phys. J. D* **2004**, *28*, 211−218.

(62) McEniry, E.; Wang, Y.; Dundas, D.; Todorov, T.; Stella, L.; Miranda, R.; Fisher, A.; Horsfield, A.; Race, C.; Mason, D.; et al. Modelling non-adiabatic processes using correlated electron-ion dynamics. *Eur. Phys. J. B* **2010**, *77*, 305−329.

(63) Rozzi, C. A.; Falke, S. M.; Spallanzani, N.; Rubio, A.; Molinari, E.; Brida, D.; Maiuri, M.; Cerullo, G.; Schramm, H.; Christoffers, J.; et al.

Quantum coherence controls the charge separation in a prototypical artificial light-harvesting system. *Nat. Commun.* **2013**, *4*, No. 1602.

(64) Zhao, L.; Wildman, A.; Pavosevic, F.; Tully, J. C.; Hammes-Schiffer, S.; Li, X. Excited State Intramolecular Proton Transfer with Nuclear-Electronic Orbital Ehrenfest Dynamics. *J. Phys. Chem. Lett.* **2021**, *12*, 3497−3502.

(65) Tully, J. C. Molecular dynamics with electronic transitions. *J. Chem. Phys.* **1990**, *93*, 1061−1071.

(66) Parandekar, P. V.; Tully, J. C. Mixed quantum-classical equilibrium. *J. Chem. Phys.* **2005**, *122*, No. 094102.

(67) Nielsen, S.; Kapral, R.; Ciccotti, G. Statistical mechanics of quantum-classical systems. *J. Chem. Phys.* **2001**, *115*, 5805−5815.

(68) Albareda, G.; Appel, H.; Franco, I.; Abedi, A.; Rubio, A. Correlated electron-nuclear dynamics with conditional wave functions. *Phys. Rev. Lett.* **2014**, *113*, No. 083003.

(69) The history of conditional wave functions is mainly linked to the quantum measurement problem. Bohmian conditional wave functions were originally introduced as the proper mathematical object to represent, in terms of state vectors, an arbitrary subset of degrees of freedom.[115] More recently, it has been formally shown that collapse models and their primitive ontology can be exactly recast in terms of conditional wave functions.[116−118]

(70) Albareda, G.; Bofill, J. M.; Tavernelli, I.; Huarte-Larranaga, F.; Illas, F.; Rubio, A. Conditional Born-Oppenheimer dynamics: Quantum dynamics simulations for the model porphine. *J. Phys. Chem. Lett.* **2015**, *6*, 1529−1535.

(71) Albareda, G.; Abedi, A.; Tavernelli, I.; Rubio, A. Universal steps in quantum dynamics with time-dependent potential-energy surfaces: Beyond the Born-Oppenheimer picture. *Phys. Rev. A* **2016**, *94*, No. 062511.

(72) Albareda, G.; Kelly, A.; Rubio, A. Nonadiabatic quantum dynamics without potential energy surfaces. *Phys. Rev. Mater.* **2019**, *3*, No. 023803.

(73) Albareda, G.; Tavernelli, I. *Quantum Chemistry and Dynamics of Excited States*; John Wiley & Sons, Ltd., 2020; Chapter 18, pp 563−594.

(74) Littlejohn, R. G.; Reinsch, M. Gauge fields in the separation of rotations and internal motions in the n-body problem. *Rev. Mod. Phys.* **1997**, *69*, 213.

(75) Kreibich, T.; van Leeuwen, R.; Gross, E. Multicomponent density-functional theory for electrons and nuclei. *Phys. Rev. A* **2008**, *78*, No. 022501.

(76) Khoromskaia, V.; Khoromskij, B. N. Tensor numerical methods in quantum chemistry: from Hartree-Fock to excitation energies. *Phys. Chem. Chem. Phys.* **2015**, *17*, 31491−31509.

(77) Ulusoy, I. S.; Nest, M. The multi-configuration electron-nuclear dynamics method applied to LiH. *J. Chem. Phys.* **2012**, *136*, No. 054112.

(78) Vendrell, O.; Meyer, H. D. Multilayer multiconfiguration time-dependent Hartree method: Implementation and applications to a Henon-Heiles Hamiltonian and to pyrazine. *J. Chem. Phys.* **2011**, *134*, No. 044135.

(79) Manthe, U. A multilayer multiconfigurational time-dependent Hartree approach for quantum dynamics on general potential energy surfaces. *J. Chem. Phys.* **2008**, *128*, No. 164116.

(80) Kosloff, R.; Tal-Ezer, H. A direct relaxation method for calculating eigenfunctions and eigenvalues of the Schrödinger equation on a grid. *Chem. Phys. Lett.* **1986**, *127*, 223−230.

(81) Javanainen, J.; Eberly, J. H.; Su, Q. Numerical simulations of multiphoton ionization and above-threshold electron spectra. *Phys. Rev. A* **1988**, *38*, 3430.

(82) Lein, M.; Kreibich, T.; Gross, E.; Engel, V. Strong-field ionization dynamics of a model H 2 molecule. *Phys. Rev. A* **2002**, *65*, No. 033403.

(83) Eberly, J.; Su, Q.; Javanainen, J. Nonlinear light scattering accompanying multiphoton ionization. *Phys. Rev. Lett.* **1989**, *62*, 881.

(84) Su, Q.; Eberly, J. Model atom for multiphoton physics. *Phys. Rev. A* **1991**, *44*, 5997.

(85) Schwengelbeck, U.; Faisal, F. Ionization of the one-dimensional Coulomb atom in an intense laser field. *Phys. Rev. A* **1994**, *50*, 632.

(86) Lein, M.; Gross, E. K.; Engel, V. Intense-field double ionization of helium: identifying the mechanism. *Phys. Rev. Lett.* **2000**, *85*, 4707.

(87) Bauer, D. Two-dimensional, two-electron model atom in a laser pulse: Exact treatment, single-active-electron analysis, time-dependent density-functional theory, classical calculations, and nonsequential ionization. *Phys. Rev. A* **1997**, *56*, 3028.

(88) Lappas, D. G.; Van Leeuwen, R. Electron correlation effects in the double ionization of He. *J. Phys. B: At., Mol. Opt. Phys.* **1998**, *31*, L249.

(89) Yabana, K.; Bertsch, G. Time-dependent local-density approximation in real time. *Phys. Rev. B* **1996**, *54*, 4484−4487.

(90) Albareda, G.; Marian, D.; Benali, A.; Yaro, S.; Zanghì, N.; Oriols, X. Time-resolved electron transport with quantum trajectories. *J. Comput. Electron.* **2013**, *12*, 405−419.

(91) Albareda, G.; Suñé, J.; Oriols, X. Many-particle Hamiltonian for open systems with full Coulomb interaction: Application to classical and quantum time-dependent simulations of nanoscale electron devices. *Phys. Rev. B* **2009**, *79*, No. 075315.

(92) Albareda, G.; López, H.; Cartoixà, X.; Suñé, J.; Oriols, X. Time-dependent boundary conditions with lead-sample Coulomb correlations: Application to classical and quantum nanoscale electron device simulators. *Phys. Rev. B* **2010**, *82*, No. 085301.

(93) Albareda, G.; Marian, D.; Benali, A.; Alarcón, A.; Moises, S.; Oriols, X. *Simulation of Transport in Nanodevices*; John Wiley & Sons, Ltd., 2016; Chapter 7, pp 261−318.

(94) Oriols, X. Quantum-trajectory approach to time-dependent transport in mesoscopic systems with electron-electron interactions. *Phys. Rev. Lett.* **2007**, *98*, No. 066803.

(95) Albareda, G.; Saura, X.; Oriols, X.; Suñé, J. Many-particle transport in the channel of quantum wire double-gate field-effect transistors with charged atomistic impurities. *J. Appl. Phys.* **2010**, *108*, No. 043706.

(96) Scheer, E.; Cuevas, J. C. *Molecular Electronics: An Introduction to Theory and Experiment*; World Scientific, 2017; Vol. 15.

(97) Krausz, F.; Ivanov, M. Attosecond physics. *Rev. Mod. Phys.* **2009**, *81*, 163.

(98) Suzuki, Y.; Lacombe, L.; Watanabe, K.; Maitra, N. T. Exact time-dependent exchange-correlation potential in electron scattering processes. *Phys. Rev. Lett.* **2017**, *119*, No. 263401.

(99) Shin, S.; Metiu, H. Nonadiabatic effects on the charge transfer rate constant: A numerical study of a simple model system. *J. Chem. Phys.* **1995**, *102*, 9285−9295.

(100) Min, S. K.; Abedi, A.; Kim, K. S.; Gross, E. Is the molecular Berry phase an artifact of the Born-Oppenheimer approximation? *Phys. Rev. Lett.* **2014**, *113*, No. 263004.

(101) Schaupp, T.; Engel, V. A classical ride through a conical intersection. *J. Chem. Phys.* **2019**, *150*, No. 034301.

(102) The CWF *ab initio* methods sta-ICWF and dyn-ICWF are currently being implemented in OCTOPUS software. The codes used in this work are available upon request.

(103) Milder, A.; Katz, J.; Boni, R.; Palastro, J.; Sherlock, M.; Rozmus, W.; Froula, D. Measurements of Non-Maxwellian Electron Distribution Functions and Their Effect on Laser Heating. *Phys. Rev. Lett.* **2021**, *127*, No. 015001.

(104) Bonitz, M.; Dornheim, T.; Moldabekov, Z. A.; Zhang, S.; Hamann, P.; Kählert, H.; Filinov, A.; Ramakrishna, K.; Vorberger, J. Ab initio simulation of warm dense matter. *Phys. Plasmas* **2020**, *27*, No. 042710.

(105) Dal Forno, S.; Lischner, J. Electron-phonon coupling and hot electron thermalization in titanium nitride. *Phys. Rev. Mater.* **2019**, *3*, No. 115203.

(106) Wang, L.; Long, R.; Prezhdo, O. V. Time-domain ab initio modeling of photoinduced dynamics at nanoscale interfaces. *Annu. Rev. Phys. Chem.* **2015**, *66*, 549−579.

(107) Chen, H.-Y.; Sangalli, D.; Bernardi, M. Exciton-phonon interaction and relaxation times from first principles. *Phys. Rev. Lett.* **2020**, *125*, No. 107401.

(108) Bernardi, M.; Vigil-Fowler, D.; Lischner, J.; Neaton, J. B.; Louie, S. G. Ab initio study of hot carriers in the first picosecond after sunlight absorption in silicon. *Phys. Rev. Lett.* **2014**, *112*, No. 257402.

(109) Eichberger, M.; Schäfer, H.; Krumova, M.; Beyer, M.; Demsar, J.; Berger, H.; Moriena, G.; Sciaini, G.; Miller, R. D. Snapshots of cooperative atomic motions in the optical suppression of charge density waves. *Nature* **2010**, *468*, 799−802.

(110) Lan, Y.; Dringoli, B. J.; Valverde-Chávez, D. A.; Ponseca, C. S.; Sutton, M.; He, Y.; Kanatzidis, M. G.; Cooke, D. G. Ultrafast correlated charge and lattice motion in a hybrid metal halide perovskite. *Sci. Adv.* **2019**, *5*, No. eaaw5558.

(111) Konstantinova, T.; Rameau, J. D.; Reid, A. H.; Abdurazakov, O.; Wu, L.; Li, R.; Shen, X.; Gu, G.; Huang, Y.; Rettig, L.; et al. Nonequilibrium electron and lattice dynamics of strongly correlated Bi2Sr2CaCu2O8+ δ single crystals. *Sci. Adv.* **2018**, *4*, No. eaap7427.

(112) Cudazzo, P.; Profeta, G.; Sanna, A.; Floris, A.; Continenza, A.; Massidda, S.; Gross, E. Ab initio description of high-temperature superconductivity in dense molecular hydrogen. *Phys. Rev. Lett.* **2008**, *100*, No. 257001.

(113) Gartner, T. E.; Zhang, L.; Piaggi, P. M.; Car, R.; Panagiotopoulos, A. Z.; Debenedetti, P. G. Signatures of a liquid−liquid transition in an ab initio deep neural network model for water. *Proc. Natl. Acad. Sci. U.S.A.* **2020**, *117*, 26040−26046.

(114) Shin, D.; Latini, S.; Schäfer, C.; Sato, S. A.; De Giovannini, U.; Hübener, H.; Rubio, A. Quantum paraelectric phase of $SrTiO_3$ from first principles. *Phys. Rev. B* **2021**, *104*, No. L060103.

(115) Dürr, D.; Goldstein, S.; Zanghi, N. Quantum equilibrium and the origin of absolute uncertainty. *J. Stat. Phys.* **1992**, *67*, 843−907.

(116) Gambetta, J.; Wiseman, H. Interpretation of non-Markovian stochastic Schrödinger equations as a hidden-variable theory. *Phys. Rev. A* **2003**, *68*, No. 062104.

(117) Pandey, D.; Colomés, E.; Albareda, G.; Oriols, X. Stochastic Schrödinger equations and conditional states: A general non-Markovian quantum electron transport simulator for THz electronics. *Entropy* **2019**, *21*, No. 1148.

(118) Tilloy, A.; Wiseman, H. M. Non-Markovian Wave-Function Collapse Models Are Bohmianlike Theories in Disguise 2021, arXiv:2105.06115. arXiv.org e-Print archive. https://arxiv.org/abs/2105.06115.

5 | Simulating Vibronic Spectra without Born-Oppenheimer Surfaces

The problem with wavefunction dynamics ultimately lies in its non-locality, which subsequently requires information about the coupling between the component parts of the system for all possible configurations. Thus the only way to truly scale simulations beyond small molecules is to have a quasi-local representation of one of the subsystems, i.e. treating their constituent parts like point particles. In the subsequent discussion, and in paper **II** we will treat the electrons as the quantum mechanical subsystem and the nuclei as the classical-like subsystem, but it's important to note that this approximation can be done between other component subsystems. In particular one can treat the cavity modes *and nuclear subsystem* semi-classically simultaneously, with both coupled to a quantum mechanically treated electronic system [148–150].

When treating the nuclei semi-classically, oftentimes the forces dictating their evolution come from BO derived PESs, and the electronic system is constrained to evolve between these electronic states. In contrast, we want to understand what can be captured when the electronic system is represented on a real-space grid, with the nuclear evolution being dictated by mean-field forces. Doing so, we are free to drive the electronic system in real-time to any complicated superposition of excited states desired. Simultaneously the nuclei are free to explore any part of the system phase space. Such a framework allows, in principle, for the study of driven phase transitions involving modulation of electronic properties through strongly anharmonic nuclear motion or large scale nuclear rearrangement through electronic system excitation. Furthermore, since the mean-field Ehrenfest dynamics of nuclei are widely implemented in real-time dynamics codes, any simulation protocal based on it can be widely adopted. However, given the importance quantized nuclear behavior can play in such phenomena [80, 151], it's important to know whether such effects can be captured, and what limitations arise from the real-space grid and mean-field approach. Thus in paper **II** we systematically study the capacity of mean-field semi-classical dynamics to recover quantized nuclear effects by starting with the simplest possible case of dynamical electron-nuclear coupling, vibronic absorption.

First in this chapter we provide a brief overview of semi-classical dynamics approaches, and pay particular attention to the class of algorithms derived from Quantum-Classical Liouville Equation as a starting point. A small portion of what follows is adapted from the SI section **MTEF Equation of Motion** from paper **II**.

5.1 Semi-Classical Dynamics

There are a number of ways that one can go about treating the nuclei like particles while treating the electronic system quantum mechanically, but the common challenge to all of them

is reconciling the fact that the electronic system can be in a quantum superposition between different states, while the nuclei cannot. Quantum mechanically, it makes sense to speak of a nuclear wavepacket evolving under the forces of a given electronic state n. In the Born-Huang expansion, we can envision this combined state as the electron-nuclear wavepacket $|\chi_n\rangle \otimes |\Phi_n\rangle$. Through the adiabatic theorem one can also think of a classical particle responding to the forces from a single electronic state which instantly adjusts to the nuclear motion, analogous to replacing $|\chi_n\rangle$ with a Dirac delta. However, in a fully quantum mechanical picture, one can construct the full system state out of a superposition of electron-nuclear wavepackets, and the effects of all of these distinct electronic configurations manifest in the dynamics of the nuclear subsystem's behavior simultaneously. In contrast, a point particle has a single position in its classical phase space defined by its position and momentum, and therefore must evolve according to a single force. One popular solution to this problem is the notion of 'surface hopping' such as the Fewest Switches Surface Hoppping (FSSH) algorithm [152], in which a collection of nuclear trajectories $\{\underline{\underline{\mathbf{R}}}^i, \underline{\underline{\mathbf{P}}}^i; i = 1, \dots N\}$ evolve adiabatically on a given surface $U_n(\underline{\underline{\mathbf{R}}})$:

$$
\begin{aligned}
\dot{\underline{\underline{\mathbf{R}}}}^i(t) &= \underline{\underline{M}}^{-1}\underline{\underline{\mathbf{P}}}^i(t) \\
\dot{\underline{\underline{\mathbf{P}}}}^i(t) &= -\boldsymbol{\nabla}_{\underline{\underline{\mathbf{R}}}} U_n(\underline{\underline{\mathbf{R}}})\big|_{\underline{\underline{\mathbf{R}}}^i(t)}.
\end{aligned}
\tag{5.1}
$$

When a given trajectory approaches a region with strong NACTs it will probabilistically switch surfaces (hop). By propagating an ensemble of trajectories, if the surface hopping probabilities are constructed appropriately, a pragmatic simulacrum of the branching paths of the quantum dynamics can be attained. While the equations of motion can be motivated by integrating the classical Lagrangian alongside a time dependent phase [25, 153], the probabilistic switching between surfaces is an ad-hoc choice which is constructed in an attempt to maintain detailed balance (microscopic reversibility) while minimizing hopping. In combination with on-the-fly evaluation of BOPESs and NACTs, surface hopping approaches such as Ab-Initio Multiple Spawning (AIMS) – which dresses the trajectories in gaussian wave packets – are among the most popular choices for ab-initio non-adiabatic molecular dynamics simulations [22, 25]. Nuclear quantum effects such as zero-point energy and tunneling can also be included through path integral molecular dynamics approaches such as centroid molecular dynamics or ring polymer molecular dynamics (RPMD) [37, 154–156]. These methods are based on an approximate mapping between the imaginary time Feynman path integral and a chain of copies of the classical system, connected by temperature dependent springs, which capture the delocalization of the nuclear system. In the limit of infinite copies and harmonic potentials this becomes exact. Through a Kubo-transformation, these methods can be used to calculate the real-time dynamics of systems in the short-time limit [154] and RPMD can be extended to non-adiabatic dynamics through inclusion of surface hopping [157, 158].

In general the treatment of the nuclear system via an ensemble of classical-like trajectories will lead problems of *over-coherence*. This can be understood in the Born-Huang ansatz as a failure of the nuclear states on different surfaces, $|\chi_n\rangle$, to cleanly separate following an interaction between BOPESs such that the system remains in a coherent superposition between different electronic states, i.e. $\langle\chi_n(t)|\chi_m(t)\rangle \neq 0$, in regions of the nuclear configuration space with little coupling between these two surfaces [159]. There are techniques for reducing such problems [160], and in fact a framework exists that allows for a systematic hierarchy of semi-classical dynamics which approaches more exact dynamics, while not necessarily relying on the BO picture.

The Quantum Classical Liouville Equation

Instead of starting with the assumption of a classical like-trajectory we can instead begin with an exact reformulation of the quantum mechanical system through the phase-space representation. Introduced by Eugene Wigner in 1932 [161] the Wigner transformation maps the state of a quantum system to a quasi-probability distribution in both position and momentum simultaneously. By similarly transforming operators, the expectation value of observables can be obtained by integrating over phase space [162]. Restricting the Wigner transform to just the nuclear degrees of freedom allows for systematic treatment of the electron-nuclear correlation. Starting from a density matrix representation of the full system, $\hat{\rho}$, we perform a Wigner transformation over the nuclear subsystem, producing a unique mapping onto a nuclear phase space $\underline{\underline{\mathbf{X}}} = (\underline{\underline{\mathbf{R}}}, \underline{\underline{\mathbf{P}}}) \in \mathbb{R}^{2dN_n}$ for Cartesian dimension d. The partial Wigner transform for $\hat{\rho}$ is defined as:

$$\hat{\rho}_W(\underline{\underline{\mathbf{X}}}) = \frac{1}{(2\pi)^{dN_n}} \int d\underline{\underline{\mathbf{S}}} e^{i\underline{\underline{\mathbf{P}}} \cdot \underline{\underline{\mathbf{S}}}} \langle \underline{\underline{\mathbf{R}}} - \underline{\underline{\mathbf{S}}}/2 | \hat{\rho} | \underline{\underline{\mathbf{R}}} + \underline{\underline{\mathbf{S}}}/2 \rangle , \tag{5.2}$$

for dummy variable $\underline{\underline{\mathbf{S}}}$. Note that $\hat{\rho}_W(\underline{\underline{\mathbf{X}}})$ retains a Hilbert space (operator) character over the electronic degrees of freedom, dependent on the continuous nuclear phase space parameters. In general, developing equations of motion for $\hat{\rho}_W(\underline{\underline{\mathbf{X}}})$ requires taking the partial Wigner transformation of the Liouville von-Neumann equation of motion for ρ:

$$\frac{\partial \hat{\rho}_W}{\partial t} = -i\Big((\hat{H}\hat{\rho})_W - (\hat{\rho}\hat{H})_W\Big)$$
$$(\hat{H}\hat{\rho})_W = \hat{H}_W \exp\Big(\frac{1}{2i}\overleftrightarrow{\Lambda}\Big)\hat{\rho}_W$$
$$\overleftrightarrow{\Lambda} = \overleftarrow{\nabla}_{\underline{\underline{\mathbf{P}}}} \cdot \overrightarrow{\nabla}_{\underline{\underline{\mathbf{R}}}} - \overleftarrow{\nabla}_{\underline{\underline{\mathbf{R}}}} \cdot \overrightarrow{\nabla}_{\underline{\underline{\mathbf{P}}}}$$
$$g \exp\Big(\kappa\overleftrightarrow{\Lambda}\Big)f = \sum_{s=0}^{\infty} \frac{\kappa^s}{s!} \sum_{t=0}^{s} (-1)^t \binom{s}{t} \Big[\partial_{\underline{\underline{\mathbf{R}}}}^{s-t}\partial_{\underline{\underline{\mathbf{P}}}}^{t} f\Big] \Big[\partial_{\underline{\underline{\mathbf{R}}}}^{t}\partial_{\underline{\underline{\mathbf{P}}}}^{s-t} g\Big] . \tag{5.3}$$

The last line defines the 'Moyal product' also known as the 'star product' [163]. Up to this point we have made *no assumptions*, meaning that if one is able to calculate Eq.s (5.2) and (5.3) exactly, then the any observable of interest could be calculated via:

$$\langle \hat{O}(t) \rangle = \mathrm{Tr}\left[\int d\underline{\underline{\mathbf{X}}} \hat{\rho}_W(\underline{\underline{\mathbf{X}}}, t)\hat{O}_W(\underline{\underline{\mathbf{X}}})\right]$$
$$= \mathrm{Tr}\left[\int d\underline{\underline{\mathbf{X}}} \hat{\rho}_W(\underline{\underline{\mathbf{X}}})\hat{O}_W(\underline{\underline{\mathbf{X}}}, t)\right], \tag{5.4}$$

where the equation of motion for the Wigner transformed operator is the complex conjugate of Eq. (5.3). Since this is exact it is also as difficult to deal with as the original problem. So we make the first approximation, which is similar in spirit to the Born-Oppnehimer approximation itself. By expressing the Poisson bracket operator Λ, in terms of the ratio of masses between the nuclei and the electrons $\Lambda = (m/M)^{\frac{1}{2}}\Lambda'$, and truncating the Moyal product of $e^{(m/M)^{\frac{1}{2}}\Lambda'}$ at first order, one can arrive at the Quantum-Classical Liouville Equation (QCLE) [164, 165]:

$$i\frac{\partial}{\partial t}\hat{\rho}_W(\underline{\underline{\mathbf{X}}}) = -i[\hat{H}_W, \hat{\rho}_W] + \frac{1}{2}\Big(\{\hat{H}_W, \hat{\rho}_W\} - \{\hat{\rho}_W, \hat{H}_W\}\Big), \tag{5.5}$$

where $\{A(\underline{\underline{\mathbf{X}}}), B(\underline{\underline{\mathbf{X}}})\} = A(\underline{\underline{\mathbf{X}}})\overleftrightarrow{\Lambda} B(\underline{\underline{\mathbf{X}}})$ refers to the normal classical Poisson bracket. This expression has also been shown to be related to 'linearization approaches' such as Linearized

Semi-Classical Initial Value Representation (LSC-IVR) which approximate the path integral representation of the time evolution of an operator [166]. The QCLE and LSC-IVR expressions form a starting point for a large variety of semi-classical dynamics methods, and while in principle Eq. (5.5) can be resolved in an arbitrary electronic basis $|\phi_i\rangle$ and the generalized phase space distributions $\rho_{W,ij}(\underline{\mathbf{X}}) = \langle\phi_i|\hat{\rho}_W(\underline{\mathbf{X}})|\phi_j\rangle$ can be directly propagated on a phase space grid [167], this still scales exponentially with with the number of quantum and classical degrees of freedom [168], meaning that almost all practical integration methods have been based on ensembles of trajectories.

There exists a hierarchy of solutions to the QCLE with regard to the degree of correlation between the electronic and nuclear degrees of freedom. At the highest level of correlation there are direct integration schemes where the electronic degrees of freedom are resolved in the adiabatic (BO) basis and branching ensembles of trajectories transition between surfaces [169]. The computational overhead of this approach is prohibitive, and there are methods like the Generalized Quantum Master Equation (GQME) [170] and its mean field version [171], which retains a finite memory kernel of the quantum-classical interaction to alleviate the complexity. There are also schemes to explicitly entangle otherwise independent trajectories together with a non-local full system-state dependent force [172] and approaches based on further mappings of the electronic system to auxillary variables with such as the Poisson Bracket Mapping Equation [173–175] and the Forward-Backward Trajectory Solution (FBTS) [74, 176, 177] which further disregard some portions of the fully coupled dynamics. Work on novel trajectory based integration schemes is very much on going; for a recent review see [178]. These methods are important because they can serve as a formal framework to understand exactly which components of electron-nuclear correlation are lost as one makes more and more assumptions, and conversely provide inspiration for how to build these back in when starting from the mean-field approach: Multi-trajectory Ehrenfest (MTEF).

5.2 Multi-Trajectory Ehrenfest

Whereas many of the above mentioned methods have been primarily applied to models meant to test non-adiabatic coupling scenarios such as the spin-boson, Su-Schrieffer-Heeger [74], Shin-Metiu, and Tully's models [152], the simplicity of MTEF allows for its use in any model or ab-initio simulation. To derive MTEF equations of motion from the QCLE, one takes the mean field approximation by assuming that the full system can be written as a sum of electron-nuclear correlated (entangled) and uncorrelated (factorizable) parts:

$$\hat{\rho}_W(\underline{\mathbf{X}}, t) = \hat{\rho}_e(t)\rho_{n,W}(\underline{\mathbf{X}}, t) + \hat{\rho}_{corr,W}(\underline{\mathbf{X}}, t). \tag{5.6}$$

The key step is neglecting the contribution of the correlated part in the *dynamics*. Note that while the ensuing dynamics do not explicitly treat the effect of electron-nuclear correlation, the initial state generally *is* correlated, and this can implicitly affect the dynamics. Under this approximation, the electronic density matrix at all times can be written as:

$$\hat{\rho}_e(t) = \text{Tr}_n\left[\hat{\rho}_W(t)\right] = \int d\underline{\mathbf{X}}\hat{\rho}_W(\underline{\mathbf{X}}, t), \tag{5.7}$$

and the nuclear phase space probability distribution is $\rho_n(\underline{\underline{\mathbf{X}}}, t) = \text{Tr}_e[\hat{\rho}_W(\underline{\underline{\mathbf{X}}}, t)]$, where Tr_s refers to the trace over subsystem s. By assuming the system is factorizabile at all times, the equations of motion resulting from the QCLE can be exactly solved via the method of characteristics through a sufficiently large ensemble of independent trajectories $\underline{\underline{\mathbf{X}}}_i$ each sampled from $\rho_{n,W}(\underline{\underline{\mathbf{X}}})$ [179]. Formally this corresponds to $\rho_{n,W}(\underline{\underline{\mathbf{X}}}, t) = \frac{1}{N_t} \sum_i^{N_t} \delta(\underline{\underline{\mathbf{X}}}_i - \underline{\underline{\mathbf{X}}}(t))$, where N_t is the number of trajectories in the ensemble. Each trajectory evolves according to Hamilton's equations of motion generated from the mean-field effective Hamiltonian,

$$\partial_t \underline{\underline{\mathbf{R}}}_i = \frac{\partial H_{n,W}^{Eff}}{\partial \underline{\underline{\mathbf{P}}}_i}, \quad \partial_t \underline{\underline{\mathbf{P}}}_i = -\frac{\partial H_{n,W}^{Eff}}{\partial \underline{\underline{\mathbf{R}}}_i}$$
$$H_{n,W}^{Eff} = H_{n,W}(\underline{\underline{\mathbf{X}}}_i(t)) + \text{Tr}_e\left[\hat{H}_{en,W}(\underline{\underline{\mathbf{X}}}_i(t))\hat{\rho}_e^i(t)\right]. \tag{5.8}$$

Where $H_{n,W}$ and $\hat{H}_{en,W}$ refer to the partially Wigner transformed nuclear and electron-nuclear coupling operators, respectively. The electronic density associated with each trajectory, $\rho_e^i(t)$, evolves according to the following commutator:

$$\frac{d}{dt}\hat{\rho}_e^i(t) = -i\left[\hat{H}_e + \hat{H}_{en,W}(\underline{\underline{\mathbf{X}}}_i(t)), \; \hat{\rho}_e^i(t)\right]. \tag{5.9}$$

With this integration approach calculating the expectation value of observables via Eq. (5.4) becomes:

$$\langle O(t) \rangle = \frac{1}{N_t} \sum_{i=1}^{N_t} \text{Tr}_e\left[\hat{O}_W(\underline{\underline{\mathbf{X}}}_i(t))\hat{\rho}_e^i(t)\right]. \tag{5.10}$$

In summary, to perform an MTEF calculation the only required input is an approximate initial nuclear density matrix $\hat{\rho}_n$, which one then Wigner transforms via Eq. (5.2) to give $\rho_{n,W}$. A key point is that at this stage no constraints have been made on the electronic system. We only require a basis which spans the space of the electronic Hamiltonian, and a particular choice of the initial electronic density matrix in Eq. (5.6). For example in thermodynamic equilibrium at a given temperature T, for a given nuclear configuration $\underline{\underline{\mathbf{X}}}_i$, one could treat the electronic system as being in the canonical ensemble initialized on the BO states:

$$\hat{\rho}_e^i = \frac{1}{Z} \sum_n f(U_n(\underline{\underline{\mathbf{R}}}_i); T) |\Phi_n(\underline{\underline{\mathbf{R}}}_i)\rangle \langle \Phi_n(\underline{\underline{\mathbf{R}}}_i)|, \tag{5.11}$$

where $f(E; T)$ is the Fermi-Dirac distribution, and Z is the partition function. We utilize such an approach in paper III. The electronic system can also be initialized in a non-equilibrium configuration, in either case the steps to performing an MTEF calculation are:

1. Sample $\{\underline{\underline{\mathbf{X}}}_i(0)\} \sim \rho_{n,W}$, and for each $\underline{\underline{\mathbf{X}}}_i$ initialize $\hat{\rho}_e^i(0)$.

2. Propagate $\hat{\rho}_e^i(t)$ and $\underline{\underline{\mathbf{X}}}_i(t)$ simultanesouly according to Eq. (5.9) and Eq. (5.8). This can be done for example with Runge-Kutta integration for the electronic degrees of freedom alongside Velocity Verlet for $\underline{\underline{\mathbf{X}}}$. For pure electronic states Eq. (5.9) can of course be replaced by the Schrödinger equation.

3. Calculate observables at each desired time step. Since the trajectories are completely independent, each contribution on the right hand side of Eq. (5.10) can be calculated and

stored in parallel and post-processed.

Given the exponential scaling at the root of why we've come to this approximated method in the first place, in general it's unreasonable to expect that one will be able to produce an initial nuclear state which takes into account coupling with electronic system at all orders of interaction. When available and applicable, one can in principle take the BO vibrational states $|\chi_{n\nu}\rangle$, which of course encode the effects of the electronic state up to the adiabatic approximation via the BOPES. However, one can also get a low order approximation to the BOPES through a harmonic approximation around the lowest energy configuration. This of course leads to the normal mode decomposition, where the nuclear configuration space (for 3 Cartesian dimensions) $\underline{\underline{\mathbf{R}}} \in \mathbb{R}^{3N_n}$ is linearly transformed to the (non-translational, non-rotational) normal mode coordinates $\underline{\underline{\mathbf{Q}}}(\underline{\underline{\mathbf{R}}}) \in \mathbb{R}^{3N_n-6}$. Each normal mode can be treated as an independent quantum harmonic oscillator (QHO), giving the initial nuclear state as:

$$\chi_\nu(\underline{\underline{\mathbf{R}}}) \approx \chi_1(Q_1) \otimes \ldots \otimes \chi_{3N_n-6}(Q_{3N_n-6}). \tag{5.12}$$

The Wigner transform of the quantum harmonic oscillator, its excited states and temperature dependence is well known [162, 180] and require only the harmonic frequency as input, a quantity that is easy to calculate for arbitrary (non-floppy) systems using Density Functional Perturbation Theory.

There are many paths to the equations of motion (5.9) and (5.8) [181, 182], and subsequently there is confusion throughout the literature as to what 'Ehrenfest dynamics' means. Oftentimes, the term Ehrenfest is used when initializing the nuclear degrees of freedom in the equilibrium geometry with zero velocity or taking an arbitary displacement of the nuclei [183]. As we demonstrate in paper II and paper III, the former choice (Single Trajectory Ehrenfest – STEF) generally fails to account for the effects of the nuclear subsystem on the electronic system, while the latter leads to strong artifacts in the spectrum. Despite the manner in which they're used, the Ehrenfest equations of motion are ubiquitous in real time dynamics literature, having been implemented with the electronic system treated through Hartree-Fock [184], CASSCF [185], TDDFT [186–190], tight-binding TDDFT [191] and NEO theory [192] to name a few. Thus the MTEF algorithm can be adapted across the ab-initio real time dynamics community at the cost of running a series of trajectories in parallel rather than just a single one as is often done.

5.3 Scientific Contribution and Outlook

In paper II we explore the application of MTEF when the electronic system is treated through a real-space basis using both an H_2, and in the real-space real-time TDDFT code Octopus [82]. We calculated the vibronic absorption of the H_2 model and the benzene molecule with TDDFT, utilizing an non-perturbative real-time dynamics approach via an instantaneous electic field or 'kick':

$$\mathbf{E}(t) = \kappa\delta(t - 0^+). \tag{5.13}$$

Being instantaneous in time, this electric field has uniform spectral weight, thereby inducing an electronic transition to every allowed electronic state instantaneously. By setting the field strength $\kappa << 1$ [a.u.] we restrain the response to be in the linear regime, though this can

also be used to study non-linear response properties by increasing the magnitude of κ [193]. This method has been used in real time dynamics to study the out-of-equilibrium response of systems since at least the 70s in nuclear dynamics [194], and has been a standard technique for calculating spectra in TDDFT since 1996 [65].

In paper **II** we demonstrate that by including the quantized nuclear subsystem through MTEF, the electronic absorption spectra is split and demonstrates vibronic peaks, which as explained in section 3.2.1 is usually attributed to quantized vibronic states. We also demonstrate that ICWF, being a more strongly correlated method, can capture this effect with greater numerical accuracy. Throughout the paper and the SI we systematically study the origin of the defects in the MTEF spectral lines in the H_2 model and subsequently found that as a consequence of exciting the system perturbatively while using mean field forces, the dominant contribution to the nuclear forces comes from the initial electronic state. Thus the spacing of the vibronic peaks corresponds to the vibrational states of the initial electronic surface, rather than the target electronic state. Naturally this implies that with strong driving and similar BOPESs between excited states, the MTEF results will become more quantitatively accurate, which we demonstrate in the SI. We conclude the paper with a calculation of the vibronic absorption spectrum of the benzene molecule, finding significant reweighting of the spectrum with regards to STEF and making a qualitatively better agreement with experiment.

Paper **II** conclusively demonstrated that treating the electronic system quantum mechanically in the real-space basis and nuclear subsystem via MTEF can capture nuclear quantization effects arising from dynamical interactions between the electronic and nuclear subsystems. We demonstrated that by introducing methods which account for dynamical correlation the accuracy can be improved, giving motivation for incorporating methods from the hierarchy of QCLE approaches into the real-space representation. Finally we showed that, being a mean field method, the degree of error in MTEF is proportional to the degree to which the forces of the nuclear subsystem change upon reorganization of the electronic configuration. For molecules such as H_2 or benzene, given the small number of electrons in the system, it's reasonable to expect that the character of forces on the nuclear subsystem would be highly sensitive to rearrangements of the electronic structure.

Thus for extended systems it's also reasonable to expect that the character of forces on the ionic system would be relatively unperturbed by modest excitation densities. Given that the electronic system in the real-space basis can capture any excited state properties (up to the grid spacing), alongside the fact that MTEF scales favorably with system size, allows for dynamic rearrangement of nuclei, and can be easily integrated into existing simulation workflows, this method offers a promising intersection of capabilities to simulate non-equilibrium phenomena. Thus in paper **III** we extend MTEF to periodic systems, and return to the question of the effects of static disorder vs dynamics in the context of the system response to strong laser driving.

Simulating Vibronic Spectra without Born−Oppenheimer Surfaces

Kevin Lively, Guillermo Albareda, Shunsuke A. Sato, Aaron Kelly,* and Angel Rubio*

ACCESS | Metrics & More | Article Recommendations | Supporting Information

ABSTRACT: We show how linear vibronic spectra in molecular systems can be simulated efficiently using first-principles approaches without relying on the explicit use of multiple Born−Oppenheimer potential energy surfaces. We demonstrate and analyze the performance of mean-field and beyond-mean-field dynamics techniques for the H_2 molecule in one dimension, in the later case capturing the vibronic structure quite accurately, including quantum Franck−Condon effects. In a practical application of this methodology we simulate the absorption spectrum of benzene in full dimensionality using time-dependent density functional theory at the multitrajectory Ehrenfest level, finding good qualitative agreement with experiment and significant spectral reweighting compared to commonly used single-trajectory Ehrenfest dynamics. These results form the foundation for nonlinear spectral calculations and show promise for future application in capturing phenomena associated with vibronic coupling in more complex molecular and potentially condensed phase systems.
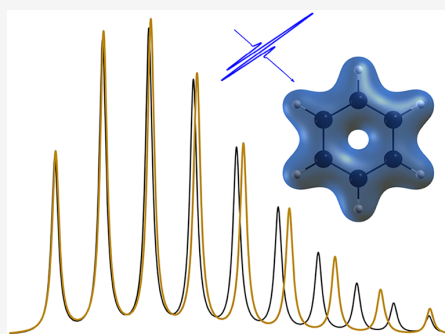
Simulating vibronic effects from first-principles calculations is one of the central goals in theoretical spectroscopy that has implications in chemistry, physics, and materials science. The involvement of nuclear vibrational quantum states during electronic transitions plays a decisive role in determining the spectral features associated with these processes. This has been well-established by the utility of the Franck−Condon principle, for example, which represents an early paradigm for the role of nuclear quantum effects in electronically nonadiabatic processes. Describing this interplay between the electronic and vibrational degrees of freedom requires a quantum mechanical description that is both accurate and scalable to relatively large system sizes. One popular method to calculate vibronic spectra is to take a sum-over-states approach, where matrix elements of the transition operators between the states involved in generating the desired spectral signal are constructed. In this approach the states of interest can be represented using the Born−Oppenheimer (BO) basis; one must already have some *a priori* knowledge of the BO states that are involved, along with the associated potential energy surfaces and nonadiabatic couplings.

An alternative strategy to summing over states in the BO basis is to take a coordinate space perspective and construct the response function for the system of interest from direct time-propagation of the system in that picture.[1,2] This invariably requires some level of approximation in the representation dynamics of the electronic and nuclear degrees of freedom, with different consequences for their coupling depending on the method chosen. The mixed quantum−classical Ehrenfest approach is a practical approximation to the fully quantum mechanical dynamics of the system, and despite

its approximate *dynamics*, provides a formally exact representation of the quantum *equilibrium* structure of the correlated electronic and vibrational degrees of freedom via a multitrajectory Ehrenfest (MTEF) simulation through the use of the Wigner representation.[3−5] In this case, the Wigner transform maps the vibrational quantum states onto phase space distributions of continuous position and momentum coordinates which can be sampled by an appropriate Monte Carlo procedure to capture the quantum equilibrium structure of the problem. The limitations of the Ehrenfest approach and other independent trajectory semiclassical methods are well-known,[6−10] and while there have been many attempts to ameliorate these shortcomings, with some exceptions,[11,12] most rely on the BO framework in their implementation.[13−17]

In this work we take a different approach to go beyond mean-field theory based on the recently introduced interacting conditional wave function (ICWF) formalism, which is able to capture correlated electronic and nuclear dynamics.[18−21] We apply MTEF and ICWF dynamics to an exactly solvable one-dimensional H_2 model and show that these methods are able to recover electron−nuclear correlations in linear vibronic spectra *without the need to calculate multiple BO surfaces*. In addition, we show that the MTEF method can be easily extended to *ab initio* nonadiabatic molecular dynamics

simulations by calculating the vibronic spectra for benzene, where we find good agreement with experimental results.

The linear spectrum of a system is given by the Fourier transform of time correlation function (TCF) $C_{AB}(t) = \langle [\hat{A}(t), \hat{B}] \rangle$ of the transition dipole operator, $\hat{\mu}$, $C_{\mu\mu}(t) = \langle \hat{\mu}(t)\hat{\mu}(0) \rangle$[1,22] (unless otherwise stated all expressions are in atomic units):

$$I(\omega) = \frac{4\pi\omega}{3c} \int_{-\infty}^{\infty} dt \, e^{i\omega t} \langle [\hat{\mu}(t), \hat{\mu}] \rangle$$
$$= \frac{8\pi\omega}{3c} \Re \int_{0}^{\infty} dt \, e^{i\omega t} Tr(\hat{\mu}(t)\hat{\rho}_{eq}\hat{\mu}(t=0)) \quad (1)$$

where the trace occurs over nuclear and electronic degrees of freedom; $\hat{\rho}_{eq}$ is the equilibrium density matrix for the coupled system, and we evolve $\hat{\mu}(t)$ in the Hilbert representation. Traditionally, vibronic spectra are explained by invoking the Franck−Condon approximation in the BO picture, where the electronic system is instantly excited, thus promoting the unperturbed ground-state nuclear system to a different electronic surface. If one has access to the electronic states involved in a particular spectral range then the contributions to the spectrum due to each electronic transition can be identified by resolving the transition dipole operator in the basis of the electronic states of interest, and the vibronic side peaks of that transition can be calculated by propagating the initial state's nuclear subsystem under the effect of the nonequilibrium electronic occupation. When it is feasible to resolve the nuclear wave function dynamics, this can be one of the most accurate methods of calculating molecular vibronic spectra.[23,24]

Although resolving eq 1 in the BO framework is a powerful analysis tool, it is computationally impractical for systems with many nuclear degrees of freedom, particularly when one desires spectra over multiple surfaces. One can bypass this computational bottleneck by representing the system in a real space basis and using the "δ-kick" method,[25] which captures electronic transitions to all dipole-transition allowed states (resolved on the grid) within a single calculation by utilizing the dipole response to a perturbative, but impulsive external field $H_{field} = E(t)\hat{\mu}$, with $E(t) = \kappa\delta(t)$ and $\kappa \ll 1$. Using first-order perturbation theory, the dipole response $\langle \Delta\mu(t) \rangle = \langle \mu(t) \rangle - \langle \mu(0) \rangle$ can be written in powers of the field[1,2]

$$\langle \Delta\mu(t) \rangle = iTr([\hat{\mu}^I(t), \hat{\mu}^I(0)]\hat{\rho}_{eq})\kappa + O(\kappa^2) \quad (2)$$

where $\hat{\mu}^I(t)$ is evolved in the interaction representation. Hence, the linear response spectra may also be obtained via the relation

$$C_{\mu\mu}(t) = \frac{-i}{\kappa} \langle \Delta\mu(t) \rangle \quad (3)$$

provided the strength of the perturbing field, κ, is sufficiently small. This δ-kick approach requires only the initial state of the full system as input, followed by time propagation for a sufficient duration so as to obtain the desired energy resolution. Importantly, this technique can also serve as a foundation for calculating nonlinear optical response spectra.[26]

While the methods described above are formally equivalent, differences between the calculated spectra can arise when approximations are made. Here we briefly describe two methods for performing coupled electron nuclear dynamics simulations: the quantum−classical mean-field MTEF method and the ICWF formalism, which was designed to go beyond the mean-field limit.

A typical approach to Ehrenfest theory is to assume a separable electronic−nuclear wave function ansatz, take the classical limit of the nuclear portion, and initialize the nuclei at the equilibrium position with zero nuclear momentum.[27,28] This single-trajectory Ehrenfest (STEF) method is often employed when a mixed quantum−classical method is needed to couple electronic and nuclear dynamics,[29] in some cases providing a stark difference in electronic dynamics compared to fixed nuclei.[30,31] Although attempts at capturing quantized vibrational effects in STEF with the δ-kick method have been made,[32] they can contain unphysical spectral features (see the Supporting Information) which make them unsuitable for application to nonlinear spectra

An alternative route to Ehrenfest is also possible in the density matrix picture and proceeds via the quantum−classical Liouville equation.[33] The major difference is that this representation results in a *multitrajectory Ehrenfest* picture of the dynamics, where the initial quantum statistics of the correlated system can, in principle, be captured exactly. Here, we outline the evolution equations, and we offer more details in the Supporting Information. The time evolution of the reduced electronic density is

$$\frac{d}{dt}\hat{\rho}_e(t) = -i[\hat{H}_{e,W}^{Eff}(\mathbf{X}(t)), \hat{\rho}_e(t)] \quad (4)$$

where the subscript W refers to the partial Wigner transform over the nuclei; $\mathbf{X} = (\mathbf{R}, \mathbf{P})$ is a collective variable for the nuclear position $\mathbf{R}$ and momentum $\mathbf{P}$, and the effective electronic mean-field Hamiltonian is $\hat{H}_{e,W}^{Eff}(\mathbf{X}(t)) = \hat{H}_e + \hat{H}_{en,W}(\mathbf{X}(t))$, where $\hat{H}_e$ refers to the electronic portion of the Hamiltonian and $\hat{H}_{en}$ to the electron nuclear coupling. The nuclear dynamics is represented as an ensemble of N independent Wigner phase-space trajectories, $\rho_{n,W}(\mathbf{X},t) = 1/N\sum_i^N \delta(\mathbf{X}_i - \mathbf{X}_i(t))$, that evolve according to Hamilton's equations of motion generated from the effective nuclear mean-field Hamiltonian

$$\frac{\partial \mathbf{R}_i}{\partial t} = \frac{\partial H_{n,W}^{Eff}}{\partial \mathbf{P}_i}, \frac{\partial \mathbf{P}_i}{\partial t} = -\frac{\partial H_{n,W}^{Eff}}{\partial \mathbf{R}_i}$$
$$H_{n,W}^{Eff} = H_{n,W}(\mathbf{R}_i(t)) + Tr_e(\hat{\rho}_e(t)\hat{H}_{en,W}(\mathbf{X}_i(t))) \quad (5)$$

The average value of any observable, $\langle O(t) \rangle$, can then be written as

$$\langle O(t) \rangle = Tr_e \int d\mathbf{X} \hat{O}_W(\mathbf{X}, t)\hat{\rho}_W(\mathbf{X}, 0) \quad (6)$$

which can be evaluated by sampling initial conditions from $\hat{\rho}_W(\mathbf{X},0)$ and evolving the expectation value of the observable according to the above equations of motion. Using this dynamics method in conjunction with the BO basis representation to evaluate eqs 1 and 4−6 ultimately leads to the following equations of motion, with sums over BO states denoted by a (see the Supporting Information for details)

$$\partial_t \rho_e^{aa'} = -i\rho_e^{aa'}(t)(\epsilon_a(\mathbf{R}_i(t)) - \epsilon_{a'}(\mathbf{R}_i(t)))$$

$$+ \sum_{a''} \frac{\mathbf{P}_i(t)}{M}(\rho_e^{aa''}(t)d_{a''a'}^i(t) - d_{aa''}^i(t)\rho_e^{a''a'}(t))$$

$$\partial_t \mathbf{R}_i(t) = \mathbf{P}_i(t)/M$$

$$\partial_t \mathbf{P}_i(t) = \sum_a -\partial_\mathbf{R}\epsilon_a(\mathbf{R}_i(t))\rho_e^{aa}(t)$$

$$+ \sum_{aa'} \Re[(\epsilon_a(\mathbf{R}_i(t))d_{aa'}^i(t) - \epsilon_{a'}(\mathbf{R}_i(t))d_{a'a}^i(t))\rho_e^{a'a}(t)]$$

$$\partial_t \mu_W^{aa'}(\mathbf{R}_i(t)) = i\mu_W^{aa'}(\mathbf{R}_i(t))(\epsilon_a(\mathbf{R}_i(t)) - \epsilon_{a'}(\mathbf{R}_i(t)))$$

$$(7)$$

where $\epsilon_a(\mathbf{R})$ are the BO surfaces and $d_{aa'}$ are the nonadiabatic coupling vectors (NACVs) between states a and a'.

In contrast to the previous expression, utilizing MTEF in the real space δ-kick approach requires initializing the electronic wave function as the BO eigenstate for each initially sampled nuclear geometry. The δ-kick is applied and the electronic wave function is propagated using the time-dependent Schrödinger equation equivalent to eq 4 alongside the nuclei according to eq 5. Calculating the spectrum via MTEF dynamics in the BO picture is from here on referred to as MTEF-BO, and calculating it via the δ−kick method is referred to as MTEF-kick.

Moving beyond semiclassical dynamics, the formally exact CWF method and its practical ICWF implementation are recently developed methods which have shown to be able to capture nonequilibrium correlated nuclear−nuclear and electron−nuclear phenomena beyond the mean-field limit.[18−21] This approach is based on taking single-particle slices (the CWFs) of the time-dependent wave function of the full system; approximating the equations of motion for these CWFs by the Hermitian components of the sliced Hamiltonian; and finally, in the ICWF extension, utilizing these electron−nuclear CWFs as a basis of Hartree products in a wave function ansatz.

Here we describe an implementation of this approach utilizing the static and time-dependent variational principles for the expansion coefficients in a *static* CWF basis. The basis is chosen via sampling electronic and nuclear positions $(\mathbf{r}^\alpha, \mathbf{R}^\alpha)$, $\alpha \in \{1,\cdots,N_c\}$, where $\mathbf{r}$ and $\mathbf{R}$ are understood to be collective position variables, from initial guesses to the electronic and nuclear densities. These are used to construct the Hermitian limit of the CWF propagators[18]

$$h_e^\alpha(\mathbf{r}_i) = -\frac{1}{2}\nabla_{\mathbf{r}_i}^2 + \sum_{j\neq i}^{N_e} V_{ee}(\mathbf{r}_i, \mathbf{r}_j^\alpha) + \sum_l^{N_n} V_{en}(\mathbf{r}_i, \mathbf{R}_l^\alpha)$$

$$h_n^\alpha(\mathbf{R}_l) = -\frac{1}{2M_l}\nabla_{\mathbf{R}_l}^2 + \sum_j^{N_e} V_{en}(\mathbf{R}_l, \mathbf{r}_j^\alpha) + \sum_{m\neq l}^{N_n} V_{nn}(\mathbf{R}_l, \mathbf{R}_m^\alpha)$$

$$(8)$$

for a system with N_e electrons and N_n nuclear degrees of freedom. Taking eigenstates of $h_e^\alpha(\mathbf{r}_i)$ and $h_n^\alpha(\mathbf{R}_l)$, denoted $\phi^\alpha(\mathbf{r}_i)$ and $\chi^\alpha(\mathbf{R}_l)$. respectively, as our (static) CWF basis we write the following single-index, multiconfigurational, mixed-species, wave function ansatz:

$$\Psi(\mathbf{r}, \mathbf{R}, t) = \sum_\alpha^{N_c} C_\alpha(t) \prod_i^{N_e} \phi^\alpha(\mathbf{r}_i) \prod_l^{N_n} \chi^\alpha(\mathbf{R}_l)$$

$$(9)$$

where we have taken a Hartree product of electronic and nuclear CWFs for each degree of freedom. While the Hartree product over electronic degrees of freedom and a single expansion index has been sufficient for accuracy in applications of ICWF so far, this ansatz can in principle be trivially extended to a multi-index expansion and to have Fermionic antisymmetry via inclusion of Slater determinants. We then utilize the Dirac−Frenkel variational procedure[34−36] to develop equations of motion for $\vec{C}(t)$, which leads to the following standard evolution equation for the expansion coefficients of a nonorthogonal static basis:

$$\frac{d}{dt}\vec{C} = -i\mathbf{S}^{-1}\mathbf{H}\vec{C}$$

$$(10)$$

where

$$\mathbf{S}_{\alpha\beta} = \prod_i^{N_e} \int d\mathbf{r}_i(\phi^\alpha(\mathbf{r}_i))^*\phi^\beta(\mathbf{r}_i) \prod_l^{N_n} \int d\mathbf{R}_l(\chi^\alpha(\mathbf{R}_l))^*\chi^\beta(\mathbf{R}_l)$$

$$\mathbf{H}_{\alpha\beta} = \prod_i^{N_e} \prod_l^{N_n} \int d\mathbf{R}_l d\mathbf{r}_i(\phi^\alpha(\mathbf{r}_i)\chi^\alpha(\mathbf{R}_l))^*\hat{H}(\mathbf{r}, \mathbf{R})\phi^\beta(\mathbf{r}_i)\chi^\beta(\mathbf{R}_l)$$

for the full molecular Hamiltonian $\hat{H}$.

While the general form of this wave function ansatz is not unique, the mixed-species CWF basis treats the electronic and nuclear subsystems on an equal footing without relying on any adjustable parameters, using the Hermitian limit of the solutions to the conditionalized time-independent Schrödinger equations.

The ground-state wave function is obtained from this approach using imaginary time evolution,[37,38] and the δ-kick spectra (ICWF-kick) is calculated by applying the perturbative field to the CWFs at time zero and recalculating the $\mathbf{S}$ and $\mathbf{H}$ matrices, equivalent to propagating in the interaction representation. In practice, $\mathbf{S}$ may be nearly singular, but its inverse can be approximated by the Moore−Penrose pseudoinverse.[39] This "closed-loop" of initial state preparation and time-propagation ensures that our ICWF approach is a fully self-consistent method that increases in accuracy with increasing N_c and requires no BO state information.

To investigate the performance of the MTEF and ICWF approaches to vibronic spectral lineshapes we studied the vibronic transitions in an exactly solvable one-dimensional model system for molecular hydrogen.[40−42] The total Hamiltonian can be written in the center of mass frame in atomic units as

$$\hat{H}(r_1, r_2, R) = -\frac{\partial_R^2}{2\mu_n} - \sum_{i=1}^2 \frac{\partial_{r_i}^2}{2\mu_e} + \frac{1}{\sqrt{(r_1 - r_2)^2 + 1}} + \frac{1}{R}$$

$$- \sum_{i=1}^2 \left(\frac{1}{\sqrt{\left(r_i + \frac{1}{2}R\right)^2 + 1}} + \frac{1}{\sqrt{\left(r_i - \frac{1}{2}R\right)^2 + 1}} \right)$$

$$(11)$$

where $\mu_n = m_p/2$ and $\mu_e = 2m_p/(2m_p + 1)$ are the reduced nuclear and electronic masses; R is the internuclear separation, and r_i are the electronic positions. We take the proton mass to be $m_p = 1836$. The electronic and nuclear degrees of freedom were each resolved on grids for the numerically exact solution and ICWF-kick approaches, while the MTEF-kick electronic wave functions were time-evolved on the (r_1, r_2) grid, and the
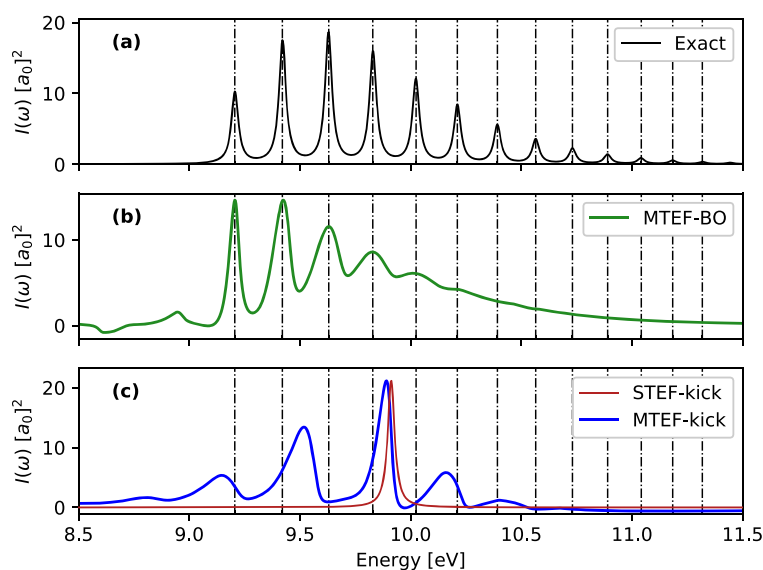
Figure 1. 1D H_2, $S_2 \leftarrow S_0$ spectra calculated via the MTEF-TCF, MTEF-kick, and STEF-kick approaches, with the exact peak placements overlaid as dashed vertical lines. Spectral cross sections are reported in square Bohr radii a_0^2. For clarity the STEF-kick spectrum has been multiplied by a factor of 0.175 to match the scale of the MTEF-kick results.
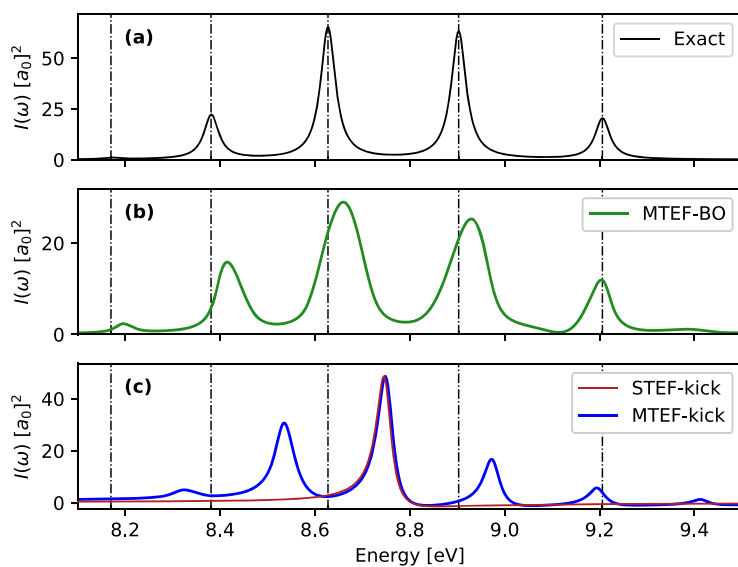
Figure 2. $S_0 \leftarrow S_2$ spectra compared between the MTEF-TCF, MTEF-kick, and STEF-kick approaches, with exact peak placement overlaid as dashed vertical lines. MTEF nuclear initial conditions are sampled from the lowest-lying vibrational state on S_2. The sign of all spectra here is inverted for ease of comparison to other figures, and for legibility the STEF-kick spectrum was multiplied by a factor of 0.4 to match the MTEF-kick spectra maximum.

MTEF-BO information was calculated by solving the electronic subsystem across the nuclear grid; see Computational Methods for more details. A kick strength of $\kappa = 10^{-4} a_0^{-1}$. was sufficient to generate the kick spectra within the linear response regime and, unless otherwise stated, a total propagation time of 10 000 au $\approx$ 242 fs was used to generate the spectra.

In Figure 1 we show mean-field spectra calculated both with (MTEF-BO) and without (MTEF-kick) the use of multiple BO surfaces for the absorption from S_0 to S_2 in comparison with the numerically exact results. We see that in the BO

picture the MTEF method recovers the vibronic absorption peak placement quite accurately for the first five peaks, with a broadening occurring for the higher-energy peaks that leads to a loss of structure. This broadening of the spectral signal is due to the well-known fact that the MTEF dynamics does not preserve the correct quantum statistics and thus cannot fully capture the electron−nuclear correlation in the problem (see the Supporting Information for a detailed discussion of this issue). The prepeak features in Figure 1b are also unphysical artifacts of MTEF. The MTEF-BO spectra were converged to within graphical accuracy using $N = 50\,000$ trajectories,
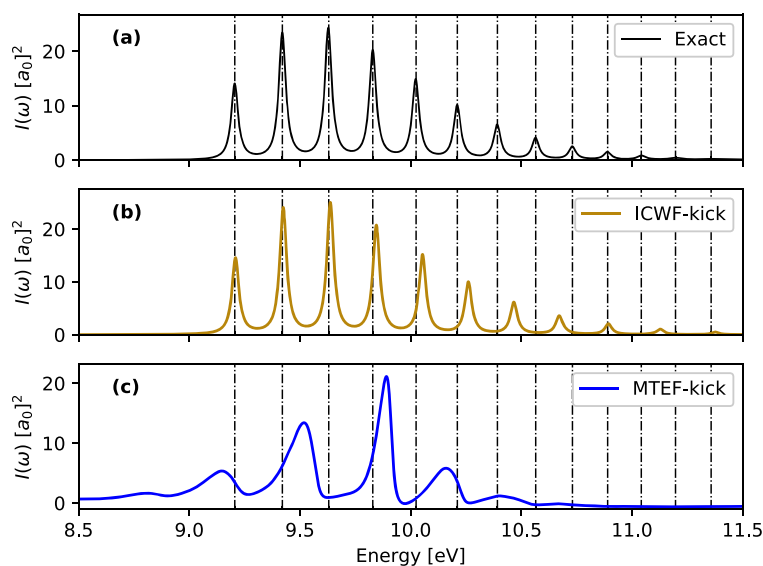
Figure 3. $S_2 \leftarrow S_0$ spectra of the ICWF-kick and MTEF-kick methods, with the exact peak placement overlaid as dashed lines.
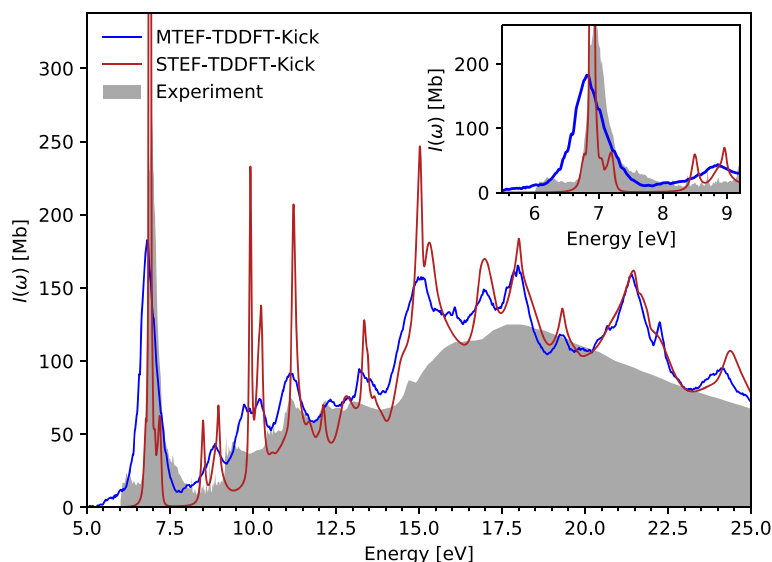

Figure 4. Experimental vibronic spectra for the lowest-lying optical transitions of benzene[46] compared to the MTEF and STEF kick spectra calculated with TDDFT.

although an ensemble size of approximately $N = 500-1000$ also yields reasonable results.

Focusing on the MTEF-kick results in Figure 1c, we see that this approach recovers vibronic side peak structures again without any BO surface information, albeit with inaccurate spacing, while STEF-kick captures only the vertical electronic transition from the minimum of the S_0 surface. The average peak spacing in the MTEF-kick spectra is approximately 0.32 eV; this corresponds remarkably well with the natural frequency of the harmonic approximation to the ground-state surface expanded around the equilibrium geometry, which is also 0.32 eV in this case. This result is unsurprising as the electronic kick induces a very small population transfer to the upper surface proportional to the square of the kick strength,

which results in the mean forces on the nuclei in MTEF-kick essentially corresponding to those of the initial state.

The influence of the initial state on the MTEF-kick spectra is further demonstrated by analyzing the emission spectra in Figure 2. The initial state here was chosen by hand as the lowest-lying nuclear state on the S_2 surface. Once again we see that MTEF-BO recovers the peak placement quite well, while the MTEF-kick data has a less accurate vibronic spacing. Fitting the MTEF-kick peaks, we find an excellent correspondence between mean spacing of the five lowest-energy MTEF peaks and the excited surface natural frequency of 0.21 eV. Although the nuclear dynamics within MTEF-kick are primarily governed by the properties of the initial electronic state, the electron−nuclear coupling modulates the electronic linear response in a nontrivial manner, fundamen-

tally changing the system response calculation compared to simply averaging the electronic transition properties over the equilibrium nuclear configuration, as is done in the nuclear ensemble approach[43] (see the Supporting Information).

For ICWF-kick, we found that N_c = 4096 and mixing the three lowest-energy CWF eigenstates in roughly equal proportion was sufficient to obtain quite accurate results. In Figure 3 we demonstrate that the ICWF ansatz used in a variational context achieves a much more accurate vibronic spacing than the MTEF-kick approach, without the failing of peak broadening or unphysical spectral negativity apparent in the MTEF-BO results. The accuracy of these results underscores that the ICWF ansatz is a robust framework to capture the electronic and vibronic quantum dynamics, being accurate for not only the electron−nuclear correlation inherent to vibronic spectra but also the electronic subsystem itself, which in the MTEF results was solved exactly either on a grid or using explicit BO state information. The deviation from the exact results does grow with increasing energy, although this is ameliorated with increasing N_c and can in principle be eliminated at large enough values of N_c (see the Supporting Information).

Finally we demonstrate the application of MTEF-kick to real 3D molecular systems using the *ab initio* Octopus[44] real-space time-dependent density functional theory (TDDFT)[45] package to calculate the linear vibronic MTEF-kick spectra of benzene. The initial conditions for the nuclear subsystem were obtained by calculating the normal-mode frequencies and dynamical matrix of the molecule and sampling Wigner transforms of the ground-state wave functions in the harmonic approximation (see the Supporting Information for more details). The adiabatic-LDA functional was used, along with norm-conserving Troullier−Martins pseudopotentials, and the trajectories were evolved for $201 \frac{\hbar}{\mathrm{eV}} \approx 132$ fs with a time step of $\Delta t = 0.0015 \frac{\hbar}{\mathrm{eV}} \approx 1$ as. A kick strength of $\kappa = 5 \times 10^{-3}$ Å^{-1} was used to generate the kick spectra within the linear response regime in this case, and the graphical convergence of the MTEF results was found to be achieved with N = 500 trajectories.

In Figure 4, we compare the MTEF-TDDFT-kick results, its STEF-TDDFT-kick counterpart, and gas-phase experimental data.[46] There is remarkably good agreement across the wide energy range available from experiment, before molecular dissociation pathways become available around 13.8 eV. Again, this full linear absorption spectrum is obtained without resorting to the calculation of individual transitions between states as would be required in a BO-state-based calculation. Principally, there is a significant spectral reweighting between STEF and MTEF below 17.5 eV, above which the electronic density of states is so high as to obscure the difference between the two methods. In the inset of Figure 4, in the 7 eV region corresponding to the energy range of the doubly degenerate, dipole-allowed $^1E_{1u} \leftarrow {}^1A_{1g}$, $\pi^* \leftarrow \pi$ transition,[31,47,48] the STEF spectral weight is distributed across a much wider energy range in the MTEF signal, encompassing the experimental bands from 6 to 8 eV. The two STEF peaks at 8.5 and 8.95 eV are also spread across the 8−9 eV range. It is reasonable to expect that the broadening of the MTEF signal relative to the experimental signal is due to the effects discussed above that arise because of the mean-field treatment. In the Supporting Information we also compare these results to the broadening

from the nuclear ensemble average calculation of the spectrum and find good agreement, given the high density of electronic states and many nuclear degrees of freedom in this system. By comparison with the standard STEF dynamics results used in large *ab initio* simulations, we see that utilizing multiple trajectories with equilibrium quantum nuclear statistics fundamentally changes the properties of the spectrum.

We have demonstrated that semiclassical MTEF simulations can capture vibronic structure with the correct spectral sign in the region of the transition. Moreover, we have shown how this can be achieved without using multiple BO surfaces via the δ-kick method and that the vibronic spacing calculated with the MTEF-kick approach matches the profile of the initial state. We have shown that utilizing a dynamics method that can accurately capture the correlated electron−nuclear dynamics, such as the ICWF method, in tandem with the δ-kick approach allows one to accurately recover the vibronic spectra. Finally, we demonstrated that MTEF-kick is easily applied to *ab initio* molecular systems by simulating the vibronic spectra of benzene and finding good agreement to experimental results.

These linear response results establish a solid basis for further investigations into nonlinear response of field driven molecular systems utilizing the practical and efficient MTEF and ICWF techniques along with *ab initio* electronic structure methods. Work in preparation by the present authors also explores the utility of ICWF with electron−electron and electron−nuclear correlated systems and explores the response of these systems under nonperturbative electric fields. Furthermore, we expect that MTEF-kick will improve in accuracy for periodic systems, as changes in the electronic configuration are often to likely produce smaller changes in the nuclear forces than in molecular hydrogen. This makes this method interesting to pursue in periodic systems in particular, where there is a dearth of theoretical frameworks for *ab initio*, nonpertubative electron−nuclear coupling.[49] Work in this direction is in progress, as is the implementation of the ICWF method within an *ab initio* framework for molecular and periodic systems.

■ COMPUTATIONAL METHODS

In the 1D H$_2$ model, the electronic coordinates are each resolved on a $65a_0$ wide interval with spacing of $0.6a_0$, while the nuclear grid extends to $R_{\max} = 6.3125a_0$ with $0.0625a_0$ spacing. Quadratic complex absorbing potentials were also added to the Hamiltonian to prevent reflection from the simulation box edge (see the Supporting Information). To generate the exact results we evolved the full wave function under the δ-kick on the three-dimensional electron−nuclear grid, while for MTEF-kick, the electronic subsystem's Schrödinger equation, dependent on $\mathbf{R}_i(t)$, was solved exactly on the two-dimensional electronic grid for each trajectory. All wave functions were time-propagated using a fourth-order Runge−Kutta integration scheme with a time-step size of Δt = 0.05 au. For the MTEF trajectories, the nuclear degree of freedom was propagated via a velocity Verlet type scheme with the same time-step size.[50] An exponential damping mask function $\exp(-\gamma t)$ was applied to all time-dependent signals in the Fourier transform, and the damping factor was set to damp the signal to 0.1% of its strength at the final time.

For the 1D H$_2$ MTEF-BO results, the potential energy surfaces $\epsilon_a(R)$ and $\mu_W^{aa'}(R)$ were calculated on a nuclear grid with $\Delta R = 0.02a_0$ up to $R_{\max} = 8a_0$, fit to a cubic spline function, and interpolated every $0.01\Delta R$. The NACV between

S_0 and S_2 in this model is numerically zero. These quantities were resolved for the first allowed dipole transition, between the ground state (S_0) and the second excited state (S_2), and the results were found to be well converged within about 5×10^4 trajectories.

For the MTEF-TDDFT-kick simulations we used a real space grid formed from overlapping spheres of radius 8 Å centered on the initial positions of the nuclei, with an isotropic grid spacing of 0.16 Å, which was found to be sufficient to converge the energies of the lowest-lying absorption lines. The reported results were calculated on a hyperthreaded 16 CPU core Xeon E5-2698 v3 requiring approximately 880 core hours per trajectory. Being composed of independent trajectories the cost of the MTEF method over the STEF simulation scales linearly with the number of trajectories, requiring approximately 440 000 core hours for graphical convergence at 500 trajectories.

ASSOCIATED CONTENT

Ⓢ Supporting Information

The Supporting Information is available free of charge at https://pubs.acs.org/doi/10.1021/acs.jpclett.1c00073.

> Details on MTEF, STEF, and ICWF as referenced in the main text (PDF)

AUTHOR INFORMATION

Corresponding Authors

Aaron Kelly − *Max Planck Institute for the Structure and Dynamics of Matter and Center for Free-Electron Laser Science, 22761 Hamburg, Germany; Department of Chemistry, Dalhousie University, Halifax B3H 4R2, Canada;* Email: aaron.kelly@mpsd.mpg.de

Angel Rubio − *Max Planck Institute for the Structure and Dynamics of Matter and Center for Free-Electron Laser Science, 22761 Hamburg, Germany; Nano-Bio Spectroscopy Group and ETSF, Universidad del País Vasco, 20018 San Sebastián, Spain; Center for Computational Quantum Physics (CCQ), Flatiron Institute, New York 10010, United States;* ⓞ orcid.org/0000-0003-2060-3151; Email: angel.rubio@mpsd.mpg.de

Authors

Kevin Lively − *Max Planck Institute for the Structure and Dynamics of Matter and Center for Free-Electron Laser Science, 22761 Hamburg, Germany;* ⓞ orcid.org/0000-0003-2098-1494

Guillermo Albareda − *Max Planck Institute for the Structure and Dynamics of Matter and Center for Free-Electron Laser Science, 22761 Hamburg, Germany; Institute of Theoretical and Computational Chemistry, University of Barcelona, 08028 Barcelona, Spain; Nano-Bio Spectroscopy Group and ETSF, Universidad del País Vasco, 20018 San Sebastián, Spain;* ⓞ orcid.org/0000-0002-2181-7023

Shunsuke A. Sato − *Max Planck Institute for the Structure and Dynamics of Matter and Center for Free-Electron Laser Science, 22761 Hamburg, Germany; Center for Computational Sciences, University of Tsukuba, Tsukuba 305-8577, Japan*

Complete contact information is available at:
https://pubs.acs.org/10.1021/acs.jpclett.1c00073

Notes

The authors declare no competing financial interest.

REFERENCES

(1) May, V.; Kühn, O. *Charge and Energy Transfer Dynamics in Molecular Systems*, 3rd ed.; 2011.

(2) Ullrich, C. A. *Time-Dependent Density-Functional Theory: Concepts and Applications*; Oxford Graduate Texts; 2011.

(3) Wigner, E. On the quantum correction for thermodynamic equilibrium. *Phys. Rev.* **1932**, *40*, 749−759.

(4) Case, W. B. Wigner functions and Weyl transforms for pedestrians. *Am. J. Phys.* **2008**, *76*, 937−946.

(5) Grunwald, R.; Kelly, A.; Kapral, R. Quantum Dynamics in Almost Classical Environments. In *Energy Transfer Dynamics in Biomaterial Systems*, 2009.

(6) Jasper, A. W.; Zhu, C.; Nangia, S.; Truhlar, D. G. Introductory lecture: Nonadiabatic effects in chemical dynamics. *Faraday Discuss.* **2004**, *127*, 1−22.

(7) Karsten, S.; Ivanov, S. D.; Bokarev, S. I.; Kühn, O. Quasi-classical approaches to vibronic spectra revisited. *J. Chem. Phys.* **2018**, 102337.

(8) Tully, J. C. Mixed quantum-classical dynamics. *Faraday Discussions* **1998**, *110*, 407.

(9) Kapral, R. Progress in the theory of mixed quantum-classical dynamics. *Annu. Rev. Phys. Chem.* **2006**, *57*, 129−157.

(10) Lee, M. K.; Huo, P.; Coker, D. F. Semiclassical Path Integral Dynamics: Photosynthetic Energy Transfer With Realistic Environment Interactions. *Annu. Rev. Phys. Chem.* **2016**, *67*, 639−668.

(11) Agostini, F.; Min, S. K.; Abedi, A.; Gross, E. K. U. Quantum-classical nonadiabatic dynamics: coupled- vs independent-trajectory methods. *J. Chem. Theory Comput.* **2016**, *12*, 2127−2143.

(12) Talotta, F.; Agostini, F.; Ciccotti, G. Quantum trajectories for the dynamics in the exact factorization framework: A proof-of-principle test. *J. Phys. Chem. A* **2020**, *124*, 6764−6777.

(13) Tully, J. C. Molecular dynamics with electronic transitions. *J. Chem. Phys.* **1990**, *93*, 1061−1071.

(14) Donoso, A.; Martens, C. C. Simulation of coherent non-adiabatic dynamics using classical trajectories. *J. Phys. Chem. A* **1998**, *102*, 4291−4300.

(15) Shalashilin, D. V. Multiconfigurational Ehrenfest approach to quantum coherent dynamics in large molecular systems. *Faraday Discuss.* **2011**, *153*, 105−116.

(16) Mignolet, B.; Curchod, B. F. A walk through the approximations of ab initio multiple spawning. *J. Chem. Phys.* **2018**, *148*, 134110.

(17) Nijjar, P.; Jankowska, J.; Prezhdo, O. V. Ehrenfest and classical path dynamics with decoherence and detailed balance. *J. Chem. Phys.* **2019**, *150*, 204124.

(18) Albareda, G.; Appel, H.; Franco, I.; Abedi, A.; Rubio, A. Correlated electron-nuclear dynamics with conditional wave functions. *Phys. Rev. Lett.* **2014**, *113*, 083003.

(19) Albareda, G.; Bofill, J. M.; Tavernelli, I.; Huarte-Larranaga, F.; Illas, F.; Rubio, A. Conditional Born-Oppenheimer dynamics: Quantum dynamics simulations for the model porphine. *J. Phys. Chem. Lett.* **2015**, *6*, 1529.

(20) Albareda, G.; Abedi, A.; Tavernelli, I.; Rubio, A. Universal steps in quantum dynamics with time-dependent potential-energy surfaces: Beyond the Born-Oppenheimer picture. *Phys. Rev. A: At., Mol., Opt. Phys.* **2016**, *94*, 062511.

(21) Albareda, G.; Kelly, A.; Rubio, A. Nonadiabatic quantum dynamics without potential energy surfaces. *Physical Review Materials* **2019**, *3*, 023803.

(22) Tokmakoff, A. Time-dependent quantum mechanics and spectroscopy. Lecture, 2014.

(23) Raab, A.; Worth, G. A.; Meyer, H.-D.; Cederbaum, L. S. Molecular dynamics of pyrazine after excitation to the S2 electronic state using a realistic 24-mode model Hamiltonian. *J. Chem. Phys.* **1999**, *110*, 936−946.

(24) Vendrell, O.; Meyer, H. D. Multilayer multiconfiguration time-dependent Hartree method: Implementation and applications to a Henon-Heiles Hamiltonian and to pyrazine. *J. Chem. Phys.* **2011**, *134*, 044135.

(25) Yabana, K.; Bertsch, G. Time-dependent local-density approximation in real time. *Phys. Rev. B: Condens. Matter Mater. Phys.* **1996**, *54*, 4484−4487.

(26) De Giovannini, U.; Brunetto, G.; Castro, A.; Walkenhorst, J.; Rubio, A. Simulating pump-probe photoelectron and absorption spectroscopy on the attosecond timescale with time-dependent density functional theory. *ChemPhysChem* **2013**, *14*, 1363−1376.

(27) McLachlan, A. D. A variational solution of the time-dependent Schrodinger equation. *Mol. Phys.* **1964**, *8*, 39−44.

(28) Vacher, M.; Bearpark, M. J.; Robb, M. A. Direct methods for non-adiabatic dynamics: connecting the single-set variational multi-configuration Gaussian (vMCG) and Ehrenfest perspectives. *Theor. Chem. Acc.* **2016**, *135*, 187.

(29) Li, X.; Tully, J. C.; Schlegel, H. B.; Frisch, M. J. Ab initio Ehrenfest dynamics. *J. Chem. Phys.* **2005**, *123*, 084106.

(30) Andrea Rozzi, C.; Maria Falke, S.; Spallanzani, N.; Rubio, A.; Molinari, E.; Brida, D.; Maiuri, M.; Cerullo, G.; Schramm, H.; Christoffers, J. Quantum coherence controls the charge separation in a prototypical artificial light-harvesting system. *Nat. Commun.* **2013**, *4*, 1602.

(31) Krumland, J.; Valencia, A. M.; Pittalis, S.; Rozzi, C. A.; Cocchi, C. Understanding real-time time-dependent density-functional theory simulations of ultrafast laser-induced dynamics in organic molecules. *J. Chem. Phys.* **2020**, *153*, 054106.

(32) Goings, J. J.; Lingerfelt, D. B.; Li, X. Can quantized vibrational effects be obtained from ehrenfest mixed quantum-classical dynamics? *J. Phys. Chem. Lett.* **2016**, *7*, 5193−5197.

(33) Kapral, R.; Ciccotti, G. Mixed quantum-classical dynamics. *J. Chem. Phys.* **1999**, *110*, 8919−8929.

(34) Broeckhove, J.; Lathouwers, L.; Kesteloot, E.; Van Leuven, P. On the equivalence of time-dependent variational principles. *Chem. Phys. Lett.* **1988**, *149*, 547−550.

(35) Lubich, C. On variational approximations in quantum molecular dynamics. *Mathematics of Computation* **2005**, *74*, 765−780.

(36) Ohta, K. Time-dependent variational principle with constraints for parametrized wave functions. *Phys. Rev. A: At., Mol., Opt. Phys.* **2004**, *70*, 022503.

(37) Kosloff, R.; Tal-Ezer, H. A direct relaxation method for calculating eigenfunctions and eigenvalues of the schrödinger equation on a grid. *Chem. Phys. Lett.* **1986**, *127*, 223.

(38) Shi, T.; Demler, E.; Ignacio Cirac, J. Variational study of fermionic and bosonic systems with non-Gaussian states: Theory and applications. *Ann. Phys.* **2018**, *390*, 245−302.

(39) *Generalized Inverses*; Springer: New York, NY, 2006.

(40) Kreibich, T.; Lein, M.; Engel, V.; Gross, E. K. Even-harmonic generation due to beyond-born-oppenheimer dynamics. *Phys. Rev. Lett.* **2001**, *87*, 103901.

(41) Lein, M.; Kreibich, T.; Gross, E. K.; Engel, V. Strong-field ionization dynamics of a model [Formula Presented] molecule. *Phys. Rev. A: At., Mol., Opt. Phys.* **2002**, *65*, 033403.

(42) Bandrauk, A. D.; Shon, N. H. Attosecond control of ionization and high-order harmonic generation in molecules. *Phys. Rev. A: At., Mol., Opt. Phys.* **2002**, *66*, 031401.

(43) Crespo-Otero, R.; Barbatti, M. Spectrum simulation and decomposition with nuclear ensemble: Formal derivation and application to benzene, furan and 2-phenylfuran. *Theor. Chem. Acc.* **2012**, *131*, 1237.

(44) Tancogne-Dejean, N.; Oliveira, M. J.; Andrade, X.; Appel, H.; Borca, C. H.; le Breton, G.; Buchholz, F.; Castro, A.; Corni, S.; Correa, A. A.; et al. Octopus, a computational framework for exploring light-driven phenomena and quantum dynamics in extended and finite systems. *J. Chem. Phys.* **2020**, *152*, 124119.

(45) Gross, E. K. U.; Maitra, N. T. Introduction to TDDFT. *Fundamentals of Time-Dependent Density Functional Theory* **2012**, *837*, 53−99.

(46) Pantos, E.; Philis, J.; Bolovinos, A. The extinction coefficient of benzene vapor in the region 4.6 to 36 eV. *J. Mol. Spectrosc.* **1978**, *72*, 36−43.

(47) Koch, E. E.; Otto, A. Optical absorption of benzene vapour for photon energies from 6 to 35 eV. *Chem. Phys. Lett.* **1972**, *12*, 476−480.

(48) Gingell, J. M.; Marston, G.; Mason, N. J.; Zhao, H.; Siggel, M. R. On the electronic spectroscopy of benzyl alcohol. *Chem. Phys.* **1998**, *237*, 443−449.

(49) Ridolfi, E.; Trevisanutto, P. E.; Pereira, V. M. Expeditious computation of nonlinear optical properties of arbitrary order with native electronic interactions in the time domain. *Phys. Rev. B: Condens. Matter Mater. Phys.* **2020**, *102*, 245110.

(50) Verlet, L. Computer "experiments" on classical fluids. I. Thermodynamical properties of Lennard-Jones molecules. *Phys. Rev.* **1967**, *159*, 98.

Simulating Vibronic Spectra without Born-Oppenheimer Surfaces: Supplemental Information

Kevin Lively,[†] Guillermo Albareda,[†,‡,¶] Shunsuke A. Sato,[†,§] Aaron Kelly,[∗,†,∥] and Angel Rubio[∗,†,¶,⊥]

[†]Max Planck Institute for the Structure and Dynamics of Matter and Center for Free-Electron Laser Science, Luruper Chaussee 149, 22761 Hamburg, Germany

[‡]Institute of Theoretical and Computational Chemistry, University of Barcelona, Martí i Franquès 1-11, 08028 Barcelona, Spain

[¶]Nano-Bio Spectroscopy Group and ETSF, Universidad del País Vasco, 20018 San Sebastían, Spain

[§]Center for Computational Sciences, University of Tsukuba, Tsukuba 305-8577, Japan

[∥]Department of Chemistry, Dalhousie University, Halifax B3H 4R2, Canada

[⊥]Center for Computational Quantum Physics (CCQ), Flatiron Institute, 162 Fifth avenue, New York NY 10010, USA

E-mail: aaron.kelly@mpsd.mpg.de; angel.rubio@mpsd.mpg.de

MTEF Equations of Motion

Starting from a density matrix representation of the full system, $\hat{\rho}$, we Wigner transform over the nuclear subsystem, producing a unique mapping onto a nuclear position $\mathbf{R}$ and momentum $\mathbf{P}$ phase space $\mathbf{X} = (\mathbf{R}, \mathbf{P})$, where $\mathbf{R}$ and $\mathbf{P}$ are collective variables $\mathbf{R} = (\mathbf{R}_1, \ldots, \mathbf{R}_{N_n})$, $\mathbf{P} = (\mathbf{P}_1, \ldots, \mathbf{P}_{N_n})$, with $\mathbf{R}_i, \mathbf{P}_i \in \mathbb{R}^d$. The partial wigner transform is defined for any operator as

$$\hat{\rho}_W(\mathbf{R}, \mathbf{P}) = \frac{1}{(2\pi)^{dN_n}} \int d\mathbf{X} e^{i\mathbf{P}\cdot\mathbf{X}} \langle \mathbf{R} - \frac{\mathbf{X}}{2}|\hat{\rho}|\mathbf{R} + \frac{\mathbf{X}}{2}\rangle, \tag{1}$$

leaving a Hilbert space operator character over the electronic degrees of freedom, dependent on the continuous nuclear phase space parameters. In general, developing equations of motion for $\hat{\rho}_W(\mathbf{R}, \mathbf{P})$, (or any operator), requires taking the partial Wigner transformation of the Liouville von-Neumann equation of motion for ρ:

$$
\begin{aligned}
\frac{\partial \hat{\rho}_W}{\partial t} &= -i\Big((\hat{H}\hat{\rho})_W - (\hat{\rho}\hat{H})_W\Big) \\
(\hat{H}\hat{\rho})_W &= \hat{H}_W \exp\Big(\frac{1}{2i}\Lambda\Big)\hat{\rho}_W \\
\Lambda &= \overleftarrow{\nabla}_\mathbf{P} \cdot \overrightarrow{\nabla}_\mathbf{R} - \overleftarrow{\nabla}_\mathbf{R} \cdot \overrightarrow{\nabla}_\mathbf{P} \\
g \exp\Big(\kappa\Lambda\Big)f &= \sum_{s=0}^{\infty} \frac{\kappa^s}{s!} \sum_{t=0}^{s} (-1)^t \binom{s}{t} \left[\partial_\mathbf{R}^{s-t}\partial_\mathbf{P}^t \ f\right]\left[\partial_\mathbf{R}^t\partial_\mathbf{P}^{s-t} \ g\right].
\end{aligned}
\tag{2}
$$

Where the final line defines the "Moyal product" also known as the "star product".[1] By expressing the Poisson braket operator Λ, in terms of the ratio of masses between the nuclei and the electrons $\Lambda = (m/M)^{\frac{1}{2}}\Lambda'$, and truncating the Moyal product of $e^{(m/M)^{\frac{1}{2}}\Lambda'}$ at first order, one can arrive at the Quantum-Classical Liouville Equation (QCLE):[2]

$$i\frac{\partial}{\partial t}\hat{\rho}_W(\mathbf{R}, \mathbf{P}) = -i[\hat{H}_W, \hat{\rho}_W] + \frac{1}{2}\Big(\{\hat{H}_W, \hat{\rho}_W\} - \{\hat{\rho}_W, \hat{H}_W\}\Big), \tag{3}$$

where $\{A(\mathbf{R}, \mathbf{P}), B(\mathbf{R}, \mathbf{P})\}$ refers to the normal Poisson bracket.

To derive MTEF equations of motion from the QCLE, one takes the mean field approximation by assuming that the full system can be written as a sum of correlated and uncorrelated parts,

$$\hat{\rho}_W(\mathbf{X}, t) = \hat{\rho}_e(t)\rho_{n,W}(\mathbf{X}, t) + \hat{\rho}_{corr,W}(\mathbf{X}, t), \tag{4}$$

and then neglecting the contribution of the correlated part in the *dynamics*. Note that while the ensuing dynamics do not explicitly treat the effect of subsystem correlation, the initial state generally *is* correlated, and therefore is implicitly included in the dynamics.

Under this approximation, the electronic density matrix is

$$\hat{\rho}_e(t) = Tr_n\left(\hat{\rho}(t)\right) = \int d\mathbf{X}\hat{\rho}_W(\mathbf{X}, t), \tag{5}$$

and the nuclear (quasi) probability phase space distribution is $\rho_n(\mathbf{X}, t) = Tr_e\left(\hat{\rho}_W(\mathbf{X}, t)\right)$.

In the equations of motion resulting from inserting this approximation into the QCLE, the evolution of the reduced Wigner density of the nuclear subsystem can be exactly represented, via the method of characteristics, by a sufficiently large ensemble of multiple independent trajectories, $\rho_{n,W}(\mathbf{X}, t) = \frac{1}{N}\sum_i^N \delta(\mathbf{X}_i - \mathbf{X}(t))$. Each trajectory evolves according to Hamilton's equations of motion generated from the mean-field effective Hamiltonian,

$$\frac{\partial \mathbf{R}_i}{\partial t} = \frac{\partial H_{n,W}^{Eff}}{\partial \mathbf{P}_i}, \quad \frac{\partial \mathbf{P}_i}{\partial t} = -\frac{\partial H_{n,W}^{Eff}}{\partial \mathbf{R}_i}$$
$$H_{n,W}^{Eff} = H_{n,W}(\mathbf{X}_i(t)) + Tr_e\left(\hat{H}_{en,W}(\mathbf{X}_i(t))\hat{\rho}_e^i(t)\right). \tag{6}$$

Where $H_{n,W}$ and $H_{en,W}$ refer to the partially Wigner transformed nuclear and electron-nuclear coupling operators, respectively. The electronic density associated with each trajectory , $\rho_e^i(t)$, evolves according to the following commutator:

$$\frac{d}{dt}\hat{\rho}_e^i(t) = -i\left[\hat{H}_e + \hat{H}_{en,W}(\mathbf{X}_i(t)), \ \hat{\rho}_e^i(t)\right]. \tag{7}$$

The exact expression for the average value of any observable, $\langle O(t) \rangle$, can be written as

$$
\begin{aligned}
\langle O(t) \rangle &= Tr_e \int d\mathbf{X} \hat{O}_W(\mathbf{X}, t) \hat{\rho}_W(\mathbf{X}, 0) = Tr_e \int d\mathbf{X} \hat{O}_W(\mathbf{X}) \hat{\rho}_W(\mathbf{X}, t) \\
&= \frac{1}{N} \sum_i^N Tr_e \left(\hat{O}_W(\mathbf{X}_i(t)) \hat{\rho}_e^i(t) \right)
\end{aligned}
\tag{8}
$$

The mean field limit of this expression simple corresponds to evaluating the integral by sampling initial conditions for an ensemble of independent trajectories from $\hat{\rho}_W(\mathbf{X}, 0)$, and then generating the time evolution for each trajectory by approximating $\hat{O}_W(\mathbf{X}, t)$ by it's mean-field counterpart.

Following the sampling of an initial nuclear condition, $\mathbf{X}_i$, from the Wigner distribution associated to the nuclear subsystem wave function, the electronic system is initialised as:

$$
(\hat{H}_e + \hat{H}_{en,W}(\mathbf{R}_i))\phi_a(r) = \epsilon_a(\mathbf{R}_i)\phi_a(r),
\tag{9}
$$

i.e. implicitly as the BO electronic state at $\mathbf{R}_i$. Under this scheme, the electronic subsystem's initial conditions are implicitly correlated with the nuclear subsystem's quantum statistics.

In cases where the nuclear initial state is impractical to calculate exactly one may utilise the normal modes of the molecular system, or phonon coordinates of a periodic system, to treat the full nuclear wavefunction as a Hartree product of N uncoupled harmonic oscillators, where N is the number of non-rotational and non-translational nuclear degrees of freedom:

$$
\begin{aligned}
\chi_n(\mathbf{R}) &\approx \chi_1(Q_1) \otimes \ldots \otimes \chi_N(Q_N) \\
\chi_i(Q_i) &= \sum_l c_l^{(i)} \chi_i^l(Q_i).
\end{aligned}
\tag{10}
$$

With $c_l^{(i)}$ referring to the occupation of the l^{th} excited state of normal mode i with wavefunction, χ_i^l, and $Q_i(\mathbf{R})$ the normal mode coordinate. Formally, this is exactly equivalent to taking a second order Taylor expansion approximation of the BO surface about the equilib-

rium nuclear position R^0:

$$H_{nuc}(\mathbf{R}, \mathbf{P}) = \sum_l \frac{1}{2M_l}\mathbf{P}_l^2 + \sum_{lm} \frac{1}{2}(\mathbf{R}_l - \mathbf{R}_l^0)\frac{\partial^2 V_{BO}}{\partial\mathbf{R}_l\partial\mathbf{R}_m}\bigg|_{\mathbf{R}^0}(\mathbf{R}_m - \mathbf{R}_m^0). \tag{11}$$

Defining the dynamical matrix, $\mathcal{H}_{lm} = \frac{1}{\sqrt{M_l}}\frac{\partial^2 V}{\partial\mathbf{R}_l\partial\mathbf{R}_m}\frac{1}{\sqrt{M_m}}$, and it's diagonalizing unitary transform, $D^T\mathcal{H}D = \Omega$, $D^TD = \mathbf{1}$, where $\Omega_{ij} = \omega_i^2\delta_{ij}$, we construct the normal coordinate transform for all non-rotational, non-translational (imaginary) ω_i^2, (here we include $\hbar$ for clarity):

$$\sqrt{M_l}(\mathbf{R}_l - \mathbf{R}_l^0) = \sum_i D_{li}q_i , \quad \frac{\mathbf{P}_l}{\sqrt{M_l}} = \sum_i D_{li}s_i$$

$$s_i = \sqrt{\hbar\omega_i}S_i , \quad q_i = \sqrt{\frac{\hbar}{\omega_i}}Q_i, \tag{12}$$

such that we obtain the nuclear Hamiltonian in dimensionless normal mode coodinates:

$$H(Q, S) = \sum_i \frac{\hbar\omega_i}{2}(S_i^2 + Q_i^2). \tag{13}$$

Of course, the simple harmonic wave function solutions to the above Hamiltonian have well known analytical expressions and are trivially Wigner transformed, the ground state harmonic oscillator wavefunction's Wigner function for instance is:[3]

$$W_0(Q, S) = \frac{1}{\pi}\exp\left(-S^2 - Q^2\right). \tag{14}$$

We can therefore sample these transforms for (Q, S) and then use eq. (12) to back transform to from normal mode coordinates to cartesian coordinates.

MTEF-BO Equations of Motion in the Born Oppenheimer Basis

In deriving the MTEF equations of motion in the BO basis, we start by writing the molecular hamiltonian in terms of position and momentum space operators for the electrons (light particles), $\hat{r}, \hat{p}$ and nuclei (heavy particles) $\hat{R}, \hat{P}$. These are again understood to be collective variables.

$$\hat{H}(\hat{r}, \hat{p}, \hat{R}, \hat{P}) = \frac{1}{2M}\hat{P}^2 + \hat{h}_e(\hat{r}, \hat{p}, \hat{R})$$

$$\hat{h}(\hat{r}, \hat{p}, \hat{R}) = \frac{1}{2}\hat{p}^2 + \hat{V}(\hat{r}, \hat{R}) \tag{15}$$

$$\hat{V}(\hat{r}, \hat{R}) = \hat{V}_{ee}(\hat{r}) + \hat{V}_{en}(\hat{r}, \hat{R}) + \hat{V}_{nn}(\hat{R}).$$

We then utilise a position representation in the nuclear dof by expanding in the space of nuclear position states $1_{\mathbf{R}} = \int d\mathbf{R} \, |\mathbf{R}\rangle \langle \mathbf{R}|$, leading to

$$\hat{H}(\mathbf{R}) = -\frac{1}{2M}\nabla_{\mathbf{R}}^2 + \hat{h}_e(\hat{r}, \hat{p}, \mathbf{R}) \tag{16}$$

For a transition between two electronic states g and e, we can expand in the adiabatic basis $|\phi_a(\mathbf{R})\rangle, (a = g, e)$ which are dependent on the nuclear positions $\mathbf{R}$ defined by,

$$\hat{h}_e(\mathbf{R}) |\phi_a(\mathbf{R})\rangle = \epsilon_a(\mathbf{R}) |\phi_a(\mathbf{R})\rangle. \tag{17}$$

Taking the partial Wigner transform of eq. (16) leads to

$$\hat{H}_W(\mathbf{R}, \mathbf{P}) = \frac{1}{2M}\mathbf{P}^2 + \hat{h}_{e,W}(\hat{r}, \hat{p}, \mathbf{R}) \tag{18}$$

where $\hat{h}_{e,W}(\mathbf{R})$ is the normal electronic hamiltonian operator, now dependent on R in the Wigner nuclear phase space. Starting with the separability approximation for the density

operator, and neglecting correlations, we have $\hat{\rho}_W = \hat{\rho}_e \rho_n(\mathbf{R}, \mathbf{P})$, with

$$\partial_t \hat{\rho}_e = -i \left[Tr_{\mathbf{X}} \langle \hat{h}_{e,W}(\mathbf{R}) \rangle, \hat{\rho}_e \right] \tag{19}$$

where $Tr_{\mathbf{X}} \langle \ldots \rangle = \int \ldots d\mathbf{R}d\mathbf{P}$, and $\mathbf{P}$ scalar terms are cancelled by the commutator. We are of course interested in evaluating the dipole-dipole correlation function:

$$\begin{aligned} C_{\mu\mu}(t) &= \int d\mathbf{R}d\mathbf{P} Tr_e \left\{ \hat{\mu}_W \hat{\sigma}(t) \right\} \\ &= \int d\mathbf{R}d\mathbf{P} Tr_e \left\{ \hat{\mu}_W(t) \hat{\sigma}(0) \right\}, \end{aligned} \tag{20}$$

where $\hat{\sigma} = [\hat{\mu}_W, \hat{\rho}_W]$, and we resolve the dipole operator as

$$\begin{aligned} \hat{\mu}_W(\mathbf{R}, t=0) &= -\hat{r} + Z_{\mathbf{R}}\mathbf{R} \\ &= \sum_{aa'} |\phi_a\rangle \langle \phi_a|(-\hat{r})|\phi_{a'}\rangle \langle \phi_{a'}| + \delta_{aa'} Z_{\mathbf{R}}\mathbf{R} |\phi_a\rangle \langle \phi_{a'}| \\ &= \begin{pmatrix} \mathbf{R} & \mu^{ge}(\mathbf{R}) \\ \mu^{eg}(\mathbf{R}) & \mathbf{R} \end{pmatrix} \end{aligned} \tag{21}$$

Where $Z_{\mathbf{R}}$ refers to the ionic charge of each nuclei. In practice we can neglect the intra-state $\mathbf{R}$ term as we are focused entirely on the *transition* dipole moment.

Taking the initial state as the ground state, $(|\Psi\rangle = |\chi_g^0 \phi_g\rangle)$

$$\hat{\rho}_W(\mathbf{R}, \mathbf{P}, 0) = \rho_g^n(\mathbf{R}, \mathbf{P}) \begin{pmatrix} 1 & 0 \\ 0 & 0 \end{pmatrix}, \tag{22}$$

leads to

$$\sigma\hat{}(0) = [\hat{\mu}_W, \hat{\rho}_W(\mathbf{R}, \mathbf{P}, 0)]$$

$$= \rho_g^n(\mathbf{R}, \mathbf{P}) \begin{pmatrix} 0 & -\mu^{ge}(\mathbf{R}) \\ \mu^{eg}(\mathbf{R}) & 0 \end{pmatrix}. \tag{23}$$

And therefore the correlation function becomes

$$C_{\mu\mu}(t) = \int d\mathbf{R} d\mathbf{P} \left(\mu_W^{ge}(\mathbf{R}, t)\sigma^{eg}(0) + \mu_W^{eg}(\mathbf{R}, t)\sigma^{ge}(0) \right)$$

$$= \int d\mathbf{R} d\mathbf{P} \left(\mu_W^{ge}(\mathbf{R}, t)\mu_W^{eg}(\mathbf{R}, 0) \right.$$

$$\left. - \mu_W^{eg}(\mathbf{R}, t)\mu_W^{ge}(\mathbf{R}, 0) \right) \rho_g^n(\mathbf{R}, \mathbf{P}). \tag{24}$$

We can construct an identical quantity from a different initial condition as a superposition state $(|\Psi\rangle = \frac{1}{\sqrt{2}} |\chi_g\rangle (|\phi_g\rangle + i |\phi_e\rangle))$ giving,

$$\hat{\tilde{\rho}}_W(\mathbf{R}, P, 0) = \rho_g^n(\mathbf{R}, \mathbf{P}) \frac{1}{2} \begin{pmatrix} 1 & -i \\ i & 1 \end{pmatrix} \tag{25}$$

For this different initial condition we propagate

$$\tilde{C}_{\mu\mu}(t) = \frac{i}{2} \int dR dP \left(\mu_W^{ge}(\mathbf{R}, t)\mu_W^{eg}(\mathbf{R}, 0) - \mu_W^{eg}(\mathbf{R}, t)\mu_W^{ge}(\mathbf{R}, 0) \right) \rho_g^n(\mathbf{R}, \mathbf{P})$$

$$= \frac{i}{2} C_{\mu\mu}(t) \tag{26}$$

With this different initial condition, we take the MTEF form of the nuclear density arising from the Monte Carlo integration described above,

$$\rho_n(\mathbf{R}, \mathbf{P}) = \frac{1}{N} \sum_i \delta(\mathbf{R} - \mathbf{R}_i(t))\delta(\mathbf{P} - \mathbf{P}_i(t)). \tag{27}$$

The subsequent equations of motion for the system are for the electronic density, needed for

the nuclear trajectories are:

$$\partial_t \tilde{\rho}_e^{aa'} = -i\tilde{\rho}_e^{aa'}(t)(\epsilon_a(\mathbf{R}_i(t)) - \epsilon_{a'}(\mathbf{R}_i(t)))$$
$$+ \sum_{a''} \frac{\mathbf{P}_i(t)}{M} \left(\tilde{\rho}_e^{aa''}(t)d_{a''a'}^i(t) - d_{aa''}^i(t)\tilde{\rho}_e^{a''a'}(t) \right)$$

$$\partial_t \mathbf{R}_i(t) = \mathbf{P}_i(t)/M$$

$$\partial_t \mathbf{P}_i(t) = \frac{1}{2} \sum_{aa'} \left(F_W^{aa'}(t)\tilde{\rho}_e^{a'a}(t) + \tilde{\rho}_e^{aa'}(t)F_W^{a'a}(t) \right)$$

$$= \sum_{aa'} \Re \left[F_W^{aa'}(t)\tilde{\rho}_e^{a'a}(t) \right]$$

$$= \sum_a -\partial_R \epsilon_a(\mathbf{R}_i(t))\tilde{\rho}_e^{aa}(t)$$

$$+ \sum_{aa'} \Re \left[\left(\epsilon_a(\mathbf{R}_i(t))d_{aa'}^i(t) - \epsilon_{a'}(\mathbf{R}_i(t))d_{a'a}^i(t) \right) \tilde{\rho}_e^{a'a}(t) \right]$$

(28)

Where in the last two equations we have used the identity $d_{aa'}^i(t) = \langle \phi_a | \partial_{\mathbf{R}_i} \phi_{a'} \rangle |_{\mathbf{R}_i(t)} = -(d_{a'a}^i(t))^*$, to manipulate $F_W^{aa'}(t) = - \langle \phi_a(\mathbf{R}) | \partial_R \hat{H}_W | \phi_{a'}(\mathbf{R}) \rangle |_{\mathbf{R}_i(t)}$. Note that for transitions like the S_0/S_2 transition 1D H_2 focused on in the body of this paper, the non-adiabatic coupling vector (NACV) $d_{aa'} = 0$, means that the mean field force acting on the nuclei is at all times a $\frac{1}{2}$ superposition of the S_0 and S_2 surfaces.

These are propagated alongside the dipole matrix element equations of motion, needed for the correlation function:

$$\partial_t \mu_W^{aa'}(\mathbf{R}_i(t)) = i\mu_W^{aa'}(\mathbf{R}_i(t))(\epsilon_a(\mathbf{R}_i(t)) - \epsilon_{a'}(\mathbf{R}_i(t))).$$

(29)

STEF Spectral Negativity

As mentioned in the main text, previous work by Goings et. al[4] employed STEF-kick dynamics simulations to calculate spectra in fully ab-initio 3D H_2 by initialzing the nuclear geometry in non-equilibrium 'compressed' geometries. Geometries were selected corresponding to expected vibrational energies from Boltzmann distributions at arbitrary temperatures

and the $\delta-$Kick method was used to excite the electronic subsystem. Furthermore, only the *magnitude* of the spectral response was depicted, which does not show the spectral negativity resulting from initialising the mean field simulations in a non-equilibrium state. Here we utilise the canonical initial conditions of the STEF-BO picture for the 1D H_2 model. The electronic occupation is equal for each of the two surfaces ivolved in the transition, and the nuclear initial condition corresponds to the equillibrium geometry of the initial surface. In
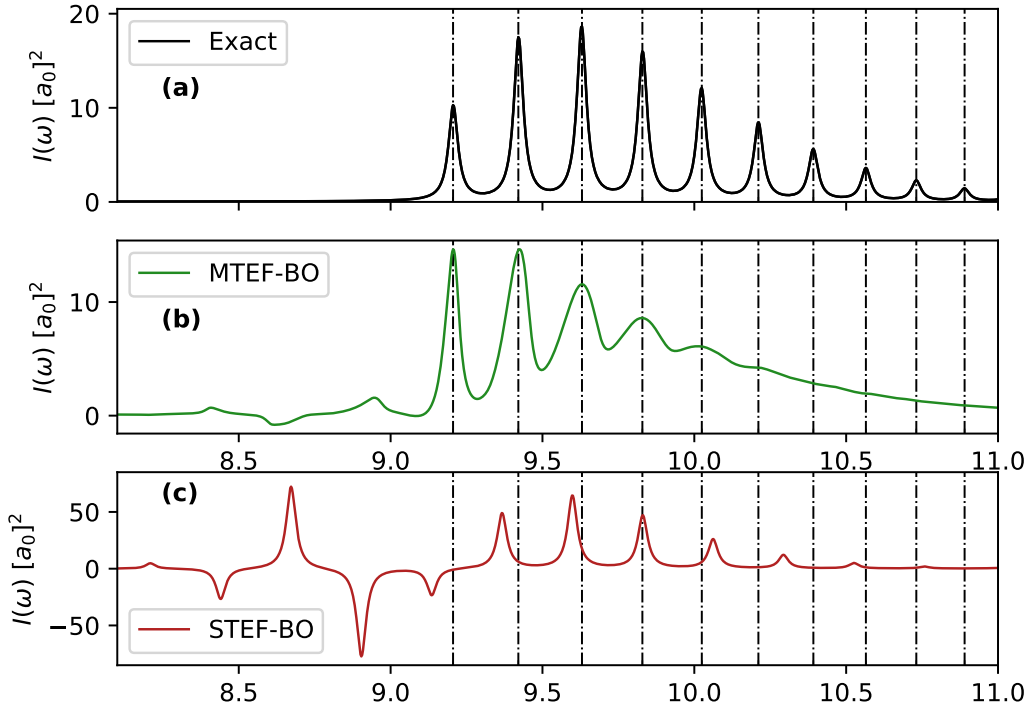

Figure S1: 1D H_2 $S_0 \leftarrow S_2$ absorption spectra, comparing exact, MTEF-BO and STEF-BO.

Fig. S1c we see the results of STEF-BO for the $S_2 \leftarrow S_0$ region of the spectrum, showing that this only captures positive spectral intensities in the vicinity of the exact results, with accurate peak placement only at the MTEF level. Furthermore the contributions to the unphysical pre-peak features of individual trajectories become apparent in the low energy tail. For completeness we also feature the $S_0 \leftarrow S_2$ results in Fig. S2, which demonstrate the same features of correct spectral sign only in the region of the exact results and alternating sign elsewhere.
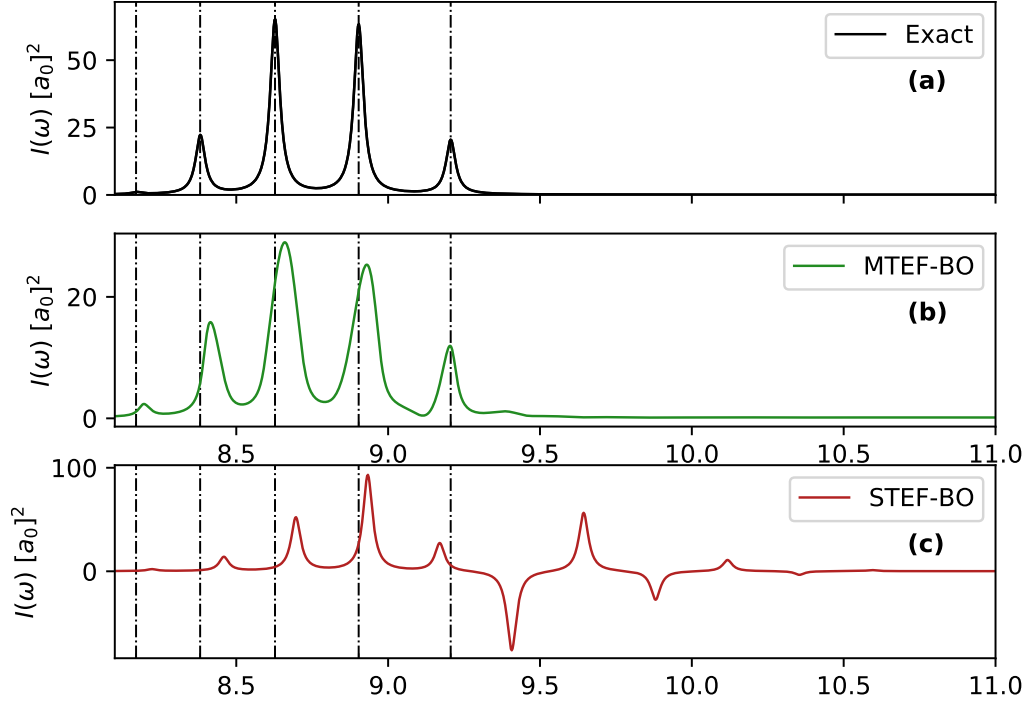
Figure S2: 1D H_2 $S_2 \leftarrow S_0$ absorption spectra, comparing exact, MTEF-BO and STEF-BO.

Application to Displaced Harmonic Oscillator Model

In order to investigate the limitations of MTEF, we can utilise a model which captures the essential physics of the S_0/S_2 1D H_2 transition which was focused on in the first portion of the main text. Recall that for this transition, the NACV's between the two electronic adiabatic states are zero, that is $\langle \phi_a(R)|\partial_R \phi_{a'}(R)\rangle = 0 \; \forall \; a, a'$ in the BO basis, with a, a' restricted to S_0/S_2 This means that matrix elements for the partially Wigner transformed molecular hamiltonian can be written as

$$\hat{H}_W(R, P) = \frac{P^2}{2M} 1 + \begin{pmatrix} \epsilon_g(R) & 0 \\ 0 & \epsilon_e(R) \end{pmatrix}. \tag{30}$$

As described in detail in the first section of this SI, MTEF is rooted in a mean field approximation to the QCLE, which is itself the first order expansion of the partially Wigner

transformed Liouville von-Neumann equation. Taking eq. (2) to second order provides,

$$\frac{\partial \hat{\rho}_W}{\partial t} = -i \left[\hat{H}_W, \hat{\rho}_W \right]$$
$$+ \frac{1}{2} \left(\{\hat{H}_W, \hat{\rho}_W\} - \{\hat{\rho}_W, \hat{H}_W\} \right) \tag{31}$$
$$- \frac{i}{8} \left(\left[\partial_P^2 \hat{H}_W, \partial_\mathbf{R}^2 \hat{\rho}_W \right] + \left[\partial_\mathbf{R}^2 \hat{H}_W, \partial_\mathbf{P}^2 \hat{\rho}_W \right] \right)$$

Which in our model Hamiltonian eq. (30) becomes,

$$\frac{\partial \rho_W^{aa'}}{\partial t} = -i(\epsilon_a(R) - \epsilon_{a'}(R))\rho_W^{aa'}$$
$$+ \left[\frac{1}{2} \left(\partial_R \epsilon_a(R) + \partial_R \epsilon_{a'}(R) \right) \partial_P - \frac{P}{M} \partial_R \right] \rho_W^{aa'} \tag{32}$$
$$- \frac{i}{8} \left(\partial_R^2 \epsilon_a(R) - \partial_R^2 \epsilon_{a'}(R) \right) \partial_P^2 \rho_W^{aa'} + \mathcal{O}\left((m/M)^{\frac{3}{2}}\right)$$

Such that the error in time propagation resultant from taking only the first order expansion, compared to the second, is proportional to the difference in energy surface curvature.

If we take the analytically solvable Displaced Harmonic Oscillator (DHO) model[5,6] by using surfaces $\epsilon_a(R) = \frac{1}{2}\omega_a^2(R - D_a)^2 + E_a$, we see that for identical surfaces $\omega_e = \omega_g$ that the 2nd order and higher terms in the Wigner transformed Liouville von-Neumann equation are zero, rendering the QCLE exact for this case.

To demonstrate the effect of varying surface curvature, we took parameters similar to harmonic surface fits to the BO surfaces in 1D H_2, and for simplicity, took the FC approximation alongside setting $\mu^{aa'}(R) = (1 - \delta_{aa'})$a.u.. We solve the exact and MTEF-TCF spectra for the DHO with different values of ω_e relative to ω_g by propagating for $T_f = 2 \cdot 10^4$a.u.. In Fig. (S3) we see iin the left column that for identical upper and lower surfaces, mean field theory is of course exact, and for varying surfaces, MTEF displays a peak broadening and prepeak features. The origin of this broadening is from an effective damping in the time dependent signal, shown in Fig. (S4).
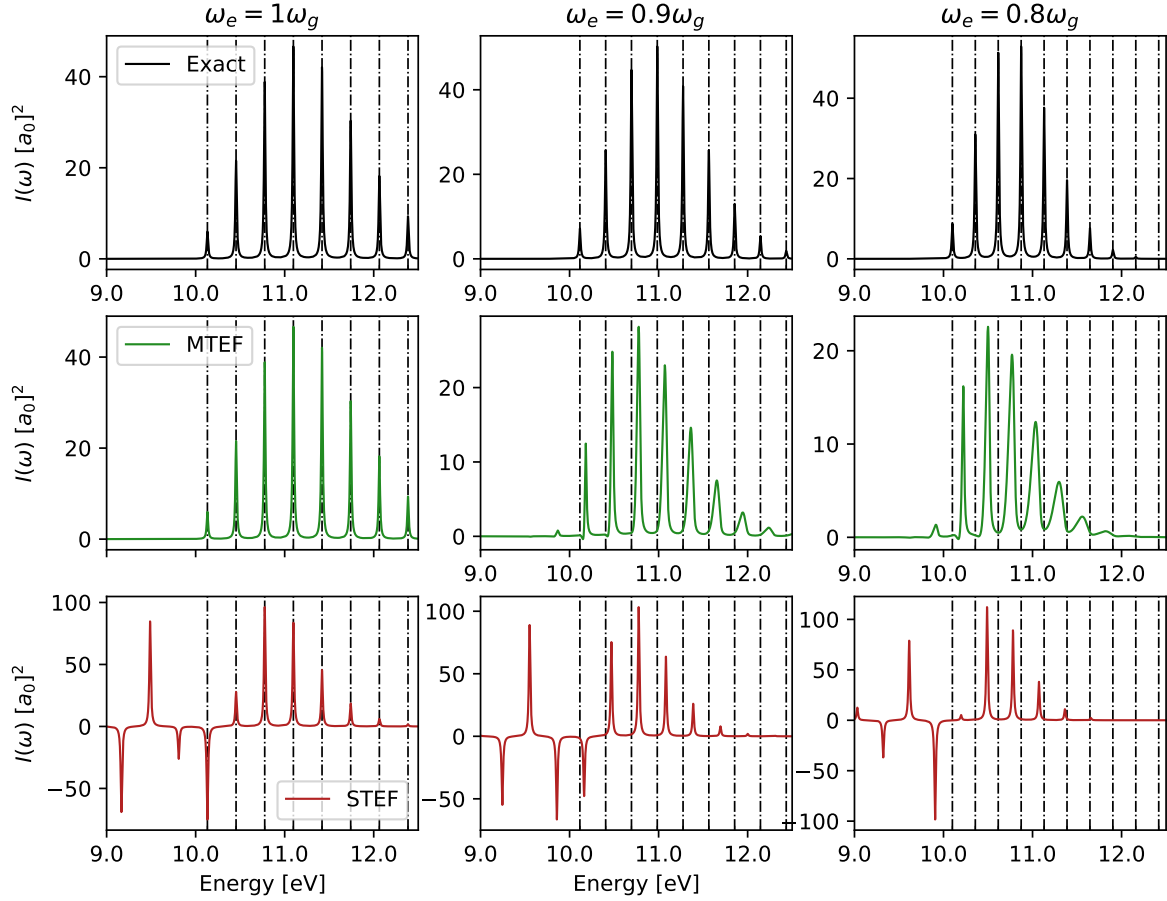
Figure S3: Spectra for the DHO model with several excited and ground state surface frequencies in each column. Each row compares exact, MTEF-BO and STEF-BO results respectively, with the Exact peak placement for each column overlaid across each as vertical dashed lines.
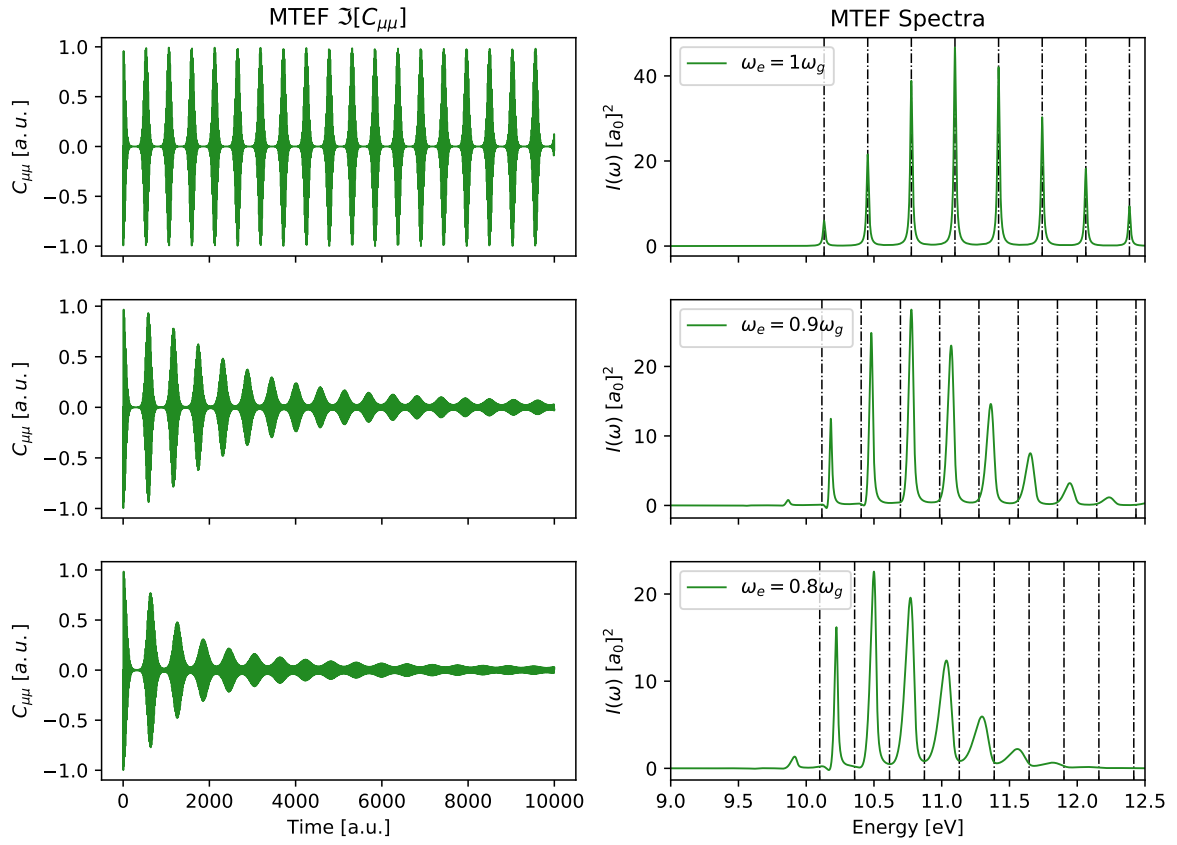
Figure S4: DHO MTEF time dependent dipole-dipole correlation signal in the left column and the resulting spectra in the right column, with the relative surface curvature denoted in the right column legend, and exact spectral peaks overlaid as vertical black dashed lines. For clarity, the time dependent signal is curtailed at $1 \cdot 10^4$ a.u..

MTEF-Kick Comparison to the Nuclear Ensemble Approach

In the Nuclear Ensemble Approach (NEA)[7] the absorption spectra is written as

$$\sigma(\omega) = \frac{4\pi^2}{c\omega} \sum_n \int dR |\chi_{00}(R)|^2 \Delta\omega_{0n}^2(R) |\langle\phi_0|\mu_e(r,R)|\phi_n\rangle_r|^2 L(\omega - \omega_{0n}(R), \delta_n)$$

$$= \frac{4\pi^2}{c\omega} \sum_n \frac{1}{N_t} \sum_{l=1}^{N_t} \Delta\omega_{0n}^2(R_l) |\langle\phi_0|\mu_e(r,R_l)|\phi_n\rangle_r|^2 L(\omega - \omega_{0n}(R_l), \delta_n) \qquad (33)$$

$$L(x - x_i, \delta) = \frac{1}{\pi} \frac{\delta}{(x - x_i)^2 + (\delta)^2}$$

Where $\Delta\omega_{0n}^2(R)$ is the vertical excitation energy between the ground and excited electronic states, μ_e is the electronic dipole operator, L is a Lorentzian broadening function dependent on a width parameter δ, and in the second line we have taken a Monte Carlo sampling integral of the first line, selecting R_l from $|\chi_{00}(R)|^2$. This Monte Carlo integral is precisely equivalent to the MTEF procedure sampling from the Wigner transform of the nuclear ground state, however unlike the MTEF-kick approach doesn't include any nuclear dynamics effects modulating the electronic properties. The NEA results for $N_t = 1.3 \times 10^5$ in the model H$_2$ system discussed in the main text are compared to the exact vibronic spectra and the MTEF-kick spectra in figure S5, showing directly that while sampling over initial equilibrium configuration naturally leads to a broadening of the resulting spectrum, the *dynamics* of the nuclear subsystem coupled to the electronic subsystem are responsible for the vibronic peak structure of the MTEF-kick results. A width parameter of $\delta = -\frac{\log(10^{-3})}{T_f\pi}$ was used for $T_f = 10,000$[a.u.], creating a width commensurate with the dynamics results which have a similar width due to the the exponential damping mask used in the Fourier transform of the dipole signal.

The NEA method was also applied to the benzene molecule, with the dipole oscillator strengths and transition energies calculated via the Casida equation with 400 unoccupied
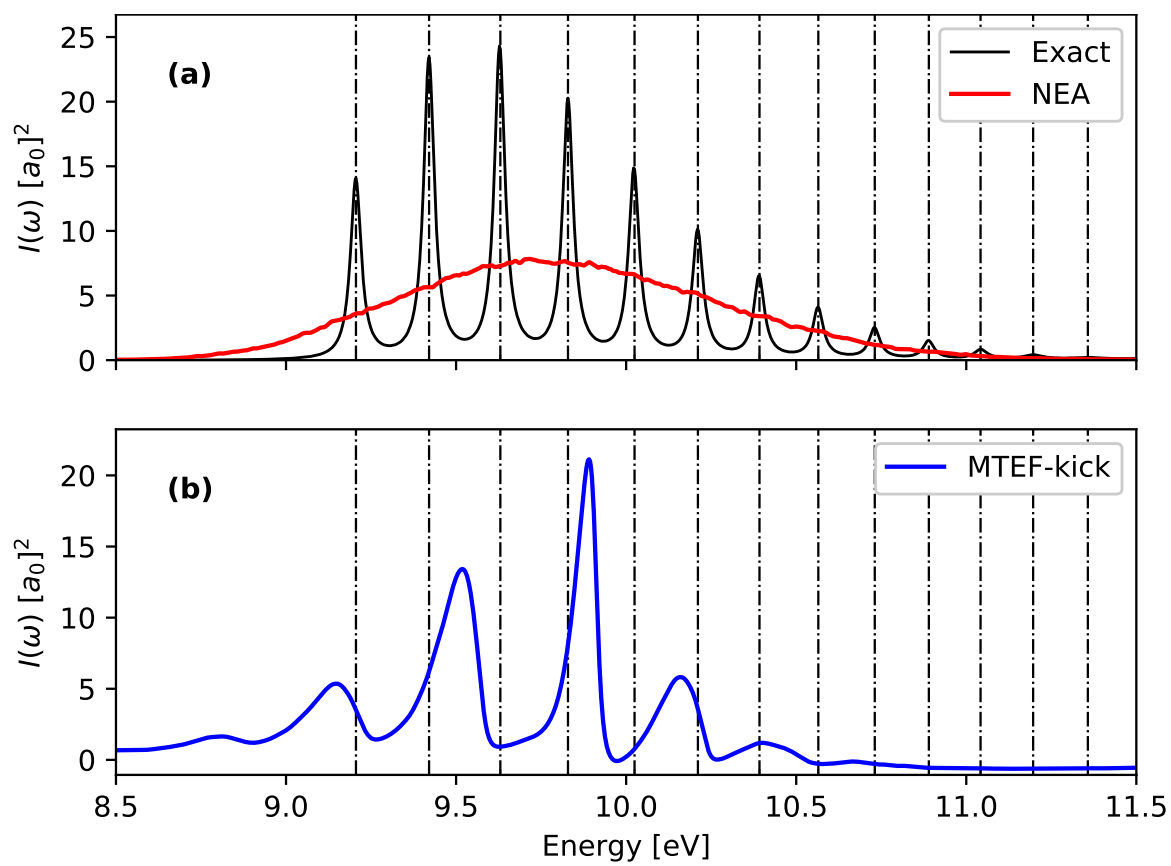
Figure S5: Exact vibronic spectra overlaid with the results of the NEA calculation in (a), with the MTEF-kick results from the main text recreated in (b).

S16

orbitals for the same set of initial nuclear geometries used for the MTEF-TDDFT-kick spectra and the same simulation box parameters reported in the main text. The results are shown in figure S6. We see that there is good qualitative agreement between the two methods in this system, due to the density of electronic and vibrational states in the energy range. For completeness we also recreate the NEA results of Crespo-Otero and Barbatti[7] calculated with a more sophisticated xc functional, and find quite good agreement, particularly in the 5.5eV to 6eV energy range.

While these two methods are qualitatively quite similar for the linear optical absorption spectra, as evidenced from the NEA H_2 calculation generally speaking the MTEF dynamics do indeed add non-trivial information. Furthermore for non-linear and time dependent spectra and phenomena, static ion ensemble approaches like NEA are either inapplicable or less suitable than our proposed framework.

More Detail on the ICWF Method

The conditional wave function (CWF) approach can be developed starting from the full molecular wave function for electrons and nuclei, $\Psi(\mathbf{r}, \mathbf{R}, t)$, which can be formally decomposed in terms of the CWFs of each subsystem:

$$\psi_e^\alpha(\mathbf{r}, t) \quad := \quad \int d\mathbf{R} \delta(\mathbf{R}^\alpha(t) - \mathbf{R}) \Psi(\mathbf{r}, \mathbf{R}, t), \tag{34}$$

$$\psi_n^\alpha(\mathbf{R}, t) \quad := \quad \int d\mathbf{r} \delta(\mathbf{r}^\alpha(t) - \mathbf{r}) \Psi(\mathbf{r}, \mathbf{R}, t). \tag{35}$$

From these definitions one can show that the CWFs, $\psi_e^\alpha(t)$ and $\psi_n^\alpha(t)$, obey non-Hermitian equations of motion involving complex potentials which are functionals of the full wave function and cause the time-evolution of the individual CWFs to be non-unitary.[8] The recently developed Interacting-CWF (ICWF) method[9] avoids the direct calculation of these
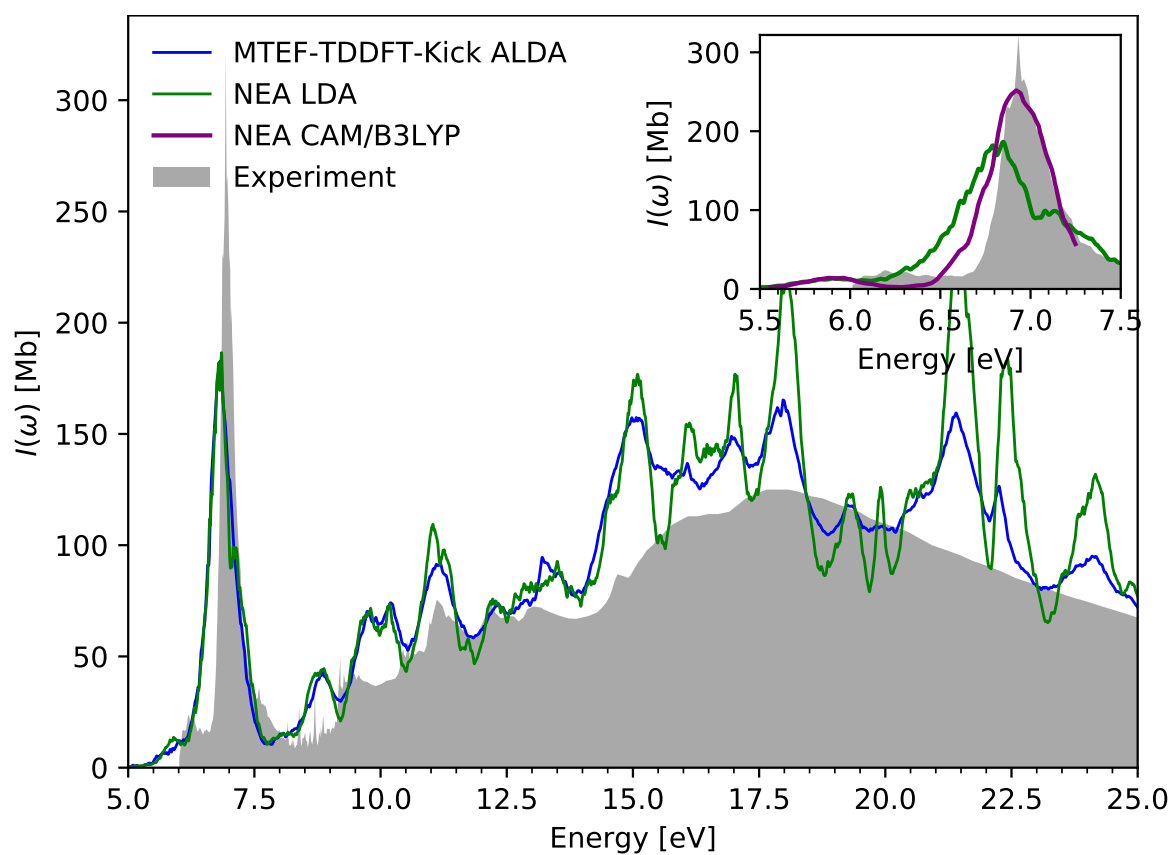
Figure S6: Benzene MTEF-TDDFT-kick spectrum calculated with the adiabatic LDA functional from the main text alongside the NEA spectrum calculated with the LDA functional and a CAM/B3LYP functional recreated from Crespo-Otero and Barbatti[7] compared to experiment.

nonlocal complex potentials by positing the following multiconfigurational CWF basis ansatz for the full many-body wave function:

$$\Psi(r, \mathbf{R}, t) = \sum_{\alpha=1}^{N_c} C_\alpha(t) \psi_e^\alpha(\mathbf{r}, t) \psi_n^\alpha(\mathbf{R}, t). \tag{36}$$

The basis functions in this sum are chosen to be single particle CWFs that satisfy the mean-field, or Hermitian, limit of the CWF equations in which the complex potentials trivially vanish. The upper limit of the sum, N_c, refers to the total number of configurations, which can be stochastically sampled. Including interactions between the trajectories in the ensemble through the coefficients $\mathbf{C}(t) = \{C_1(t), ..., C_{N_c}(t)\}$ corrects the Hermitian-CWF evolution. The time evolution of these coefficients is obtained by inserting eq. (36) directly into the TDSE.

As described in the text, for the kick spectra adapted ICWF algorithm, the CWFs are instead selected as eigenstates of the Hermitian propagators, and used as a static basis. The imaginary and real time equations of motion for the expansion coefficient $\vec{C}$ are then solved using the respective variational principles,[10–13] allowing for a completely closed-loop algorithm for wave function preparation and propagation.

To generate the kick spectra, after preparing the ground state $\vec{C}(0)$, the relevant degree of freedom of the kick operator $\exp(-i\kappa\hat{\mu})$ is applied to each CWF, the Hamiltonian and inverse overlap matrices are reconstructed, and $\vec{C}$ is propagated to the desired time. This procedure is equivalent to propagating in the interaction representation, with $\hat{V}_I(t) = \kappa\delta(t)\hat{\mu}$. Since these matrices are only constructed at time zero, this algorithm is extremely efficient, requiring only the propagation of a $N_c \times 1$ vector by a $N_c \times N_c$ matrix. For comparison, the 1D H2 MTEF-kick results reported here required the propagation of $34,000$ trajectories each consisting of $108^2 \times 1$ electronic wave functions. With a parallelized implementation and hardware allowing approximately 50traj/hr, this equates to roughly 680 compute hours. The ICWF $N_c = 4096$ results reported in the main body by contrast require 17 compute

hours on the same hardware.
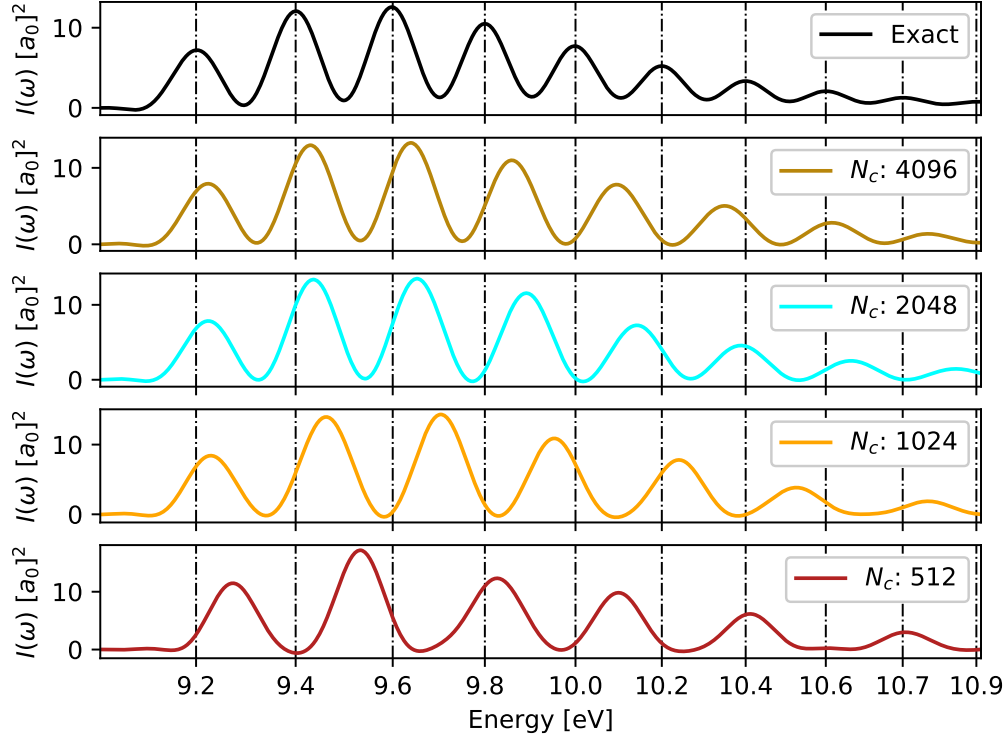
Figure S7: Convergence of the ICWF kick spectra results for increasing numbers of bases N_c. The two lowest lying peaks are mostly converged by $N_c = 1024$, but the higher energy spectra requires more variational degrees of freedom to capture.

With increasing non-redundant variational parameters, one is guaranteed to better capture the initial state and minimize the error of time dependent propagation.[12] As an example of the convergence properties of ICWF-kick, see Fig. S7. These spectra are the result of utilising only lowest energy hermitian propagator eigenstates and propagating for $T_f = 1500$ a.u. with a mask function[14] $W(x) = 1 - 3x^2 + 2x^3$, for $x = t/T_f$ applied to the time signal in the Fourier Transform. The more accurate $N_c = 4096$ results in the main body are initialised using mixes of the three lowest energy CWF eigenstates in roughly equal proportions.

Theoretical and practical developments are underway to implement the ICWF method in arbitrary ab-initio settings.

Complex Absorbing Potentials

Quadratic complex absorbing potentials[15] of the following form were used in all simulations of the one dimensional H_2 model:

$$W_e(r_i) = -i\eta \left[(r_i - r_l)^2 \Theta(r_l - r_i) + (r_i - r_r)^2 \Theta(r_i - r_r) \right]$$

$$W_n(R) = -i\eta(R - R_r)^2 \Theta(R - R_0),$$

(37)

where Θ is the Heaviside function, and η was set to $0.1 \text{Ha}/a_0$ for both subsystems.

The electronic CAP cut offs, r_l and r_r, were placed $10 a_0$ from the walls, while the nuclear CAP start was set at $R_0 = 5.6875 a_0$.

References

(1) Fairlie, D. B. Moyal brackets, star products and the generalized Wigner function. *Chaos, solitons and fractals* **1999**, *10*, 365–371.

(2) Kapral, R. Mixed quantum-classical dynamics. *Journal of Chemical Physics* **1999**, *110*, 8919–8929.

(3) Case, W. B. Wigner functions and Weyl transforms for pedestrians. *American Journal of Physics* **2008**, *76*, 937–946.

(4) Goings, J. J.; Lingerfelt, D. B.; Li, X. Can Quantized Vibrational Effects Be Obtained from Ehrenfest Mixed Quantum-Classical Dynamics? *Journal of Physical Chemistry Letters* **2016**, *7*, 5193–5197.

(5) Tokmakoff, A. Time-Dependent Quantum Mechanics and Spectroscopy. *Lecture* **2014**,

(6) McKemmish, L. K.; McKenzie, R. H.; Hush, N. S.; Reimers, J. R. Quantum entanglement between electronic and vibrational degrees of freedom in molecules. *Journal of Chemical Physics* **2011**,

(7) Crespo-Otero, R.; Barbatti, M. Spectrum simulation and decomposition with nuclear ensemble: Formal derivation and application to benzene, furan and 2-phenylfuran. *Theoretical Chemistry Accounts* **2012**, *131*, 1–14.

(8) Albareda, G.; Appel, H.; Franco, I.; Abedi, A.; Rubio, A. Correlated electron-nuclear dynamics with conditional wave functions. *Physical Review Letters* **2014**,

(9) Albareda, G.; Kelly, A.; Rubio, A. Nonadiabatic quantum dynamics without potential energy surfaces. *Physical Review Materials* **2019**, *3*.

(10) Shi, T.; Demler, E.; Ignacio Cirac, J. Variational study of fermionic and bosonic systems with non-Gaussian states: Theory and applications. *Annals of Physics* **2018**, *390*, 245–302.

(11) Broeckhove, J.; Lathouwers, L.; Kesteloot, E.; Van Leuven, P. On the equivalence of time-dependent variational principles. *Chemical Physics Letters* **1988**, *149*, 547–550.

(12) Lubich, C. On variational approximations in quantum molecular dynamics. *Mathematics of Computation* **2004**, *74*, 765–780.

(13) Ohta, K. Time-dependent variational principle with constraints for parametrized wave functions. *Physical Review A - Atomic, Molecular, and Optical Physics* **2004**, *70*.

(14) Yabana, K.; Nakatsukasa, T.; Iwata, J. I.; Bertsch, G. F. Real-time, real-space implementation of the linear response time-dependent density-functional theory. *Physica Status Solidi (B) Basic Research* **2006**, *243*, 1121–1138.

(15) Muga, J. G.; Palao, J. P.; Navarro, B.; Egusquiza, I. L. Complex absorbing potentials. 2004.

6 | Revealing Ultrafast Phonon Mediated Inter-Valley Scattering through Transient Absorption and High Harmonic Generation Spectroscopies

In recent years as researchers have been exploring the far-from-equilibrium behavior of laser driven materials, phonons have emerged as a key factor in understanding the relaxation of electronic excitations and furthermore developed as a tool to coherently manipulate material properties [4]. A notable example is experimental observation of metastable states in K_3C_{60} displaying superconductive behavior far above T_c which can be induced by resonant driving of phonon modes [13–15]. Ultrafast, laser driven, phonon-induced phase transitions have also been observed in $SrTiO_3$ upon targeted phonon driving, switching from paraelectric to ferroelectric and remaining stable for hours [16, 17], and tuned phonon parametric driving has been observed to stabilize high-temperature ferromagnetism in $YTiO_3$ at temperatures three times higher than the equilibrium thermodynamic transition [18]. Driving the inter-layer shear modes of the layered 2D Transition Metal Dichalcogenide (TMD) material WTe_2 in order to enhance or suppress centro-symmetric symmetry breaking has also been experimentally demonstrated, and is proposed to be a tool for manipulating the predicted topological Weyl semi-metal phases dictated by these symmetries [195, 196].

Thus given this plethora of experimental phenomena, there is increasing demand on theory to disentangle the role of the interactions between the electronic and lattice degrees of freedom in inducing, stabilizing and destroying metastable states. In this chapter we sketch an overview of the differences in how electron-nuclear dynamics are conceptualized within Many Body Perturbation Theory (MBPT) versus the Born-Oppenheimer/semi-classical framework. We then describe how the latter can be formally applied within periodic systems, giving rise to static disorder and Ehrenfest dynamics approaches, and summarize our contribution in paper III bringing MTEF into this field in a manner which respects the ab-initio phonon dispersion. By utilizing MTEF in periodic systems, we introduce a method to systematically capture the quantum thermodynamical equilibirum statistics of the phonons, while simultaneously capturing the far-from-equilibrium electron-phonon dynamics at the mean field level.

6.1 Electron-Phonon Dynamics

The conceptual framework for understanding electron-nuclear interactions in periodic systems can be considerably different than that for molecules. While both invoke the concept of the ground state BOPES in order to define the equilibrium geometry, and harmonic nuclear perturbations from it, the subsequent methodology rapidly begins to diverge from there. As discussed

throughout this thesis the most widely used interpretational framework for quantum nuclear dynamics in molecular systems consists of nuclear wavepackets evolving under the influence of electronic states acting as a static underlying scaffold. This arises from an explicit treatment of the correlation between the two subsystems through diagonalizing the electronic subsystem at each nuclear configuration. However what is commonly done in periodic systems is to diagonalize the electronic system at the equilibrium lattice geometry, giving the Bloch states $|\mathbf{k}n\rangle$ and bands $\epsilon_{\mathbf{k}n}$ in reciprocal space. Separately, the effects of nuclear motion are described by small deviations from the equilibrium geometry giving the phonon modes $|n_{\mathbf{q}\nu}\rangle$ and dispersion branches $\omega_{\mathbf{q}\nu}$ in reciprocal space. The interactions and correlations between these two systems (beyond the harmonic approximation built into the phonon dispersion) are then introduced by starting from this assumption of independence. Consequently, anharmonic interactions are typically truncated at the first or second order in atomic displacement, while the theoretical tools used to incorporate their effect on the static or dynamic properties of the system are generally perturbative in nature [24]. Thus in the language of MBPT, the electron system is 'dressed' or 'renormalized' by the underlying bosonic phonon field as encoded by the various diagrammatic expansions of the interaction within the self-energy of the propagator of the otherwise 'bare' state [98].

Within this perspective, the driven dynamics of an electron-phonon system can be treated by a hierarchy of approximations [23, 38]. At the lowest level are phenomenological models such as the two-temperature model, which assumes the two subsystems act as coupled thermal reservoirs [197]. In the density matrix picture of the electronic system, one can introduce diagonal and off-diagonal relaxation and dephasing times T_1, T_2 which are meant to coarsely represent the total effects of the phonon bath on the excitations and coherences of the electronic system [198]. A method which allows for explicit resolution of the populations of electronic states and phonon modes is the Time Dependent Boltzmann Equation (TDBE), which estimates the scattering between these states using Fermi's golden rule [23, 38]. This method assumes that the interaction between the two subsystems is sufficiently weak that the bare phonon and electron states accurately describe the system for all times. Explicit laser driven dynamics can be included by using the Bloch equation [199–201]. In systems with strong electron-phonon coupling one must begin directly addressing the renormalization of the phonon and electronic eigenstates using Non-Equilibrium Green's Function (NEGF) approaches such as the Kadanoff-Baym equations [36, 100, 101]. At the highest level of complexity, in one-dimensional systems variational approaches like td-DMRG [202] and the hierarchichal equations of motion [34] can be done, although these are generally limited to a small number of sites corresponding to a coarse sampling of the reciprocal space Brillouin Zone.

6.2 Static Disorder

In recent years, there has been increasing interest in incorporating the effects of phonons not through diagrammatic or phenomenological approaches, but instead in a semi-classical framework. In contrast to the picture of interacting quasi-particles painted above, this returns back to territory more familiar to quantum chemists. By treating the nuclei within a supercell (many copies of the irreducible primitive cell) as classical-like point particles, distortions of the nuclear positions within the supercell from their equilibrium positions can be decomposed into contri-

butions from particular phonon branches. By breaking the highly symmetric lattice structure, the properties of the electronic system can be substantially changed, even to the point of recovering electronic properties using uncorrelated ab-initio methods which are typically argued as being rooted in correlated behaviour [203, 204]. This type of approach was used in the 1950s by Ferd Williams [205] and Melvin Lax [206] to understand phonon renormalized optical absorption in solids by drawing comparisons to the Franck-Condon effect, and thus its derivation is an illustrative connection to the formalism of paper II.

The derivation of the Williams-Lax expression for the temperature-dependent phonon renormalized optical absorption proceeds very similarly to that for vibronic linear absorption in molecules. The time dependent transition rate between electronic states n and m induced by a perturbing field $\hat{A}$ can be obtained by summing over the contribution of the nuclear states ν, μ on both surfaces [97]:

$$
\begin{aligned}
W_{n\nu \to m\mu}(t) &= 2\pi \langle \chi_{n\nu}|\hat{A}_{nm}|\chi_{m\mu}\rangle \langle \chi_{m\mu}| \exp\left[i\left(\hat{T}+\hat{U}_m\right)\right]\hat{A}_{mn}\exp\left[-i\left(\hat{T}+\hat{U}_n\right)\right]|\chi_{n\nu}\rangle \\
\hat{A}_{nm} &= \langle \Phi_n(\underline{\underline{\mathbf{R}}})|\hat{A}|\phi_m(\underline{\underline{\mathbf{R}}})\rangle
\end{aligned}
\tag{6.1}
$$

where the transition operator between electronic states n and m, $\hat{A}_{nm}$ retains its dependence on the nuclear configuration. This corresponds to the Herzberg-Teller rate, and by evaluating it at a particular configuration $\underline{\underline{\mathbf{R}}}_0$ the above reduces to the Franck-Condon expression. The observant reader will note that this is essentially identical in form to the dipole-dipole correlation function for linear vibronic absorption in molecules Eq. (3.25). From here the commutators involving the nuclear kinetic energy are disregarded on the argument that the nuclear masses go to infinity, which in this literature is referred to as the semi-classical approximation due to the phonon energy states becoming continuous [97, 206]. By summing over the excited nuclear states and using the resolution of the identity, $\sum_\mu |\chi_{m\mu}\rangle \langle \chi_{m\mu}| = 1$, the above expression reduces to the following for transitions between the electronic ground state 0 and a given excited state n:

$$
\begin{aligned}
W_{0\nu \to n}(t) &= 2\pi \langle \chi_{0\nu}| \exp\left[it\left(\hat{U}_n - \hat{U}_0\right)\right]|\hat{A}_{nm}|^2|\chi_{0\nu}\rangle \\
&= \int d\underline{\underline{\mathbf{R}}}|\chi_{0\nu}(\underline{\underline{\mathbf{R}}})|^2 |A_{nm}(\underline{\underline{\mathbf{R}}})|^2 \exp\left[it\left(U_n(\underline{\underline{\mathbf{R}}}) - U_0(\underline{\underline{\mathbf{R}}})\right)\right],
\end{aligned}
\tag{6.2}
$$

where in the second line we have simply expressed the nuclear states in the real space supercell coordinates $\underline{\underline{\mathbf{R}}}$. The Williams-Lax transition rate is finally obtained by Fourier transforming Eq. (6.2) and performing a canonical average over the vibrational states [97]:

$$
\begin{aligned}
\Gamma_{0 \to n}(\omega, T) &= \frac{1}{Z}\sum_\nu e^{-\beta E_{0\nu}} W_{0\nu \to n}(\omega) \\
&= \frac{2\pi}{Z}\sum_\nu e^{-\beta E_{0\nu}} \int d\underline{\underline{\mathbf{R}}}|\chi_{0\nu}(\underline{\underline{\mathbf{R}}})|^2 |A_{nm}(\underline{\underline{\mathbf{R}}})|^2 \delta\left(U_n(\underline{\underline{\mathbf{R}}}) - U_0(\underline{\underline{\mathbf{R}}}) - \omega\right).
\end{aligned}
\tag{6.3}
$$

This expression tells us that the temperature dependent optical absorption of a solid (or indeed any observable which can be written in a Fermi's golden rule form) can be obtained by performing a thermally weighted average over the real space distribution of a collection of phonon induced distortions, characterized by the distribution function $|\chi_{0\nu}(\underline{\underline{\mathbf{R}}})|^2$. By Monte Carlo sampling the distribution functions, the position dependent electronic quantities can be calculated with any type of electronic structure theory. This approach has been used quite successfully in a large number of applications including calculating phonon renormalized optical absorption

[207, 208], excitonic-phonon interactions [209], and temperature dependent transient absorption (in conjunction with the two-temperature model) [197]. This method can be referred to as 'static disorder' and due to ignoring the nuclear motion is also called the 'clamped ion' or 'frozen phonon' approximation.

In 2020 the Williams-Lax expression was extended by Marios Zacharias and Feliciano Giustino to explicitly decompose the nuclear distortions into contributions from specific phonon modes. In paper III, we recap the process by which one can rewrite the phonon Hamiltonian in terms of normal mode coordinates $z_{\mathbf{q}\nu}$ [24]:

$$H_{ph}(z_{\mathbf{q}\nu}) = \sum_{\mathbf{q}\nu} \omega_{\mathbf{q}\nu} \left(\frac{z_{\mathbf{q}\nu}^2}{l_{\mathbf{q}\nu}^2} + l_{\mathbf{q}\nu}^2 \partial_{z_{\mathbf{q}\nu}}^2 \right), \tag{6.4}$$

where $l_{\mathbf{q}\nu} \propto \sqrt{\hbar/M_0\omega_{\mathbf{q}\nu}}$ is the zero-point energy characteristic length scale for some characteristic mass M_0. The eigenstate solutions of the independent quantum harmonic oscillators in Eq. (6.4) are of course Hermite polynomials written in the coordinates $z_{\mathbf{q}\nu}$. By introducing these into Eq. (6.2) as the nuclear states, and explictily performing the thermally weighted sum in Eq. (6.3), one obtains the following expression [208]:

$$\Gamma_{0\to n}(\omega) = \prod_{\mathbf{q}\nu} \int \frac{dz_{\mathbf{q}\nu}}{\pi\sigma_{\mathbf{q}\nu}^2} \exp\left[-\frac{|z_{\mathbf{q}\nu}|^2}{\sigma_{\mathbf{q}\nu}^2} \right] |A_{0n}(z_{\mathbf{q}\nu})|^2 \delta(U_n(z_{\mathbf{q}\nu}) - U_0(z_{\mathbf{q}\nu}) - \omega), \tag{6.5}$$

where $\sigma_{\mathbf{q}\nu}^2 = l_{\mathbf{q}\nu}^2(2n_{\mathbf{q}\nu,T} + 1)$ is proportional to the Bose-Einstein occupation $n_{\mathbf{q}\nu,T}$ for each phonon. This generalized expression allows one to attribute the role played by particular phonon branches to the renormalization of the electronic observable. This method was recently shown to be equivalent to taking the Feynman expansion of the electron-phonon interaction to all orders in the perturbation, within the adiabatic limit [210], meaning that for the static properties of systems it can in principle be used for arbitrarily strong electron-phonon coupling. Thus given the success of this non-perturbative method in capturing the static properties of a system, it's natural to wonder: what was lost when we chose to disregard the motion of the nuclear system in Eq. (6.1)?

Ehrenfest Dynamics

Most theoretical studies which have looked at the role of semi-classical phonon dynamics in a periodic system have been quite restrictive. Outisde a handful of applications using FSSH [211] or FBTS [74], most employ a single Ehrenfest trajectory and restrict themselves to either the Γ point phonon or a small supercell. Already this is enough to demonstrate changes in the high harmonic generation [76, 77], show evidence of modified vertical electronic excitation [212], and Floquet dress the electronic system through periodic phonon motion [92]. However, by taking larger supercells it has been shown that Ehrenfest dynamics can capture much more. For example by taking a sufficiently large supercell to capture both phases, a laser-driven phase transition in monolayer MoTe$_2$ was simulated, unveiling the microscopic details by which laser driving creates a metastable state that is unstable to anharmonic phonon-phonon scattering [213]. This approach has also been used to study the inter-layer shear-mode driving of T$_d-$WTe$_2$ theoretically supporting the experimentally proposed manipulation of the Weyl points, and has simulated the switching of charge density wave order in photoexcited TiSe$_2$ [29].

However, as discussed at length in paper **II**, single trajectory results also have critical flaws rooted in their failure to capture the quantum nature of the initial nuclear state. This can be of fundamental importance in the behavior of periodic systems. For example, it's been shown that the paraelectric ground state of $SrTiO_3$ is only stable due to the zero-point energy of the lattice [151], and that the ferroelectricity induced upon THz driving is explicable by a quantum superposition of the ground and excited lattice states [80]. Given that MTEF can recover the quantum statistics of the equilibrium thermodynamic phonon distribution and demonstrate quantized dynamical behavior in molecular systems, what can it capture in periodic systems?

6.3 Scientific Contribution and Outlook

In paper **III**, we derive the connection between the Wigner distribution of the phonon system in reciprocal space and the corresponding real space supercell displacement. By writing the thermodynamic equilibrium density matrix in terms of the normal mode coordinates $z_{\mathbf{q}\nu}$ and momenta $P_{\mathbf{q}\nu}$ via the Wigner transform of Eq. (6.4), we can exactly capture the temperature dependent quantum state of the phonon system for any material. This only requires the phonon dispersion $\omega_{\mathbf{q}\nu}$ and real space distortions $\underline{\mathbf{e}}(\mathbf{q}, \nu)$ as input, quantities which are widely available through Density Functional Perturbation Theory. We show that when disregarding the phonon momenta, the denisty matrix exactly reduces to the distribution function in the Zacharias-Giustino formulation of the Williams-Lax transition rate, Eq. (6.5), making this a natural generalization of the static disorder method to include momenta. We then utilize this Wigner function to perform MTEF simulations to study phonon mediated relaxation of selectively excited charge carriers in hexagonal Boron Nitride (hBN). Upon irradiation with circularly polarized light, 2D materials with broken inversion symmetry display selective excitation their conduction band minima, known as valley selectivity [201, 214–220]. In TMDs this 'valley polarization' degree of freedom has been proposed as a candidate for all-optical quantum information storage and manipulation, but is plagued by rapid 'depolarization' or loss of the selective valley excitation due to Coulomb scattering, excitonic effects and phonon scattering [100, 221–223].

We demonstrate that we can capture this effect *only* when including static disorder or explicit phonon dynamics beyond the primitive cell/Γ point phonons. We furthermore found that static phonons capture this relaxation exclusively through elastic scattering. We find that when using dynamic phonons, the electronic system has up-scattering as well down-scattering events, leading to a buildup of carriers outside of the valley regions at long times, at a rate which is proportional to the unphysical loss of zero-point energy (ZPE) in the phonon systems. Nonetheless we validate our approach by comparing static and dynamic phonons to a TDBE calculation. We find that the pump-induced valley asymmetry decays exponentially with a characteristic time scale below 30 fs, and we calculate its temperature dependence across $0-2000$ K, finding good agreement across all theoretical methods with analogous experimental measurements in TMDs [100, 221].

We furthermore demonstrate that this predicted valley relaxation can be measured via two different experimental techniques which can be straightforwardly simulated with MTEF. First we propose a Transient Circular Dichroism (TCD) measurement and simulate the results using TDDFT in a supercell as well as in a tight binding (TB) model. We find that the TCD results directly correspond to the TB valley asymmetry and that we can recreate the same behavior using fully ab-initio TDDFT. Secondly we directly replicate a recent experimental study of

the valley asymmetry in hBN *in-silico* [224]. This experiment tested a measure of the valley asymmetry based on the ellipticity of high harmonics generated by an extremely intense linearly polarized off-resonant field. We confirm that this signal can be recovered but that it decays rapidly due to phonon scattering. Finally in the SI we validate our TB model by recreating the renormalized spectral function in graphene calculated using static disorder thus confirming that MTEF can recover equilibrium phonon induced electronic renormalization under strong coupling regimes. [210]. Quite importantly, we also demonstrate that for the non-equilibrium electronic relaxation MTEF converges with as little as two trajectories.

In the near term, static disorder supercell approaches show the most promise for incorporation into real-time dynamics workflows. As seen in the TDDFT results in paper **III**, inclusion of static disorder leads to fundamental qualitative differences in the dynamics which bring the response more in line with expectations from TDBE and experimental observations in similar systems. Although MTEF suffers from non-physical ZPE leakage at long time scales, as discussed in chapter 5 there are numerous methods to correct for such consequences of taking the mean field approximation. For this particular problem, a recent paper proposes to separate off Wigner transform variables responsible for the ZPE coupling to the electronic system, preserving ZPE throughout the dynamics [225]. In any case, this phenomena only affects the very long-time scale dynamics, and the short-timescale MTEF dynamics agree with both the clamped ion and TDBE approaches as well as experimental observations in similar systems across 2000 K. Given that, for this particular problem, all of these methods converge with extremely small numbers of trajectories, and the ease with which researchers can include these methods, this approach promises to be a very powerful tool in the future of theoretical non-adiabatic dynamics.

Revealing Ultrafast Phonon Mediated Inter-Valley Scattering through Transient Absorption and High Harmonic Spectroscopies

Kevin Lively

Max Planck Institute for the Structure and Dynamics of Matter,
Luruper Chaussee 149, 22761 Hamburg, Germany and
German Aerospace Center (DLR), Institute for Software Technology,
Department of High-Performance Computing, Rathausallee 12, 53757 Sankt Augustin, Germany

Shunsuke A. Sato

Center for Computational Sciences, University of Tsukuba, Tsukuba, Ibaraki 305-8577, Japan and
Max Planck Institute for the Structure and Dynamics of Matter,
Luruper Chaussee 149, 22761 Hamburg, Germany

Guillermo Albareda

Max Planck Institute for the Structure and Dynamics of Matter,
Luruper Chaussee 149, 22761 Hamburg, Germany and
Ideaded, Carrer de la Tecnologia, 35, 08840 Viladecans, Barcelona, Spain

Angel Rubio

Max Planck Institute for the Structure and Dynamics of Matter,
Luruper Chaussee 149, 22761 Hamburg, Germany and
Center for Computational Quantum Physics (CCQ),
Flatiron Institute, New York 10010, New York, USA

Aaron Kelly

Max Planck Institute for the Structure and Dynamics of Matter,
Luruper Chaussee 149, 22761 Hamburg, Germany and
Hamburg Center for Ultrafast Imaging, Universität Hamburg,
Luruper Chaussee 149, 22761 Hamburg, Germany[*]
(Dated: June 22, 2023)

Processes involving ultrafast laser driven electron-phonon dynamics play a fundamental role in the response of quantum systems in a growing number of situations of interest, as evidenced by phenomena such as strongly driven phase transitions and light driven engineering of material properties. To show how these processes can be captured from a computational perspective, we simulate the transient absorption spectra and high harmonic generation signals associated with valley selective excitation and intra-band charge carrier relaxation in monolayer hexagonal boron nitride. We show that the multi-trajectory Ehrenfest dynamics approach, implemented in combination with real-time time-dependent density functional theory and tight-binding models, offers a simple, accurate and efficient method to study ultrafast electron-phonon coupled phenomena in solids under diverse pump-probe regimes which can be easily incorporated into the majority of real-time *ab initio* software packages.

I. INTRODUCTION

Time resolved spectroscopies, such as time and angle resolved photoemission, time resolved photoluminesence and transient absorption spectroscopy (TAS) constitute fundamental tools to study the flow of energy in materials following excitation by light. Understanding the microscopic details of the excitation and relaxation pathways can serve as the basis for deterministic manipulation of material properties for technological applications such as enhanced photodetectors [1, 2], long lived optically controlled qubit registers [3, 4] and attosecond control of magnetic ordering for ultrafast spintronics [5–7]. In parallel to developments pushing the time, energy, and momentum resolution of these spectroscopic techniques, there has been a plethora of phenomena studied under novel conditions such as transient phases and Floquet renormalization under strong parametric driving [8–12], chemical reaction rate modification under exposure to cavity confined fields [13, 14], and exotic quantum phases when layering 2D materials [15, 16]. The study of the microscopic origins of these phenomena pushes the boundaries of theoretical tools which are useful near equilibrium conditions, in particular for one of the most fundamental processes for understanding the behavior of materials: the electron-phonon interaction.

Treating coupled electron-phonon dynamics in simula-

---

tions of periodic systems is typically limited to either phenomenological coupling and decay terms, or coarse approximations such as the two-temperature model [17–19]. Going beyond these options leads one to consider an explicit treatment of the phonon degrees of freedom, which can be achieved through the time-dependent Boltzmann equation (TDBE) [19–24], which is derived in the perturbative limit of the electron-phonon interaction. Attempts to move beyond some of the constraints of the TDBE include approaches based on density matrix formalism, such as the Bloch equation [25–27], the Hierarchical Equations of Motion [28] or the time-dependent Density Matrix Renormalization Group [29, 30] for 1D systems, and non-equilibrium Green's function approaches based on solving the Kadanoff-Baym equations [31–33].

Conversely, the electronic system can be treated in a fully *ab initio* manner and one can still capture the effect of phonon fluctuations, even in cases with very strong coupling, via static displacement approaches which sample phonon distortions in large supercells [34, 35]. In the adiabatic limit, this approach has recently been shown to be equivalent to the Feynman expansion to all orders of the electron-phonon interaction perturbation [36], and is analogous to the nuclear ensemble average technique from molecular physics, where electronic properties are obtained by averaging over the nuclear coordinate distribution on the ground Born-Oppenheimer state [37]. Breaking the high symmetry equilibrium lattice structure of periodic systems has been found to significantly alter the results of ab-initio calculations; disorder has been argued as being responsible for capturing a significant portion of what is usually attributed to electron correlation when using ostensibly uncorrelated DFT methods [38], as well as being the dominant factor in phase transitions typically argued to be rooted in electronic structure [39].

A natural step beyond including the static disorder of the nuclei is to also consider their dynamics, which opens the possibility to treat time-dependent response properties where the nuclear forces are dependent on nonequilibrium electronic configurations. A mean field treatment that can be applied in this context is the multi-trajectory Ehrenfest approach (MTEF), which allows one to recover the quantum statistics of the equilibrium nuclear subsystem [40] whilst approximating the time-evolution using Ehrenfest trajectories. This approach has been shown to capture Franck-Condon physics [41] as well as time-resolved out of equilibrium system dynamics [42–44]. Propagating the system in real time allows for coherent electronic evolution at short time scales, while accounting for all orders of interaction with both external fields and the phonon system (at the mean field level).

Although the basic ingredients required for MTEF are already available in most real-time *ab initio* codes, and despite some existing formulations of reciprocal space semi-classical dynamics in the literature [45–47], to the authors' best knowledge, application of this method has not been widely explored in periodic systems, nor has the static displacement approach been widely applied to time-resolved phenomena. Rather, most uses of *ab initio* semi-classical dynamics in periodic systems involve only a single trajectory [48–50], typically using a primitive unit cell or initializing the phonon distortion with classical molecular dynamics simulations which often fail to capture the exact quantum statistics of the initial state [51]. Nonetheless, inclusion of more phonon modes through supercell dynamics allows for detailed study of fundamental processes such as the relaxation of excited electrons through phonon emission, anharmonic phonon-phonon scattering and phase transitions, even at the single trajectory level [52, 53].

Therefore, in this work we formulate the Wigner representation for the phonon subsystem in a generic manner using *ab initio* dispersion relations of real materials, yielding a framework that systematically captures the equilibrium properties of the phonon system. While MTEF is well known to suffer from zero point energy (ZPE) leakage and incorrect thermalization between the quantum and classical systems at long time scales, there are several schemes that can systematically correct these failures with added computational cost [54, 55]. However, as our focus here is limited to studies of the short time-scale dynamics of strongly driven systems, we will not pursue such corrections and simply aim to discover what can be achieved at the mean field level.

As an illustrative example we study ultrafast phonon mediated electronic reorganization following valley selective laser excitation in monolayer hexagonal boron nitride (hBN), demonstrating the ability of MTEF to capture many of the essential features of the process which has been argued to be a significant driver of valley selective relaxation in Transition Metal Dichalcogenides (TMDs) [31, 56–58]. Due to negligible spin-orbit coupling in hBN, the two K valleys in the Brillouin Zone (BZ) are degenerate, while valley specific selection rules are preserved upon interaction with circularly polarized light [59–62], making this a prototypical material to study the relaxation of excited charge carriers theoretically. Using a real space *ab initio* supercell approach with time-dependent density functional theory (TDDFT), and a reciprocal space tight binding (TB) model, we find that including phonon fluctuations leads to a rapid redistribution of excited charge carriers within a characteristic time scale of less than 30 fs, and that these results converge with as little as two trajectories.

We show that in the static limit, the harmonic Wigner distribution of phonon momenta and coordinates reduces to the phonon distribution obtained in the reciprocal space picture of Williams-Lax theory [35]. We compare the results of propagating the electronic system with MTEF to the limit of frozen phonons, as well as the TDBE approach, finding broad qualitative agreement between these approaches across temperatures from $0-2000$ K while reproducing the experimentally observed low-temperature behaviour of analogous TMD systems. Finally, we demonstrate the flexibility of our method to predict and recreate spectroscopic experiments by simu-

lating two different transient absorption measurements. First we propose a circularly polarized TAS measurement and demonstrate the signal corresponds directly to the valley asymmetry decay. Second, we replicate a recently performed study [63] using the ellipticity of harmonics generated under extreme laser driving to track tunable valley selective excitation in hBN using bichromatic counter-rotating 'trefoil' pumps, also showing a rapid decay of the observable signal. Both cases demonstrate the ease with which our approach can be applied within tight binding and fully *ab initio* real time electronic dynamics software packages under arbitrary pump-probe setups.

II.   THEORY

Here we briefly summarize how the description of the phonon subsystem can be formulated based on the phonon dispersion of real materials within MTEF by appealing to the Wigner distribution of the phonon system. We then elaborate on the connections between this approach and the static displacement formalism, and we briefly outline the TDBE that will be used for later comparison. We generally use atomic units throughout, though sometimes for clarity $\hbar$ is written explictly.

A.   Multitrajectory Ehrenfest dynamics

While a variety of routes to derive the Ehrenfest equations of motion are available, we focus here on how the MTEF approach can be derived as the uncorrelated solution to the quantum-classical Liouville equation (QCLE) [64, 65], which describes the approximate time-evolution of the total density matrix. The partial Wigner transform is employed, which for an arbitrary operator is defined as:

$$\hat{O}_W(\mathbf{R}, \mathbf{P}) = (2\pi)^{-dN} \int d\mathbf{Q} e^{-i\mathbf{P}\cdot\mathbf{Q}} \langle \mathbf{R} + \mathbf{Q}/2|\hat{O}|\mathbf{R} - \mathbf{Q}/2\rangle .$$

$$(1)$$

Here the list of variables $(\mathbf{R}, \mathbf{P})$ represents the full set of nuclear position $\mathbf{R} = (\mathbf{R}_1, \ldots, \mathbf{R}_N)$ and momentum $\mathbf{P} = (\mathbf{P}_1, \ldots, \mathbf{P}_N)$ variables which are vectors in $N \times d$ Cartesian dimensions, and we note that the operator character of objects in the electronic Hilbert space is unchanged by the partial Wigner transform.

In the mean field limit the density operator can be factorized $\hat{\rho}_W = \rho_{\mathrm{n},W}(\mathbf{R}, \mathbf{P}, t)\hat{\rho}_\mathrm{e}(t)$, and the Wigner function of the nuclear degrees of freedom can be represented by an ensemble of N_t independent trajectories, $\rho_{\mathrm{n},W}(\mathbf{R}, \mathbf{P}, t) = \sum_{i=1}^{N_t} w_i \delta(\mathbf{R} - \mathbf{R}_i(t))\delta(\mathbf{P} - \mathbf{P}_i(t))$, with weights w_i. The time evolution of the electronic density and the phase space coordinates is given by the Ehrenfest

equations of motion [40]:

$$\partial_t \hat{\rho}_e(t) = -i\left[\hat{H}_W(\mathbf{R}_i(t), \mathbf{P}_i(t)), \hat{\rho}_e(t)\right]$$

$$\dot{\mathbf{P}}_i = -\mathrm{Tr}\left[\hat{\rho}_e(t)\nabla_\mathbf{R}\hat{H}_W(\mathbf{R}, \mathbf{P})\Big|_{(\mathbf{R}_i(t), \mathbf{P}_i(t))}\right] \quad (2)$$

$$\dot{\mathbf{R}}_i = \frac{\mathbf{P}_i}{\mathbf{M}},$$

where $\mathbf{M}$ are the nuclear masses. These equations are solved for the independent trajectories with initial conditions $(\mathbf{R}_i(0), \mathbf{P}_i(0))$ sampled from $\rho_{\mathrm{n},W}$. Observables are constructed by averaging over the ensemble of trajectories; in the case of equal trajectory weights, $\langle O(t)\rangle = \frac{1}{N_t}\sum_{i=1}^{N_t} \mathrm{Tr}\left[\hat{O}_W(\mathbf{R}_i(t), \mathbf{P}_i(t))\hat{\rho}_W(\mathbf{R}_i(0), \mathbf{P}_i(0))\right]$.

B.   The Phonon Subsystem

For completeness we restate some textbook definitions of the phonon coordinates, in particular drawing from the work of Brüesch [66] and Giustino [67], with special emphasis on the often less well described conjugate momenta, which play an important role in the MTEF method (however, for a notable exception see [68]).

For a supercell composed of $N_p = N_1 \times \ldots \times N_l$ primitive cells in l periodic dimensions, we utilize the Born von-Karman (BvK) boundary conditions (see SI.1 A). Each primitive cell contains N_c unique atoms which for a given lattice configuration have equilibrium positions in the primitive cell of $\mathbf{R}_\alpha^0$, for $\alpha = 1, \ldots, N_c$. The equilibrium position of a given atom α within the supercell is specified by the primitive cell position $\mathbf{R}_p$; for primitve cell index $p = 1, \ldots, N_p$, and the primitive cell equilibrium position, $\mathbf{R}_{\alpha p}^0 = \mathbf{R}_p + \mathbf{R}_\alpha^0$. We further denote small displacements from these positions via $\delta\mathbf{R}_{\alpha p} = \mathbf{R}_{\alpha p} - \mathbf{R}_{\alpha p}^0$. Canonically conjugate momenta, $\mathbf{P}_{\alpha p}$, can then be defined by the commutation relation $[\mathbf{R}_{\alpha p}, \mathbf{P}_{\alpha p}] = i\hbar\delta_{\alpha,\alpha'}\delta_{p,p'}$.

Using the textbook definition of the interatomic force constant matrix and it's Fourier transform, the dynamical matrix (see SI.1 B), we define the complex normal coordinates and momentum for a given phonon quasi-momentum $\mathbf{q}$ and branch ν as the following linear transformation :

$$z_{\mathbf{q}\nu} = N_p^{-1/2} \sum_{\alpha p} e^{-i\mathbf{q}\cdot\mathbf{R}_p}(M_\alpha/M_0)^{1/2}\mathbf{e}_{\alpha\nu}^*(\mathbf{q}) \cdot \delta\mathbf{R}_{\alpha p}$$

$$P_{\mathbf{q}\nu} = N_p^{-1/2} \sum_{\alpha p} e^{-i\mathbf{q}\cdot\mathbf{R}_p}(M_0/M_\alpha)^{1/2}\mathbf{e}_{\alpha\nu}^*(\mathbf{q}) \cdot \mathbf{P}_{\alpha p}.$$

$$(3)$$

Here, $\mathbf{e}_{\alpha\nu}(\mathbf{q}) \in \mathbb{C}^d$ is the normal mode of vibration describing the displacement of atom α in the primitive cell with mass M_α. M_0 is a reference mass, taken to be the mass of the proton. The inverse of this transformation

reads as

$$\delta\mathbf{R}_{\alpha p} = N_p^{-1/2} \sum_{\mathbf{q}\nu} e^{i\mathbf{q}\cdot\mathbf{R}_p}(M_0/M_\alpha)^{1/2}\mathbf{e}_{\alpha\nu}(q)z_{\mathbf{q}\nu}$$
$$\mathbf{P}_{\alpha p} = N_p^{-1/2} \sum_{\mathbf{q}\nu} e^{i\mathbf{q}\cdot\mathbf{R}_p}(M_\alpha/M_0)^{1/2}\mathbf{e}_{\alpha\nu}(q)P_{\mathbf{q}\nu}. \quad (4)$$

It is easily shown that the complex normal position and momenta obey the normal commutation relations for phonons [66–69]:

$$[z_{\mathbf{q}\nu}, P_{-\mathbf{q}'\nu'}] = i\hbar\delta_{\mathbf{q}\mathbf{q}'}\delta_{\nu\nu'}. \quad (5)$$

The redundancy in the complex normal coordinates, seen by $z_{-\mathbf{q}\nu} = z_{\mathbf{q}\nu}^*$, can be removed by introducing the so called real normal coordinates [66, 67]. To show how this is done, we start by partitioning the $\mathbf{q}$ grid in the first BZ into three sets, in the manner of Giustino and Brüesch. Call set $\mathcal{A}$ the set of vectors invariant under inversion modulo addition with a reciprocal lattice vector $\mathbf{G}$, i.e. $\mathbf{q} = -\mathbf{q}+\mathbf{G}$. Set $\mathcal{B}$ and $\mathcal{C}$ are partitioned in such a way that all vectors $\mathbf{q} \in \mathcal{C}$ are obtained from $\mathbf{q}' \in \mathcal{B}$ via inversion, i.e. $\mathbf{q}' = -\mathbf{q}+\mathbf{G}$. This leads to the following definitions

$$z_{\mathbf{q}\nu} = \begin{cases} x_{\mathbf{q}\nu} & \text{for } \mathbf{q} \in \mathcal{A} \\ x_{\mathbf{q}\nu} + iy_{\mathbf{q}\nu} & \text{for } \mathbf{q} \in \mathcal{B} \end{cases} \quad (6)$$

$$P_{\mathbf{q}\nu} = \begin{cases} r_{\mathbf{q}\nu} & \text{for } \mathbf{q} \in \mathcal{A} \\ r_{\mathbf{q}\nu} + is_{\mathbf{q}\nu} & \text{for } \mathbf{q} \in \mathcal{B} \end{cases} \quad (7)$$

whereby the following properties hold true

$$\begin{aligned} x_{-\mathbf{q}\nu} = x_{\mathbf{q}\nu}, & \quad r_{-\mathbf{q}\nu} = r_{\mathbf{q}\nu} \\ y_{-\mathbf{q}\nu} = -y_{\mathbf{q}\nu}, & \quad s_{-\mathbf{q}\nu} = -s_{\mathbf{q}\nu} \end{aligned} \quad (8)$$

Now we can rewrite (4) as

$$\delta\mathbf{R}_{\alpha p} = N_p^{-1/2}(M_0/M_\alpha)^{1/2} \left(\sum_{\mathbf{q}\in\mathcal{A},\nu} \mathbf{e}_{\alpha\nu}(\mathbf{q})x_{\mathbf{q}\nu}\cos(\mathbf{q}\cdot\mathbf{R}_p) \right.$$
$$\left. + 2\mathrm{Re}\left[\sum_{\mathbf{q}\in\mathcal{B},\nu} e^{i\mathbf{q}\cdot\mathbf{R}_p}\mathbf{e}_{\alpha\nu}(\mathbf{q})(x_{\mathbf{q}\nu}+iy_{\mathbf{q}\nu}) \right] \right)$$
$$\mathbf{P}_{\alpha p} = N_p^{-1/2}(M_\alpha/M_0)^{1/2} \left(\sum_{\mathbf{q}\in\mathcal{A},\nu} \mathbf{e}_{\alpha\nu}(\mathbf{q})r_{\mathbf{q}\nu}\cos(\mathbf{q}\cdot\mathbf{R}_p) \right.$$
$$\left. + 2\mathrm{Re}\left[\sum_{\mathbf{q}\in\mathcal{B},\nu} e^{i\mathbf{q}\cdot\mathbf{R}_p}\mathbf{e}_{\alpha\nu}(\mathbf{q})(r_{\mathbf{q}\nu}+is_{\mathbf{q}\nu}) \right] \right), \quad (9)$$

where the sum over $\mathcal{C}$ has been included by taking twice the real part of the sum over $\mathcal{B}$. With this removal of the redundancy, one can see that this linear transformation contains dN_cN_p independent variables corresponding to

$x_{\mathbf{q}\nu}$ for $\mathbf{q} \in \mathcal{A}$ and $x_{\mathbf{q}\nu}, y_{\mathbf{q}\nu} \in B$, with canonical conjugates $r_{\mathbf{q}\nu}$ for $\mathbf{q} \in \mathcal{A}$ and $r_{\mathbf{q}\nu}, s_{\mathbf{q}\nu}$ for $\mathbf{q} \in \mathcal{B}$, defining canonical commutation relations

$$\begin{aligned} [x_{\mathbf{q}\nu}, r_{\mathbf{q}'\nu'}] = [y_{\mathbf{q}\nu}, s_{\mathbf{q}'\nu'}] = i\hbar\delta_{\mathbf{q}\mathbf{q}'}\delta_{\nu\nu'} \\ [x_{\mathbf{q}\nu}, y_{\mathbf{q}'\nu'}] = [r_{\mathbf{q}\nu}, s_{\mathbf{q}'\nu'}] = 0 \\ [x_{\mathbf{q}\nu}, s_{\mathbf{q}'\nu'}] = [y_{\mathbf{q}\nu}, r_{\mathbf{q}'\nu'}] = 0. \end{aligned} \quad (10)$$

Following Giustino we define the characteristic length scale of the phonon frequencies as

$$l_{\mathbf{q}\nu} = \begin{cases} \left(\frac{\hbar}{2M_0\omega_{\mathbf{q}\nu}}\right)^{1/2} & \text{for } \mathbf{q} \in \mathcal{B}, \mathcal{C} \\ 2\left(\frac{\hbar}{2M_0\omega_{\mathbf{q}\nu}}\right)^{1/2} & \text{for } \mathbf{q} \in \mathcal{A} \end{cases} \quad (11)$$

and rescale the coordinates as $\tilde{z}_{\mathbf{q}\nu} = z_{\mathbf{q}\nu}/l_{\mathbf{q}\nu}$ and $\tilde{P}_{\mathbf{q}\nu} = P_{\mathbf{q}\nu}l_{\mathbf{q}\nu}/\hbar$. With this linear transformation we use the properties of the normal modes subject to the BvK boundary conditions to rewrite the real space nuclear Hamiltonian in the harmonic limit as:

$$\hat{H}_{\mathrm{ph}} = \frac{1}{2}\sum_{\mathbf{q}\in\mathcal{A},\nu} \omega_{\mathbf{q}\nu}\left(\tilde{r}_{\mathbf{q}\nu}^2 + \tilde{x}_{\mathbf{q}\nu}^2\right)$$
$$+ \frac{1}{2}\sum_{\mathbf{q}\in\mathcal{B},\nu} \omega_{\mathbf{q}\nu}\left(\tilde{r}_{\mathbf{q}\nu}^2 + \tilde{x}_{\mathbf{q}\nu}^2 + \tilde{s}_{\mathbf{q}\nu}^2 + \tilde{y}_{\mathbf{q}\nu}^2\right). \quad (12)$$

1. Phonon Wigner function

The Wigner transform of the density matrix of a set of uncoupled phonons in the canonical ensemble can be written in terms of the reduced coordinates as [70]:

$$\rho_{\mathrm{ph},W} =$$
$$\prod_{\nu,\mathbf{q}\in\mathcal{A},\mathcal{B}} \frac{\tanh(\beta\omega_{\mathbf{q}\nu}/2)}{\pi} \exp\left[-\tanh(\beta\omega_{\mathbf{q}\nu}/2)\left(\tilde{r}_{\mathbf{q}\nu}^2 + \tilde{x}_{\mathbf{q}\nu}^2\right)\right]$$
$$\times \prod_{\nu,\mathbf{q}\in\mathcal{B}} \frac{\tanh(\beta\omega_{\mathbf{q}\nu}/2)}{\pi} \exp\left[-\tanh(\beta\omega_{\mathbf{q}\nu}/2)\left(\tilde{s}_{\mathbf{q}\nu}^2 + \tilde{y}_{\mathbf{q}\nu}^2\right)\right], \quad (13)$$

for $\beta = 1/k_bT$, where the reduced coordinates are now treated as continuous degrees of freedom. We use this distribution to sample the phonon modes when performing real space supercell calculations; the nuclear configuration associated with a particular phonon coordinate configuration is obtained by simply using Eq. (9) after sampling the reduced coordinates from Eq. (13). The required inputs are $\mathbf{e}_{\alpha\nu}(\mathbf{q})$ and $\omega_{\mathbf{q}\nu}$, which are easily obtained via Density Functional Perturbation Theory (DFPT) calculations such as the implementation in Quantum Espresso [71, 72].

We note here that while sampling the equilibrium phonon distribution in Eq. (13) exactly captures the quantum statistics of the phonon system only in the harmonic limit, the time evolution is not constrained to this limit as the nuclei are subject to the (Ehrenfest) forces

coming from the driven electronic system. In this sense, the phonon coordinate picture can be viewed as a convenient basis in which the nuclear system can be initialized, rather than a limitation of MTEF to the harmonic approximation.

C. Connection to Static Displacement Methods

In the special displacement method (SDM) introduced by Zacharias and Giustino [34, 35], static thermodynamic properties of periodic systems (within the Born-Oppenheimer approximation) are calculated by taking specific phonon coordinate configurations from the Williams-Lax nuclear coordinate distribution, written in reciprocal space [35]. For an arbitrary operator $\hat{O}$ the expectation value at a given temperature is given as

$$O(T) = \prod_{\nu,\mathbf{q} \in \mathcal{A}} \int \frac{dx_{\mathbf{q}\nu}}{\sqrt{\pi}\sigma_{\mathbf{q}\nu}} e^{-\frac{x_{\mathbf{q}\nu}^2}{\sigma_{\mathbf{q}\nu}^2}}$$
$$\times \prod_{\nu,\mathbf{q} \in \mathcal{B}} \int \frac{dx_{\mathbf{q}\nu} dy_{\mathbf{q}\nu}}{\pi\sigma_{\mathbf{q}\nu}^2} e^{-\frac{x_{\mathbf{q}\nu}^2 + y_{\mathbf{q}\nu}^2}{\sigma_{\mathbf{q}\nu}^2}} O^{\{x_{\mathbf{q}\nu}, y_{\mathbf{q}\nu}\}}(T), \quad (14)$$

with $\sigma_{\mathbf{q}\nu}^2 = l_{\mathbf{q}\nu}^2 (2n_{\mathbf{q}\nu,T} + 1)$, for the Bose-Einstein occupation of the mode, $n_{\mathbf{q}\nu,T} = [\exp(\beta\hbar\omega_{\mathbf{q}\nu}) - 1]^{-1}$, and $O^{\{x_{\mathbf{q}\nu}, y_{\mathbf{q}\nu}\}}(T)$ referring to the expectation value of $\hat{O}$ at temperature T with respect to the electronic system, evaluated at phonon configuration $\{x_{\mathbf{q}\nu}, y_{\mathbf{q}\nu}\}$.

The connection to the Wigner transformation of the phonon coordinates can been seen by inserting $\sigma_{\mathbf{q}\nu}$ and $n_{\mathbf{q}\nu,T}$ for the distribution functions of Eq. (14). Keeping in mind our definition of $l_{\mathbf{q}\nu}$ in Eq. (11), one immediately arrives at Eq. (13) for the position coordinates. Therefore, including the phonon momenta is in some sense an extension of this method to dynamic ions. Thus, given the success of the SDM in capturing phonon renormalization using small numbers of displacement samples, one can consider sampling approaches inspired by this method which incorporate momenta. We explore this possibility in SI.6, but find no significant advantage for the observables studied here.

In what follows, we refer to a simulation protocol as 'static' when we sample exclusively positions from Eq. (13) (i.e. from the distribution function in Eq. (14)), constrain the phonon coordinates at this initial configuration and evolve only the electronic system in time. This approximation is sometimes referred to as the 'clamped ion', 'frozen phonon', or 'static disorder' approximation. In contrast we refer to a protocol as 'dynamic' when both phonon coordinate and momenta initial conditions are sampled from Eq. (13) and the phonon coordinates evolve along with the electronic system according to Eq. (2).

D. Time-dependent Boltzmann equation

In order to make connections with statistical mechanics approaches based on perturbation theory, we also make comparisons with a time-dependent Boltzmann equation treatment of the problem. Starting from Fermi's golden rule for the first-order rate equation for electron occupation in band n at crystal momentum $\mathbf{k}$, $f_{n\mathbf{k}}$ and phonon occupation $n_{\mathbf{q}\nu}$ due to electron-phonon scattering processes: [19, 21]

$$\partial_t f_{n\mathbf{k}} = 2\pi \sum_{m\nu\mathbf{q}} |g_{mn}^\nu(\mathbf{k}, \mathbf{q})|^2$$
$$\times \{(1 - f_{n\mathbf{k}}) f_{m\mathbf{k}+\mathbf{q}} \delta(\epsilon_{n\mathbf{k}} - \epsilon_{m\mathbf{k}+\mathbf{q}} + \omega_{\mathbf{q}\nu})(n_{\mathbf{q}\nu} + 1)$$
$$+ (1 - f_{n\mathbf{k}}) f_{m\mathbf{k}+\mathbf{q}} \delta(\epsilon_{n\mathbf{k}} - \epsilon_{m\mathbf{k}-\mathbf{q}} - \omega_{\mathbf{q}\nu}) n_{\mathbf{q}\nu}$$
$$+ f_{n\mathbf{k}}(1 - f_{m\mathbf{k}+\mathbf{q}}) \delta(\epsilon_{n\mathbf{k}} - \epsilon_{m\mathbf{k}-\mathbf{q}} - \omega_{\mathbf{q}\nu})(n_{\mathbf{q}\nu} + 1)$$
$$+ f_{n\mathbf{k}}(1 - f_{m\mathbf{k}+\mathbf{q}}) \delta(\epsilon_{n\mathbf{k}} - \epsilon_{m\mathbf{k}-\mathbf{q}} + \omega_{\mathbf{q}\nu}) n_{\mathbf{q}\nu}\}, \quad (15)$$

and

$$\partial_t n_{\mathbf{q}\nu} = 4\pi \sum_{mn\mathbf{k}} |g_{mn}^\nu(\mathbf{k}, \mathbf{q})|^2 f_{n\mathbf{k}}(1 - f_{m\mathbf{k}+\mathbf{q}})$$
$$\times \{\delta(\epsilon_{n\mathbf{k}} - \epsilon_{m\mathbf{k}+\mathbf{q}} - \omega_{\mathbf{q}\nu})(n_{\mathbf{q}\nu} + 1)$$
$$- \delta(\epsilon_{n\mathbf{k}} - \epsilon_{m\mathbf{k}+\mathbf{q}} + \omega_{\mathbf{q}\nu}) n_{\mathbf{q}\nu}\}. \quad (16)$$

Here $g_{mn}^\nu(\mathbf{k}, \mathbf{q})$ are the electron-phonon matrix elements in the band basis. Since we focus mainly on the short time scale dynamics, we do not include phonon-phonon scattering in our TDBE analysis.

III. TIGHT BINDING MODEL

We treat the electronic structure of hBN in a widely used DFT-based tight binding model with nearest neighbor hopping between the two inequivalent sublattice sites. While, in principle, the electron-phonon coupling matrix elements can be extracted from existing DFPT packages, these quantities are almost always given as absolute values which can be used in the TDBE. As the time evolution of the electronic dynamics in MTEF also requires the complex phase of the coupling matrix elements, we derive a BZ extensive expression for the coupling. We treat the nuclear dependence of the electronic Hamiltonian by modeling the hopping term to be exponentially dependent on interatomic distance:

$$t(\mathbf{R}_i, \mathbf{R}_j) = t_0 \exp\left(-b\left[\frac{|\mathbf{R}_i - \mathbf{R}_j|}{d_0} - 1\right]\right), \quad (17)$$

where t_0 is the equilibrium hopping term, b is the electron-phonon coupling factor, and d_0 is the equilibrium distance between sublattice sites i and j. This fitting is common in literature for graphene tight binding models, and b can be related to experimental observables [73–75].

For simplicity we restrict our study to two dimensions by only considering phonon branches with no out of plane component. We perform a second order expansion of ionic displacement from equilibrium while restricting the hopping term expansion to first order, ignoring the second order electron-phonon coupling coefficients, or Debye-Waller terms, which is quite often done in literature [67, 75]. By rewriting the electronic operators in terms of plane waves and the nuclear displacements in terms of phonon complex normal coordinates, we obtain the following reciprocal space Hamiltonian (see SI.2 for details):

$$
\hat{H}_W(\mathbf{X}) = \frac{1}{2} \sum_{\mathbf{q}\nu} \omega_{\mathbf{q}\nu} \left(\tilde{P}_{\mathbf{q}\nu}^2 + \tilde{z}_{\mathbf{q}\nu}^2 \right) + \sum_{\alpha \in \{a,b\}} \Delta_\alpha \hat{\alpha}_\mathbf{k}^\dagger \hat{\alpha}_\mathbf{k}
$$
$$
- t_0 \sum_\mathbf{k} \left(\hat{a}_\mathbf{k}^\dagger \hat{b}_\mathbf{k} \sum_{\boldsymbol{\delta}} e^{i\mathbf{k}\cdot\boldsymbol{\delta}} + c.c. \right) + \sum_{\mathbf{q}\nu} \tilde{z}_{\mathbf{q}\nu} l_{\mathbf{q}\nu} \hat{M}(\mathbf{q},\nu),
$$
$$
\hat{M}(\mathbf{q},\nu) = \sum_{\mathbf{k}\boldsymbol{\delta}} g_\nu^\delta(\mathbf{q}) \left(\hat{a}_{\mathbf{k}+\mathbf{q}}^\dagger \hat{b}_\mathbf{k} e^{i\mathbf{k}\cdot\boldsymbol{\delta}} + \hat{b}_\mathbf{k}^\dagger \hat{a}_{\mathbf{k}-\mathbf{q}} e^{-i\mathbf{k}\cdot\boldsymbol{\delta}} \right).
$$
$$
(18)
$$

Here $\mathbf{X} = (\mathbf{z}, \mathbf{P})$ is the collection of phonon coordinates, $\hat{\alpha}_\mathbf{k}$ are the electronic site operators for sites $\alpha = \{a, b\}$ with onsite energies $\Delta_\alpha = \pm\Delta$ responsible for opening the gap $E_g = 2|\Delta|$. Nearest neighbor sites are connected by vectors $\boldsymbol{\delta}$. The matrices $\hat{M}(\mathbf{q}, \nu)$ describe the coupling of the phonon normal coordinates to the electronic system, resulting in the scattering of electronic planewaves from $\mathbf{k} \to \mathbf{k} \pm \mathbf{q}$, and depend on coupling terms $g_\nu^\delta(\mathbf{q})$, which themselves depend on $\mathbf{e}_{\alpha\nu}(\mathbf{q})$.

The required inputs for this model are the lattice constant a_0, onsite energies Δ_α, hopping term t_0, phonon dispersion $\omega_{\mathbf{q}\nu}$, polarization $\mathbf{e}_\nu(\mathbf{q})$ and electron-phonon coupling factor b. In this work, we obtained the lattice constant and phonon information from Quantum Espresso cell relaxation and phonon dispersion calculations, and fit the hopping term, onsite energies and coupling factor from a symmetric two band approximation to the conduction band calculated using an uncorrected LDA xc functional. See the Computational Methods section for further details.

The present tight-binding model clearly involves a major simplification, as it treats the electronic system at the independent particle level. However, this simplified treatment is not entirely unreasonable as one can eliminate excitonic effects in experimental setups by placing the monolayer onto a conductive substrate, which screens the electric field and allows the study of free carriers [76, 77]. Furthermore, the purpose of the TB model is mainly in developing comparisons with *ab initio* simulations, which go beyond this limitation. Nevertheless, it would be interesting to go beyond this limit in future applications.

1. Implementing the MTEF Method with the TB Model

For each initial condition $\mathbf{X}^0$ that is sampled from $\rho_{\text{ph},W}(\mathbf{X})$, one can find the single particle orbitals for $\hat{H}_W(\mathbf{X}^0)$,

$$
\hat{H}_W(\mathbf{X}^0) |\psi_l(\mathbf{X}^0)\rangle = \epsilon_l(\mathbf{X}^0) |\psi_l(\mathbf{X}^0)\rangle \quad (19)
$$

and construct the density operator,

$$
\hat{\rho}_{\text{e}} = \sum_l f(\epsilon_l^0, T) |\psi_l\rangle \langle\psi_l|, \quad (20)
$$

where $f(\epsilon_l^0, T)$ is the Fermi occupation at temperature T evaluated for the orbital energy $\epsilon_l(\mathbf{X}^0) = \epsilon_l^0$ at this initial configuration. In the above expression for the electronic density we have suppressed the dependence of the orbital on the phonon coordinates. One may then propagate a set of trajectories, associated with the set of initial conditions, according to the MTEF equations of motion (Eq.(2)), which in the case of the present TB model are more conveniently expressed as follows,

$$
\dot{\tilde{P}}_{\mathbf{q}\nu}^i = - \left(\omega_{\mathbf{q}\nu} \tilde{z}_{\mathbf{q}\nu}^i + l_{\mathbf{q}\nu} \text{Tr}\left[M_{\mathbf{q}\nu} \rho_e^i(t) \right] \right)
$$
$$
\dot{\tilde{z}}_{\mathbf{q}\nu}^i = \omega_{\mathbf{q}\nu} \tilde{P}_{\mathbf{q}\nu}^i \quad (21)
$$
$$
i\partial_t |\psi_l^i\rangle = \hat{H}_W(\mathbf{X}^i(t)) |\psi_l^i\rangle.
$$

We have validated the accuracy of the MTEF treatment of this form of tight binding model by comparing with the nonequilibrium Green's function (NEGF) results of Nery and Mauri [36] for the phonon renormalization of the electronic spectral function in graphene, and we find that the spectral function generated from MTEF simulations is in good agreement with the NEGF results. See the SI.4 for details.

IV. RESULTS

A. Excited Carrier Relaxation in hBN

Due to the lack of inversion symmetry, hBN is a strong insulator with a gap around the K/K' points that is depicted in panel (b) of Fig. 1.

This also leads to the potential for selective excitation in the BZ around the K/K' points upon irradiation with circularly polarized light.

For simplicity, we did not include direct coupling between the laser field and the phonon modes, and as such the laser field is only indirectly coupled to the phonons via the modification of the electronic occupations. To couple the electronic system to the laser field in the longwave approximation we use a Peierls substitution to modify the electronic wavevector $\mathbf{k}$:

$$
\mathbf{k}(t) = \mathbf{k} - \int^t \mathbf{E}(t')dt' = \mathbf{k} + \frac{1}{c}\mathbf{A}(t). \quad (22)
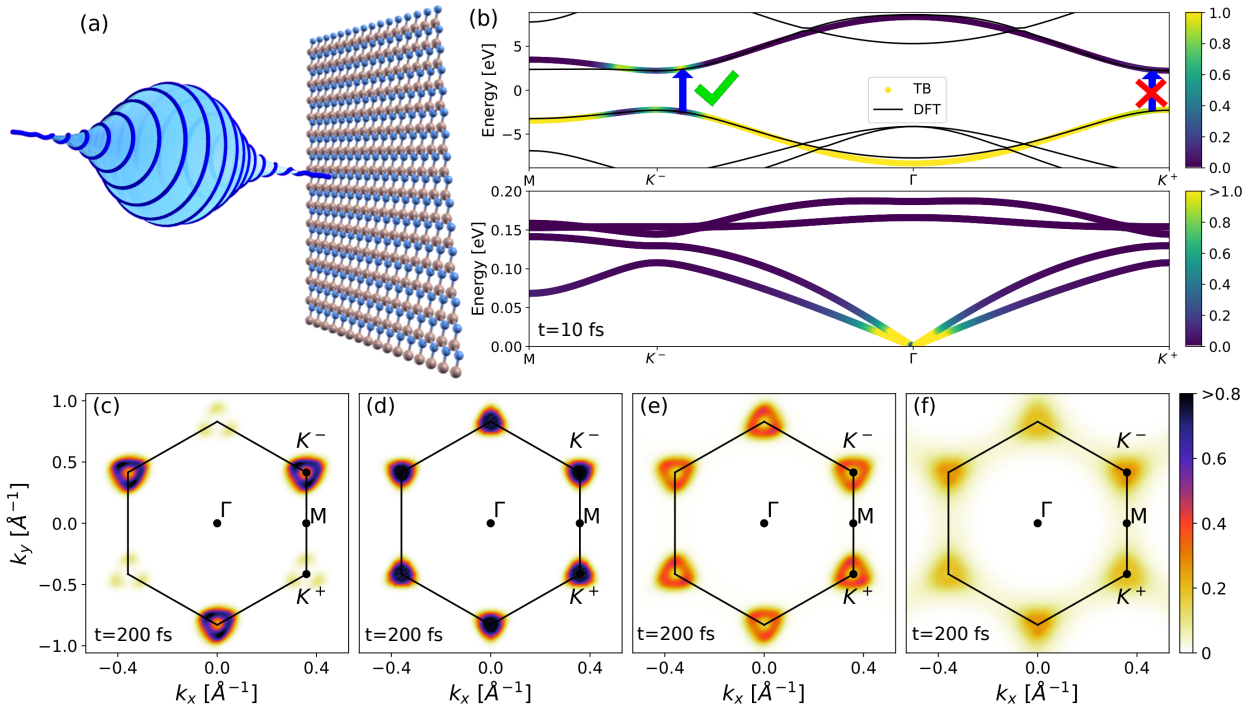$$

FIG. 1. Panel (a) shows a schematic of circularly polarized light exciting a sheet of hBN. The upper half of panel (b) shows the electron bands calculated using DFT with an LDA xc functional, alongside the tight binding (TB) bands fit to match the band onset. The Fermi level has been centered between the conduction and valence bands. The arrow indicates the approximate energy of excitation around a specific K valley, and the shading indicates the occupation of states in the TB model just after the laser pulse, interpolated from the MTEF results. The lower half of panel (b) shows the phonon dispersion calculated using DFPT, with shading indicating the initial phonon occupation number at 300 K, with the translational modes at Γ set to zero. The bottom four panels show the occupation of the conduction band 200 fs after the laser pulse under different approximations to the electron-phonon dynamics: (c) initially equilibrium geometry with zero velocity, (d) TDBE, (e) static displacement, and (f) MTEF dynamics. The phonon system in panels (d-f) is sampled at/set to 300 K. The labeling of the otherwise degenerate K^+/K^- points is based off the polarization of the pump and the scale is capped at 0.8, to emphasize small differences.

We use a circularly polarized laser pulse $\mathbf{A}(t)$ using a $\cos^2$ envelope with polarization defined by:

$$\mathbf{A}(t) = \begin{cases} \mathbf{A}_0(t)\cos^2\left(\frac{\pi}{T_{\text{pump}}}(t - T_{\text{pump}}/2)\right) & , t < T_{\text{pump}} \\ 0 & , \text{else} \end{cases}$$

$$\mathbf{A}_0(t) = \frac{A_0}{\sqrt{2}}\left(\text{Re}\left[e^{is\omega t}\right]\hat{\mathbf{x}} + \text{Im}\left[e^{is\omega t}\right]\hat{\mathbf{y}}\right).$$

(23)

We utilize a pump pulse duration of ten optical cycles at carrier frequency $\omega = 5$ eV, such that $T_{\text{pump}} \approx 8.3$ fs (FWHM ≈ 4.1 fs), with amplitude $A_0 = 5$ a.u. corresponding to a peak intensity of 7.88×10^{11} W/cm^2. The handedness of the laser is controlled by $s = \{1, -1\}$, creating left and right circularly polarized light, and we distinguish the K points by which sign of s excites them as K^+/K^-.

After exposure to the pump pulse we track the occupation of the conduction band states, $f_{c\mathbf{k}} = |c_{\mathbf{k}}|^2$, by taking

the expectation value of the projector:

$$c_{\mathbf{k}}(t) = \frac{1}{N_t}\sum_i^{N_t}\text{Tr}\left[\hat{\rho}_i(t)|c\mathbf{k}\rangle\langle c\mathbf{k}|\right].$$

(24)

Strictly speaking this projector is only valid when the laser field is turned off, otherwise one must project onto the Houston states $|c\mathbf{k}(t)\rangle$ [78, 79]. For simplicity we project onto the equilibrium band states, and indicate when the laser field is on (and therefore where this measure is only approximate) using grey shading in the background. In panels (c-f) of Fig. 1 we show a snapshot of the conduction band occupations taken 200 fs after the circularly polarized pump pulse, using the different approaches mentioned above. In all cases the system is initialized at 300 K. In Fig. 1 (c) we initialize the ionic system at the equilibrium geometry with zero velocity. The excited population established after the pulse has a large imbalance between the K^- and K^+ valley carrier distributions and remains completely static throughout the propagation in this case due to a lack of decay channels.

The marginal population around K^+, mostly around the $K^\pm M$ lines, and the dip at K^- is due to pumping slightly above the gap, as seen in Fig. 1 (b), though there is no population at the symmetry forbidden K^+ point itself.

Often in literature, a dynamics simulation will be referred to as Ehrenfest if the ions are allowed to move according to mean field forces, without a unique specification of their initial conditions. We show that performing the simulation with fixed ions or with dynamic ions starting with zero initial velocity, but in either case starting from the equilibrium geometry, results in no qualitative change in the excited electron occupation. By breaking the symmetries of the equilibrium geometry and including static disorder in the phonon system, there is a fundamental difference in the evolution of the excited electronic system.

The results of TDBE dynamics are shown in panel (d) of Fig. 1. The initial carrier distribution rapidly equalizes between the K^-/K^+ valleys, while simultaneously contracting towards the lowest energy states available in the valley bottoms. These dynamics are restricted exclusively to relaxation of the electronic occupations because, as seen in panel (b), the optical phonons initially have no energy available to contribute to scattering the electronic system uphill in energy.

For the case of static disorder, shown in Fig. 1(e), the valley occupations are effectively equalized by 200 fs, however there is no change in occupied energy levels, as seen by the ring around $K^\pm$ which is present in the occupation immediately after excitation as in panel (c). This can be explained in the framework of band folding: displacing the ionic positions in a supercell is equivalent to folding over the primitive cell BZ bands. This allows the excited charge carriers at K^- to have a decay channel into the energetically degenerate folded $\mathbf{k}$ points around K^+. However, this is a strictly elastic scattering process and therefore is effectively restricted to states inside the initially excited energy window.

The results of allowing for dynamic ion motion at the MTEF level are shown in Fig. 1 (f). Here we see that in addition to homogenization of valley population, there is also some scattering of carriers out of the energetic window in which they were initially excited. One can see that in addition to scattering downwards in energy towards the $K^\pm$ points, there is also excitation of the electrons upward in the valleys along the $K^\pm M$ lines. Without exact numerical results it is difficult to address the accuracy of this phenomena, however it could be related to the ZPE leakage of the mean-field dynamics: although the optical phonon occupation is approximately zero initially, over time the ZPE of phonons near the gamma point is drained into the electronic system, incrementally exciting the charge carriers beyond what one sees in the TDBE results at this temperature. However, note that when propagating without pumping the electronic system, there is no loss of phonon ZPE and no heating of the electronic system as the band gap forbids the promotion of electrons due to the order of magnitude smaller
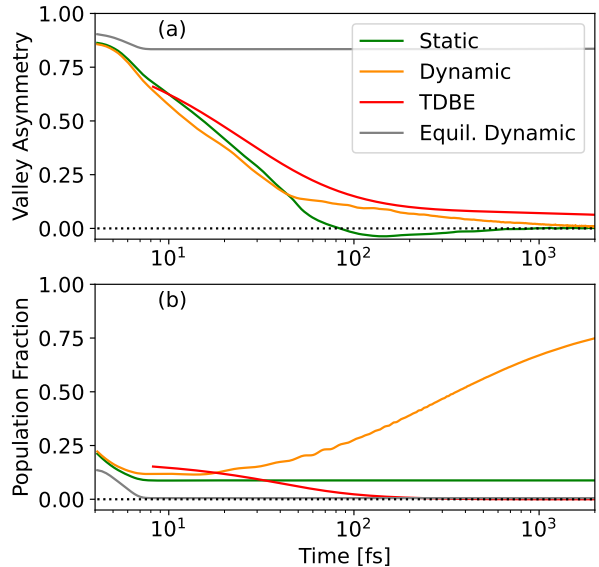

FIG. 2. (a): Valley population asymmetry at $T = 300$ K defined by Equation (25). Panel (b) shows the fraction of conduction band population outside the $K^\pm$ regions. The grey region corresponds to when the pump is turned on and the dotted line at zero is a guide to the eye.

phonon energies. See SI.7 for further details.

To assess the relaxation timescales in more detail, we can track the flow of excited charge carriers throughout the BZ by integration of the conduction band occupation within the populated region $A_{K\pm}$ around the $K^\pm$ points:

$$\mathrm{VA}_{\mathrm{occ}}(t) = \frac{\int_{A_{K^-}} d^2\mathbf{k}\ f_{c\mathbf{k}}(t) - \int_{A_{K^+}} d^2\mathbf{k}\ f_{c\mathbf{k}}(t)}{\int_{A_{K^-}} d^2\mathbf{k}\ f_{c\mathbf{k}}(t) + \int_{A_{K^+}} d^2\mathbf{k}\ f_{c\mathbf{k}}(t)}. \quad (25)$$

In the valleytronics literature this measure has been used to define the 'valley polarization' or 'valley asymmetry' [4, 58, 62] and (for TMDs) has been shown by perturbation theory to be strongly influenced by electron-phonon coupling [80]. For our purposes we use this term to refer strictly to the population imbalance between the $K^\pm$ valleys, without reference to the spin resolved bands typically associated. We choose the integration regions to be $|\mathbf{k} - K^\pm| < 0.36\text{Å}^{-1}$, roughly corresponding to the populated areas Fig. 1(c). In Fig. 2(a), we see that static displacement, MTEF dynamics and TDBE all capture an extremely rapid population rearrangement within the first 50 fs. In the static displacement method there is a slight inversion of polarization which slowly decays over a 50 fs-2 ps timescale, and the total population outside the valley regions in Fig. 2(b) remains fixed due to carrier energies being confined to their initial excitation energy window. Small changes to the radius of integration do not change the characteristics of these plots due to the normalization with respect to region population in Eq. (25), and simply changes the quantitative values in Fig.
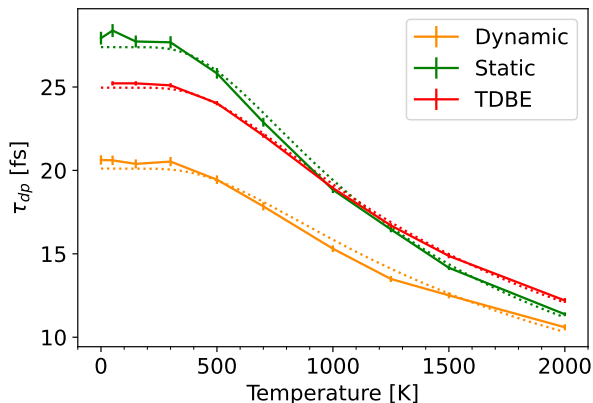
FIG. 3. The timescale of an exponential fit of the valley depolarization rates calculated with Eq. (25) over the first 50 fs, with an inverse scattering rate γ fit to these data shown as the dotted line.

2(b).

The TDBE and MTEF dynamics clearly display a second time scale, starting from about 50 fs in the case of MTEF and about 100 fs for TDBE, where the valley equalization slows into an asymptotic-like behavior when the population imbalance dips below 0.15. Simultaneously, in the TDBE results there is a down-scattering of carriers which were initially outside of the valley regions as the excited electronic population emits energy into the phonon bath and assumes a more thermal distribution. In contrast, MTEF shows the presence of up-scattering processes as the ZPE from the phonon system is absorbed by the electronic system due to the classical nature of the approximation. See SI.7 for further details.

We gain further insight to the effect of the phonon bath on the ultra-fast excited carrier relaxation or 'valley depolarization' by varying the initial temperature of the system. In Fig. 3 we show the characteristic time scales of depolarization obtained from fitting the valley asymmetry in the first 50 fs to an exponential decay function, $f(t) = a_0 + a_1 \exp(-t/\tau_{\mathrm{dp}})$, across multiple temperatures. The most apparent feature is an effective independence of the depolarization rate on temperature until about 300K which can be easily attributed to the high phonon energies in hBN, meaning that the optical phonon branches only begin to have significant occupation at higher temperatures. This behavior has been experimentally observed in the steady-state photoluminescence polarization of MoS_2, which is directly proportional to the valley lifetime [56], as well as in valley asymmetry decay times in WSe_2 measured by time-dependent Kerr rotation measurements [31].

The depolarization timescales τ_{dp} can be related to the average phonon occupation via a linear function of the scattering rate: $\gamma = 1/\tau_{\mathrm{dp}}$ where $\gamma = \gamma_0 + \alpha \langle n_{\mathrm{ph}} \rangle$. Using the fit τ_{dp} values, we further fit the scattering rates by taking at each temperature the expected oc-

cupation value of the Bose-Einstein distribution at the average optical phonon energy, 0.16 eV, showing very good agreement with the data. The fit scattering parameters are $\alpha_{\mathrm{Dynamic}} = 0.072\ \mathrm{fs}^{-1}$, $\alpha_{\mathrm{Static}} = 0.081\ \mathrm{fs}^{-1}$, and $\alpha_{\mathrm{TDBE}} = 0.065\ \mathrm{fs}^{-1}$. Although the ZPE leakage present in the MTEF dynamics can affect electronic populations at long time scales, these results show that for short time scales the MTEF decay rates broadly agree with the TDBE and static displacement approaches; all methods predict this timescale to depend on thermal activation of the phonon optical modes in a consistent manner.

In the context of the MTEF and static disorder simulations, it is worth pointing out that these results converge with an extremely small number of trajectories. For example, while the data shown in Fig. 2 was obtained with $N_t = 380$ trajectories, we can reproduce a graphically converged result with high probability through as little as two random samples. See SI.5 for further analysis.

B. Tracking Valley Asymmetry with Transient Circular Dichroism

Direct experimental observations of time dependent valley populations has been done in TMDs by performing time resolved measurements, such as time and angle resolved photoemission [76, 77], time dependent Kerr rotation spectroscopy [31], helicity resolved two-dimensional electronic spectroscopy [81], and TAS [27, 82]. In this section we focus on TAS using circularly polarized light, Transient Circular Dichroism (TCD).

Pumping the system with circularly polarized light produces an electronic current, $\mathbf{j}_{\mathrm{pump}}(t)$, that depends on the polarization of the pump. Next, one probes the system with a much weaker circularly polarized probe pulse with a time delay between it's envelope center and the pump center of τ and a duration of T_{pr} to generate the pump-probe current $\mathbf{j}_{\mathrm{pump\text{-}probe}}(t, \tau)$, which encodes the excitation of the system induced by the pump at this delay, and depends on the polarization of the probe. Taking the difference between these currents

$$\mathbf{j}_{\mathrm{TAS}}(t, \tau) = \mathbf{j}_{\mathrm{pump\text{-}probe}}(t, \tau) - \mathbf{j}_{\mathrm{pump}}(t), \quad (26)$$

allows one to calculate the intermediary transient optical conductivity (TOC) [83]:

$$\tilde{\sigma}_{ij}(\omega, \tau) = \frac{\int_{\tau - T_{\mathrm{pr}}/2}^{T_f + \tau + T_{\mathrm{pr}}/2} dt\, W(t/T_f) j_{\mathrm{TAS}}^i(t, \tau) e^{i\omega t}}{\int_{\tau - T_{\mathrm{pr}}/2}^{T_f + \tau + T_{\mathrm{pr}}/2} dt\, W(t/T_f) E_{\mathrm{probe}}^j(t) e^{i\omega t}}. \quad (27)$$

Here i, j are the cartesian directions of the pump and probe, and we have inserted the mask function $W(x) = \exp(-\kappa x)$, $\kappa = -\ln(10^{-3}/T_f)$ to damp the integrand of the Fourier transform, given the finite propagation time T_f. The trace of the optical conductivity is used throughout, $\sigma(\omega) = \mathrm{Tr}\left[\sigma_{ij}(\omega)\right]$. Finally by comparing the difference to the response of the system with no pump pulse
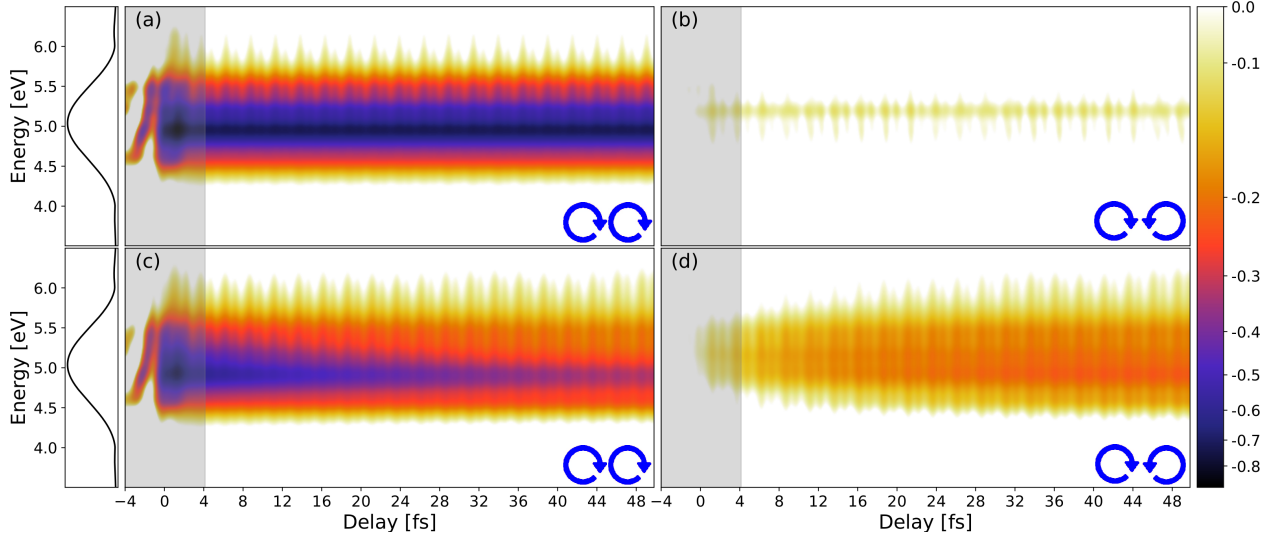
FIG. 4. The real part of the TOC: $\mathrm{Re}\,[\sigma(\omega,\tau)]$ calculated in the TB model. The arrows indicate the chirality of the pump and probe, either pumping and probing with the the same handedness or opposite handedness. Panels (a) and (b) are the equilibrium geometry results and the MTEF results at 300 K are shown in panels (c) and (d). The left most panels show the spectral weight of the pump, $|E(\omega)|$ which is active during the grey highlighted time span. The logarithmic scale has been set to emphasize the signal in the cross valley data, while minimizing the fluctuations arising from CEP locking.

but the same probe, $\sigma_{\mathrm{no\text{-}pump}}(\omega)$ we obtain the true TOC:

$$\sigma(\omega,\tau) = \tilde{\sigma}(\omega,\tau) - \sigma_{\mathrm{no\text{-}pump}}(\omega). \qquad (28)$$

As with the pump pulse, we also use a $\cos^2$ envelope for the probe, with a strength of $A_0 = 0.01$ a.u. at the same frequency as the pump for a single optical cycle, $T_{\mathrm{pr}} \approx 0.8$ fs. The carrier envelope phase (CEP) between the pump and probe for each delay is fixed to zero. See SI.3 for the explicit formulas for the electronic current operator in the TB model and section VI E for the MTEF simulation protocol.

The results for the real component of the TOC calculated in the TB model are shown in Fig. 4, with a delay spacing of $\Delta\tau = 0.5$fs and a propagation time of $T_f = 30$fs. The pump chirality in all cases is $s_{\mathrm{pump}} = -1$, the same used in the results of Fig. 1, and the chirality of the probe is $s_{\mathrm{probe}} = -1$ in the left column and $s_{\mathrm{probe}} = +1$ in the right column. The periodic fluctuation of the signal is due to the CEP locking, and can in principle be removed if desired by averaging the results over several CEPs [84, 85]. Starting with the static equilibrium geometry results on the top row, in panel (a), we see that after the pump, at around $\tau = 4$fs, the signal is saturated around the pumping frequency, whereas in panel (b) following the same pump, but with a probe pulse of the opposite chirality, there is a minimal response indicating a very small population slightly above 5eV. By directly comparing to Fig. 1(c) we see that the signal in Fig. 4(b) corresponds to the small population around (and energetically above) K^+ induced by the pump, while the saturated signal in Fig. 4(a) corresponds clearly to the large population in the K^- valley.

The TOC signal is of course unchanging after the pulse due to the lack of decay channels, again corresponding to the equilibrium results shown in Fig. 2. Turning to the MTEF results, we see a sharp attenuation of the signal in panel (c) following the pump, as well as a broadening of the range of the signal with respect to panel (a) due to scattering within and outside the K^- valley. Concurrent with the attenuation of the K^- valley signal around 5 eV there is a buildup of signal in panel (d) indicating a buildup of carrier density in the K^+ region.

We can generalize these predictions of the TOC to the calculated conduction band populations without reliance on defining valley integration areas by taking the difference of the columns shown in in Fig. 4(d) and (c), and integrating over the energy axis:

$$\mathrm{VA}_{\mathrm{TAS}}(\tau) = \left| \frac{\int d\omega \; \mathrm{Re}\,[\sigma_{\mathrm{TAS}}^{\mathrm{cross}}(\omega,\tau) - \sigma_{\mathrm{TAS}}^{\mathrm{same}}(\omega,\tau)]}{\int d\omega \; \mathrm{Re}\,[\sigma_{\mathrm{TAS}}^{\mathrm{cross}} + \sigma_{\mathrm{TAS}}^{\mathrm{same}}(\omega,\tau)]} \right|, \qquad (29)$$

where σ^{same} indicates the TOC obtained by pumping and probing with the same chirality of light as in the left columns of Fig. 4, and σ^{cross} refers to pumping and probing with opposite circular polarizations, as in the right columns of Fig. 4. In Fig. 5 we perform a TCD calculation using frozen phonons and compare the measure in Eq. (29) coming from the TCD directly to the valley polarization calculated via Eq. (25) using the occupation data from the pump only part of the TAS calculation. It is clear that there is good agreement between these two measures.

Finally we perform a TCD calculation using the TDDFT program Octopus [86] in a 30×30 supercell with
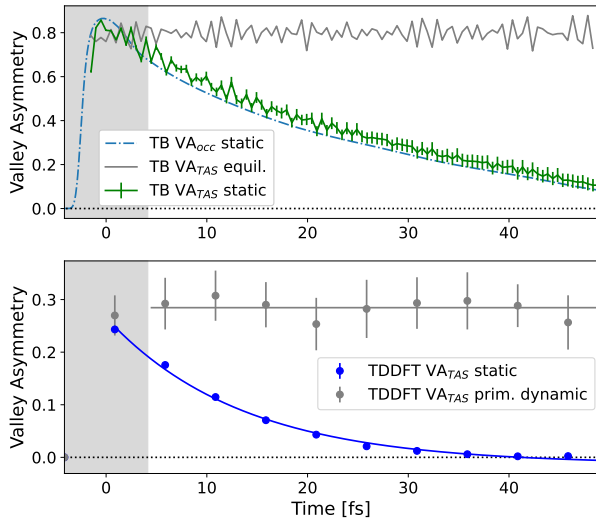
FIG. 5. Extracting Valley Asymmetry from TAS calculations via Eq. (29). The results of the same calculation done through TDDFT are also included. The grey shaded region is the time period in which the laser field is active. The characteristic decay times fit to the TAS data via an exponential starting from time 0 are $\tau_{\mathrm{dp}} = 32 \pm 2$fs for the tight binding calculation and $\tau_{\mathrm{dp}} = 13.5 \pm 0.8$fs for the TDDFT calculation. The exponential fit to the TDDFT data is also plotted, with the grey line being a guide to the eye.

a delay spacing $\Delta\tau$ of 5 fs. Due to the size of this calculation, 1800 ions in periodic boundary conditions, it was computationally infeasible to do the full calculation with dynamical ions. However we can compare to a full MTEF calculation sampling the Γ point optical phonons with ten dynamical calculations in a primitive cell in gray. The fully *ab initio* calculations show a smaller degree of valley polarization at the peak of the pulse, and the supercell calculations show an extremely rapid depolarization, on a timescale roughly two to three times faster than the tight binding model. As expected, the displacements in the primitive cell calculation, while demonstrating some fluctuation of the signal, do not depolarize due to being restricted to Γ point phonons, incapable of scattering electronic states from K^- to K^+.

C. Tracking Valley Asymmetry with Optical Harmonic Polarimetry

While testing the predictions of the above TCD calculation experimentally is in principle possible – as the generation of circularly polarized light in the range of the experimentally measured hBN gap of 6eV can be achieved via high harmonic generation (HHG) [87] – a much easier measure of the valley asymmetry has been proposed by Jiménez-Galán and colleagues [62, 88] and recently experimentally tested by Mitra et. al [63] which

is based off the ellipticity of harmonics generated by a linearly polarized, high-intensity, off-resonant probe. In this section we recreate this experiment *in silico* and test the robustness of this measure when including phonon induced scattering in the simulation.

The basic idea was explained succinctly in the SI of [62]: when driving the system with an off-resonant probe aligned in the $\Gamma - M$ direction of the BZ, the current response induced parallel to the driving field $(j_\parallel)$ will not be affected by the population of the K^+/K^- valleys, however the current response in the perpendicular direction $(j_\perp)$ must be. The contribution to $j_\perp$ is proportional to the anomalous Hall conductivity arising from conduction band population in regions of non-zero Berry curvature. For equal K^+ and K^- valley populations the anomalous Hall current will have exactly counteracting contributions from these two regions. For unequal population, a non-zero $j_\perp$ will emerge, which has been used as an experimental measure for valley polarization in TMDs for nearly a decade [89].

Furthermore, since the Berry curvature around the two valleys have opposite sign, the anomalous current arising from a population imbalance around either valley will always be completely out of phase (π) with respect to one another, and both $\pi/2$ out of phase with respect to $j_\parallel$. This means that the radiation emitted as a result of this current will have an elliptical polarization, with ellipticity $\epsilon \in [-1, 1]$ corresponding to the K^-/K^+ population imbalance, and gives an all-optical measure of the valley asymmetry. Mitra et. al [63] use this phenomenon as a measure of the degree of valley asymmetry in hBN following a bichromatic 'trefoil' light pulse – which has been proposed as a tunable driver of valley selective excitation in monolayer hBN and graphene, as well as bulk TMDs and twisted bilayer graphene [90, 91] – finding a small but apparently valley selective signal about 100 fs after excitation.

While the ellipticity of emitted harmonics has been proposed to detect other system properties such as topologically insulating phases, the utility of this measure has been called into question by *ab initio* simulations due in part to the many technical difficulties related to the generation and interpretation of HHG signals, even in theoretically ideal conditions [51, 92–95]. Furthermore the HHG spectrum has been found to be very sensitive to Γ point phonon distortions [50]. Given these open questions in the literature, along with the results in Sections IV A and IV B indicating that phonons should induce ultrafast sub-30 fs homogenization of any valley asymmetry in monolayer hBN, in this section we test the robustness of this measure of valley asymmetry upon inclusion of phonon degrees of freedom and the time dependence of the asymmetric valley population signal following a trefoil pump in our TB and TDDFT approaches.

1. Robustness of Harmonic Ellipticity under Phonon-Induced Valley Equilibration

We define the intensity of light emitted due to the non-equilibrium current in a given Cartesian direction x, y, as:

$$|I_{x,y}(\omega)|^2 = \left| \int_{t_0}^{t_f} dt e^{i\omega t} m\left(t, \frac{1}{2}\left[t_f - t_0\right]\right) \partial_t j_{x,y}(t) \right|^2, \quad (30)$$

where $m(t, x)$ is a mask function. For clean high harmonic generation, we utilize a probe pulse which is far from resonance with the energy gap in hBN, $\omega_{\text{probe}} << E_g$, allowing us to drive the system at very high intensities, and utilize a 'super-sine' envelope for both the probe pulse and the Fourier transform [96]:

$$m(t, \tau) = \left(\sin\left(\pi \frac{t - \tau}{T_{\text{probe}}}\right) \right)^{\left(\frac{\left| \pi\left(\frac{t-\tau}{T_{\text{probe}}} - \frac{1}{2}\right) \right|}{\text{w}} \right)} \quad (31)$$

where w $= 0.75$, τ is the center of the mask, and $m(t, \tau)$ is defined to be zero when $|t - \tau| \geq T_{\text{probe}}/2$. This mask is useful as it begins and ends exactly at 0 while having a short and smooth ramp time, maximizing the number of optical cycles present at full intensity. We drive the system along the mirror axis, parallel to the B-N bond, and define this to be the y direction corresponding to pumping along the $\Gamma - M$ line in the BZ. The probe is depolyed at multiple delays τ relative to the center of a pump envelope:

$$\mathbf{A}(t; \tau_{\text{probe}}) = \frac{c\sqrt{I_{\text{probe}}}}{\omega_{\text{probe}}} m(t, \tau) \cos(\omega_{\text{probe}} t + \phi)\hat{\mathbf{y}} \quad (32)$$

Where I_{probe} is the probe intensity, c is the speed of light, and ϕ is the CEP, which is always fixed from the start time, i.e., $\phi = \omega_{\text{probe}}(\tau - T_{\text{probe}}/2)$.

The ellipticity of emitted light calculated by Eq. (30) at a given energy ω can be determined via the Stokes parameters ([97] Eq. SI.2):

$$\epsilon(\omega) = h\frac{|I_x|^2 + |I_y|^2 - \sqrt{(I_x - I_y)^2 + 4I_x I_y \cos^2(\phi_y - \phi_x)}}{|I_x|^2 + |I_y|^2 + \sqrt{(I_x - I_y)^2 + 4I_x I_y \cos^2(\phi_y - \phi_x)}}$$
$$\phi_x = \arg(I_x), \quad \phi_y = \arg(I_y),$$
$$h = \text{sign}\left[\left| |I_x + iI_y| - |I_x - iI_y| \right|\right], \quad (33)$$

where h is the helicity of the signal corresponding to the handedness: -1 for right, 1 for left, 0 for linear, and $\phi_{x,y}$ is the phase of the signal. The ellipticity ranges continuously from $[-1, 1]$ defining fully right circularly polarized light to fully left circularly polarized light.

One can define the ellipticity of a given harmonic by taking the normalized harmonic yield for each harmonic
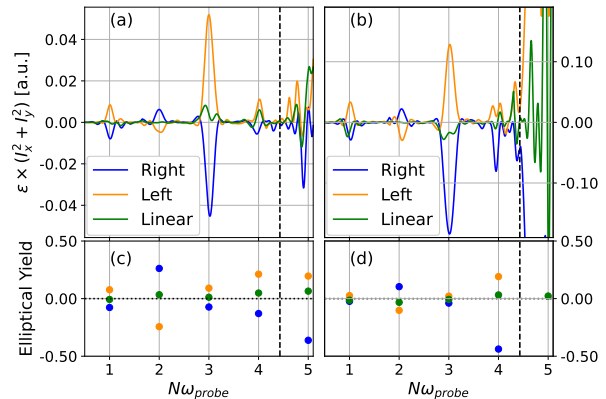

FIG. 6. The intensity weighted ellipticity and corresponding elliptical yield of the harmonics generated in a fixed-equilibrium geometry calculation 25 fs after excitation with left circularly, right circularly or linearly polarized light using the same pump parameters as in sections IV A and IV B. The vertical dashed line indicates the conduction band edge at 4.43 eV. (a): the TB model results, (b): TDDFT results, (c): the elliptical yield of panel (a) calculated with Eq. (34), (d): the elliptical yield of panel (b).

n, weighted by the ellipticity:

$$\text{Elliptical Yield } (n) = \frac{\int_{n-1/2}^{n+1/2} d\omega \epsilon(\omega) \left(|I_x|^2 + |I_y|^2\right)}{\int_{n-1/2}^{n+1/2} d\omega \left(|I_x|^2 + |I_y|^2\right)}, \quad (34)$$

where the integral goes from the energy at $(n-1)\omega_{\text{probe}}$ to $(n+1/2)\omega_{\text{probe}}$. With these definitions in hand we can test the ellipticity of the harmonics generated in hBN after irradiation by the on-resonant pump from sections IV A and IV B which, as already demonstrated, produces very strong valley asymmetry.

In Fig. 6, we see the HHG spectrum for a fixed-equilibrium geometry calculation, 25 fs after being pumped with left circularlry, right circularly or linearly polarized light at $\omega_{\text{pump}} = 5$ eV and $T_{\text{pump}} \approx 8.3$ fs, generated by a probe with $\omega_{\text{probe}} = 1$ eV, and $T_{\text{probe}} = 30$ fs. As one would expect, the fundamental matches the polarization of the driving probe field, while there is flipping of the ellipticity at each subsequent harmonic, until reaching the band edge at 4.43 eV, whereupon the conduction band electron response dominates the signal. These results hold for both the TB and the TDDFT spectra, though there are naturally some quantitative differences, in particular concerning the intensity of the emitted light. Under linearly polarized pumping, the ellipticity of the spectrum is effectively flat for the TB model, with a small signal at the 3^{rd} harmonic, however the TDDFT results show an elliptical response at both the fundamental and 3^{rd} harmonic, which nonetheless is washed out in the yield calculation. Although the intensity weighted ellip-
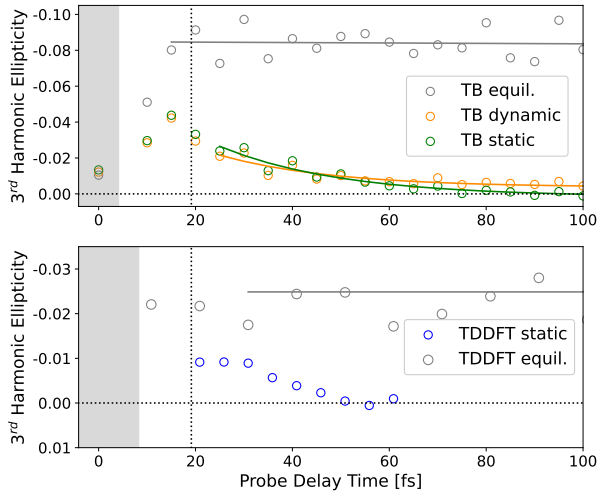
FIG. 7. The elliptical yield of the 3rd harmonic calculated with Eq. (34), following excitation with the same circularly polarized resonant pump from sections IV A and IV B. The grey region corresponds to the duration of the pump, while the vertical dotted line indicates the final time of pump-probe overlap.

ticity can be quite large, due to the normalization in Eq. (34) the calculated yield does not necessarily reflect this.

Although the 3rd harmonic signal is small, we find that it provides the cleanest time resolved information when scanning over probe delays, shown in Fig. 7. Here we see precisely the same behavior as in the previous results. When the ions are fixed at the equilibrium geometry, there is a fluctuation in the signal for both the TB and TDDFT results, but it remains non-zero due to a lack of valley asymmetry decay channels. In contrast when including phonon dynamics either via MTEF or static disorder there is a suppression of the initial signal followed by a rapid decay corresponding to the equilibration of valley population seen in Fig. 2.

2. Robustness of Trefoil Valley Selectivity under Phonon-Induced Valley Homogenization

By combining two counter-rotating circularly polarized fields with a fundamental frequency ω_{tr} and it's second harmonic $2\omega_{tr}$ with a relative amplitude of 2:1, and a delay t_d of the $2\omega_{tr}$ field relative to the fundamental, one obtains a laser with a triangular 'trefoil' shape in the plane which can be arbitrarily rotated by tuning t_d. The orientation of the trefoil was shown numerically via the semi-conductor Bloch equation to preferentially excite electrons into the K^+ or K^- valleys in monolayer hBN [62, 63]. The explicit form of the trefoil gauge field we use is:

$$
\begin{aligned}
\mathbf{A}_{trefoil}(t) = A_0 m(t) &\left(\mathrm{Re}\left[\frac{2}{3} e^{-i\omega_{tr}t} + \frac{1}{3} e^{i2\omega_{tr}(t-t_d)} \right] \hat{\mathbf{x}} \right. \\
&\left. + \mathrm{Im}\left[\frac{2}{3} e^{-i\omega_{tr}t} + \frac{1}{3} e^{i2\omega_{tr}(t-t_d)} \right] \hat{\mathbf{y}} \right),
\end{aligned}
\tag{35}
$$

where again $m(t)$ is an envelope function. We chose $\omega_{tr} = 0.6$ eV for a duration $T_{pump} = 30$ fs as in the experimental paper, with a super-sine envelope and an intensity of 1.67×10^{12} W/cm^2. The effect of driving the TB system with this laser is shown via the conduction band occupations plotted in Fig 8.

In Fig. 8, panels (a-c) show the results for the static equilibrium geometry with the trefoil pulse oriented at $-30°$, $0°$, and $30°$ rotations relative to the x axis in the BZ. The excitation at K^+ for the 30° rotation in Fig. 8(c) is quite strong and agrees qualitatively with Fig. 2e of Ref. [62], which shows a similar pumping frequency. At the opposite tuning in panel (a) when K^- should be more populated, there is indeed some excitation, and looking closely one can see that it's texture also resembles the 'grape-cluster' structure of the K^+ valley in panel (c), although the magnitude of excitation is lower. Qualitatively this reproduces the relative difference in excitation density reported in Fig. 3d and 3e in [62], confirming that our model also captures this phenomenon. Halfway between these two tunings, in panel (b), one still sees a strong preferential excitement in the K^+ valley over the K^- valley.

Incorporating phonon dynamics via MTEF in panels (d), (e), and (f), these trends broadly remain 50 fs after pumping, though the fine structure of the excitation seen away from the K valleys is washed out by electron-phonon scattering, causing a radially symmetric distribution away from the BZ boundaries that decreases towards Γ. Inclusion of the phonon system via static disorder produces BZ occupations virtually identical to the MTEF results at this timescale.

In all cases, looking within a small region around K^+/K^- when pumping at $-30°$ versus $30°$ one sees there is indeed an asymmetry in the excitation at the extrema of trefoil orientation. To see how this manifests in the HHG signal, we recreate the experimental setup by utilizing a linearly polarized probe of the same intensity and fundamental frequency as the trefoil pump ($\omega_{probe} = \omega_{tr}$) to create an HHG spectrum. As the HHG from the pump alone has no contribution to the $3\omega_{tr}$ harmonic channel it serves as a natural signal region to study with the probe. In Fig. 9 we compare the ellipticity of the 3rd harmonic to the valley asymmetry calculated directly from the conduction band occupation induced exclusively by the trefoil pump for fixed equilibrium geometry in panels (a) and (b), and MTEF/static displacement in panels (c) and (d). Because of the diffuse excitation, we choose integration regions for Eq. (25) in the BZ formed from vertices at the high symmetry points bisecting the lines
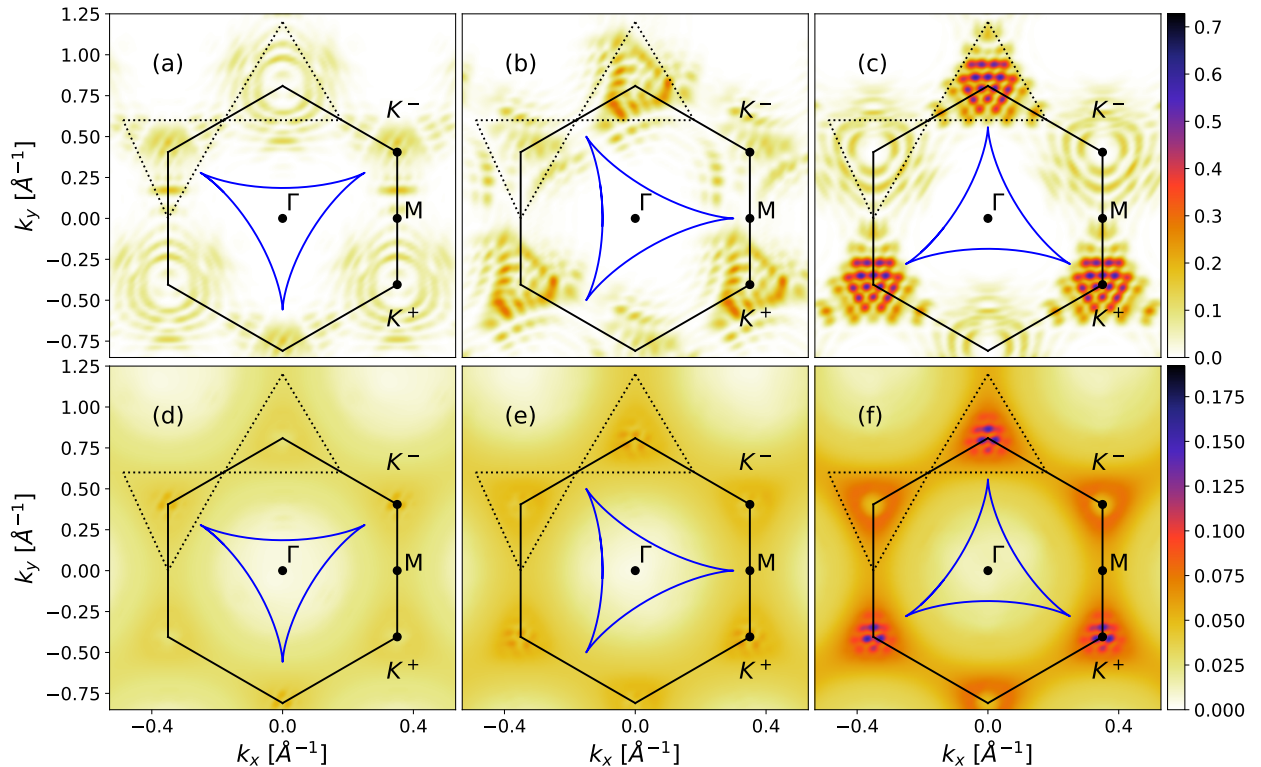
FIG. 8. The occupation of the conduction band 50 fs after irradiation with the trefoil pump in the TB model. The path of the trefoil pump in the plane is arbitrarily rescaled and drawn within the BZ as the blue line. Panels (a), (b) and (c) show the results for the static equilibrium geometry when the degree of rotation of the trefoil with respect to the BZ x axis is at $-30°$, $0°$ and $30°$ respectively. Panels (d), (e) and (f) show the MTEF results at the same rotations – Note the smaller colormap scale. The triangular regions inscribed by the dotted lines are formed by vertices at the high symmetry points between the K^+/K^- points, and are used to define the integration regions for the valley asymmetry calculation in Fig. 9.

between adjacent K^+/K^- valleys, which neatly encapsulates the excitation around K^+ for a $30°$ trefoil pump.

The equilibrium geometry results in panel (b) show that while the valley asymmetry integrated in the conduction band generally shows a tuning of the valley occupations, beginning preferentially in the K^- valley at $-30°$ and in the K^+ valley at $30°$, it is not exact, as at $0°$ there should in principle be more equal population, yet there is clearly a preferential excitation. This is partially reflected in the ellipticity in panel (a), where there is a strong polarization signal at $30°$ and $0°$, however, the small degree of K^- population under $-30°$ pumping fails to contribute to a significant negative elliptical emission.

These signals become cleaner when looking at the MTEF/static results in panel (c). There is a much smaller degree of polarization at $0°$, while $-30°$ is negative throughout. In all pump cases, there is a decay in the signal over the 70 fs depicted which is commensurate with the decay of valley asymmetry seen in panel (d). Comparing the strength of the signal when using oppositely tuned pumps, these simulations indicate that the relative signal difference is very weak after 100 fs.

V. CONCLUSION

We have derived a general expression for the Wigner transformation of the phonon thermal density matrix applicable to the phonon dispersion for real materials taken from *ab initio* calculations, and utilized it to perform MTEF calculations in both a reciprocal space TB model and a real space TDDFT supercell approach. This methodology allowed us to simulate the relaxation of asymmetrically excited charge carriers in hBN, to track this through the transient absorption spectra using circularly polarized probes, and to recreate an experimental observation of harmonic ellipticity as a measure of valley population imbalance. The inclusion of phonon degrees of freedom, either dynamically (including anharmonic effects) or statically, produced fundamentally different spectroscopic simulation results due to the complete exclusion of a critical decay channel in the common equilibrium geometry framework.

We discussed connections between the MTEF method and static displacement approaches, finding that MTEF is analogous to an extension of the reciprocal space
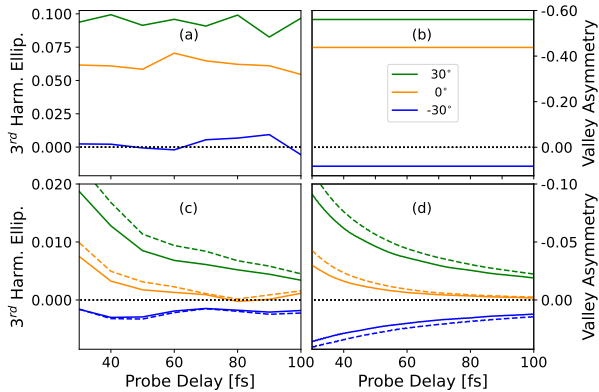
FIG. 9. The left column shows the ellipticity yield of the 3^{rd} harmonic generated after irradiation with the three trefoil pulse rotations seen in Fig. 8, compared to the right column showing valley asymmetry calculated by applying Eq. (25) to the triangular dotted regions in Fig. 8. Panels (a) and (b) show the static equilibrium geometry results while panels (c) and (d) show the MTEF results in bold lines and static results in dashed lines. Note the order of magnitude difference between the y-axes scales for the two approaches.

William-Lax / Zacharias-Giustino coordinate distribution to include nuclear velocities/momenta. We have also demonstrated that MTEF and static displacement methods can capture the phonon driven sub-30 fs valley depolarization on time scales commensurate with the TDBE results. Further, we showed that while static displacement methods are restricted to elastic scattering, MTEF suffers from unrealistic electron heating at long time scales due to ZPE leakage. Despite this, we showed that the temperature dependence of the short time scale relaxation of excited charge carriers agrees well across these simulation methods, exhibiting a plateau in inter-valley relaxation lifetimes at low temperature that agrees relatively well with experimental measurements in similar systems [31, 56]. Furthermore we found that these results converge with a very small number of samples.

This work extends MTEF into the domain of the *ab initio* treatment of periodic systems, providing a starting point for the hierarchy of semiclassical dynamics approaches which build on from the mean field limit, correcting for some of it's most serious shortcomings. However, even with issues in the long time-scale behavior of MTEF, this simulation method provides a unique tool to study the ultrafast response behavior of systems with strong electron-phonon coupling in laser driven regimes far from thermal equilibrium. Inclusion of phonon dynamics has the potential to be utilized to incorporate phonon dynamics into fully *ab initio* simulations of parametric driving, Floquet engineering and driven phase transitions, while already inclusion of static disorder can substantially change predictions of spectroscopic measurements via inclusion of elastic electron-phonon scattering under arbitrarily complex pump-probe configura-

tions.

The rapidity with which our results converge for the results presented here is highly encouraging for other far from equilibrium observables, and given the simplicity of incorporating our method into existing real time simulation protocols of non-equilibrium driven phenomena in quantum materials, as well as the fundamental qualitative differences in the resulting temperature dependent dynamics resolved in a systematic framework, we think that this will be a valuable tool going forward.

VI. COMPUTATIONAL DETAILS

A. Tight Binding Model

The lattice parameter of $a_0 = 4.734$ Bohr was obtained from cell relaxation in Quantum Espresso. The phonon frequencies and displacements were calculated on a Monckhorst-Pack (MP) grid of 30×30 using Quantum Espresso, with a 64×64 MP electronic k point grid. We utilize a 30^2 **k** and **q** grid in the BZ for our Equilibrium, MTEF and static TB simulations in sections IV A and IV B which is sufficiently dense to converge our results compared to a 36^2 grid. In section IV C we used a 60×60 **k**-grid.

The tight binding parameters t_0 and $\Delta_\alpha = \pm|\Delta|$ were fit from the conduction band calculated over a 30×30 MP grid in the TDDFT code Octopus according to the analytical dispersion relation of the equilibrium geometry tight binding model:

$$E_\mathbf{k} = \sqrt{\Delta^2 + t_0^2|\gamma(\mathbf{k})|^2}, \quad \gamma(\mathbf{k}) = \sum_\boldsymbol{\delta} e^{i\mathbf{k}\cdot\boldsymbol{\delta}}. \quad (36)$$

An LDA functional was used with Hartwigsen-Goedeker-Hutter (HGH) norm-conserving pseudopotentials with the simulation box having a real space grid spacing of 0.35 Bohr, and being periodic only in two dimensions with a vacuum of $1a_0$ on either side of the monolayer. The band gap of $E_g = 2|\Delta|$ corresponds to the uncorrected LDA direct gap of 4.43 eV, and $t_0 = 2.68$ eV. Although hBN has rather high energy phonons compared to many other materials, the electronic gap remains an order of magnitude larger, meaning that none of the physics of the electron dynamics within the upper band presented here is affected by not correcting this gap.

The hopping parameter b was calculated by fitting the bands to Eq. (36) for a range of ionic configurations with maximum displacement of 3% of the lattice constant, about 0.14 Bohr from equilibrium in steps of 0.005 Bohr, using a first order expansion of Eq.(17). The resulting value of $b = 2.87$ is quite close to the value suggested in [74] ($b = 3.3$), where it was approximated from Slater-Koster parameters between nearest and next nearest neighbors, and is also in a similar range to the value of 3.37 which has been estimated for graphene [75].

The tight binding model is written in Python and C++/CUDA, and is available at gitlab.com under

`kevin.lively_mpsd/graphene-tight-binding`

B. MTEF Simulations

We integrated the MTEF equations of motion with an fourth order Runge-Kutta algorithm for the electronic portion simultaneously with a velocity-Verlet type scheme for the phonon configuration, using a time step of 0.1 a.u..

C. TDDFT Simulations

The TDDFT simulation was done with a time step of 5×10^{-3} fs using a 16^{th} order Lanczos expansion of the exponential propagator in an approximated enforced time reversal symmetry framework. Only the Γ point was included in the 30×30 supercell BZ, i.e. equivalent to a 30×30 $\mathbf{k}$ grid in the primitive cell BZ under the BvK boundary conditions. We used the same grid spacing, pseudopotentials, and simulation box geometry that were used to fit the tight binding model.

D. TDBE Simulations

All of our TDBE results are generated using input from the tight-binding model Eq. (18) in the main text, with band energies $\epsilon_{n\mathbf{k}} = \pm|\epsilon_l(\mathbf{X} = 0)|$, and electron-phonon matrix elements taken via projection of the coupling terms onto the band states $g_{mn}^{\nu}(\mathbf{k}, \mathbf{q}) = \langle\psi_{n\mathbf{k}}|l_{\mathbf{q}\nu}\hat{M}(\mathbf{q}\nu)|\psi_{m\mathbf{k}}\rangle$.

The delta functions used in the TDBE scattering rate equations are approximated by Gaussian distributions $\delta(x) \approx \frac{1}{\eta\sqrt{\pi}}e^{-\left(\frac{x}{\eta}\right)^2}$ with $\eta = 10$ meV, and the resultant scattering rates converged with respect to number of $\mathbf{k}/\mathbf{q}$ points and η [24, 98]. The equations of motion themselves are integrated using a fourth order Runge-Kutta algorithm with $f_{n\mathbf{k}}(t)$, $n_{\mathbf{q}\nu}(t)$ inserted into each derivative and a timestep of 1fs. The initial excited electronic carrier population is set via interpolation of the carrier occupations from the equilibrium geometry using a 72^2 $\mathbf{k}$ MP grid just after the cessation of the pulse onto a denser 90^2 $\mathbf{k}$ grid. Because we are working with highly non-thermal electronic distributions in a system with extremely strong electron-phonon coupling on top of this gaussian approximation, we find there is a slight drift in the total excited population, and that the ratio of population drift to total population decreases as the initial total excited population decreases. Therefore with the exception of Fig. 1(d), which is included on the same scale for illustrative purposes, the initial TDBE electronic population distribution is set as $1/100^{\text{th}}$ of the MTEF occupation at the end of the pump, i.e. $f_{c\mathbf{k}}^{\text{TDBE}}(T_{\text{pump}}) = 0.01 f_{c\mathbf{k}}^{\text{MTEF}}(T_{\text{pump}})$.

E. Transient Optical Conductivity

The simulation protocol for calculating the transient optical conductivity is as follows:

1. Sample a phonon system initial condition and initialize the electronic system according to Eq. (20), giving a total system initial condition IC_0.

2. Expose the system to a probe of a given chirality s_{probe} from IC_0, and propagate for a duration of T_f.

3. Reset to IC_0 and propagate the system under the influence of the pump to the maximum delay time desired $\tau_{\max}+T_f$. At each time τ that one wants to have data for, save the instantaneous state of the system IC_τ.

4. Load each IC_τ and propagate under the same pump, but with an added probe of chirality s_{probe} centered at $\tau + T_{\text{probe}}/2$.

5. Apply Eqs. (26-28), using the response from step (2) to calculate $\sigma_{\text{equil}}(\omega)$.

6. Repeat steps (2-5) with a probe of the opposite chirality.

7. Repeat steps (1-6) for N_t samples and average the results

F. Graphical Representation of Data

The data in figures 1, 4 and 8 were interpolated with the bicubic interpolation function of matplotlib.

[1] K. J. Tielrooij, L. Piatkowski, M. Massicotte, A. Woessner, Q. Ma, Y. Lee, K. S. Myhro, C. N. Lau, P. Jarillo-Herrero, N. F. V. Hulst, and F. H. Koppens, Generation of photovoltage in graphene on a femtosecond timescale through efficient carrier heating, Nature Nanotechnology **10**, 437 (2015).

[2] C. Trovatello, G. Piccinini, S. Forti, F. Fabbri, A. Rossi, S. D. Silvestri, C. Coletti, G. Cerullo, and S. D. Conte, Ultrafast hot carrier transfer in ws2/graphene large area heterostructures, npj 2D Materials and Applications **6**, 10.1038/s41699-022-00299-4 (2022).

[3] K. F. Mak, K. He, J. Shan, and T. F. Heinz, Control of valley polarization in monolayer mos2 by optical helicity, Nature Nanotechnology **7**, 494 (2012).

[4] Y. Liu, Y. Gao, S. Zhang, J. He, J. Yu, and Z. Liu, Valleytronics in transition metal dichalcogenides materials, Nano Research **12**, 2695 (2019).

[5] J. K. Dewhurst, P. Elliott, S. Shallcross, E. K. Gross, and S. Sharma, Laser-induced intersite spin transfer, Nano Letters **18**, 1842 (2018).

[6] F. Siegrist, J. A. Gessner, M. Ossiander, C. Denker, Y. P. Chang, M. C. Schröder, A. Guggenmos, Y. Cui, J. Walowski, U. Martens, J. K. Dewhurst, U. Kleineberg, M. Münzenberg, S. Sharma, and M. Schultze, Light-wave dynamic control of magnetism, Nature **571**, 240 (2019).

[7] O. Neufeld, N. Tancogne-Dejean, U. D. Giovannini, H. Hübener, and A. Rubio, Attosecond magnetization dynamics in non-magnetic materials driven by intense femtosecond lasers, npj Computational Materials **9**, 39 (2023).

[8] M. Mitrano, A. Cantaluppi, D. Nicoletti, S. Kaiser, A. Perucchi, S. Lupi, P. D. Pietro, D. Pontiroli, M. Riccò, S. R. Clark, D. Jaksch, and A. Cavalleri, Possible light-induced superconductivity in k3 c60 at high temperature, Nature **530**, 461 (2016).

[9] H. Hübener, U. D. Giovannini, and A. Rubio, Phonon driven floquet matter, Nano Letters **18**, 1535 (2018).

[10] T. F. Nova, A. S. Disa, M. Fechner, and A. Cavalleri, Metastable ferroelectricity in optically strained srtio3, Science **364**, 1075 (2019).

[11] X. Li, T. Qiu, J. Zhang, E. Baldini, J. Lu, A. M. Rappe, and K. A. Nelson, Terahertz field-induced ferroelectricity in quantum paraelectric srtio3, Science **364**, 1079 (2019).

[12] A. S. Disa, J. Curtis, M. Fechner, A. Liu, A. von Hoegen, M. Först, T. F. Nova, P. Narang, A. Maljuk, A. V. Boris, B. Keimer, and A. Cavalleri, Photo-induced high-temperature ferromagnetism in ytio3, Nature **617**, 73 (2023).

[13] A. F. Kockum, A. Miranowicz, S. D. Liberato, S. Savasta, and F. Nori, Ultrastrong coupling between light and matter, Nature Reviews Physics **1**, 19 (2019).

[14] J. Fregoni, F. J. Garcia-Vidal, and J. Feist, Theoretical challenges in polaritonic chemistry, ACS Photonics **9**, 1096 (2022).

[15] T. Li, S. Jiang, L. Li, Y. Zhang, K. Kang, J. Zhu, K. Watanabe, T. Taniguchi, D. Chowdhury, L. Fu, J. Shan, and K. F. Mak, Continuous mott transition in semiconductor moiré superlattices, Nature **597**, 350 (2021).

[16] F. Wu, T. Lovorn, E. Tutuc, I. Martin, and A. H. Macdonald, Topological insulators in twisted transition metal dichalcogenide homobilayers, Physical Review Letters **122**, 10.1103/PhysRevLett.122.086402 (2019).

[17] S. A. Sato, J. W. McIver, M. Nuske, P. Tang, G. Jotzu, B. Schulte, H. Hübener, U. D. Giovannini, L. Mathey, M. A. Sentef, A. Cavalleri, and A. Rubio, Microscopic theory for the light-induced anomalous hall effect in graphene, Physical Review B **99**, 10.1103/PhysRevB.99.214302 (2019).

[18] W. Mao, A. Rubio, and S. A. Sato, Terahertz-induced high-order harmonic generation and nonlinear charge transport in graphene, Physical Review B **106**, 10.1103/PhysRevB.106.024313 (2022).

[19] F. Caruso and D. Novko, Ultrafast dynamics of electrons and phonons: from the two-temperature model to the time-dependent boltzmann equation, Advances in Physics: X **7**, 2095925 (2022).

[20] E. Malic, T. Winzer, E. Bobkin, and A. Knorr, Microscopic theory of absorption and ultrafast many-particle kinetics in graphene, Physical Review B - Condensed Matter and Materials Physics **84**, 10.1103/PhysRevB.84.205406 (2011).

[21] M. Bernardi, First-principles dynamics of electrons and phonons*, The European Physical Journal B **89**, 239 (2016).

[22] J.-J. Zhou, J. Park, I.-T. Lu, I. Maliyov, X. Tong, and M. Bernardi, Perturbo: A software package for ab initio electron–phonon interactions, charge transport and ultrafast dynamics, Computer Physics Communications **264**, 107970 (2021).

[23] F. Caruso, Nonequilibrium lattice dynamics in monolayer mos2, Journal of Physical Chemistry Letters **12**, 1734 (2021).

[24] X. Tong and M. Bernardi, Toward precise simulations of the coupled ultrafast dynamics of electrons and atomic vibrations in materials, Physical Review Research **3**, 10.1103/PhysRevResearch.3.023072 (2021).

[25] T. Winzer and E. Malić, Impact of auger processes on carrier dynamics in graphene, Physical Review B - Condensed Matter and Materials Physics **85**, 10.1103/PhysRevB.85.241404 (2012).

[26] T. Winzer and E. Malic, The impact of pump fluence on carrier relaxation dynamics in optically excited graphene, Journal of Physics Condensed Matter **25**, 10.1088/0953-8984/25/5/054201 (2013).

[27] G. Berghäuser, I. Bernal-Villamil, R. Schmidt, R. Schneider, I. Niehues, P. Erhart, S. M. D. Vasconcellos, R. Bratschitsch, A. Knorr, and E. Malic, Inverted valley polarization in optically excited transition metal dichalcogenides, Nature Communications **9**, 10.1038/s41467-018-03354-1 (2018).

[28] V. Janković and N. Vukmirović, Spectral and thermodynamic properties of the holstein polaron: Hierarchical equations of motion approach, Physical Review B **105**, 10.1103/PhysRevB.105.054311 (2022).

[29] W. Li, J. Ren, and Z. Shuai, A general charge transport picture for organic semiconductors with nonlocal electron-phonon couplings, Nature Communications **12**, 4260 (2021).

[30] J. Sous, B. Kloss, D. M. Kennes, D. R. Reichman, and A. J. Millis, Phonon-induced disorder in dynamics of optically pumped metals from nonlinear electron-phonon

coupling, Nature Communications **12**, 5803 (2021).

[31] A. Molina-Sánchez, D. Sangalli, L. Wirtz, and A. Marini, Ab initio calculations of ultrashort carrier dynamics in two-dimensional materials: Valley depolarization in single-layer wse2, Nano Letters **17**, 4549 (2017).

[32] N. Schlünzen, J. P. Joost, and M. Bonitz, Achieving the scaling limit for nonequilibrium green functions simulations, Physical Review Letters **124**, 10.1103/PhysRevLett.124.076601 (2020).

[33] E. Perfetto and G. Stefanucci, Real-time gw-ehrenfest-fan-migdal method for nonequilibrium 2d materials (2023), arXiv:2305.07458 [cond-mat.mes-hall].

[34] M. Zacharias and F. Giustino, One-shot calculation of temperature-dependent optical spectra and phonon-induced band-gap renormalization, Physical Review B **94**, 10.1103/PhysRevB.94.075125 (2016).

[35] M. Zacharias and F. Giustino, Theory of the special displacement method for electronic structure calculations at finite temperature, Physical Review Research **2**, 10.1103/PhysRevResearch.2.013357 (2020).

[36] J. P. Nery and F. Mauri, Nonperturbative green's function method to determine the electronic spectral function due to electron-phonon interactions: Application to a graphene model from weak to strong coupling, Physical Review B **105**, 245120 (2022).

[37] R. Crespo-Otero and M. Barbatti, Spectrum simulation and decomposition with nuclear ensemble: Formal derivation and application to benzene, furan and 2-phenylfuran, Theoretical Chemistry Accounts **131**, 1 (2012).

[38] A. Zunger, Bridging the gap between density functional theory and quantum materials, Nature Computational Science **2**, 529 (2022).

[39] E. Baldini, A. Zong, D. Choi, C. Lee, M. H. Michael, L. Windgaetter, I. I. Mazin, S. Latini, D. Azoury, B. Lv, A. Kogar, Y. Su, Y. Wang, Y. Lu, T. Takayama, H. Takagi, A. J. Millis, A. Rubio, E. Demler, and N. Gedik, The spontaneous symmetry breaking in ta2nise5 is structural in nature, Proceedings of the National Academy of Sciences **120**, e2221688120 (2023).

[40] R. Grunwald, A. Kelly, and R. Kapral, Quantum dynamics in almost classical environments, in *Energy Transfer Dynamics in Biomaterial Systems*, edited by I. Burghardt, V. May, D. A. Micha, and E. R. Bittner (Springer Berlin Heidelberg, Berlin, Heidelberg, 2009) pp. 383–413.

[41] K. Lively, G. Albareda, S. A. Sato, A. Kelly, and A. Rubio, Simulating vibronic spectra without born–oppenheimer surfaces, The Journal of Physical Chemistry Letters **12**, 3074 (2021).

[42] N. M. Hoffmann, C. Schäfer, A. Rubio, A. Kelly, and H. Appel, Capturing vacuum fluctuations and photon correlations in cavity quantum electrodynamics with multitrajectory ehrenfest dynamics, Phys. Rev. A **99**, 063819 (2019).

[43] J. Krumland, M. Jacobs, and C. Cocchi, Ab initio simulation of laser-induced electronic and vibrational coherence, PHYSICAL REVIEW B **106**, 144304 (2022).

[44] M. ten Brink, S. Gräber, M. Hopjan, D. Jansen, J. Stolpp, F. Heidrich-Meisner, and P. E. Blöchl, Real-time non-adiabatic dynamics in the one-dimensional holstein model: Trajectory-based vs exact methods, The Journal of Chemical Physics **156**, 234109 (2022).

[45] L. Li, R. Long, and O. V. Prezhdo, Charge separation and recombination in two-dimensional mos2/ws2: Time-domain ab initio modeling, Chemistry of Materials **29**, 2466 (2017).

[46] S. A. Sato, A. Kelly, and A. Rubio, Coupled forward-backward trajectory approach for nonequilibrium electron-ion dynamics, Physical Review B **97**, 10.1103/PhysRevB.97.134308 (2018).

[47] A. Krotz, J. Provazza, and R. Tempelaar, A reciprocal-space formulation of mixed quantum-classical dynamics, Journal of Chemical Physics **154**, 10.1063/5.0053177 (2021).

[48] Y. Shinohara, K. Yabana, Y. Kawashita, J. I. Iwata, T. Otobe, and G. F. Bertsch, Coherent phonon generation in time-dependent density functional theory, Physical Review B - Condensed Matter and Materials Physics **82**, 155110 (2010).

[49] S. Q. Hu, H. Zhao, C. Lian, X. B. Liu, M. X. Guan, and S. Meng, Tracking photocarrier-enhanced electron-phonon coupling in nonequilibrium, npj Quantum Materials **7**, 10.1038/s41535-021-00421-7 (2022).

[50] O. Neufeld, J. Zhang, U. D. Giovannini, H. Hubener, and A. Rubio, Probing phonon dynamics with multidimensional high harmonic carrier-envelope-phase spectroscopy, Proceedings of the National Academy of Sciences of the United States of America **119**, 10.1073/PNAS.2204219119 (2022).

[51] D. Freeman, A. Kheifets, S. Yamada, A. Yamada, and K. Yabana, High-order harmonic generation in semiconductors driven at near- and mid-infrared wavelengths, Physical Review B **106**, 10.1103/PhysRevB.106.075202 (2022).

[52] M.-X. Guan, X.-B. Liu, D.-Q. Chen, X.-Y. Li, Y.-P. Qi, Q. Yang, P.-W. You, and S. Meng, Optical control of multistage phase transition via phonon coupling in mote2, Phys. Rev. Lett. **128**, 015702 (2022).

[53] M. Guan, D. Chen, S. Hu, H. Zhao, P. You, and S. Meng, Theoretical insights into ultrafast dynamics in quantum materials, Ultrafast Science **2022** (2022), https://spj.science.org/doi/pdf/10.34133/2022/9767251.

[54] A. Kelly, N. Brackbill, and T. E. Markland, Accurate nonadiabatic quantum dynamics on the cheap: Making the most of mean field theory with master equations, Journal of Chemical Physics **142**, 10.1063/1.4913686 (2015).

[55] M.-H. Hsieh, A. Krotz, and R. Tempelaar, A mean-field treatment of vacuum fluctuations in strong light–matter coupling, The Journal of Physical Chemistry Letters **14**, 1253 (2023).

[56] H. Zeng, J. Dai, W. Yao, D. Xiao, and X. Cui, Valley polarization in mos 2 monolayers by optical pumping, Nature Nanotechnology **7**, 490 (2012).

[57] M. Selig, G. Berghäuser, A. Raja, P. Nagler, C. Schüller, T. F. Heinz, T. Korn, A. Chernikov, E. Malic, and A. Knorr, Excitonic linewidth and coherence lifetime in monolayer transition metal dichalcogenides, Nature Communications **7**, 13279 (2016).

[58] S. Xu, C. Si, Y. Li, B. L. Gu, and W. Duan, Valley depolarization dynamics in monolayer transition-metal dichalcogenides: Role of the satellite valley, Nano Letters **21**, 1785 (2021).

[59] A. Geondzhian, A. Rubio, and M. Altarelli, Valley selectivity of soft x-ray excitations of core electrons in two-dimensional transition metal dichalcogenides, Physical

Review B **106**, 115433 (2022).

[60] P. Hewageegana, Interaction of ultrafast optical pulse with monolayer hexagonal boron nitride (h-bn), Physica E: Low-dimensional Systems and Nanostructures **134**, 114906 (2021).

[61] Álvaro Jiménez-Galán, R. E. F. Silva, O. Smirnova, O. Smirnova, M. Ivanov, M. Ivanov, and M. Ivanov, Sub-cycle valleytronics: control of valley polarization using few-cycle linearly polarized pulses, Optica, Vol. 8, Issue 3, pp. 277-280 **8**, 277 (2021).

[62] Jiménez-Galán, R. E. Silva, O. Smirnova, and M. Ivanov, Lightwave control of topological properties in 2d materials for sub-cycle and non-resonant valley manipulation, Nature Photonics **14**, 728 (2020).

[63] S. Mitra, Álvaro Jiménez-Galán, M. Neuhaus, R. E. F. Silva, V. Pervak, M. F. Kling, and S. Biswas, Lightwave-controlled band engineering in quantum materials, ArXiv (2023).

[64] I. Aleksandrov, The statistical dynamics of a system consisting of a classical and a quantum subsystem, Z.Naturforschung A **36**, 902 (1981).

[65] R. Kapral, Mixed quantum-classical dynamics, Journal of Chemical Physics **110**, 8919 (1999).

[66] P. Brüesch, *Phonons: Theory and Experiments I*, Vol. 34 (Springer Berlin Heidelberg, 1982).

[67] F. Giustino, Electron-phonon interactions from first principles, Reviews of Modern Physics **89**, 10.1103/RevMod-Phys.89.015003 (2017).

[68] F. Caruso and M. Zacharias, Quantum theory of light-driven coherent lattice dynamics, Phys. Rev. B **107**, 054102 (2023).

[69] P. Coleman, *Introduction to Many-Body Physics* (Cambridge University Press, 2015).

[70] M. Hillery, R. F. O'Connell, M. O. Scully, and E. P. Wigner, Distribution functions in physics: Fundamentals, Physics Reports **106**, 121 (1984).

[71] P. Giannozzi, S. Baroni, N. Bonini, M. Calandra, R. Car, C. Cavazzoni, D. Ceresoli, G. L. Chiarotti, M. Cococcioni, I. Dabo, A. D. Corso, S. de Gironcoli, S. Fabris, G. Fratesi, R. Gebauer, U. Gerstmann, C. Gougoussis, A. Kokalj, M. Lazzeri, L. Martin-Samos, N. Marzari, F. Mauri, R. Mazzarello, S. Paolini, A. Pasquarello, L. Paulatto, C. Sbraccia, S. Scandolo, G. Sclauzero, A. P. Seitsonen, A. Smogunov, P. Umari, and R. M. Wentzcovitch, Quantum espresso: a modular and open-source software project for quantum simulations of materials, Journal of Physics: Condensed Matter **21**, 395502 (2009).

[72] P. Giannozzi, O. Andreussi, T. Brumme, O. Bunau, M. B. Nardelli, M. Calandra, R. Car, C. Cavazzoni, D. Ceresoli, M. Cococcioni, N. Colonna, I. Carnimeo, A. D. Corso, S. de Gironcoli, P. Delugas, R. A. DiStasio, A. Ferretti, A. Floris, G. Fratesi, G. Fugallo, R. Gebauer, U. Gerstmann, F. Giustino, T. Gorni, J. Jia, M. Kawamura, H.-Y. Ko, A. Kokalj, E. Küçükbenli, M. Lazzeri, M. Marsili, N. Marzari, F. Mauri, N. L. Nguyen, H.-V. Nguyen, A. O. de-la Roza, L. Paulatto, S. Poncé, D. Rocca, R. Sabatini, B. Santra, M. Schlipf, A. P. Seitsonen, A. Smogunov, I. Timrov, T. Thonhauser, P. Umari, N. Vast, X. Wu, and S. Baroni, Advanced capabilities for materials modelling with quantum espresso, Journal of Physics: Condensed Matter **29**, 465901 (2017).

[73] V. M. Pereira, A. H. C. Neto, and N. M. Peres, Tight-binding approach to uniaxial strain in graphene, Physical Review B - Condensed Matter and Materials Physics **80**, 10.1103/PhysRevB.80.045401 (2009).

[74] M. Droth, G. Burkard, and V. M. Pereira, Piezoelectricity in planar boron nitride via a geometric phase, Physical Review B **94**, 10.1103/PhysRevB.94.075404 (2016).

[75] V. Mohanty and E. J. Heller, Lazy electrons in graphene, Proceedings of the National Academy of Sciences **116**, 18316 (2019), https://www.pnas.org/doi/pdf/10.1073/pnas.1908624116.

[76] A. G. Čabo, J. A. Miwa, S. S. Grønborg, J. M. Riley, J. C. Johannsen, C. Cacho, O. Alexander, R. T. Chapman, E. Springate, M. Grioni, J. V. Lauritsen, P. D. King, P. Hofmann, and S. Ulstrup, Observation of ultrafast free carrier dynamics in single layer mos2, Nano Letters **15**, 5883 (2015).

[77] S. Ulstrup, A. G. Čabo, D. Biswas, J. M. Riley, M. Dendzik, C. E. Sanders, M. Bianchi, C. Cacho, D. Matselyukh, R. T. Chapman, E. Springate, P. D. King, J. A. Miwa, and P. Hofmann, Spin and valley control of free carriers in single-layer ws2, Physical Review B **95**, 10.1103/PhysRevB.95.041405 (2017).

[78] W. V. Houston, Acceleration of electrons in a crystal lattice, Phys. Rev. **57**, 184 (1940).

[79] J. B. Krieger and G. J. Iafrate, Time evolution of bloch electrons in a homogeneous electric field, Phys. Rev. B **33**, 5494 (1986).

[80] Z. Lin, Y. Liu, Z. Wang, S. Xu, S. Chen, W. Duan, and B. Monserrat, Phonon-limited valley polarization in transition-metal dichalcogenides, Physical Review Letters **129**, 10.1103/PhysRevLett.129.027401 (2022).

[81] L. T. Lloyd, R. E. Wood, F. Mujid, S. Sohoni, K. L. Ji, P.-C. Ting, J. S. Higgins, J. Park, and G. S. Engel, Sub-10 fs intervalley exciton coupling in monolayer mos 2 revealed by helicity-resolved two-dimensional electronic spectroscopy, ACS Nano **15**, 26 (2021).

[82] C. Mai, A. Barrette, Y. Yu, Y. G. Semenov, K. W. Kim, L. Cao, and K. Gundogdu, Many-body effects in valleytronics: Direct measurement of valley lifetimes in single-layer mos2, Nano Letters **14**, 202 (2014).

[83] S. A. Sato, K. Yabana, Y. Shinohara, T. Otobe, and G. F. Bertsch, Numerical pump-probe experiments of laser-excited silicon in nonequilibrium phase, Physical Review B - Condensed Matter and Materials Physics **89**, 10.1103/PhysRevB.89.064304 (2014).

[84] J. Walkenhorst, U. D. Giovannini, A. Castro, and A. Rubio, Tailored pump-probe transient spectroscopy with time-dependent density-functional theory: controlling absorption spectra, European Physical Journal B **89**, 10.1140/epjb/e2016-70064-0 (2016).

[85] F. P. Bonafé, B. Aradi, B. Hourahine, C. R. Medrano, F. J. Hernández, T. Frauenheim, and C. G. Sánchez, A real-time time-dependent density functional tight-binding implementation for semiclassical excited state electron-nuclear dynamics and pump-probe spectroscopy simulations, Journal of Chemical Theory and Computation **16**, 4454 (2020).

[86] N. Tancogne-Dejean, M. J. T. Oliveira, X. Andrade, H. Appel, C. H. Borca, G. L. Breton, F. Buchholz, A. Castro, S. Corni, A. A. Correa, U. D. Giovannini, A. Delgado, F. G. Eich, J. Flick, G. Gil, A. Gomez, N. Helbig, H. Hübener, R. Jestädt, J. Jornet-Somoza, A. H. Larsen, I. V. Lebedeva, M. Lüders, M. A. L. Marques, S. T. Ohlmann, S. Pipolo, M. Rampp, C. A. Rozzi, D. A. Strubbe, S. A. Sato, C. Schäfer, I. Theophilou,

A. Welden, and A. Rubio, Octopus, a computational framework for exploring light-driven phenomena and quantum dynamics in extended and finite systems, The Journal of Chemical Physics **152**, 10.1063/1.5142502 (2020), 124119.

[87] N. Klemke, N. Tancogne-Dejean, G. M. Rossi, Y. Yang, F. Scheiba, R. E. Mainz, G. D. Sciacca, A. Rubio, F. X. Kärtner, and O. D. Mücke, Polarization-state-resolved high-harmonic spectroscopy of solids, Nature Communications **10**, 10.1038/s41467-019-09328-1 (2019).

[88] M. S. Mrudul, Álvaro Jiménez-Galán, M. Ivanov, and G. Dixit, Light-induced valleytronics in pristine graphene, Optica **8**, 422 (2021).

[89] K. F. Mak, K. L. McGill, J. Park, and P. L. McEuen, The valley hall effect in mos₂ transistors, Science **344**, 1489 (2014).

[90] I. Tyulnev, Álvaro Jiménez-Galán, J. Poborska, L. Vamos, R. F. Silva, P. S. J. Russell, F. Tani, O. Smirnova, M. Ivanov, and J. Biegert, Valleytronics in bulk mos₂ by optical control of parity and time symmetries (2023), arXiv:2302.12564 [cond-mat.mtrl-sci].

[91] J. Chen, C. Liu, and R. Li, Valley-selective polarization in twisted bilayer graphene controlled by a counterrotating bicircular laser field, Photonics **10**, 10.3390/photonics10050516 (2023).

[92] N. Tancogne-Dejean, O. D. Mücke, F. X. Kärtner, and A. Rubio, Ellipticity dependence of high-harmonic generation in solids originating from coupled intraband and interband dynamics, Nature Communications **8**, 745 (2017).

[93] N. Tancogne-Dejean, O. D. Mücke, F. X. Kärtner, and A. Rubio, Impact of the electronic band structure in high-harmonic generation spectra of solids, Phys. Rev. Lett. **118**, 87403 (2017).

[94] E. Goulielmakis and T. Brabec, High harmonic generation in condensed matter, Nature Photonics **16**, 411 (2022).

[95] O. Neufeld, N. Tancogne-Dejean, H. Hübener, U. D. Giovannini, and A. Rubio, Are there universal signatures of topological phases in high harmonic generation? probably not (2023), arXiv:2303.17300 [cond-mat.mtrl-sci].

[96] O. Neufeld and O. Cohen, Background-free measurement of ring currents by symmetry-breaking high-harmonic spectroscopy, Phys. Rev. Lett. **123**, 103202 (2019).

[97] A. Fleischer, O. Kfir, T. Diskin, P. Sidorenko, and O. Cohen, Spin angular momentum and tunable polarization in high-harmonic generation, NATURE PHOTONICS — **8**, 543 (2014).

[98] J. J. Zhou and M. Bernardi, Ab initio electron mobility and polar phonon scattering in gaas, Physical Review B **94**, 10.1103/PhysRevB.94.201201 (2016).

Supplemental Information: Revealing Ultrafast Phonon Mediated Inter-Valley Scattering through Transient Absorption and High Harmonic Generation Spectroscopies

SI.1.   DETAILS OF THE PHONON NORMAL MODE DESCRIPTION

We follow primarily the convention from Feliciano Giustino's Rev. Mod. Phys. [1], restating many definitions here to make the text self-contained. These definitions are used in the derivation of the phonon wigner distribution and the electron-phonon coupling matrix elements.

A.   The Born-Von Kármán Boundary Conditions

The crystalline primitive unit cell is defined by the primitive lattice vectors $\mathbf{a}_i$, for $i = \{1, \ldots, l\}$ for the number of periodic dimensions l and the p^{th} unit cell is specified by $\mathbf{R}_p = \sum_i n_i \mathbf{a}_i$ with integers $n_i \in [0, N_i - 1]$. The BvK supercell contains $N_p = \prod_i N_i$ primitive unit cells. The primitive vectors of the reciprocal lattice are denoted by $\mathbf{b}_j$, fulfilling the duality condition $\mathbf{a}_i \cdot \mathbf{b}_j = 2\pi \delta_{ij}$. Consider Bloch wave vectors $\mathbf{q}_i$ defined on a uniform grid in the first Brillouin zone, $\mathbf{q} = \sum_i (m_i/N_i) \mathbf{b}_i$ with integers $m_i \in [0, N_i - 1]$. From these definitions we have the following sum rules:

$$\sum_q \exp(i\mathbf{q} \cdot \mathbf{R}_p) = N_p \delta_{p,0}$$
$$\sum_p \exp(i\mathbf{q} \cdot \mathbf{R}_p) = N_p \delta_{q,0}. \tag{SI.1}$$

B.   Normal Mode Coordinates

Within the BvK boundary conditions atoms are identified by their positions w/rt the primitive cell, $\mathbf{R}_{\alpha p}^0 = \mathbf{R}_p + \mathbf{R}_\alpha^0$, where $p = 1, \ldots, N_c$ identifies the primitive cell, α indicates the specific atom within the primitive cell, N_c is the number of atoms within each primitive unit cell, and $\mathbf{R}_\alpha^0$ denotes the equilibrium position within the primitive unit cell defined by being a minimum energy configuration for a given lattice configuration. We can further identify small displacements from these positions via $\delta\mathbf{R}_{\alpha p} = \mathbf{R}_{\alpha p} - \mathbf{R}_{\alpha p}^0$. For small displacements from the minimum energy configuration, we can write the potential as

$$U = U_0 + \frac{1}{2} \sum_{\alpha p, \alpha' p'} \frac{\partial^2 U}{\partial\mathbf{R}_{\alpha p} \partial\mathbf{R}_{\alpha' p'}} \bigg|_{\mathbf{R}_{\alpha,p}^0, \mathbf{R}_{\alpha',p'}^0} \delta\mathbf{R}_{\alpha p} \delta\mathbf{R}_{\alpha' p'}$$
$$= U_0 + \frac{1}{2} C_{\alpha p, \alpha' p'} \delta\mathbf{R}_{\alpha p} \delta\mathbf{R}_{\alpha' p'}, \tag{SI.2}$$

where we have defined the so called Interatomic Force Constant matrix (IFC) as $\underline{C}$, with $C_{\alpha p, \alpha' p'} \in \mathbb{R}^{d \times d}$. Treating the nuclear positions as operators, we define canonical momenta $\mathbf{P}_{\alpha p}$ by the canonical commutation relation $[\mathbf{R}_{\alpha p}, \mathbf{P}_{\alpha p}] = i\hbar \delta_{\alpha,\alpha'} \delta_{p,p'}$ and write the Hamiltonian operator for the nuclei in real space as

$$\hat{H}_{ph} = \frac{1}{2} \sum_{\alpha p, \alpha' p'} C_{\alpha p, \alpha' p'} \delta\mathbf{R}_{\alpha p} \delta\mathbf{R}_{\alpha' p'} + \sum_{\alpha p} \frac{1}{2M_\alpha} \mathbf{P}_{\alpha p}^2 \tag{SI.3}$$

Since the IFC must be invariant under any operation which maps between supercells, it obeys certain symmetry operations. We can encode this via the Fourier transform of the IFC, defined as the dynamical matrix [2]

$$D_{\alpha,\alpha'}(\mathbf{q}) = (M_\alpha M_{\alpha'})^{-1/2} \sum_p C_{\alpha 0, \alpha' p} \exp(i\mathbf{q} \cdot \mathbf{R}_p), \tag{SI.4}$$

where M_α is the mass of the α^{th} ion. The dynamical matrix is hermitian and positive definite allowing real eigenvalues, denoted as $\omega_{\mathbf{q}\nu}^2$

$$\sum_{\alpha'} D_{\alpha,\alpha'}(\mathbf{q}) \mathbf{e}_{\alpha' \nu}(\mathbf{q}) = \omega_{\mathbf{q}\nu}^2 \mathbf{e}_{\alpha \nu}(\mathbf{q}). \tag{SI.5}$$

In classical mechanics, $\mathbf{e}_{\alpha\nu}(\mathbf{q}) \in \mathbb{C}^d$ correspond to the normal modes of the system, i.e. independent oscillators with characteristic angular frequency $\omega_{\mathbf{q}\nu}$ for each branch ν and unique primitive cell atom α. The eigenvectors and values of the dynamical matrix have the following properties at each $\mathbf{q}$:

$$\sum_\nu e^*_{\alpha'\nu,i}(\mathbf{q}) e_{\alpha\nu,j}(\mathbf{q}) = \delta_{\alpha,\alpha'}\delta_{i,j} \quad \text{(Completeness)}$$

$$\sum_\alpha e^*_{\alpha\nu,i}(\mathbf{q}) e_{\alpha\nu',j}(\mathbf{q}) = \delta_{\nu\nu'}\delta_{i,j} \quad \text{(Orthonormality)} \tag{SI.6}$$

$$\omega^2_{-\mathbf{q},\nu} = \omega^2_{\mathbf{q}\nu}$$

$$\mathbf{e}_{\alpha\nu}(-\mathbf{q}) = \mathbf{e}^*_{\alpha\nu}(\mathbf{q}).$$

By inserting the decomposition of real space displacement into phonon coordinates, Eq. (4), into (SI.3), and using equations (SI.1) and (SI.4-SI.6) we obtain the reciprocal space Phonon Hamiltonian in reduced coordinates, Eq. (12). We can further rewrite the phonon hamiltonian by introducing the following ladder operators:

$$\hat{a}^{x,\dagger}_{\mathbf{q}\nu} = \frac{1}{\sqrt{2}}\left(\tilde{x}_{\mathbf{q}\nu} - i\tilde{r}_{\mathbf{q}\nu}\right), \quad \hat{a}^x_{\mathbf{q}\nu} = \frac{1}{\sqrt{2}}\left(\tilde{x}_{\mathbf{q}\nu} + i\tilde{r}_{\mathbf{q}\nu}\right)$$

$$\hat{a}^{y,\dagger}_{\mathbf{q}\nu} = -\frac{1}{\sqrt{2}}\left(i\tilde{y}_{\mathbf{q}\nu} + \tilde{s}_{\mathbf{q}\nu}\right), \quad \hat{a}^y_{\mathbf{q}\nu} = \frac{1}{\sqrt{2}}\left(i\tilde{y}_{\mathbf{q}\nu} - \tilde{s}_{\mathbf{q}\nu}\right), \tag{SI.7}$$

whose definitions and properties as ladder operators follow from the phonon momentum inversion properties and canonical commutation relations, Eq. (8) and (10). From here it is trivial to rewrite the reciprocal space phonon hamiltonian Eq. (12) as

$$\hat{H}_{\text{ph}} = \sum_{\mathbf{q}\in\mathcal{A},\nu} \omega_{\mathbf{q}\nu}\left(\hat{a}^{x,\dagger}_{\mathbf{q}\nu}\hat{a}^x_{\mathbf{q}\nu} + \frac{1}{2}\right) + \sum_{\mathbf{q}\in\mathcal{B},\nu} \omega_{\mathbf{q}\nu}\left(\hat{a}^{x,\dagger}_{\mathbf{q}\nu}\hat{a}^x_{\mathbf{q}\nu} + \hat{a}^{y,\dagger}_{\mathbf{q}\nu}\hat{a}^y_{\mathbf{q}\nu} + 1\right). \tag{SI.8}$$

SI.2. DERIVATION OF THE TIGHT-BINDING ELECTRON-PHONON COUPLING TERM

Generally the electron-phonon coupling constants $g^\nu_{mn}(\mathbf{q})$ are most often incorporated into semi-classical Boltzmann style equations, meaning that only their absolute value is calculated using DFPT [3], or only described analytically in small regions around high symmetry BZ points [4–7]. However, we require the complex value of the coupling throughout the entire BZ in order to have coherent electronic evolution. Therefore we describe our derivation for this in detail.

Starting with the following Hamiltonain:

$$\hat{H}_W(\mathbf{X}) = H_{\text{ph}}(\mathbf{X}) - \sum_{p\delta} t(\mathbf{R}_b, \mathbf{R}_a)\left(\hat{a}^\dagger_p \hat{b}_{p+\delta} + c.c.\right) + \sum_{p\alpha} \Delta_\alpha \hat{\alpha}^\dagger_p \hat{\alpha}_p, \tag{SI.9}$$

we expand the exponential dependence of the hopping term on the nuclear coordinates, $t(\mathbf{R}_b, \mathbf{R}_a) = t_0 \exp\left(-b\left[\frac{|\mathbf{R}_b - \mathbf{R}_a|}{d_0} - 1\right]\right)$, to first order, giving us:

$$\hat{H}_W(\mathbf{X}) = H_{\text{ph}}(\mathbf{X}) - t_0 \sum_{p\delta}\left(\hat{a}^\dagger_p \hat{b}_{p+\delta} + c.c.\right) + \sum_{p\alpha} \Delta_\alpha \hat{\alpha}^\dagger_p \hat{\alpha}_p - \frac{t_0 b}{d_0}\sum_{p\delta} \hat{\boldsymbol{\delta}} \cdot (\delta\mathbf{R}_{p+\delta,b} - \delta\mathbf{R}_{pa})\left(\hat{a}^\dagger_p \hat{b}_{p+\delta} + c.c.\right), \tag{SI.10}$$

where $\hat{\boldsymbol{\delta}}$ is the unit vector connecting the a sublattice sites to the b sublattice sites. We can rewrite the real space electron-phonon coupling (EPC) hamiltonian as:

$$\hat{H}_{\text{e-ph}} = -\frac{t_0 b}{a_0}\sum_p \sum_{p'\in\{p,p\pm1\}} \hat{\boldsymbol{\delta}}^0_{p'} \cdot (\delta\mathbf{R}_{bp'} - \delta\mathbf{R}_{ap})\left(\hat{a}^\dagger_p \hat{b}_{p'} + c.c.\right), \tag{SI.11}$$

where $\hat{a}_p$ we have organized the supercell labeling such that the nearest neighbors for each primitive cell are labeled as belonging to $p-1, p, p+1$. Furthermore, defining the equilibrium nearest neighbor distance as $\mathbf{R}^0_{bp} - \mathbf{R}^0_{ap} = \boldsymbol{\delta}^0$ we can easily write:

$$\boldsymbol{\delta}^0_{p-1} = \mathbf{R}^0_{b,p-1} - \mathbf{R}^0_{ap} = \boldsymbol{\delta}^0 - \mathbf{a}_2$$

$$\boldsymbol{\delta}^0_p = \boldsymbol{\delta}^0 \tag{SI.12}$$

$$\boldsymbol{\delta}^0_{p+1} = \boldsymbol{\delta}^0 - \mathbf{a}_2 - \mathbf{a}_1,$$

with corresponding unit vectors $\hat{\boldsymbol{\delta}}_p^0$. We take the Fourier transform by replacing the real space lattice site operators with their planewave counterparts:

$$\hat{\alpha}_p = N_p^{-1/2} \sum_{\mathbf{k}} e^{i\mathbf{k}\cdot\mathbf{R}_{\alpha p}^0} \hat{\alpha}_{\mathbf{k}} \tag{SI.13}$$

Note that we make the distinction between the primitive cell lattice sites $\mathbf{R}_p$ and sublattice sites $\mathbf{R}_{\alpha p}^0$ belonging to the $\alpha \in \{A, B\}$ sublattices: $\mathbf{R}_{\alpha p}^0$. Although we have ionic displacements $\delta\mathbf{R}_{\alpha p}$, these are fundamentally defined w/rt to the sublattice sites $\mathbf{R}_{\alpha p}^0$ which define the periodicity of the crystal, and therefore how the Fourier transform is defined.

Inserting equations (SI.13) and (4) into equation (SI.11), we have the following:

$$\hat{H}_{\text{e-ph}} = -\frac{t_0 b}{d_0} N_p^{-3/2} \sum_{p\delta} \sum_{q\nu} \sum_{\mathbf{k}\mathbf{k}'} \hat{\boldsymbol{\delta}} \cdot \left(\left(\frac{M_0}{M_b}\right)^{\frac{1}{2}} e^{i\mathbf{q}\cdot\boldsymbol{\mu}_\delta} \mathbf{e}_{b\nu}(\mathbf{q}) - \left(\frac{M_0}{M_a}\right)^{\frac{1}{2}} \mathbf{e}_{a\nu}(\mathbf{q}) \right) z_{\mathbf{q}\nu}$$
$$\times \left(e^{i\mathbf{R}_p\cdot(\mathbf{q}+\mathbf{k}'-\mathbf{k})} e^{i\mathbf{k}'\cdot\boldsymbol{\delta}} \hat{a}_{\mathbf{k}'}^\dagger \hat{b}_{\mathbf{k}} + e^{i\mathbf{R}_p\cdot(\mathbf{q}-\mathbf{k}'+\mathbf{k})} \hat{b}_{\mathbf{k}'}^\dagger \hat{a}_{\mathbf{k}} \right) \tag{SI.14}$$
$$= \sum_{\mathbf{q}\nu\delta} \sum_{\mathbf{k}\mathbf{k}'} g_\nu^\delta(\mathbf{q}) z_{\mathbf{q}\nu} \left(\delta_{\mathbf{q}+\mathbf{k}',\mathbf{k}} e^{i\mathbf{k}'\cdot\boldsymbol{\delta}} \hat{a}_{\mathbf{k}}^\dagger \hat{b}_{\mathbf{k}} + \delta_{\mathbf{q}-\mathbf{k}',\mathbf{k}} e^{-i\mathbf{k}'\cdot\boldsymbol{\delta}} \hat{b}_{\mathbf{k}'}^\dagger \hat{a}_{\mathbf{k}} \right),$$

Where $\mu_\delta = \{\mathbf{0}, -\mathbf{a}_2, -\mathbf{a}_2 - \mathbf{a}_1\}$ are the primitive lattice vectors connecting primitive cell $\mathbf{R}_p$ to $p' = \{p-1, p, p+1\}$, and in the second line we have summed through p, applying the BvK boundary conditions Eq. (SI.2), and defined the electron-phonon coupling term as

$$g_\nu^\delta(\mathbf{q}) := -\frac{t_0 b}{N_p^{1/2} d_0} \hat{\boldsymbol{\delta}} \cdot \left(\left(\frac{M_0}{M_b}\right)^{\frac{1}{2}} e^{i\mathbf{q}\cdot\boldsymbol{\mu}_\delta} \mathbf{e}_{b\nu}(\mathbf{q}) - \left(\frac{M_0}{M_a}\right)^{\frac{1}{2}} \mathbf{e}_{a\nu}(\mathbf{q}) \right). \tag{SI.15}$$

We can group $g_\nu^\delta(\mathbf{q})$ and everything in parentheses together and call it the electron-phonon coupling operator $\hat{M}(\mathbf{q}, \nu)$.

By summing $\mathbf{q}$ through $\mathcal{C}$, we obtain the actually implemented form of the tight binding Hamiltonian in Eq. (18):

$$\hat{H}_W(\mathbf{X}) = H_{\text{ph}}(\mathbf{X}) + \hat{H}_e + \sum_{\nu,\mathbf{q}\in\mathcal{A}} x_{\mathbf{q}\nu} \hat{M}(\mathbf{q}, \nu) + \sum_{\nu,\mathbf{q}\in\mathcal{B}} x_{\mathbf{q}\nu} \left(\hat{M}(\mathbf{q}, \nu) + \hat{M}^\dagger(\mathbf{q}, \nu) \right) + iy_{\mathbf{q}\nu} \left(\hat{M}(\mathbf{q}, \nu) - \hat{M}^\dagger(\mathbf{q}, \nu) \right),$$
$$\tag{SI.16}$$

where H_e gathers the bare hopping and onsite energy terms. This means that the equations of motion for each $x_{\mathbf{q}\nu}^i$, $y_{\mathbf{q}\nu}^i$ trajectory are explicitly

$$\dot{r}_{\mathbf{q}\nu} = -\left\langle \frac{\partial H}{\partial x_{\mathbf{q}\nu}^i} \right\rangle = -\text{Tr}\left[\hat{\rho}_i(t) \left(\hat{M}(\mathbf{q}, \nu) + \hat{M}^\dagger(\mathbf{q}, \nu) \right) \right] - \frac{\omega_{\mathbf{q}\nu}}{l_{\mathbf{q}\nu}} x_{\mathbf{q}\nu}$$
$$\dot{s}_{\mathbf{q}\nu} = -\left\langle \frac{\partial H}{\partial y_{\mathbf{q}\nu}^i} \right\rangle = -i\text{Tr}\left[\hat{\rho}_i(t) \left(\hat{M}(\mathbf{q}, \nu) - \hat{M}^\dagger(\mathbf{q}, \nu) \right) \right] - \frac{\omega_{\mathbf{q}\nu}}{l_{\mathbf{q}\nu}} y_{\mathbf{q}\nu}. \tag{SI.17}$$

Looking at the structure of $\hat{M}(\mathbf{q}, \nu)$ one can see that $\hat{M}(\mathbf{q}, \nu) + \hat{M}^\dagger(\mathbf{q}, \nu)$ will be hermitian while $\hat{M}(\mathbf{q}, \nu) - \hat{M}^\dagger(\mathbf{q}, \nu)$ will be anti-hermitian. Therefore expectation values of the former will always be real and imaginary for the latter.

SI.3. ELECTRONIC CURRENT OPERATOR

The current density operator can be defined as

$$\hat{\mathbf{j}}_W = \frac{i}{\Omega} \left[\hat{\mathbf{r}}, \hat{H}_W(t) \right] \tag{SI.18}$$

for the super cell surface area Ω and the electron position operator

$$\hat{\mathbf{r}} = \sum_{i\in N_p} \sum_\delta \mathbf{r}_i \hat{a}_i^\dagger \hat{a}_i + (\mathbf{r}_i + \boldsymbol{\delta}) \hat{b}_{i+\delta}^\dagger \hat{b}_{i+\delta} = \sum_{i\in N_p} \sum_\delta \mathbf{r}_i \hat{n}_i + (\mathbf{r}_i + \boldsymbol{\delta}) \hat{n}_{i+\delta} \tag{SI.19}$$

Where i is summed over primitive cells and the number operator $\hat{n}_{i+\delta}$ is understood to be a b sublattice number operator to reduce notational clutter. We can utilize the definition of the sublattice anticommutation,

$$\{\hat{\alpha}_i, \hat{\beta}_j^\dagger\} = \delta_{i,j}\delta_{\alpha,\beta}$$
$$\{\hat{\alpha}_i, \hat{\beta}_j\} = \{\hat{\alpha}_i^\dagger, \hat{\beta}_j^\dagger\} = 0, \tag{SI.20}$$

where $\hat{\alpha}, \hat{\beta}$ can be either $\hat{a}$ or $\hat{b}$ site operators to derive the identity:

$$\left[\hat{n}_i, \hat{a}_j^\dagger \hat{b}_{j+\delta}\right] = (\delta_{ij} - \delta_{i,j+\delta})\, \hat{a}_j^\dagger \hat{b}_{j+\delta}. \tag{SI.21}$$

Taking the commutator and utilizing the identity (SI.21) we obtain

$$\hat{\mathbf{j}} = e\frac{i}{\Omega}\sum_{i \in N_p}\sum_{\delta}\boldsymbol{\delta}\left(t_0 + \frac{t_0 b}{a_0}\hat{\boldsymbol{\delta}}\cdot(\delta\mathbf{r}_{i+\delta} - \delta\mathbf{r}_i)\right)\left(\hat{a}_i^\dagger\hat{b}_{i+\delta} - c.c.\right). \tag{SI.22}$$

Expanding in plane waves and phonons as before we have:

$$\hat{\mathbf{j}} = e\frac{i}{\Omega}\left[t_0\sum_{\mathbf{k}}\sum_{\delta}\boldsymbol{\delta}\left(\hat{a}_{\mathbf{k}}^\dagger\hat{b}_{\mathbf{k}}e^{i\mathbf{k}\cdot\boldsymbol{\delta}} - c.c.\right) + \sum_{\mathbf{q}\nu}z_{\mathbf{q}\nu}\hat{D}(\mathbf{q},\nu)\right]$$
$$\hat{D}(\mathbf{q},\nu) = \sum_{\mathbf{k}}\sum_{\delta}\boldsymbol{\delta}g_\nu^\delta(\mathbf{q})\left(\hat{a}_{\mathbf{k}+\mathbf{q}}^\dagger\hat{b}_{\mathbf{k}}e^{i\mathbf{k}\cdot\boldsymbol{\delta}} - \hat{b}_{\mathbf{k}}^\dagger\hat{a}_{\mathbf{k}-\mathbf{q}}e^{-i\mathbf{k}\cdot\boldsymbol{\delta}}\right). \tag{SI.23}$$

We take Ω to be N_p times primitive cell area $\Omega_0 = 19.5\text{bohr}^2$

SI.4. ELECTRONIC STATE RENORMALIZATION IN GRAPHENE

To provide a sanity check of our derivation of $g_\nu^\delta(\mathbf{q})$ in the tight binding model, we first apply our tight binding Hamiltonian in Eq. (18) to graphene and compare with recent results from Nery and Mauri [8] using static displacement averaging to calculate the electron-phonon interaction renormalized spectral function $A_{\mathbf{k}}(\omega)$.

Reference [8] utilizes an electron-phonon coupling parameter η, which in our model corresponds to $\eta = bt_0/d_0$. We reproduced their Figure 8 results using the same parameter set of $\Delta_\alpha = 0$, $t_0 = 2.58eV$ and $d_0 = 1.413\text{Å}$ for two different coupling strengths, $\eta_{\text{expt}} = 4.42$ eV/Å(a value extracted from experiment), and $\eta_{\text{inter}} = 2.5\eta_{\text{expt}}$ by running MTEF dynamics on a 36×36 $\mathbf{k}$ and $\mathbf{q}$ grid for 12fs. We calculate the retarded Green's function for band n via:

$$G_{W,n\mathbf{k}}(t) = \frac{i}{N_t}\sum_{il}\langle n\mathbf{k}|\psi_l^i(t)\rangle\langle\psi_l^i(t=0)|n\mathbf{k}\rangle. \tag{SI.24}$$

By taking the Fourier transform of the mean field propagated Green's function, using the mask function $W(x) = 1 - 3x^2 + 2x^3$, we obtain $G_{W,n\mathbf{k}}(\omega)$. The spectral function is of course defined to be $A_{n\mathbf{k}}(\omega) = -(1/\pi)\text{Im}[G_{W,n\mathbf{k}}(\omega)]$. The results shown in Fig. SI.1, have good agreement with the Nery and Mauri results, namely a significant broadening of the signal with increasing temperature and coupling strength, as well as a decrease in signal intensity away from K and Γ for both cases. The small negativities in the spectral function for high energy $\mathbf{k}$ points near Γ in the lower panel are due to the extremely anharmonic dynamics arising from the artificially strong electron-phonon coupling constant. Such spectral negativity is a known feature of MTEF calculations with anharmonic forces [9].

We further compare our model to a specific peak at $\mathbf{k} = 0.75K$ in Fig. SI.2. The various sampling approaches that are compared are explained in section SI.6. In panels (a) and (b) we see that the sampling approaches used in the text, dynamic and static, agree very well with data extracted from [8], with the primary difference being slightly broader tails. With this check we are confident that simply replacing the parameters of our tight binding model with those fit to hBN is a reasonable approach to the electron-phonon coupling in this system.

SI.5. CONVERGENCE OF VALLEY HOMOGENIZATION

For this analysis we use the Normalized Root Mean Squared Displacement (NRMSD) to quantify how much a given time dependent signal varies from another:

$$\text{NRMSD} = \frac{\sqrt{\int_{t_i}^{t_f} dt\,(f(t) - g(t))^2/(t_f - t_i)}}{\max(f(t)) - \min(f(t))}. \tag{SI.25}$$
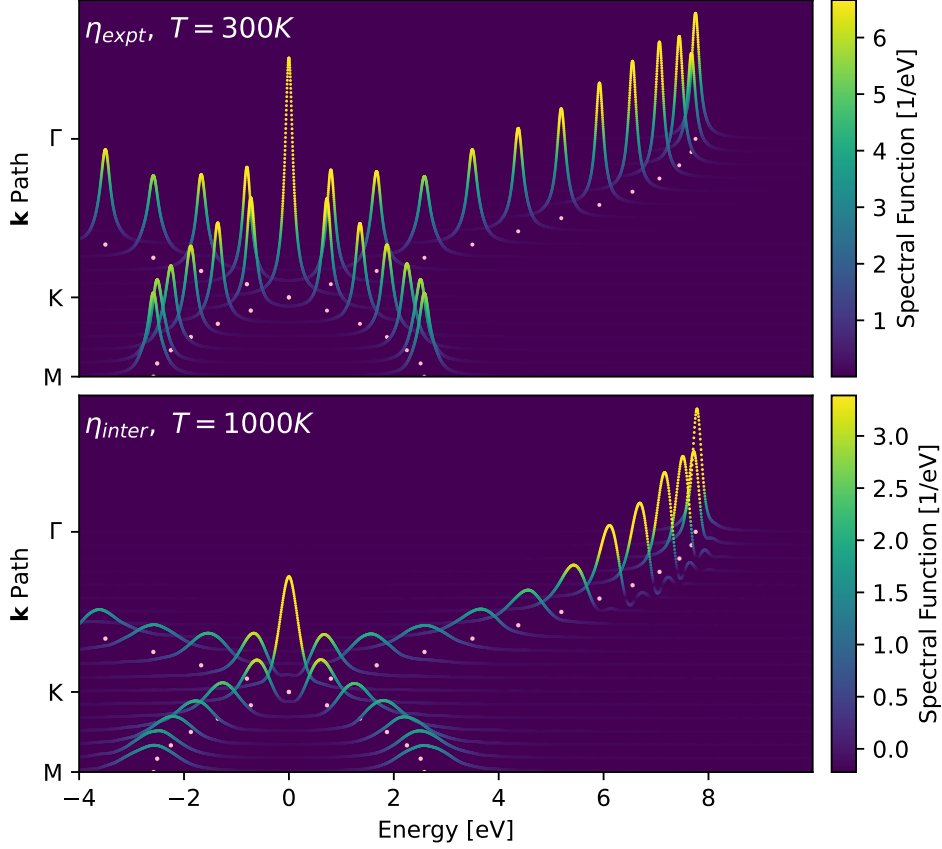
FIG. SI.1. The spectral function $A_\mathbf{k}(\omega)$ of graphene calculated in the tight binding model through MTEF, with electron-phonon coupling constants η and temperatures matching the simulations from Ref. [8], Figure 8. See text for details.

We take $f(t) = \mathrm{VA}_{N_t}(t)$ calculated with the largest number of trajectories available, in the case of the data in Fig. 2, $N_t = 380$. We let $g(t) = \mathrm{VA}_{N_t'}(t)$ be the same signal calculated with a random selection of $N_t' << N_t$ trajectories. The NRMSD value for this collection of N_t' trajectories tells us how much this signal deviates from the more converged value calculated with N_t trajectories. By pulling different random collections of size N_t' from the data we can histogram the resulting NRMSD values, giving us a probability distribution of what errors we can expect with this number of trajectories. The results of this analysis are plotted in Fig. SI.3.

Plotted in panel (a) in black is the same MTEF dynamic phonon data plotted in Fig. 2(b), alongside an example of a signal with an NRMSD of 0.02 in red. It's clear that this signal already appears qualitatively converged, yet we see from the error probability distributions in panel (b) that this a high error outlier of a result, even when using only two trajectories! Instead, with quite reasonable numbers of samples, the results rapidly converge towards signals which are graphically indistinguishable from results using over an order of magnitude more trajectories.

SI.6. ALTERNATIVE SAMPLING APPROACHES

In the special displacement method (SDM) of Zacharias and Giustino [10, 11], the convergence of sampling the configuration distribution in Eq. (14) can be accelerated for small supercell sizes (i.e. sparse $\mathbf{q}$ grids in the BZ) by taking a handful of specific configurations. These involve taking positions of magnitude $|x_{\mathbf{q}\nu}|, |y_{\mathbf{q}\nu}| = \sigma_{\mathbf{q}\nu}$ and carefully
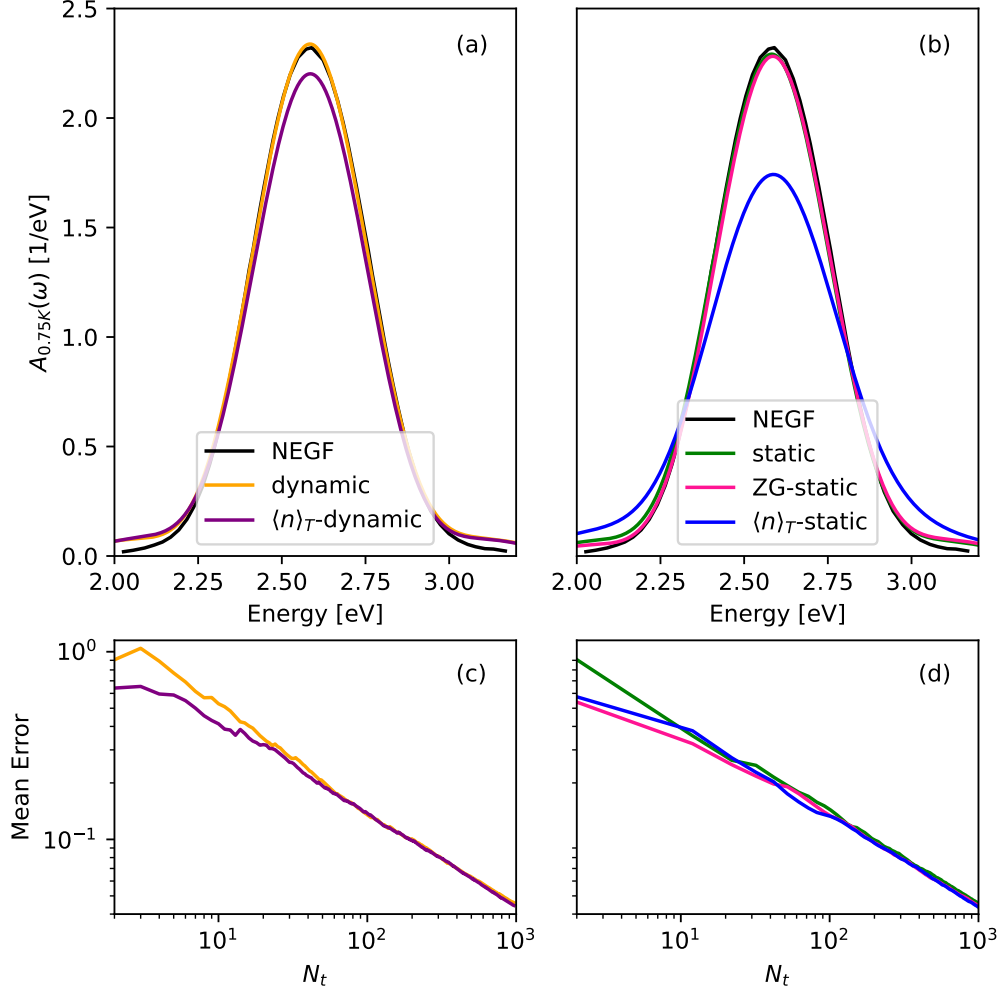
FIG. SI.2. The spectral function of graphene for $\mathbf{k} = 0.75K$, using η_{expt} and sampling at $T = 300K$ using dynamic phonon approaches in panel (a) and static phonon approaches in panel (b), with data taken from [8], Fig. 7, top left panel. The convergence of the spectral function for different sampling types in SI.6 is shown in panels (c) and (d) as the mean of the error of the time signal $G_{0.75K}(t)$ as a function of N_t, where $\text{err}(t) = \sigma_{G_{0.75K}}(t)/\sqrt{N_t}$ for $\sigma_G^2(t) = \langle G^2(t) \rangle - \langle G(t) \rangle^2$.

choosing signs $S_{\mathbf{q}\nu} = \{+1, -1\}$ of $z_{\mathbf{q}\nu} = S_{\mathbf{q}\nu}|z_{\mathbf{q}\nu}|$, which favorably cancel terms in the 2nd order perturbative expansion of observables in the phonon coordinates. This allows for capturing the thermodynamic equilibrium properties at second order which can be shown to analytically go to zero in the case of an infinitely large supercell. This is expected to be of most benefit in the case of small supercells, and has been found to not to necessarily be a sufficient configuration for convergence in cases of very strong electron-phonon coupling [8].

In our framework we can analyze this choice of displacement magnitude in terms of the phonon occupation number. Taking equations (SI.8), we clearly identify $n_{\mathbf{q}\nu}$ to be

$$n_{\mathbf{q}\nu}^x = \frac{1}{2}\left(\tilde{r}_{\mathbf{q}\nu}^2 + \tilde{x}_{\mathbf{q}\nu}^2\right) - \frac{1}{2} \quad \text{for } \mathbf{q} \in \mathcal{A}, \mathcal{B}$$

$$n_{\mathbf{q}\nu}^y = \frac{1}{2}\left(\tilde{s}_{\mathbf{q}\nu}^2 + \tilde{y}_{\mathbf{q}\nu}^2\right) - \frac{1}{2} \quad \text{for } \mathbf{q} \in \mathcal{B}.$$

$$(\text{SI.26})$$

In this picture, with the SDM choice equivalent to setting the reduced momenta $\tilde{r}, \tilde{s}$ to zero and $\tilde{x}^2 = \tilde{y}^2 = n_{\mathbf{q}\nu,T} + 1/2$ meaning $n_{\mathbf{q}\nu} = n_{\mathbf{q}\nu,T}/2 - 1/4$. That is to say, the SDM corresponds to a static displacement large enough to account for half of the thermal occupation of the phonon mode, and half of the ZPE.

We can perform an analogous sampling which obtains the thermal occupation number by construction but splits the
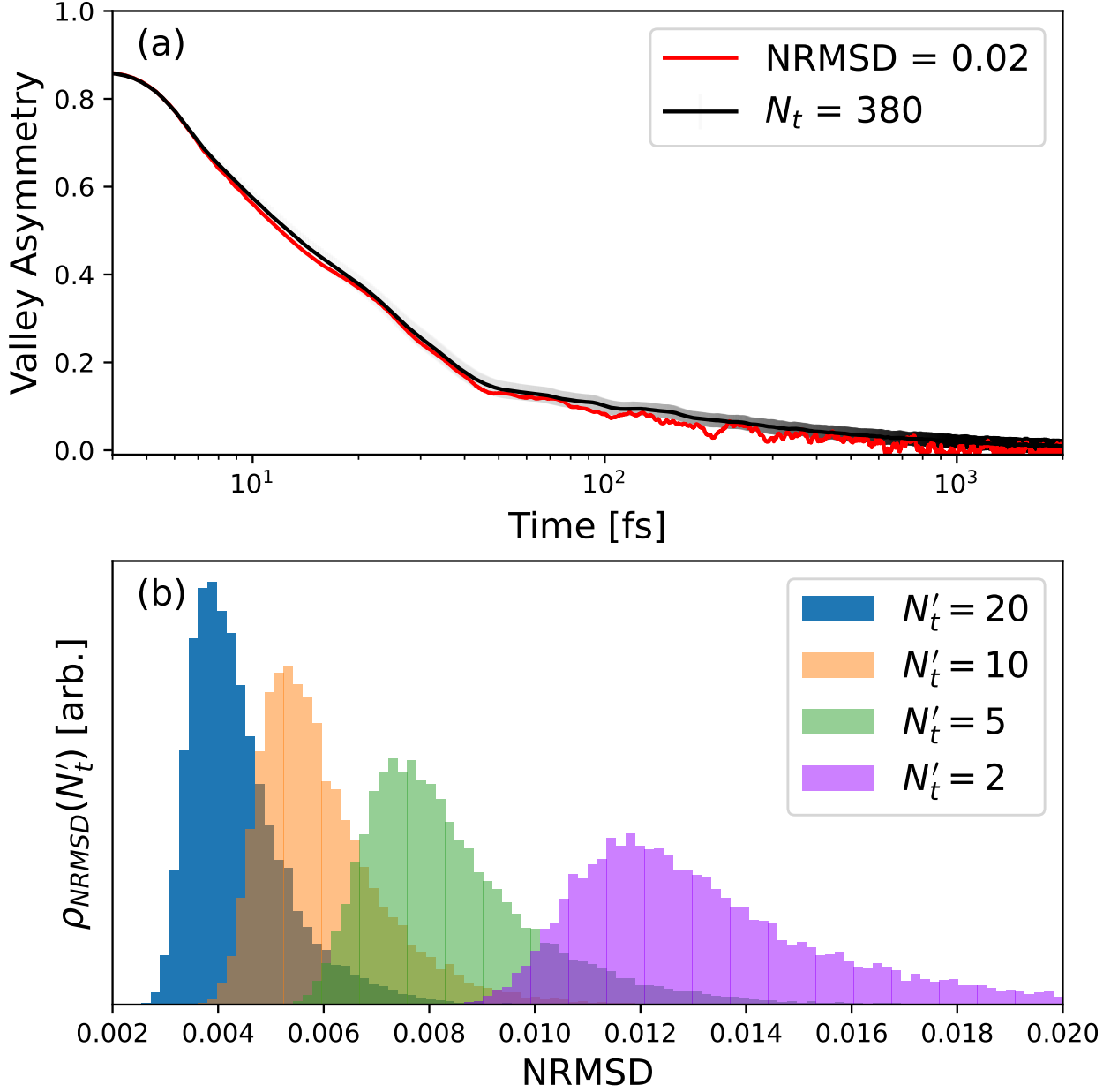
FIG. SI.3. The probability distribution of getting a particular error measured as the NRMSD of the valley polarization seen in Fig. 2 for a small number of samples with respect to the value calculated using a much larger number of samples.

weight evenly between position and momentum by choosing $\tilde{r}_{\mathbf{q}\nu}^2 = \tilde{x}_{\mathbf{q}\nu}^2 = n_{\mathbf{q}\nu,T}^x + 1/2$, and equivalently for $n_{\mathbf{q}\nu}^y$. Since in our approach, we are interested in strongly coupled electron-phonon systems where a perturbative expansion may not be sufficient, and we have dynamical phonons which can explore beyond a harmonic approximation, rather than carefully choosing signs to eliminate terms for a 2nd order thermodynamic equilibirum property, we simply randomly sample $S_{\mathbf{q}\nu}$ for every phonon branch and momenta. We refer to this as $\langle n \rangle_T$ sampling.

If on the other hand, we choose to run with frozen phonon dynamics, but still want to have initial phonon occupations corresponding to the thermal occupation, we can set $\tilde{x}_{\mathbf{q}\nu}^2 = 2n_{\mathbf{q}\nu}^x + 1$ and sample the sign of $\tilde{x}_{\mathbf{q}\nu}$ (doing the same with $\tilde{y}$), while fixing $\dot{\tilde{z}}_{\mathbf{q}\nu} = 0$. We refer to this approach as $\langle n \rangle_T$-static. For comparison, we refer to using the SDM magnitudes ($n_{\mathbf{q}\nu} = n_{\mathbf{q}\nu,T}/2$) and sampling signs with frozen phonons as ZG-static. A summary of the various initial

	$\tilde{x}_{\mathbf{q}\nu},\ \tilde{y}_{\mathbf{q}\nu}$	$\tilde{r}_{\mathbf{q}\nu},\ \tilde{s}_{\mathbf{q}\nu}$	$n_{\mathbf{q}\nu}$
dynamic	$\sim \rho_{\mathrm{ph},W}$	$\sim \rho_{\mathrm{ph},W}$	$\to n_{\mathbf{q}\nu,T}$
$\langle n\rangle_T$-dynamic	$\pm(n_{\mathbf{q}\nu}+\frac{1}{2})^{1/2}$	$\pm(n_{\mathbf{q}\nu}+\frac{1}{2})^{1/2}$	$n_{\mathbf{q}\nu,T}$
static	$\sim \rho_{\mathrm{ph},W}$	0	$\to n_{\mathbf{q}\nu,T}/2-1/4$
ZG-static	$\pm(n_{\mathbf{q}\nu}+\frac{1}{2})^{1/2}$	0	$n_{\mathbf{q}\nu,T}/2-1/4$
$\langle n\rangle_T$-static	$\pm(2n_{\mathbf{q}\nu}+1)^{1/2}$	0	$n_{\mathbf{q}\nu,T}$

TABLE SI.1. A summary of the various choices of initial conditions for the phonon reduced coordinates and momenta. Although the electronic system properties can be obtained via time evolution for all these methods, the phonon system is dynamic only when $\tilde{r}_{\mathbf{q}\nu}, \tilde{s}_{\mathbf{q}\nu} \neq 0$. The symbol "$\to n_{\mathbf{q}\nu,T}$" indicates convergence with increasing N_t.
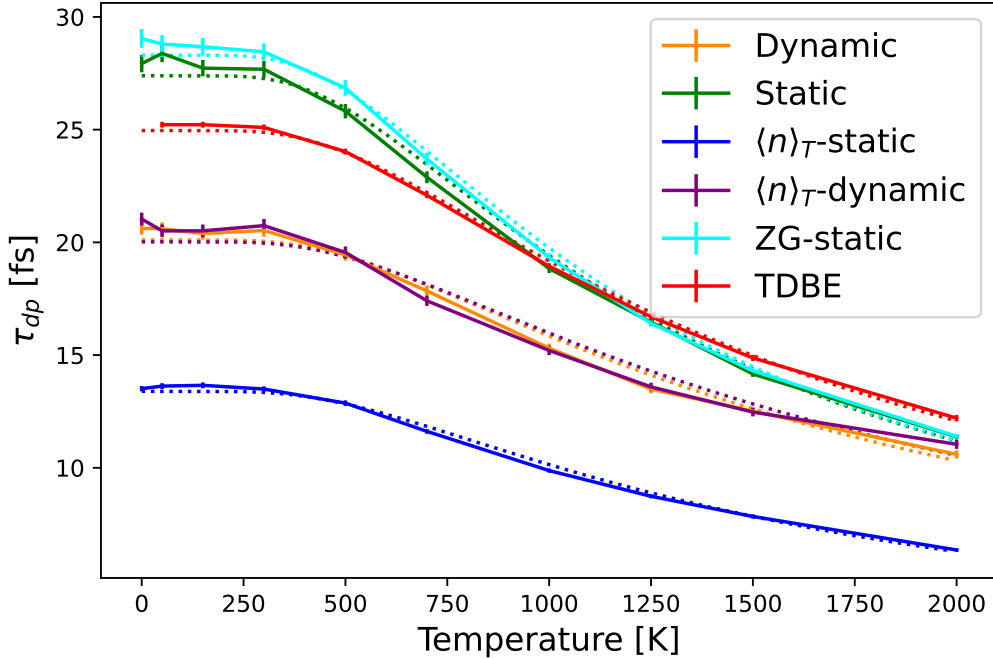

FIG. SI.4. The temperature dependence of the short time scale valley population homogenization, as seen in Fig. 2, calculated with all of the sampling techniques in Table SI.6.

conditions and dynamics choices is shown in Table SI.6.

The principle question is whether these different sampling techniques lead to altered observables, or faster convergence. We start by looking at a phonon renormalized property of the electronic system in a thermal equilibrium state. Taking the graphene spectral function in Fig. SI.2(a), we see that using 'dynamic' sampling, that is drawing phonon momenta and coordinates in a straight-forward manner from Eq. 13 and $\langle n\rangle_T$-dynamic already lead to slightly different spectral function intensities. In Fig. SI.2(c), we track the convergence of this signal by taking the average error as a function of time. Given that we are Monte Carlo sampling an initial distribution this error is defined as the standard deviation of the observable calculated with N_t trajectories, over $\sqrt{N_t}$. Panel (c) shows that the signal produced by $\langle n\rangle_T$ sampling converges marginally faster than that produced by dynamic sampling, but that at large configurations, there is virtually no difference in the two approaches.

We see something similar when comparing the 'static' and 'ZG-static' sampling approaches in Fig. SI.2(b) and Fig. SI.2(d), with the primary difference of this comparison being that the spectral function magnitudes for these two methods agree nearly exactly. The outlier however appears to be $\langle n\rangle_T$-static, which has a significantly different spectral intensity than any static or dynamic approach. This indicates that the majority of the effect responsible for renormalization of the electronic spectral function at this $\mathbf{k}$ point can be accounted for via displacement within the first standard deviation of the phonon distribution. Of course in the harmonic limit, setting phonon momentum and displacement absolute values to $\pm|\sigma_{\mathbf{q}\nu}|$ will result in motion in phase space entirely on the circumference of the phase space circle of radius $\sqrt{2}|\sigma_{\mathbf{q}\nu}|$. Fixing the initial position to $\pm 2|\sigma_{\mathbf{q}\nu}|$ apparently exceeds the renormalization effect
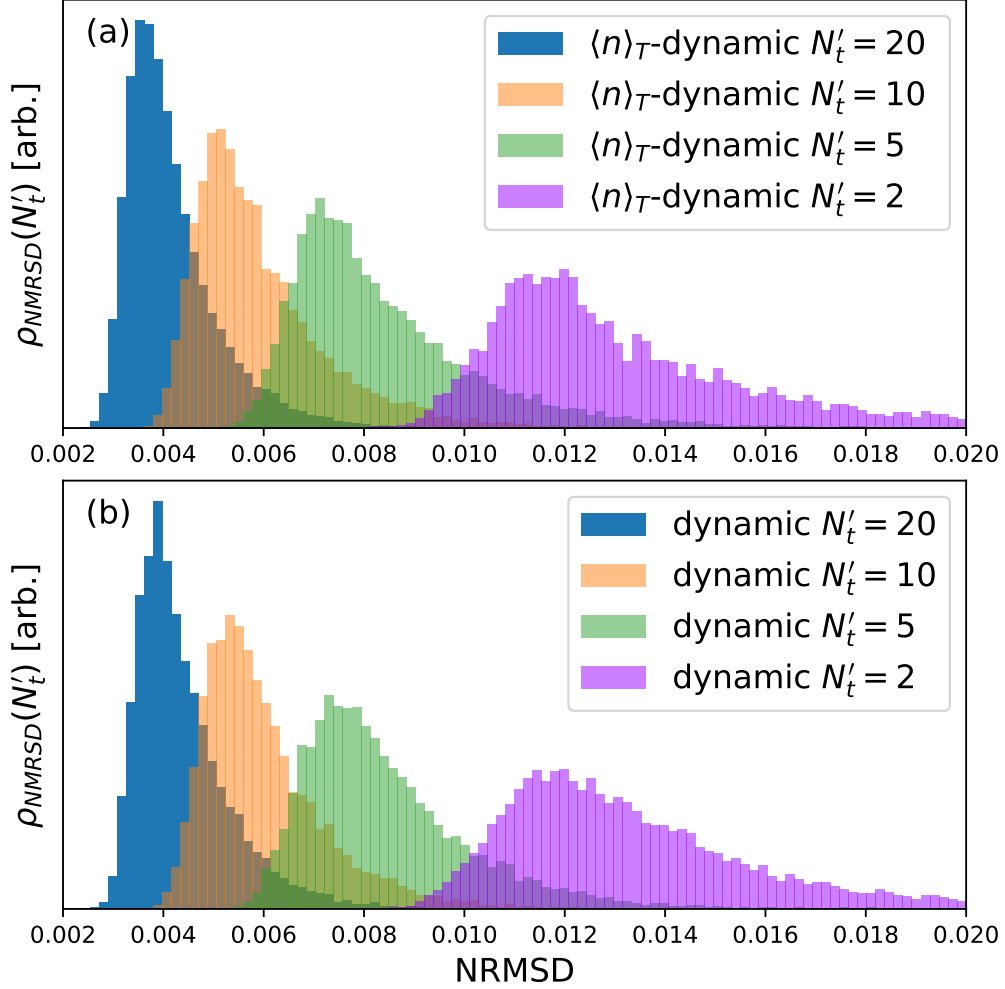
FIG. SI.5. The probability distribution of getting a particular NRMSD of the valley polarization seen in Fig. 2 when selecting an arbitrary N_t number samples taken via $\langle n \rangle_T$-dynamic sampling versus straight forward Monte Carlo sampling.

obtained by full Monte Carlo sampling, or even Monte Carlo sampling on the $\pm\sqrt{2}|\sigma_{\mathbf{q}\nu}|$ radial points.

However, this is a value calculated at thermodynamic equilibrium. To see the effect for far from equilibrium properties, we turn to the temperature dependence of the valley homogenization timescale in the TB hBN model, seen in Fig. SI.4. The $\langle n \rangle_T$-dynamic and ZG-static sampling approaches sit almost precisely on top of their corresponding dynamic and static results. Quite notably the $\langle n \rangle_T$-static results again constitute an outlier to the other methods, with a scattering fit parameter of $\alpha_{\langle n \rangle_T-\text{static}} = 0.129\text{fs}^{-1}$, compared to $\alpha_{\text{Static}} = 0.081\text{fs}^{-1}$, $\alpha_{ZG-\text{static}} = 0.082\text{fs}^{-1}$, $\alpha_{\text{Dynamic}} = 0.072\text{fs}^{-1}$, $\alpha_{\langle n \rangle_T-\text{Dynamic}} = 0.068\text{fs}^{-1}$ and $\alpha_{\text{TDBE}} = 0.065\text{fs}^{-1}$. Clearly this sampling method, while producing the correct thermal occupation value through strong static displacement, appears to overestimate the effect of phonon renormalization, when compared to Monte Carlo sampling of the phonon coordinate / momenta distribution.

Finally we can investigate whether there is any significant advantage in the dynamical case to sampling with the $\langle n \rangle_T$-dynamic approach. We repeat the NRMSD probability analysis of SI.5 for the time dependent valley asymmetry in an MTEF calculation and report the results in Fig. SI.5. We find that the probability of obtaining a signal using a small number of trajectories, which has a small deviation from the signal one would obtain using a much larger number, looks effectively identical between the two sampling approaches, thus in this case this sampling method confers no appreciable advantage.

SI.7. ZPE LEAKAGE

We track the effects of ZPE leakage when propagating with dynamic MTEF by looking at the phonon occupation number $n_{\mathbf{q}\nu}$ calculated via Eq. (SI.26). Given sufficient samples, $n_{\mathbf{q}\nu}$ will converge towards the expected thermal occupation $n_{\mathbf{q}\nu,T}$, which for the optical phonons at 300K means approximately 0. Therefore as the ZPE drains out of a given phonon mode, the occupation will go towards $-1/2$.

In Fig. SI.6 we show a selection of the occupation numbers of the highest energy optical branch phonon modes over time. In panel (a) when the system is exposed to a laser pulse, we see that on timescales commensurate with the long time scale excitation outside the valleys in Fig. 2(b), there is a loss of energy in the phonon modes. The initial occupation value of 0 requires a large number of trajectories to converge to exactly, but as discussed throughout the text, the dynamical electronic observables of interest converge rapidly. Panel (b) shows the phonon occupation when the electronic system is not pumped. In this case, due to the large electronic gap, there is nowhere for the phonon energy to go, and instead one just sees oscillation of the occupation numbers over time. This oscillation is due to anharmonic forces arising from exposure to the electronic system, and can in principle be analyzed to capture the renormalized phonon frequencies.

In Fig. SI.6(c) we take the phonon occupations from the last time step of panel (a) at 2ps and plot them against the distance of their $\mathbf{q}$ vector from Γ. There is very clearly a direct correlation between the how close a phonon mode is to Γ and the amount of energy it loses to the electronic system. This may be related to the fact that the phonon modes are coupled directly to the electronic system via a linear dependence through the nearest neighbor hopping term. Therefore the modes closer to Γ which correspond to a coherent reduction in the nearest neighbor distance throughout the system, most strongly excite the electrons and allow a conduit for vibrational energy to go into the electronic system.

---

[1] F. Giustino, Electron-phonon interactions from first principles, Reviews of Modern Physics **89**, 10.1103/RevModPhys.89.015003 (2017).

[2] A. A. Maradudin and S. H. Vosko, Symmetry properties of the normal vibrations of a crystal, Reviews of Modern Physics **40**, 10.1103/RevModPhys.40.1 (1968).

[3] J. A. Yan, W. Y. Ruan, and M. Y. Chou, Electron-phonon interactions for optical-phonon modes in few-layer graphene: First-principles calculations, Physical Review B - Condensed Matter and Materials Physics **79**, 10.1103/PhysRevB.79.115443 (2009).

[4] E. Malic, T. Winzer, E. Bobkin, and A. Knorr, Microscopic theory of absorption and ultrafast many-particle kinetics in graphene, Physical Review B - Condensed Matter and Materials Physics **84**, 10.1103/PhysRevB.84.205406 (2011).

[5] T. Winzer and E. Malic, The impact of pump fluence on carrier relaxation dynamics in optically excited graphene, Journal of Physics Condensed Matter **25**, 10.1088/0953-8984/25/5/054201 (2013).

[6] D. S. Zhang, G. Z. Kang, and J. Li, Tight-binding electron-phonon coupling and band renormalization in graphene, Chinese Physics B **24**, 10.1088/1674-1056/24/1/017301 (2015).

[7] F. Rana, P. A. George, J. H. Strait, J. Dawlaty, S. Shivaraman, M. Chandrashekhar, and M. G. Spencer, Carrier recombination and generation rates for intravalley and intervalley phonon scattering in graphene, Physical Review B - Condensed Matter and Materials Physics **79**, 10.1103/PhysRevB.79.115447 (2009).

[8] J. P. Nery and F. Mauri, Nonperturbative green's function method to determine the electronic spectral function due to electron-phonon interactions: Application to a graphene model from weak to strong coupling, Physical Review B **105**, 245120 (2022).

[9] K. Lively, G. Albareda, S. A. Sato, A. Kelly, and A. Rubio, Simulating vibronic spectra without born–oppenheimer surfaces, The Journal of Physical Chemistry Letters **12**, 3074 (2021).

[10] M. Zacharias and F. Giustino, One-shot calculation of temperature-dependent optical spectra and phonon-induced band-gap renormalization, Physical Review B **94**, 10.1103/PhysRevB.94.075125 (2016).

[11] M. Zacharias and F. Giustino, Theory of the special displacement method for electronic structure calculations at finite temperature, Physical Review Research **2**, 10.1103/PhysRevResearch.2.013357 (2020).
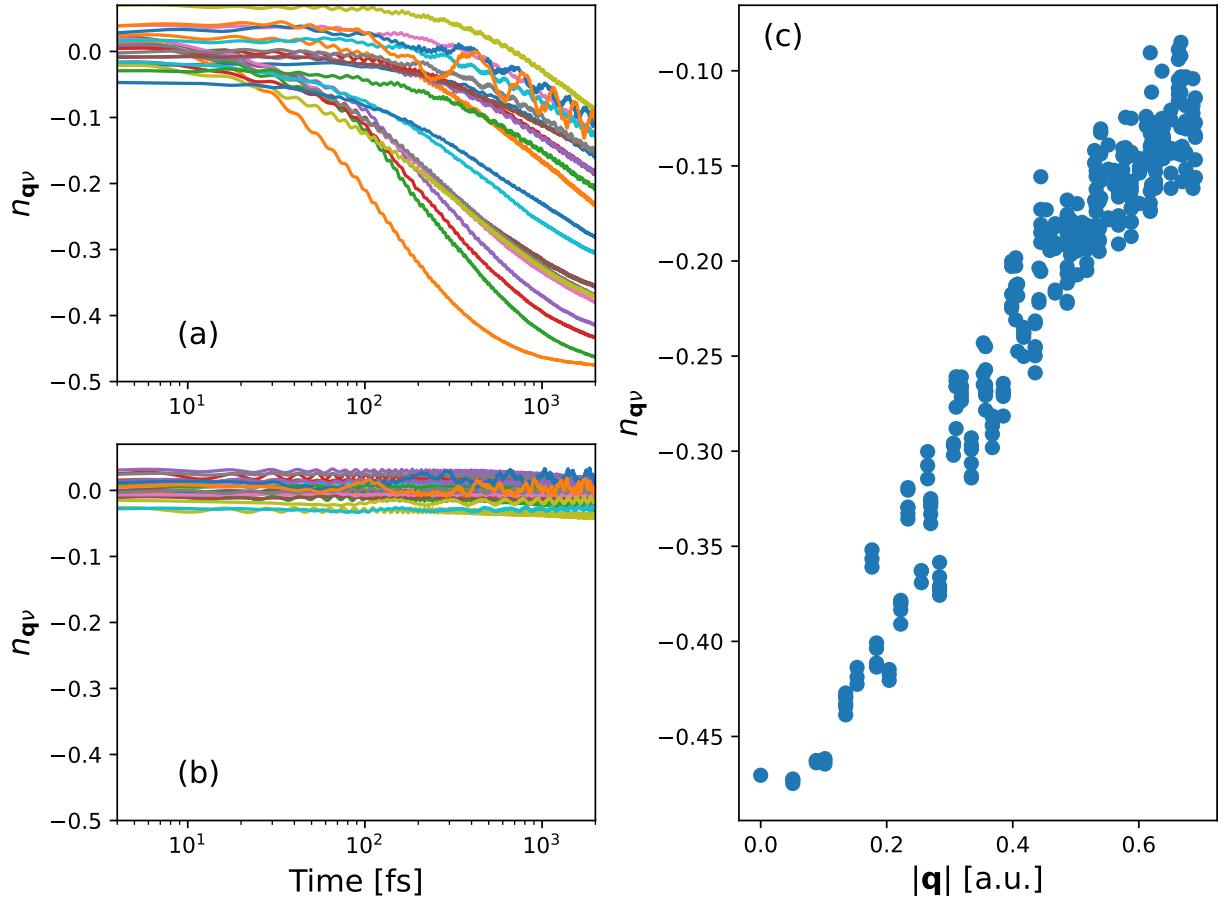
FIG. SI.6. The phonon occupation number in a selection of the highest energy optical modes over time, when the electronic system is either (a) exposed to a pump or (b) allowed to propagate without a pump. Panel (c) shows the phonon occupation numbers from panel (a) at the final time, plotted against the distance of their $\mathbf{q}$ vector from Γ.

7 | Summary, Conclusion and Outlook

In this thesis we have presented work done by the author and colleagues to develop and expand simulation techniques capable of capturing strongly driven non-equilibrium phenomena in quantum matter which can be widely utilized by the broader computational condensed matter physics community. Initially in paper **I** we explored the applicability of ICWF, a novel wavefunction dynamics approach based on decomposition of the system degrees of freedom. We tested the performance of ICWF against numerically exactly solvable problems, showcasing its performance for a variety of physical systems and quantities including the linear and beyond linear response of an H_2 model under a driving external field, elastic and inelastic electron-electron scattering, excitation non-radiative relaxation, and nuclear wavepacket self-interference effects due to propagation around a CI entirely captured in real space. Although ICWF performed well for these simple problems and has many conceptually interesting facets, as discussed in chapter 4, its further development would ultimately require a great deal of optimization in order to make it competitive with already widely utilized variational tensor decomposition based wavefunction dynamics approaches.

Therefore in paper **II** we turned to a refinement of semi-classical dynamics methods based on the Ehrenfest equations of motion which are already implemented almost universally throughout the real-time dynamics community. As discussed in chapter 5, by deriving the Ehrenfest equations of motion through the QCLE, one can contextualize them as the mean-field limit of a broader semi-classical dynamics framework, giving rise to the MTEF method. MTEF consists of evolving multiple independent trajectories with the standard Ehrenfest equations of motion but with initial conditions sampled from the Wigner transform of the initial nuclear state, which systematically recovers its exact quantum statistics. Viewed in this context, MTEF can be thought of as the lowest order approximation in a series of systematic improvements in the treatment of electron-nuclear dynamical correlation. Unlike wavefunction approaches, semi-classical trajectory ensemble based methods like MTEF and extensions beyond it are simple to scale up to very large system sizes. Furthermore since MTEF is independent of the choice of the electronic representation, using a real-space grid basis alongside TDDFT allows one to treat the coupled electron-nuclear dynamics of large systems under arbitrarily strong driving at the mean field level, limited only by the grid spacing and xc-functional.

Thus in paper **II**, we applied MTEF in conjunction with a real-space grid basis for the electronic system in order to calculate the linear vibronic absorption spectra of a numerically solvable H_2 and benzene treated with TDDFT. Utilizing the H_2 model we demonstrated that one can capture quantized nuclear effects in the form of Franck-Condon absorption lineshapes only when allowing the nuclear position to evolve. Thus we found that this quantization effect requires electron-nuclear dynamical interaction at least at the mean-field level. We found that due to the combination of mean-field forces and an explicit, though weak, external laser, the MTEF vibronic lineshape corresponds to the quantized vibrational states of the initial rather than target BOPES. We furthermore demonstrated that incorporating dynamical correlations between the electronic and nuclear subsystem beyond the mean-field level through ICWF can correct for

this phenomena and accurately capture the exact vibronic lineshape while remaining entirely in the real-space basis. These conclusions from the H_2 model informed our interpretation of the results we obtained by applying MTEF to the vibronic absorption of the benzene molecule using TDDFT. Here we found that MTEF qualitatively agreed better with the experimental spectrum, covering parts of the spectrum which are entirely absent in the single trajectory results and showing similar low energy shoulders, albeit across a broader energy range. The primary import of paper **II** is to emphasize to the broader community that quantized nuclear dynamics effects are achievable within fully ab-initio contexts through minor modifications of their existing simulation workflows, as well as to provide a detailed accounting of the origin of artifacts which may arise when doing so with a real-space basis. Furthermore we found that this particular combination of approaches displays attributes which indicate that rather than calculating equilibrium excited state properties of small molecules, the mean-field MTEF approach may be better suited to simulations of strongly driven, far from equilibrium large scale systems.

Therefore in manuscript **III** we extended MTEF to simulate the response of periodic solid state systems beyond weak field driving. By explicitly deriving the connection between the Wigner transformation of the phonon subsystem to distortions of the ions in real space supercells, we were able to utilize MTEF in extended systems in a generic manner which can systematically capture the quantum thermal equilibrium distribution of the ab-initio calculated phonon system. We found that the Wigner distribution of the phonon degrees of freedom exactly corresponds to the Zacharias-Giustino reciprocal space formulation of the Williams-Lax supercell distortion probability distribution when disregarding the phonon momentum. Thus MTEF constitutes a natural extension of the static displacement methods which have been quite successful at calculating phonon induced renormalization across a broad range of equilibrium phenomena. We utilized MTEF in both a reciprocal space TB model and a real space supercell TDDFT treatment in order to study the phonon driven reorganization of valley selectively excited charge carriers in hBN. We compared MTEF and static displacement approaches to TDBE calculations, and the temperature dependent behavior to experimental measurements in analagous systems finding agreement across these theoretical and experimental benchmarks. On top of reproducing the NEGF calculated equilibrium renormalization of electronic spectral functions in graphene, these results unambiguously validate the accuracy of MTEF in solids.

Due to the simplicity of our approach we were able to directly simulate the transient circular dichroism (TCD) absorption of hBN using both the TB model and TDDFT as well as replicate a recent experiment [224] utilizing bichromatic counter-rotating 'trefoil' pumps and high harmonic generation (HHG) as a probe for carrier imbalance in hBN *in-silico*. This paper demonstrates that the phonon degrees of freedom can be easily, accurately and systematically included in ab-initio simulations at any temperature with fundamental qualitative differences in the subsequent system dynamics. Furthermore, we found that for the dynamical observables studied, the MTEF and static disorder results converge extremely rapidly, with graphical convergence obtained in some cases at a high probability within two trajectories. Finally by explicitly deriving the Wigner distribution for the ab-initio phonon dispersion of real materials, we open the door to the full suite of QCLE based extensions beyond the mean-field approximation, allowing for corrections to ZPE leakage and the neglect of dynamical electron-phonon correlation.

In conclusion the MTEF method in solids as presented in manuscript **III** constitutes a fundamental advance in the capacity of computational ab-initio methods to simulate non-equilibrium

phenomena in extended systems under arbitrarily complex pump-probe protocols. This method can systematically capture the equilibrium quantum mechanical nature of the phonon subsystem while its dynamics at the mean field level is not restricted to small perturbations from equilibrium. In principle, this approach can capture wide ranges of motion up to and including driven phase transitions and strongly anharmonic driving; a dynamical regime which lies at the heart of many of the most compelling experimental findings in the field. Furthermore, the capacity to simulate very large supercells naturally lends itself towards application in the non-equilibrium dynamics of Moiré layered materials, Van der Waals heterostructures, and the effects of differential lattice expansion between bilayers, applications which are already being pursued further in the Rubio group. Given that QCLE based ensemble trajectory based approaches can also be used to capture cavity confined photons, exploration of this methodology to capture the non-equilibrium dynamics of coupled electron-phonon-cavity photon systems will be of great interest. In order to be generically applied to all non-equilibrium regimes, some of the most serious unphysical artifacts of the mean-field dynamics will have to be addressed, in particular for long time scale phenomena such as Floquet engineered states. Nonetheless, applications in the immediate future of the static disorder method to simulate the far-from-equilibrium properties of matter, although limited to elastic phonon scattering, will undoubtedly enable the ab-initio prediction of fundamentally different system properties than the limited high-symmetry equilibrium geometry calculation can acquire, and can serve as a valuable and easily incorporated tool to the entire community.

Bibliography

1. Mauro Nisoli, Piero Decleva, Francesca Calegari, Alicia Palacios, and Fernando Martín. Attosecond electron dynamics in molecules. *Chemical Reviews*, 117:10760–10825, 8 2017.

2. Mark S Rudner and Netanel H Lindner. Band structure engineering and non-equilibrium dynamics in floquet topological insulators. *Nature Reviews Physics*, 2:229–244, 2020. URL https://doi.org/10.1038/s42254-020-0170-z.

3. J Lloyd-Hughes, P M Oppeneer, T Pereira dos Santos, A Schleife, S Meng, M A Sentef, M Ruggenthaler, A Rubio, I Radu, M Murnane, X Shi, H Kapteyn, B Stadtmüller, K M Dani, F H da Jornada, E Prinz, M Aeschlimann, R L Milot, M Burdanova, J Boland, T Cocker, and F Hegmann. The 2021 ultrafast spectroscopic probes of condensed matter roadmap. *Journal of Physics: Condensed Matter*, 33:353001, 9 2021.

4. Ankit S. Disa, Tobia F. Nova, and Andrea Cavalleri. Engineering crystal structures with light. *Nature Physics*, 17:1087–1092, 10 2021.

5. Alberto de la Torre, Dante M Kennes, Martin Claassen, Simon Gerber, James W McIver, and Michael A Sentef. Colloquium: Nonthermal pathways to ultrafast control in quantum materials. *Reviews of Modern Physics*, 93:41002, 10 2021. URL https://link.aps.org/doi/10.1103/RevModPhys.93.041002.

6. Changhua Bao, Peizhe Tang, Dong Sun, and Shuyun Zhou. Light-induced emergent phenomena in 2d materials and topological materials. *Nature Reviews Physics*, 4:33–48, 2022. URL https://doi.org/10.1038/s42254-021-00388-1.

7. Anton Frisk Kockum, Adam Miranowicz, Simone De Liberato, Salvatore Savasta, and Franco Nori. Ultrastrong coupling between light and matter. *Nature Reviews Physics*, 1: 19–40, 1 2019.

8. Yuan Cao, Valla Fatemi, Shiang Fang, Kenji Watanabe, Takashi Taniguchi, Efthimios Kaxiras, and Pablo Jarillo-Herrero. Unconventional superconductivity in magic-angle graphene superlattices. *Nature*, 556:43–50, 2018. URL https://doi.org/10.1038/nature26160.

9. Tingxin Li, Shengwei Jiang, Lizhong Li, Yang Zhang, Kaifei Kang, Jiacheng Zhu, Kenji Watanabe, Takashi Taniguchi, Debanjan Chowdhury, Liang Fu, Jie Shan, and Kin Fai Mak. Continuous mott transition in semiconductor moiré superlattices. *Nature*, 597:350–354, 9 2021.

10. Yanhao Tang, Jie Gu, Song Liu, Kenji Watanabe, Takashi Taniguchi, James C Hone, Kin Fai Mak, and Jie Shan. Dielectric catastrophe at the wigner-mott transition in a moiré superlattice. *Nature Communications*, 13:4271, 2022. URL https://doi.org/10.1038/s41467-022-32037-1.

Bibliography

11. Feliciano Giustino, Jin Hong Lee, Felix Trier, Manuel Bibes, Stephen M Winter, Roser Valentí, Young-Woo Son, Louis Taillefer, Christoph Heil, Adriana I Figueroa, Bernard Plaçais, QuanSheng Wu, Oleg V Yazyev, Erik P A M Bakkers, Jesper Nygård, Pol Forn-Díaz, Silvano De Franceschi, J W McIver, L E F Foa Torres, Tony Low, Anshuman Kumar, Regina Galceran, Sergio O Valenzuela, Marius V Costache, Aurélien Manchon, Eun-Ah Kim, Gabriel R Schleder, Adalberto Fazzio, and Stephan Roche. The 2021 quantum materials roadmap. *Journal of Physics: Materials*, 3:042006, 10 2020.

12. Paolo G. Radaelli. Breaking symmetry with light: Ultrafast ferroelectricity and magnetism from three-phonon coupling. *Physical Review B*, 97:085145, 2 2018.

13. M. Mitrano, A. Cantaluppi, D. Nicoletti, S. Kaiser, A. Perucchi, S. Lupi, P. Di Pietro, D. Pontiroli, M. Riccò, S. R. Clark, D. Jaksch, and A. Cavalleri. Possible light-induced superconductivity in k3 c60 at high temperature. *Nature*, 530:461–464, 2 2016.

14. M. Budden, T. Gebert, M. Buzzi, G. Jotzu, E. Wang, T. Matsuyama, G. Meier, Y. Laplace, D. Pontiroli, M. Riccò, F. Schlawin, D. Jaksch, and A. Cavalleri. Evidence for metastable photo-induced superconductivity in k3c60. *Nature Physics*, 17:611–618, 5 2021.

15. E Rowe, B Yuan, M Buzzi, G Jotzu, Y Zhu, M Fechner, M Först, B Liu, D Pontiroli, M Riccò, and A Cavalleri. Giant resonant enhancement for photo-induced superconductivity in $k_3c_6$0, 2023.

16. Xian Li, Tian Qiu, Jiahao Zhang, Edoardo Baldini, Jian Lu, Andrew M Rappe, and Keith A Nelson. Terahertz field–induced ferroelectricity in quantum paraelectric srtio3. *Science*, 364:1079–1082, 6 2019. URL https://doi.org/10.1126/science.aaw4913. doi: 10.1126/science.aaw4913.

17. T. F. Nova, A. S. Disa, M. Fechner, and A. Cavalleri. Metastable ferroelectricity in optically strained srtio $_3$. *Science*, 364:1075–1079, 6 2019.

18. A S Disa, J Curtis, M Fechner, A Liu, A von Hoegen, M Först, T F Nova, P Narang, A Maljuk, A V Boris, B Keimer, and A Cavalleri. Photo-induced high-temperature ferromagnetism in ytio3. *Nature*, 617:73–78, 2023. URL https://doi.org/10.1038/s41586-023-05853-8.

19. J W McIver, B Schulte, F.-U. Stein, T Matsuyama, G Jotzu, G Meier, and A Cavalleri. Light-induced anomalous hall effect in graphene. *Nature Physics*, 16:38–41, 2020. URL https://doi.org/10.1038/s41567-019-0698-y.

20. Florian Siegrist, Julia A. Gessner, Marcus Ossiander, Christian Denker, Yi Ping Chang, Malte C. Schröder, Alexander Guggenmos, Yang Cui, Jakob Walowski, Ulrike Martens, J. K. Dewhurst, Ulf Kleineberg, Markus Münzenberg, Sangeeta Sharma, and Martin Schultze. Light-wave dynamic control of magnetism. *Nature*, 571:240–244, 7 2019.

21. H. Beyer, G. Rohde, A. Grubišić Čabo, A. Stange, T. Jacobsen, L. Bignardi, D. Lizzit, P. Lacovig, C. E. Sanders, S. Lizzit, K. Rossnagel, P. Hofmann, and M. Bauer. 80single-layer ws2 on au(111). *Physical Review Letters*, 123, 12 2019.

22. Irene Conti, Giulio Cerullo, Artur Nenov, and Marco Garavelli. Ultrafast spectroscopy of photoactive molecular systems from first principles: Where we stand today and where we are going. *Journal of the American Chemical Society*, 142:16117–16139, 2020.

23. Marco Bernardi. First-principles dynamics of electrons and phonons, 11 2016.

24. Feliciano Giustino. Electron-phonon interactions from first principles. *Reviews of Modern Physics*, 89, 2017.

25. Basile F.E. Curchod and Todd J. Martínez. Ab initio nonadiabatic quantum molecular dynamics. *Chemical Reviews*, 118:3305–3336, 4 2018.

26. Ali Abedi, Federica Agostini, and E. K. U. Gross. Mixed quantum-classical dynamics from the exact decomposition of electron-nuclear motion. *EPL (Europhysics Letters)*, 2014.

27. Guillermo Albareda, Aaron Kelly, and Angel Rubio. Nonadiabatic quantum dynamics without potential energy surfaces. *Physical Review Materials*, 3, 2019.

28. Luning Zhao, Zhen Tao, Fabijan Pavošević, Andrew Wildman, Sharon Hammes-Schiffer, and Xiaosong Li. Real-time time-dependent nuclear-electronic orbital approach: Dynamics beyond the born-oppenheimer approximation. *Journal of Physical Chemistry Letters*, 11:4052–4058, 5 2020.

29. Mengxue Guan, Daqiang Chen, Shiqi Hu, Hui Zhao, Peiwei You, and Sheng Meng. Theoretical insights into ultrafast dynamics in quantum materials. *Ultrafast Science*, 2022, 1 2022.

30. Andrea Muolo, Alberto Baiardi, Robin Feldmann, and Markus Reiher. Nuclear-electronic all-particle density matrix renormalization group. *The Journal of Chemical Physics*, 152:204103, 5 2020. URL https://doi.org/10.1063/5.0007166.

31. Sudip Sasmal and Oriol Vendrell. Non-adiabatic quantum dynamics without potential energy surfaces based on second-quantized electrons: Application within the framework of the mctdh method. *Journal of Chemical Physics*, 153, 10 2020.

32. Francesco Segatta, Daniel Aranda Ruiz, Flavia Aleotti, Martha Yaghoubi, Shaul Mukamel, Marco Garavelli, Fabrizio Santoro, and Artur Nenov. Nonlinear molecular electronic spectroscopy via mctdh quantum dynamics: From exact to approximate expressions. *Journal of Chemical Theory and Computation*, 19:2075–2091, 4 2023. URL https://doi.org/10.1021/acs.jctc.2c01059. doi: 10.1021/acs.jctc.2c01059.

33. Yoshitaka Tanimura. Numerically "exact" approach to open quantum dynamics: The hierarchical equations of motion (heom). *Journal of Chemical Physics*, 153, 7 2020.

34. Veljko Janković and Nenad Vukmirović. Spectral and thermodynamic properties of the holstein polaron: Hierarchical equations of motion approach. *Physical Review B*, 105, 2 2022.

35. R. Tuovinen, Y. Pavlyukh, E. Perfetto, and G. Stefanucci. Time-linear quantum transport simulations with correlated nonequilibrium green's functions. *Physical Review Letters*, 130:246301, 6 2023.

36. Enrico Perfetto and Gianluca Stefanucci. Real-time gw-ehrenfest-fan-migdal method for nonequilibrium 2d materials. 2023.

37. Maximilian A. C. Saller, Johan E. Runeson, and Jeremy O. Richardson. Path-integral approaches to non-adiabatic dynamics, 11 2020.

Bibliography

38. Fabio Caruso and Dino Novko. Ultrafast dynamics of electrons and phonons: from the two-temperature model to the time-dependent boltzmann equation, 2022.

39. M Born and R Oppenheimer. Zur quantentheorie der molekeln. *Annalen der Physik*, 389:457–484, 1 1927. URL https://doi.org/10.1002/andp.19273892002. https://doi.org/10.1002/andp.19273892002.

40. Max Born and Kun Huang. Dynamical theory of crystal lattices, 1954.

41. Brian T Sutcliffe and R Guy Woolley. On the quantum theory of molecules. *The Journal of Chemical Physics*, 137:22A544, 2012. URL https://doi.org/10.1063/1.4755287.

42. Thierry Jecko. On the mathematical treatment of the born-oppenheimer approximation. *Journal of Mathematical Physics*, 55, 5 2014.

43. Brian Sutcliffe. Treating nuclei in molecules with quantum mechanical respect. *Theoretical Chemistry Accounts*, 140, 3 2021.

44. M Baer. Born-oppenheimer approach: Diabatization and topological matrix, 2006. URL https://onlinelibrary.wiley.com/doi/abs/10.1002/0471780081.ch2.

45. Richard Dawes and Ernesto Quintas-Sánchez. The construction of ab initio-based potential energy surfaces, 2018. URL https://onlinelibrary.wiley.com/doi/abs/10.1002/9781119518068.ch5.

46. A Bohm, B Kendrick, Mark E Loewe, and L J Boya. The berry connection and born–oppenheimer method. *Journal of Mathematical Physics*, 33:977–989, 1992. URL https://doi.org/10.1063/1.529751.

47. David Vanderbilt. Review of electronic structure theory, 2018.

48. Dario Polli, Piero Altoè, Oliver Weingart, Katelyn M Spillane, Cristian Manzoni, Daniele Brida, Gaia Tomasello, Giorgio Orlandi, Philipp Kukura, Richard A Mathies, Marco Garavelli, and Giulio Cerullo. Conical intersection dynamics of the primary photoisomerization event in vision. *Nature*, 467:440–443, 2010. URL https://doi.org/10.1038/nature09346.

49. Carlos E Crespo-Hernández. Photorelaxation and photorepair processes in nucleic and amino acid derivatives. *Molecules*, 22, 2017. URL https://www.mdpi.com/1420-3049/22/12/2203.

50. David P Hoffman, Scott R Ellis, and Richard A Mathies. Characterization of a conical intersection in a charge-transfer dimer with two-dimensional time-resolved stimulated raman spectroscopy. *The Journal of Physical Chemistry A*, 118:4955–4965, 7 2014. URL https://doi.org/10.1021/jp5041986. doi: 10.1021/jp5041986.

51. Joseph E. Subotnik, Ethan C. Alguire, Qi Ou, Brian R. Landry, and Shervin Fatehi. The requisite electronic structure theory to describe photoexcited nonadiabatic dynamics: Nonadiabatic derivative couplings and diabatic electronic couplings. *Accounts of Chemical Research*, 48:1340–1350, 5 2015.

52. Miquel Huix-Rotllant, Nicolas Ferré, and Mario Barbatti. Time-dependent density functional theory, 11 2020. URL https://doi.org/10.1002/9781119417774.ch2. Wiley Online Books.

53. Yinan Shu, Zoltan Varga, Siriluk Kanchanakungwankul, Linyao Zhang, and Donald G. Truhlar. Diabatic states of molecules. *Journal of Physical Chemistry A*, 126:992–1018, 2 2022.

54. G A Worth, H.-D. Meyer, H Köppel, L S Cederbaum, and I Burghardt. Using the mctdh wavepacket propagation method to describe multimode non-adiabatic dynamics. *International Reviews in Physical Chemistry*, 27:569–606, 7 2008. URL https://doi.org/10.1080/01442350802137656. doi: 10.1080/01442350802137656.

55. Flavia Aleotti, Daniel Aranda, Martha Yaghoubi Jouybari, Marco Garavelli, Artur Nenov, and Fabrizio Santoro. Parameterization of a linear vibronic coupling model with multiconfigurational electronic structure methods to study the quantum dynamics of photoexcited pyrene. *The Journal of Chemical Physics*, 154:104106, 3 2021. URL https://doi.org/10.1063/5.0044693.

56. Robert W Boyd. Chapter 1 - the nonlinear optical susceptibility, 2008. URL https://www.sciencedirect.com/science/article/pii/B9780123694706000010.

57. Volkhard May and Oliver Kühn. *Charge and energy transfer dynamics in molecular systems: Third edition.* 2011. ISBN 9783527407323.

58. Gene, Cronin Stephen B., Gomes Souza Filho Antonio Dresselhaus Mildred, and Dresselhaus. Review of fundamental relations for optical phenomena, 2018. URL https://doi.org/10.1007/978-3-662-55922-2_15.

59. Thomas G. Mayerhöfer, Susanne Pahlow, and Jürgen Popp. The bouguer-beer-lambert law: Shining light on the obscure. *Chemphyschem : a European journal of chemical physics and physical chemistry*, 21:2029–2046, 9 2020.

60. Carsten A Ullrich. Time-dependent density-functional theory: Concepts and applications. *Oxford Graduate Texts*, 2011.

61. Gene, Cronin Stephen B., Gomes Souza Filho Antonio Dresselhaus Mildred, and Dresselhaus. Absorption of light in solids, 2018. URL https://doi.org/10.1007/978-3-662-55922-2_18.

62. John C. Tully and Richard K. Pkeston. Trajectory surface hopping approach to nonadiabatic molecular collisions: The reaction of h+ with d2. *The Journal of Chemical Physics*, 55:562–572, 1971.

63. Eric J. Heller. Time dependent variational approach to semiclassical dynamics. *The Journal of Chemical Physics*, 64:63–73, 1 1976.

64. Ronnie Kosloff. Time-dependent quantum-mechanical methods for molecular dynamics. *The Journal of Physical Chemistry*, 92:2087–2100, 1988. URL https://doi.org/10.1021/j100319a003.

65. K. Yabana and G. Bertsch. Time-dependent local-density approximation in real time. *Physical Review B - Condensed Matter and Materials Physics*, 54:4484–4487, 1996.

66. K. Yabana, T. Nakatsukasa, J. I. Iwata, and G. F. Bertsch. Real-time, real-space implementation of the linear response time-dependent density-functional theory. volume 243, pages 1121–1138, 4 2006.

Bibliography

67. Shaul Mukamel. *Principles of Nonlinear Optical Spectroscopy*. Oxford University Press, 1995.

68. Tomislav Begušić and Jiří Vaníček. Finite-temperature, anharmonicity, and duschinsky effects on the two-dimensional electronic spectra from ab initio thermo-field gaussian wavepacket dynamics. *The Journal of Physical Chemistry Letters*, 12:2997–3005, 3 2021. URL https://doi.org/10.1021/acs.jpclett.1c00123. doi: 10.1021/acs.jpclett.1c00123.

69. Austin O Atsango, Andrés Montoya-Castillo, and Thomas E Markland. An accurate and efficient ehrenfest dynamics approach for calculating linear and nonlinear electronic spectra. *The Journal of Chemical Physics*, 158:074107, 2 2023. URL https://doi.org/10.1063/5.0138671.

70. Y. Takimoto, F. D. Vila, and J. J. Rehr. Real-time time-dependent density functional theory approach for frequency-dependent nonlinear optical response in photonic molecules. *The Journal of Chemical Physics*, 127:154114, 10 2007.

71. Haobin Wang and Michael Thoss. Nonperturbative quantum simulation of time-resolved nonlinear spectra: Methodology and application to electron transfer reactions in the condensed phase. *Chemical Physics*, 347:139–151, 2008. URL https://www.sciencedirect.com/science/article/pii/S0301010407005599.

72. S. A. Sato, K. Yabana, Y. Shinohara, T. Otobe, and G. F. Bertsch. Numerical pump-probe experiments of laser-excited silicon in nonequilibrium phase. *Physical Review B - Condensed Matter and Materials Physics*, 89, 2 2014.

73. Jessica Walkenhorst, Umberto De Giovannini, Alberto Castro, and Angel Rubio. Tailored pump-probe transient spectroscopy with time-dependent density-functional theory: controlling absorption spectra. *European Physical Journal B*, 89, 2016.

74. Shunsuke A. Sato, Aaron Kelly, and Angel Rubio. Coupled forward-backward trajectory approach for nonequilibrium electron-ion dynamics. *Physical Review B*, 97, 4 2018.

75. Nicolas Tancogne-Dejean, Oliver D Mücke, Franz X Kärtner, and Angel Rubio. Impact of the electronic band structure in high-harmonic generation spectra of solids. *Phys. Rev. Lett.*, 118:87403, 2 2017. URL https://link.aps.org/doi/10.1103/PhysRevLett.118.087403.

76. David Freeman, Anatoli Kheifets, Shunsuke Yamada, Atsushi Yamada, and Kazuhiro Yabana. High-order harmonic generation in semiconductors driven at near- and mid-infrared wavelengths. *Physical Review B*, 106, 8 2022.

77. Ofer Neufeld, Jin Zhang, Umberto De Giovannini, Hannes Hubener, and Angel Rubio. Probing phonon dynamics with multidimensional high harmonic carrier-envelope-phase spectroscopy. *Proceedings of the National Academy of Sciences of the United States of America*, 119, 6 2022. URL http://www.pnas.org/lookup/suppl/doi:10.1073/pnas.2204219119/-/DCSupplemental.

78. Umberto De Giovannini, Gustavo Brunetto, Alberto Castro, Jessica Walkenhorst, and Angel Rubio. Simulating pump-probe photoelectron and absorption spectroscopy on the attosecond timescale with time-dependent density functional theory. *ChemPhysChem*, 14:1363–1376, 5 2013.

79. Umberto De Giovannini, Hannes Hübener, and Angel Rubio. A first-principles time-dependent

density functional theory framework for spin and time-resolved angular-resolved photoelectron spectroscopy in periodic systems. *Journal of Chemical Theory and Computation*, 13:265–273, 1 2017.

80. Dongbin Shin, Simone Latini, Christian Schäfer, Shunsuke A Sato, Edoardo Baldini, Umberto De Giovannini, Hannes Hübener, and Angel Rubio. Simulating terahertz field-induced ferroelectricity in quantum paraelectric srtio 3. *PHYSICAL REVIEW LETTERS*, 129:167401, 2022.

81. Ofer Neufeld, Nicolas Tancogne-Dejean, Umberto De Giovannini, Hannes Hübener, and Angel Rubio. Attosecond magnetization dynamics in non-magnetic materials driven by intense femtosecond lasers. *npj Computational Materials*, 9:39, 3 2023. URL https://www.nature.com/articles/s41524-023-00997-7.

82. Nicolas Tancogne-Dejean, Micael J T Oliveira, Xavier Andrade, Heiko Appel, Carlos H Borca, Guillaume Le Breton, Florian Buchholz, Alberto Castro, Stefano Corni, Alfredo A Correa, Umberto De Giovannini, Alain Delgado, Florian G Eich, Johannes Flick, Gabriel Gil, Adrián Gomez, Nicole Helbig, Hannes Hübener, René Jestädt, Joaquim Jornet-Somoza, Ask H Larsen, Irina V Lebedeva, Martin Lüders, Miguel A L Marques, Sebastian T Ohlmann, Silvio Pipolo, Markus Rampp, Carlo A Rozzi, David A Strubbe, Shunsuke A Sato, Christian Schäfer, Iris Theophilou, Alicia Welden, and Angel Rubio. Octopus, a computational framework for exploring light-driven phenomena and quantum dynamics in extended and finite systems. *The Journal of Chemical Physics*, 152, 4 2020. URL https://doi.org/10.1063/1.5142502. 124119.

83. G W Richings, I Polyak, K E Spinlove, G A Worth, I Burghardt, and B Lasorne. Quantum dynamics simulations using gaussian wavepackets: the vmcg method. *International Reviews in Physical Chemistry*, 34:269–308, 2015. URL https://doi.org/10.1080/0144235X.2015.1051354.

84. Gareth W. Richings, Christopher Robertson, and Scott Habershon. Improved on-the-fly mctdh simulations with many-body-potential tensor decomposition and projection diabatization. *Journal of Chemical Theory and Computation*, 15:857–870, 2 2019.

85. Dmitry V. Makhov, Christopher Symonds, Sebastian Fernandez-Alberti, and Dmitrii V. Shalashilin. Ab initio quantum direct dynamics simulations of ultrafast photochemistry with multiconfigurational ehrenfest approach. *Chemical Physics*, 493:200–218, 8 2017.

86. Rachel Crespo-Otero and Mario Barbatti. Recent advances and perspectives on nonadiabatic mixed quantum-classical dynamics. *Chemical Reviews*, 118:7026–7068, 8 2018.

87. Markus Kowalewski, Kochise Bennett, and Shaul Mukamel. Cavity femtochemistry: Manipulating nonadiabatic dynamics at avoided crossings. *The Journal of Physical Chemistry Letters*, 7:2050–2054, 6 2016. URL https://doi.org/10.1021/acs.jpclett.6b00864. doi: 10.1021/acs.jpclett.6b00864.

88. Johannes Flick, Heiko Appel, Michael Ruggenthaler, and Angel Rubio. Cavity born–oppenheimer approximation for correlated electron–nuclear-photon systems. *Journal of Chemical Theory and Computation*, 13:1616–1625, 4 2017. URL https://doi.org/10.1021/acs.jctc.6b01126. doi: 10.1021/acs.jctc.6b01126.

Bibliography

89. John Bonini and Johannes Flick. Ab initio linear-response approach to vibro-polaritons in the cavity born–oppenheimer approximation. *Journal of Chemical Theory and Computation*, 18:2764–2773, 5 2022. URL https://doi.org/10.1021/acs.jctc.1c01035. doi: 10.1021/acs.jctc.1c01035.

90. Christian Schäfer, Michael Ruggenthaler, and Angel Rubio. Ab initio nonrelativistic quantum electrodynamics: Bridging quantum chemistry and quantum optics from weak to strong coupling. *Physical Review A*, 98:43801, 10 2018. URL https://link.aps.org/doi/10.1103/PhysRevA.98.043801.

91. Simone Latini, Dongbin Shin, Shunsuke A Sato, Christian Schäfer, Umberto De Giovannini, Hannes Hübener, and Angel Rubio. The ferroelectric photo ground state of srtio3: Cavity materials engineering. *Proceedings of the National Academy of Sciences*, 118:e2105618118, 8 2021. URL https://doi.org/10.1073/pnas.2105618118. doi: 10.1073/pnas.2105618118.

92. Hannes Hübener, Umberto De Giovannini, and Angel Rubio. Phonon driven floquet matter. *Nano Letters*, 18:1535–1542, 2 2018.

93. J Fregoni, G Granucci, E Coccia, M Persico, and S Corni. Manipulating azobenzene photoisomerization through strong light–molecule coupling. *Nature Communications*, 9:4688, 2018. URL https://doi.org/10.1038/s41467-018-06971-y.

94. Mark Kamper Svendsen, Kristian Sommer Thygesen, Angel Rubio, and Johannes Flick. Molecules in real cavities with quantum electroynamical density functional theory. 2023.

95. Zeyu Zhou, Hsing-Ta Chen, Abraham Nitzan, and Joseph Eli Subotnik. Nonadiabatic dynamics in a laser field: Using floquet fewest switches surface hopping to calculate electronic populations for slow nuclear velocities. *Journal of Chemical Theory and Computation*, 16:821–834, 2 2020. URL https://doi.org/10.1021/acs.jctc.9b00950. doi: 10.1021/acs.jctc.9b00950.

96. Marco Schirò, Florian G Eich, and Federica Agostini. Quantum–classical nonadiabatic dynamics of floquet driven systems. *The Journal of Chemical Physics*, 154:114101, 3 2021. URL https://doi.org/10.1063/5.0043790.

97. Christopher E. Patrick and Feliciano Giustino. Unified theory of electron-phonon renormalization and phonon-assisted optical absorption. *Journal of Physics Condensed Matter*, 26, 9 2014.

98. Piers Coleman. *Introduction to Many-Body Physics*. Cambridge University Press, 2015.

99. Alex Kamenev. *Field Theory of Non-Equilibrium Systems*. Cambridge University Press, 9 2011. ISBN 9780521760829.

100. Alejandro Molina-Sánchez, Davide Sangalli, Ludger Wirtz, and Andrea Marini. Ab initio calculations of ultrashort carrier dynamics in two-dimensional materials: Valley depolarization in single-layer wse2. *Nano Letters*, 17:4549–4555, 8 2017.

101. Niclas Schlünzen, Jan Philip Joost, and Michael Bonitz. Achieving the scaling limit for nonequilibrium green functions simulations. *Physical Review Letters*, 124, 2 2020.

102. Frank Arute, Kunal Arya, Ryan Babbush, Dave Bacon, Joseph C Bardin, Rami Barends, Rupak Biswas, Sergio Boixo, Fernando G S L Brandao, David A Buell, Brian Burkett, Yu Chen, Zijun Chen, Ben Chiaro, Roberto Collins, William Courtney, Andrew Dunsworth, Edward Farhi, Brooks Foxen, Austin Fowler, Craig Gidney, Marissa Giustina, Rob Graff, Keith Guerin, Steve Habegger, Matthew P Harrigan, Michael J Hartmann, Alan Ho, Markus Hoffmann, Trent Huang, Travis S Humble, Sergei V Isakov, Evan Jeffrey, Zhang Jiang, Dvir Kafri, Kostyantyn Kechedzhi, Julian Kelly, Paul V Klimov, Sergey Knysh, Alexander Korotkov, Fedor Kostritsa, David Landhuis, Mike Lindmark, Erik Lucero, Dmitry Lyakh, Salvatore Mandrà, Jarrod R McClean, Matthew McEwen, Anthony Megrant, Xiao Mi, Kristel Michielsen, Masoud Mohseni, Josh Mutus, Ofer Naaman, Matthew Neeley, Charles Neill, Murphy Yuezhen Niu, Eric Ostby, Andre Petukhov, John C Platt, Chris Quintana, Eleanor G Rieffel, Pedram Roushan, Nicholas C Rubin, Daniel Sank, Kevin J Satzinger, Vadim Smelyanskiy, Kevin J Sung, Matthew D Trevithick, Amit Vainsencher, Benjamin Villalonga, Theodore White, Z Jamie Yao, Ping Yeh, Adam Zalcman, Hartmut Neven, and John M Martinis. Quantum supremacy using a programmable superconducting processor. *Nature*, 574:505–510, 2019. URL https://doi.org/10.1038/s41586-019-1666-5.

103. Feng Pan, Keyang Chen, and Pan Zhang. Solving the sampling problem of the sycamore quantum circuits. *Physical Review Letters*, 129:90502, 8 2022. URL https://link.aps.org/doi/10.1103/PhysRevLett.129.090502.

104. Ledyard R Tucker. Some mathematical notes on three-mode factor analysis. *Psychometrika*, 31:279–311, 1966. URL https://doi.org/10.1007/BF02289464.

105. Lieven De Lathauwer, Bart De Moor, and Joos Vandewalle. A multilinear singular value decomposition. *SIAM Journal on Matrix Analysis and Applications*, 21:1253–1278, 1 2000. URL https://doi.org/10.1137/S0895479896305696. doi: 10.1137/S0895479896305696.

106. Steven R White. Density matrix formulation for quantum renormalization groups. *Physical Review Letters*, 69:2863–2866, 11 1992. URL https://link.aps.org/doi/10.1103/PhysRevLett.69.2863.

107. A. Jäckle and H. D. Meyer. Product representation of potential energy surfaces. *Journal of Chemical Physics*, 104:7974–7984, 5 1996.

108. A spectral theory for rectangular matrices, 2006. URL https://doi.org/10.1007/0-387-21634-0_8.

109. Ramesh Naidu Annavarapu. Singular value decomposition and the centrality of löwdin orthogonalizations. *American Journal of Computational and Applied Mathematics*, 3:33–35, 2013.

110. Larsson Omberg, Gene H Golub, and Orly Alter. A tensor higher-order singular value decomposition for integrative analysis of dna microarray data from different studies. *Proceedings of the National Academy of Sciences*, 104:18371–18376, 11 2007. URL https://doi.org/10.1073/pnas.0709146104. doi: 10.1073/pnas.0709146104.

111. A Zare, A Ozdemir, M A Iwen, and S Aviyente. Extension of pca to higher order data structures: An introduction to tensors, tensor decompositions, and tensor pca. *Proceedings of the IEEE*, 106:1341–1358, 2018.

Bibliography

112. Frank Otto. Multi-layer potfit: An accurate potential representation for efficient high-dimensional quantum dynamics. *The Journal of Chemical Physics*, 140:014106, 1 2014. URL https://doi.org/10.1063/1.4856135.

113. M H Beck, A Jäckle, G A Worth, and H.-D. Meyer. The multiconfiguration time-dependent hartree (mctdh) method: a highly efficient algorithm for propagating wavepackets. *Physics Reports*, 324:1–105, 2000. URL https://www.sciencedirect.com/science/article/pii/S0370157399000472.

114. Hans-Dieter Meyer, Faabien Gatti, and Graham Worth. *Multidimensional Quantum Dynamics*. Wiley, 4 2009. ISBN 9783527320189.

115. J. Broeckhove, L. Lathouwers, E. Kesteloot, and P. Van Leuven. On the equivalence of time-dependent variational principles. *Chemical Physics Letters*, 149:547–550, 1988.

116. Christian Lubich. On variational approximations in quantum molecular dynamics. *Mathematics of Computation*, 74:765–780, 2004.

117. Oriol Vendrell. Coherent dynamics in cavity femtochemistry: Application of the multi-configuration time-dependent hartree method. *Chemical Physics*, 509:55–65, 2018. URL https://www.sciencedirect.com/science/article/pii/S0301010417310273.

118. Uwe Manthe. Wavepacket dynamics and the multi-configurational time-dependent hartree approach. *Journal of Physics Condensed Matter*, 29, 5 2017.

119. M Bonfanti, G A Worth, and I Burghardt. Multi-configuration time-dependent hartree methods: From quantum to semiclassical and quantum-classical, 2020. URL https://onlinelibrary.wiley.com/doi/abs/10.1002/9781119417774.ch12.

120. Haobin Wang. Multilayer multiconfiguration time-dependent hartree theory, 7 2015.

121. Oriol Vendrell and Hans Dieter Meyer. Multilayer multiconfiguration time-dependent hartree method: Implementation and applications to a henon-heiles hamiltonian and to pyrazine. *Journal of Chemical Physics*, 134, 1 2011.

122. David Mendive-Tapia, Etienne Mangaud, Thiago Firmino, Aurélien De La Lande, Michèle Desouter-Lecomte, Hans Dieter Meyer, and Fabien Gatti. Multidimensional quantum mechanical modeling of electron transfer and electronic coherence in plant cryptochromes: The role of initial bath conditions. *Journal of Physical Chemistry B*, 122:126–136, 1 2018.

123. David Mendive-Tapia, Thiago Firmino, Hans-Dieter Meyer, and Fabien Gatti. Towards a systematic convergence of multi-layer (ml) multi-configuration time-dependent hartree nuclear wavefunctions: The ml-spawning algorithm. *Chemical Physics*, 482:113–123, 2017. URL https://www.sciencedirect.com/science/article/pii/S0301010416305134. Electrons and nuclei in motion - correlation and dynamics in molecules (on the occasion of the 70th birthday of Lorenz S. Cederbaum).

124. David Mendive-Tapia, Hans Dieter Meyer, and Oriol Vendrell. Optimal mode combination in the multiconfiguration time-dependent hartree method through multivariate statistics: Factor analysis and hierarchical clustering. *Journal of Chemical Theory and Computation*, 19:1144–

1156, 2 2023.

125. Florian A Y N Schröder, David H P Turban, Andrew J Musser, Nicholas D M Hine, and Alex W Chin. Tensor network simulation of multi-environmental open quantum dynamics via machine learning and entanglement renormalisation. *Nature Communications*, 10:1062, 2019. URL https://doi.org/10.1038/s41467-019-09039-7.

126. Mari Carmen Bañuls. Tensor network algorithms: A route map. *Annu. Rev. Condens. Matter Phys. 2023*, 14:173–191, 2023. URL https://doi.org/10.1146/annurev-conmatphys-.

127. M A Cazalilla and J B Marston. Time-dependent density-matrix renormalization group: A systematic method for the study of quantum many-body out-of-equilibrium systems. *Physical Review Letters*, 88:256403, 6 2002. URL https://link.aps.org/doi/10.1103/PhysRevLett.88.256403.

128. Alberto Baiardi and Markus Reiher. The density matrix renormalization group in chemistry and molecular physics: Recent developments and new challenges. *Journal of Chemical Physics*, 152, 1 2020.

129. Sebastian Paeckel, Thomas Köhler, Andreas Swoboda, Salvatore R. Manmana, Ulrich Schollwöck, and Claudius Hubig. Time-evolution methods for matrix-product states. *Annals of Physics*, 411, 12 2019.

130. Alberto Baiardi and Markus Reiher. Large-scale quantum dynamics with matrix product states. *Journal of Chemical Theory and Computation*, 2019.

131. Xiaoyu Xie, Yuyang Liu, Yao Yao, Ulrich Schollwöck, Chungen Liu, and Haibo Ma. Time-dependent density matrix renormalization group quantum dynamics for realistic chemical systems. *Journal of Chemical Physics*, 151, 12 2019.

132. Kentaro Hino and Yuki Kurashige. Matrix product state formulation of the mctdh theory in local mode representations for anharmonic potentials. *Journal of chemical theory and computation*, 18:3347–3356, 6 2022.

133. T Kreibich and E K U Gross. Multicomponent density-functional theory for electrons and nuclei. *Physical Review Letters*, 86:2984–2987, 4 2001. URL https://link.aps.org/doi/10.1103/PhysRevLett.86.2984.

134. Fabijan Pavošević, Tanner Culpitt, and Sharon Hammes-Schiffer. Multicomponent quantum chemistry: Integrating electronic and nuclear quantum effects via the nuclear-electronic orbital method. *Chemical Reviews*, 120:4222–4253, 5 2020.

135. Marat Sibaev, Iakov Polyak, Frederick R. Manby, and Peter J. Knowles. Molecular second-quantized hamiltonian: Electron correlation and non-adiabatic coupling treated on an equal footing. *Journal of Chemical Physics*, 153, 9 2020.

136. Robin Feldmann, Andrea Muolo, Alberto Baiardi, and Markus Reiher. Quantum proton effects from density matrix renormalization group calculations. *Journal of Chemical Theory and Computation*, 18:234–250, 1 2022.

Bibliography

137. Dario Bressanini and Peter J Reynolds. Generalized variational principle for excited states using nodes of trial functions. *Physical Review E*, 84:46705, 10 2011. URL https://link.aps.org/doi/10.1103/PhysRevE.84.046705.

138. Guillermo Albareda, Heiko Appel, Ignacio Franco, Ali Abedi, and Angel Rubio. Correlated electron-nuclear dynamics with conditional wave functions. *Physical Review Letters*, 113, 2014.

139. Guillermo Albareda, Ali Abedi, Ivano Tavernelli, and Angel Rubio. Universal steps in quantum dynamics with time-dependent potential-energy surfaces: Beyond the born-oppenheimer picture. *Physical Review A*, 94:62511, 12 2016. URL https://link.aps.org/doi/10.1103/PhysRevA.94.062511.

140. Xavier Oriols and Jordi Mompart. Overview of bohmian mechanics, 2019.

141. Basile F.E. Curchod, Federica Agostini, and Ivano Tavernelli. Ct-mqc – a coupled-trajectory mixed quantum/classical method including nonadiabatic quantum coherence effects. *European Physical Journal B*, 91, 7 2018.

142. Guillermo Albareda, Josep Maria Bofill, Ivano Tavernelli, Fermin Huarte-Larranaga, Francesc Illas, and Angel Rubio. Conditional born-oppenheimer dynamics: Quantum dynamics simulations for the model porphine. *Journal of Physical Chemistry Letters*, 6:1529–1535, 2015.

143. Venera Khoromskaia and Boris N Khoromskij. Tensor numerical methods in quantum chemistry: from hartree–fock to excitation energies. *Phys. Chem. Chem. Phys.*, 17:31491–31509, 2015. URL http://dx.doi.org/10.1039/C5CP01215E.

144. Markus Schröder. Transforming high-dimensional potential energy surfaces into a canonical polyadic decomposition using monte carlo methods. *Journal of Chemical Physics*, 152, 1 2020.

145. Nataša Nadoveza, Ramón L. Panadés-Barrueta, Lei Shi, Fabien Gatti, and Daniel Peláez. Analytical high-dimensional operators in canonical polyadic finite basis representation (cp-fbr). *The Journal of Chemical Physics*, 158:114109, 3 2023.

146. Scott Habershon. Linear dependence and energy conservation in gaussian wavepacket basis sets. *The Journal of Chemical Physics*, 136:014109, 1 2012.

147. Loïc Joubert-Doriol. Variational approach for linearly dependent moving bases in quantum dynamics: Application to gaussian functions. *Journal of Chemical Theory and Computation*, 18:5799–5809, 10 2022.

148. Norah M Hoffmann, Christian Schäfer, Angel Rubio, Aaron Kelly, and Heiko Appel. Capturing vacuum fluctuations and photon correlations in cavity quantum electrodynamics with multitrajectory ehrenfest dynamics. 2019.

149. Norah M. Hoffmann, Christian Schäfer, Niko Säkkinen, Angel Rubio, Heiko Appel, and Aaron Kelly. Benchmarking semiclassical and perturbative methods for real-time simulations of cavity-bound emission and interference. *The Journal of Chemical Physics*, 151:244113, 12 2019.

150. Norah M. Hoffmann, Lionel Lacombe, Angel Rubio, and Neepa T. Maitra. Effect of many modes on self-polarization and photochemical suppression in cavities. *The Journal of Chemical Physics*,

153:104103, 9 2020.

151. Dongbin Shin, Simone Latini, Christian Schäfer, Shunsuke A. Sato, Umberto De Giovannini, Hannes Hübener, and Angel Rubio. Quantum paraelectric phase of <math> <msub> <mi>srtio</mi> <mn>3</mn> </msub> </math> from first principles. *Physical Review B*, 104:L060103, 8 2021.

152. John C. Tully. Molecular dynamics with electronic transitions. *The Journal of Chemical Physics*, 93:1061–1071, 1990.

153. Eric J Heller. Time-dependent approach to semiclassical dynamics. *The Journal of Chemical Physics*, 62:1544–1555, 1975. URL https://doi.org/10.1063/1.430620.

154. Bastiaan J. Braams and David E. Manolopoulos. On the short-time limit of ring polymer molecular dynamics. *The Journal of Chemical Physics*, 125:124105, 9 2006.

155. Scott Habershon, David E. Manolopoulos, Thomas E. Markland, and Thomas F. Miller. Ring-polymer molecular dynamics: Quantum effects in chemical dynamics from classical trajectories in an extended phase space. *Annual Review of Physical Chemistry*, 64:387–413, 2013. URL http://www.annualreviews.org/doi/10.1146/annurev-physchem-040412-110122.

156. Timothy J.H. Hele, Michael J. Willatt, Andrea Muolo, and Stuart C. Althorpe. Communication: Relation of centroid molecular dynamics and ring-polymer molecular dynamics to exact quantum dynamics. *Journal of Chemical Physics*, 142, 5 2015.

157. Philip Shushkov, Richard Li, and John C. Tully. Ring polymer molecular dynamics with surface hopping. *The Journal of Chemical Physics*, 137:22A549, 2012. URL http://aip.scitation.org/doi/10.1063/1.4766449.

158. Farnaz A. Shakib and Pengfei Huo. Ring polymer surface hopping: Incorporating nuclear quantum effects into nonadiabatic molecular dynamics simulations. *Journal of Physical Chemistry Letters*, 8:3073–3080, 2017.

159. Alexey V. Akimov, Run Long, and Oleg V. Prezhdo. Coherence penalty functional: A simple method for adding decoherence in ehrenfest dynamics. *The Journal of Chemical Physics*, 140:194107, 5 2014.

160. Parmeet Nijjar, Joanna Jankowska, and Oleg V. Prezhdo. Ehrenfest and classical path dynamics with decoherence and detailed balance. *The Journal of Chemical Physics*, 150:204124, 5 2019.

161. E. Wigner. On the quantum correction for thermodynamic equilibrium. *Physical Review*, 40:749–759, 1932.

162. William B. Case. Wigner functions and weyl transforms for pedestrians. *American Journal of Physics*, 76:937–946, 2008. URL http://aapt.scitation.org/doi/10.1119/1.2957889.

163. David B. Fairlie. Moyal brackets, star products and the generalized wigner function. *Chaos, solitons and fractals*, 10:365–371, 1999. URL http://www.sciencedirect.com/science/article/pii/S0960077998001581.

164. IV Aleksandrov. The statistical dynamics of a system consisting of a classical and a quantum

subsystem. *Z.Naturforschung A*, 36:902–908, 1981.

165. Raymond Kapral. Mixed quantum-classical dynamics. *Journal of Chemical Physics*, 110:8919–8929, 1999.

166. Sara Bonella, Giovanni Ciccotti, and Raymond Kapral. Linearization approximations and liouville quantum–classical dynamics. *Chemical Physics Letters*, 484:399–404, 2010. URL https://www.sciencedirect.com/science/article/pii/S000926140901495X.

167. Craig C. Martens and Jian Yun Fang. Semiclassical-limit molecular dynamics on multiple electronic surfaces. *Journal of Chemical Physics*, 106:4918–4930, 2 1997.

168. Mark Sanier, Uwe Manthe, and Gerhard Stock. Quantum-classical liouville description of multidimensional nonadiabatic molecular dynamics. *Journal of Chemical Physics*, 114:2001–2012, 2001.

169. Steve Nielsen, Raymond Kapral, and Giovanni Ciccotti. Mixed quantum-classical surface hopping dynamics. *Journal of Chemical Physics*, 112:6543–6553, 4 2000.

170. Aaron Kelly and Thomas E. Markland. Efficient and accurate surface hopping for long time nonadiabatic quantum dynamics. *Journal of Chemical Physics*, 139, 7 2013.

171. William C. Pfalzgraff, Aaron Kelly, and Thomas E. Markland. Nonadiabatic dynamics in atomistic environments: Harnessing quantum-classical theory with generalized quantum master equations. *Journal of Physical Chemistry Letters*, 6:4743–4748, 12 2015.

172. Arnaldo Donoso, Yujun Zheng, and Craig C. Martens. Simulation of quantum processes using entangled trajectory molecular dynamics. *Journal of Chemical Physics*, 119:5010–5020, 9 2003.

173. Hyojoon Kim, Ali Nassimi, and Raymond Kapral. Quantum-classical liouville dynamics in the mapping basis. *Journal of Chemical Physics*, 129, 2008.

174. Aaron Kelly, Ramses Van Zon, Jeremy Schofield, and Raymond Kapral. Mapping quantum-classical liouville equation: Projectors and trajectories. *Journal of Chemical Physics*, 136, 2 2012.

175. Hyun Woo Kim and Young Min Rhee. Two-oscillator mapping modification of the poisson bracket mapping equation formulation of the quantum–classical liouville equation. *The Journal of Chemical Physics*, 153:214103, 12 2020.

176. Chang Yu Hsieh and Raymond Kapral. Nonadiabatic dynamics in open quantum-classical systems: Forward-backward trajectory solution. *Journal of Chemical Physics*, 137, 12 2012.

177. Yakov Braver, Leonas Valkunas, and Andrius Gelzinis. Benchmarking the forward-backward trajectory solution of the quantum-classical liouville equation. *The Journal of chemical physics*, 152:214116, 6 2020.

178. Xin He, Baihua Wu, Youhao Shang, Bingqi Li, Xiangsong Cheng, and Jian Liu. New phase space formulations and quantum dynamics approaches. *WIREs Computational Molecular Science*, 12: e1619, 2022. URL https://wires.onlinelibrary.wiley.com/doi/abs/10.1002/wcms.1619.

179. Robbie Grunwald, Aaron Kelly, and Raymond Kapral. Quantum dynamics in almost classical environments. pages 383–413, 2009. URL https://link.springer.com/chapter/10.1007/978-3-642-02306-4_12.

180. M. Hillery, R. F. O'Connell, M. O. Scully, and E. P. Wigner. Distribution functions in physics: Fundamentals. *Physics Reports*, 106:121–167, 4 1984.

181. John C. Tully. Mixed quantum-classical dynamics. *Faraday Discussions*, 110:407–419, 1998.

182. Morgane Vacher, Michael J. Bearpark, and Michael A. Robb. Direct methods for non-adiabatic dynamics: connecting the single-set variational multi-configuration gaussian (vmcg) and ehrenfest perspectives. *Theoretical Chemistry Accounts*, 135, 2016.

183. Joshua J. Goings, David B. Lingerfelt, and Xiaosong Li. Can quantized vibrational effects be obtained from ehrenfest mixed quantum-classical dynamics? *Journal of Physical Chemistry Letters*, 7:5193–5197, 2016.

184. Xiaosong Li, John C. Tully, H. Bernhard Schlegel, and Michael J. Frisch. Ab initio ehrenfest dynamics. *Journal of Chemical Physics*, 123, 2005.

185. David Mendive-Tapia, Morgane Vacher, Michael J. Bearpark, and Michael A. Robb. Coupled electron-nuclear dynamics: Charge migration and charge transfer initiated near a conical intersection. *Journal of Chemical Physics*, 139, 7 2013.

186. Alberto Castro, Heiko Appel, Micael Oliveira, Carlo A Rozzi, Xavier Andrade, Florian Lorenzen, M A L Marques, E K U Gross, and Angel Rubio. octopus: a tool for the application of time-dependent density functional theory. *physica status solidi (b)*, 243:2465–2488, 9 2006. URL https://doi.org/10.1002/pssb.200642067. https://doi.org/10.1002/pssb.200642067.

187. Christine M. Isborn, Xiaosong Li, and John C. Tully. Time-dependent density functional theory ehrenfest dynamics: Collisions between atomic oxygen and graphite clusters. *Journal of Chemical Physics*, 126, 2007.

188. Fan Wang, Chi Yung Yam, LiHong Hu, and GuanHua Chen. Time-dependent density functional theory based ehrenfest dynamics. *The Journal of Chemical Physics*, 135:044126, 7 2011.

189. Ari Ojanperä, Ville Havu, Lauri Lehtovaara, and Martti Puska. Nonadiabatic ehrenfest molecular dynamics within the projector augmented-wave method. *The Journal of Chemical Physics*, 136, 4 2012. URL https://doi.org/10.1063/1.3700800. 144103.

190. Joscha Hekele, Yi Yao, Yosuke Kanai, Volker Blum, and Peter Kratzer. All-electron real-time and imaginary-time time-dependent density functional theory within a numeric atom-centered basis function framework. *Journal of Chemical Physics*, 155, 10 2021.

191. Franco P. Bonafé, Bálint Aradi, Ben Hourahine, Carlos R. Medrano, Federico J. Hernández, Thomas Frauenheim, and Cristián G. Sánchez. A real-time time-dependent density functional tight-binding implementation for semiclassical excited state electron-nuclear dynamics and pump-probe spectroscopy simulations. *Journal of Chemical Theory and Computation*, 16: 4454–4469, 7 2020.

Bibliography

192. Luning Zhao, Andrew Wildman, Zhen Tao, Patrick Schneider, Sharon Hammes-Schiffer, and Xiaosong Li. Nuclear-electronic orbital ehrenfest dynamics. *Journal of Chemical Physics*, 153, 12 2020.

193. Alberto Guandalini, Caterina Cocchi, Stefano Pittalis, Alice Ruini, and Carlo Andrea Rozzi. Nonlinear light absorption in many-electron systems excited by an instantaneous electric field: a non-perturbative approach. *Physical Chemistry Chemical Physics*, 23:10059–10069, 2021.

194. H Flocard, S E Koonin, and M S Weiss. Three-dimensional time-dependent hartree-fock calculations: Application to ${}^{16}\{O\} + {}^{16}\{O\}$ collisions. *Physical Review C*, 17:1682–1699, 5 1978. URL https://link.aps.org/doi/10.1103/PhysRevC.17.1682.

195. Edbert J Sie, Clara M Nyby, C D Pemmaraju, Su Ji Park, Xiaozhe Shen, Jie Yang, Matthias C Hoffmann, B K Ofori-Okai, Renkai Li, Alexander H Reid, Stephen Weathersby, Ehren Mannebach, Nathan Finney, Daniel Rhodes, Daniel Chenet, Abhinandan Antony, Luis Balicas, James Hone, Thomas P Devereaux, Tony F Heinz, Xijie Wang, and Aaron M Lindenberg. An ultrafast symmetry switch in a weyl semimetal. *Nature*, 565:61–66, 2019. URL https://doi.org/10.1038/s41586-018-0809-4.

196. Petra Hein, Stephan Jauernik, Hermann Erk, Lexian Yang, Yanpeng Qi, Yan Sun, Claudia Felser, and Michael Bauer. Mode-resolved reciprocal space mapping of electron-phonon interaction in the weyl semimetal candidate td-wte2. *Nature Communications*, 11, 12 2020.

197. Dino Novko and Marko Kralj. Phonon-assisted processes in the ultraviolet-transient optical response of graphene. *npj 2D Materials and Applications*, 3, 12 2019.

198. S. A. Sato, J. W. McIver, M. Nuske, P. Tang, G. Jotzu, B. Schulte, H. Hübener, U. De Giovannini, L. Mathey, M. A. Sentef, A. Cavalleri, and A. Rubio. Microscopic theory for the light-induced anomalous hall effect in graphene. *Physical Review B*, 99, 6 2019.

199. Torben Winzer and Ermin Malić. Impact of auger processes on carrier dynamics in graphene. *Physical Review B - Condensed Matter and Materials Physics*, 85, 6 2012.

200. T. Winzer and E. Malic. The impact of pump fluence on carrier relaxation dynamics in optically excited graphene. *Journal of Physics Condensed Matter*, 25, 2 2013.

201. Gunnar Berghäuser, Ivan Bernal-Villamil, Robert Schmidt, Robert Schneider, Iris Niehues, Paul Erhart, Steffen Michaelis De Vasconcellos, Rudolf Bratschitsch, Andreas Knorr, and Ermin Malic. Inverted valley polarization in optically excited transition metal dichalcogenides. *Nature Communications*, 9, 12 2018.

202. Weitang Li, Jiajun Ren, and Zhigang Shuai. A general charge transport picture for organic semiconductors with nonlocal electron-phonon couplings. *Nature Communications*, 12:4260, 2021. URL https://doi.org/10.1038/s41467-021-24520-y.

203. Alex Zunger. Bridging the gap between density functional theory and quantum materials. *Nature Computational Science*, 2:529–532, 2022. URL https://doi.org/10.1038/s43588-022-00323-z.

204. Edoardo Baldini, Alfred Zong, Dongsung Choi, Changmin Lee, Marios H Michael, Lukas

Windgaetter, Igor I Mazin, Simone Latini, Doron Azoury, Baiqing Lv, Anshul Kogar, Yifan Su, Yao Wang, Yangfan Lu, Tomohiro Takayama, Hidenori Takagi, Andrew J Millis, Angel Rubio, Eugene Demler, and Nuh Gedik. The spontaneous symmetry breaking in ta2nise5 is structural in nature. *Proceedings of the National Academy of Sciences*, 120:e2221688120, 2023. URL https://www.pnas.org/doi/abs/10.1073/pnas.2221688120.

205. Ferd E Williams. Theoretical low temperature spectra of the thallium activated potassium chloride phosphor. *Physical Review*, 82:281–282, 4 1951. URL https://link.aps.org/doi/10.1103/PhysRev.82.281.2.

206. Melvin Lax. The franck-condon principle and its application to crystals. *The Journal of Chemical Physics*, 20:1752–1760, 11 1952.

207. Marios Zacharias and Feliciano Giustino. One-shot calculation of temperature-dependent optical spectra and phonon-induced band-gap renormalization. *Physical Review B*, 94, 2016.

208. Marios Zacharias and Feliciano Giustino. Theory of the special displacement method for electronic structure calculations at finite temperature. *Physical Review Research*, 2, 2020.

209. Tianlun Allan Huang, Marios Zacharias, D Kirk Lewis, Feliciano Giustino, and Sahar Sharifzadeh. Exciton–phonon interactions in monolayer germanium selenide from first principles. *The Journal of Physical Chemistry Letters*, 12:3802–3808, 4 2021. URL https://doi.org/10.1021/acs.jpclett.1c00264. doi: 10.1021/acs.jpclett.1c00264.

210. Jean Paul Nery and Francesco Mauri. Nonperturbative green's function method to determine the electronic spectral function due to electron-phonon interactions: Application to a graphene model from weak to strong coupling. *Physical Review B*, 105:245120, 2022.

211. Linqiu Li, Run Long, and Oleg V. Prezhdo. Charge separation and recombination in two-dimensional mos2/ws2: Time-domain ab initio modeling. *Chemistry of Materials*, 29:2466–2473, 3 2017. URL https://pubs.acs.org/doi/full/10.1021/acs.chemmater.6b03727.

212. Shi Qi Hu, Hui Zhao, Chao Lian, Xin Bao Liu, Meng Xue Guan, and Sheng Meng. Tracking photocarrier-enhanced electron-phonon coupling in nonequilibrium. *npj Quantum Materials*, 7, 12 2022.

213. Meng-Xue Guan, Xin-Bao Liu, Da-Qiang Chen, Xuan-Yi Li, Ying-Peng Qi, Qing Yang, Pei-Wei You, and Sheng Meng. Optical control of multistage phase transition via phonon coupling in $\{\{mote\}\}_{\{2\}}$. *Physical Review Letters*, 128:15702, 1 2022. URL https://link.aps.org/doi/10.1103/PhysRevLett.128.015702.

214. Kin Fai Mak, Keliang He, Jie Shan, and Tony F. Heinz. Control of valley polarization in monolayer mos2 by optical helicity. *Nature Nanotechnology*, 7:494–498, 2012.

215. K F Mak, K L McGill, J Park, and P L McEuen. The valley hall effect in mos$_2$ transistors. *Science*, 344:1489–1492, 2014. URL https://www.science.org/doi/abs/10.1126/science.1250140.

216. Cong Mai, Andrew Barrette, Yifei Yu, Yuriy G. Semenov, Ki Wook Kim, Linyou Cao, and Kenan Gundogdu. Many-body effects in valleytronics: Direct measurement of valley lifetimes

in single-layer mos2. *Nano Letters*, 14:202–206, 1 2014.

217. Antonija Grubišić Čabo, Jill A. Miwa, Signe S. Grønborg, Jonathon M. Riley, Jens C. Johannsen, Cephise Cacho, Oliver Alexander, Richard T. Chapman, Emma Springate, Marco Grioni, Jeppe V. Lauritsen, Phil D.C. King, Philip Hofmann, and Søren Ulstrup. Observation of ultrafast free carrier dynamics in single layer mos2. *Nano Letters*, 15:5883–5887, 9 2015.

218. Søren Ulstrup, Antonija Grubišić Čabo, Deepnarayan Biswas, Jonathon M. Riley, Maciej Dendzik, Charlotte E. Sanders, Marco Bianchi, Cephise Cacho, Dan Matselyukh, Richard T. Chapman, Emma Springate, Phil D.C. King, Jill A. Miwa, and Philip Hofmann. Spin and valley control of free carriers in single-layer ws2. *Physical Review B*, 95, 1 2017.

219. Yanping Liu, Yuanji Gao, Siyu Zhang, Jun He, Juan Yu, and Zongwen Liu. Valleytronics in transition metal dichalcogenides materials, 11 2019.

220. Lawson T Lloyd, Ryan E Wood, Fauzia Mujid, Siddhartha Sohoni, Karen L Ji, Po-Chieh Ting, Jacob S Higgins, Jiwoong Park, and Gregory S Engel. Sub-10 fs intervalley exciton coupling in monolayer mos 2 revealed by helicity-resolved two-dimensional electronic spectroscopy. *ACS Nano*, 15:26, 2021. URL www.acsnano.org.

221. Hualing Zeng, Junfeng Dai, Wang Yao, Di Xiao, and Xiaodong Cui. Valley polarization in mos 2 monolayers by optical pumping. *Nature Nanotechnology*, 7:490–493, 2012.

222. Malte Selig, Gunnar Berghäuser, Archana Raja, Philipp Nagler, Christian Schüller, Tony F Heinz, Tobias Korn, Alexey Chernikov, Ermin Malic, and Andreas Knorr. Excitonic linewidth and coherence lifetime in monolayer transition metal dichalcogenides. *Nature Communications*, 7:13279, 2016. URL https://doi.org/10.1038/ncomms13279.

223. Shengnan Xu, Chen Si, Yang Li, Bing Lin Gu, and Wenhui Duan. Valley depolarization dynamics in monolayer transition-metal dichalcogenides: Role of the satellite valley. *Nano Letters*, 21: 1785–1791, 2 2021.

224. Sambit Mitra, Álvaro Jiménez-Galán, Marcel Neuhaus, Rui E F Silva, Volodymyr Pervak, Matthias F Kling, and Shubhadeep Biswas. Lightwave-controlled band engineering in quantum materials. *ArXiv*, 2023.

225. Ming-Hsiu Hsieh, Alex Krotz, and Roel Tempelaar. A mean-field treatment of vacuum fluctuations in strong light–matter coupling. *The Journal of Physical Chemistry Letters*, 14:1253–1258, 1 2023.